QUARTERLY PROGRESS REPORT

No. 79

OCTOBER 15, 1965

MASSACHUSETTS INSTITUTE OF TECHNOLOGY

RESEARCH LABORATORY OF ELECTRONICS

CAMBRIDGE, MASSACHUSETTS

The Research Laboratory of Electronics is an interdepartmental laboratory in which faculty members and graduate students from numerous academic departments conduct research.

The research reported in this document was made possible by support extended the Massachusetts Institute of Technology, Research Laboratory of Electronics, by the following agencies.

Joint Services Electronics Program
Contract DA36-039-AMC-03200(E)

U. S. Air Force—Research and Technology Division
Contract AF 33(615)-1083

U. S. Navy—Office of Naval Research
Contract Nonr-1841-(42)

National Aeronautics and Space Administration
Grant NsG-334
Grant NsG-419
Grant NsG-496

National Institutes of Health
Grant MH-04737-05
Grant 5 RO1 NB 05462-02

National Science Foundation
Grant GP-2495
Grant GK-57
Grant GK-614

U. S. Atomic Energy Commission
Contract AT (30-1)-1842
Contract AT (30-1)-3285

Support of specific projects is acknowledged in footnotes to the appropriate sections.

MASSACHUSETTS INSTITUTE OF TECHNOLOGY

RESEARCH LABORATORY OF ELECTRONICS

QUARTERLY PROGRESS REPORT No. 79

October 15, 1965

Submitted by: H. J. Zimmermann
G. G. Harvey

TABLE OF CONTENTS

Personnel vii

Publications and Reports xv

Introduction xxi

GENERAL PHYSICS

I. Molecular Beams 1

High-Resolution Measurements with a Two-Cavity Maser — Analysis of Unresolved Spectra 1

II. Microwave Spectroscopy 5

Work Completed 5

A Study of Superconducting Domain Structures Using Optical Polarization Techniques 5

The Low-Temperature Use of Electrolytic Capacitors and Bifilar Pulse Transformers 5

Incoherent Phonon Propagation in x-cut Quartz 6

Incoherent Phonon Propagation in a Born-Kármán Lattice 7

Fermi Surfaces of Gallium Single Crystals by the Size Effect 14

III. Radio Astronomy 17

Observations of Microwave Emission from Atmospheric Oxygen 17

Remote Sounding of the Upper Atmosphere by Microwave Measurements 19

Varactor Parameters 26

Spectral-Line Radiometer System at Haystack 30

Studies of Radar Echoes from the Sun 34

IV. Optical and Infrared Spectroscopy 37

Temperature Dependence of the Far Infrared Reflectivity of Magnesium Stannide 37

V. Geophysics 43

Absorption of $\lambda = 4880\,\text{Å}$ Laser Beam by Argon Ions 43

Optical Doppler Radar I 45

Investigation of a Reflex Discharge 47

CONTENTS

VI. Noise in Electron Devices 51

Signal-to-Noise Ratio of Photomultiplier Spectrum Measurement and Counting Experiment 51

Quantum Analysis of Noise in the Laser Oscillator 58

Spectral Analysis of Laser Oscillator by Means of Higher Autocorrelation Functions 64

VII. Physical Electronics and Surface Physics 67

Simple Classical Model for the Scattering of Gas Atoms from Solid Surfaces 67

VIII. Physical Acoustics 73

Instability in Parallel Hydrodynamic and Magnetohydrodynamic Flows 73

PLASMA DYNAMICS

IX. Plasma Physics 77

Electron Density Measurements with a Laser Interferometer 77

Ion Cyclotron Resonance in a Radiofrequency Discharge — High Q Mode 83

X. Gaseous Electronics 85

Oscillations of an Inhomogeneous Plasma 85

Radiofrequency Dipole Resonance Probe 95

XI. Plasma Electronics 99

Active Solid-State Plasmas 99

Stimulated Emission of Phonons by Electrons Drifting along the Magnetic Field 99

Longitudinal Interaction of Electrons with Phonons in a Magnetic Field 104

Instabilities of Waves across the Magnetic Field 107

Instabilities in Transverse Waves along B_o 107

Instabilities in Quasi-static Waves across B_o 113

Quasi-linear Interaction of a Filamentary Electron Beam with a Plasma-Filled Waveguide 118

Dispersion Diagrams for Hot-Electron Plasmas 126

Nonadiabatic Diffusion in Toroidal Geometry 131

Measurement of Optical Gain of the Hollow-Cathode Discharge 133

Interaction of Particles with Circularly Polarized Waves in Plasmas 134

Nonadiabatic Magnetic Traps 139

Study of Laser Radiation Thomson-Scattered by an Electron Beam 143

Incoherent Scattering of Light from a Plasma. II. 145

CONTENTS

XII. Plasma Magnetohydrodynamics and Energy Conversion 149

Steam-Water Condensing Ejector Test Facility 149

Magnetohydrodynamic Channel-Flow Velocity Profiles and Entry Length 152

Thermionic Emission from a Tungsten Monocrystal in Oxygen 156

Characteristics of a Pure Alkali-Metal Vapor Plasma 167

Brayton Cycle Magnetohydrodynamic Power Generation 175

COMMUNICATION SCIENCES AND ENGINEERING

XIII. Statistical Communication Theory 177

Work Completed 177

Bioelectric Control of Prostheses 177

Functional Analysis of Systems Characterized by Nonlinear Differential Equations 177

Optimum Laguerre Expansion of Symmetric N^{th}-Order Functions 177

Some Problems in the Study of Nonlinear Systems with Feedback Loops 178

Measurement of Volterra Kernels of a Nonlinear System of Finite Order 178

Several Adaptive Binary Detection Problems 178

Digital Simulation of Analog Modulation Techniques over the Rayleigh Channel 178

Space-Time Signal Processing 178

Analog Communication through Separable Multipath Channels Characterized by Time-Varying Path Delays 178

Predistortion in No-Memory Filtering and in Quantization 179

A Statistical Study of VLF Atmospheric Noise 179

Determination of Optimum Nonlinear Systems for Gaussian Inputs by Crosscorrelation 179

Useful Approximations to Optimum Quantization 185

Time Jitter in Tunnel Diode Threshold-Crossing Detectors 191

Nonlinear Minimum-Mean Square Filtering with Application to Analog Communication 199

XIV. Processing and Transmission of Information 205

Optical Communication Systems 205

CONTENTS

XV. Cognitive Information Processing 207

Cognitive Processes 207

Variations of Perceived Distance with Apparent Motion 207

Picture Processing 211

Efficient Facsimile Transmission by Superposition of Pseudorandomly Scanned Pictures 211

Optimum Binary Code 214

Sensory Aids 216

Mobility Aid Simulator 216

Optical Character Recognition for Reading Machine Applications 219

Perceptual Model 227

Experiments in Reading Nonvisual Text 237

XVI. Communications Biophysics 247

Tissue Dynamics of Brain Tissue In Vitro 247

XVII. Computation Research 263

Generalized Polynomial Root-Finding Program for a Time-Shared Computer 263

Author Index 267

PERSONNEL

Administration

Professor H. J. Zimmermann, Director
Professor G. G. Harvey, Associate Director
Mr. R. A. Sayers, Assistant Director

Advisory Committee

Dean G. S. Brown
Prof. W. W. Buechner
Prof. W. B. Davenport, Jr.
Prof. P. Elias
Prof. G. G. Harvey
Prof. A. G. Hill
Prof. I. W. Sizer
Dean J. B. Wiesner
Prof. H. J. Zimmermann (Chairman)

Research Committee

Prof. S. C. Brown
Prof. L. J. Chu
Prof. M. Halle
Prof. G. G. Harvey
Prof. W. A. Rosenblith
Mr. R. A. Sayers
Prof. W. M. Siebert
Prof. L. D. Smullin
Prof. M. W. P. Strandberg
Prof. P. D. Wall
Prof. J. R. Zacharias
Prof. H. J. Zimmermann (Chairman)

Professors

Allis, W. P.
Barrett, A. H.
Bitter, F.
Brown, S. C.
Burke, G. F.
Chomsky, A. N.
Chu, L. J.
Eden, M.
Edgerton, H. E.
Elias, P.
Gold, B. (Visiting)
Gyftopoulos, E. P.
Halle, M.
Harvey, G. G.
Haus, H. A.
Hill, A. G.
Huffman, D. A.
Jakobson, R.
Kerrebrock, J. L.
King, J. G.
Kurylowicz, J. (Visiting)
Lee, Y. W.
Mason, S. J.
Minsky, M. L.
Rose, D. J.
Rosenblith, W. A.
Shannon, C. E.
Shapiro, A. H.
Siebert, W. M.
Smullin, L. D. (Absent)
Stevens, K. N.
Strandberg, M. W. P.
Wall, P. D.
Warren, B. E.
Waugh, J. S.
Wozencraft, J. M. (Absent)
Yilmaz, H. (Visiting)
Zacharias, J. R.
Zimmermann, H. J.

Associate Professors

Bekefi, G.
Bers, A.
Bolz, G. (Visiting)
Bose, A. G.
Brown, G. A.
Dennis, J. B.
Fodor, J. A.
Gallager, R. G.
Garland, C. W.
Geselowitz, D. B. (Visiting)
Hoffman, M. A.
Ingard, K. U.
Jackson, W. D.
Jacobs, I. M.
Katz, J. J.
Klima, E. S.
Kyhl, R. L.
Loewenthal, M.
Matthews, G. H.
McCune, J. E.
Oates, G. C.
Peake, W. T.
Penfield, P. L., Jr.

Associate Professors (continued)

Pomorska, Krystyna
Rafuse, R. P.
Schreiber, W. F.
Searle, C. L.
Taylor, E. F. (Visiting)
Teager, H. M.
Van Trees, H. L., Jr.

Assistant Professors

Andersen, J. (1)
Bernard, G. D. (1)
Billman, K. W.
Black, W. L. (1)
Blum, M.
Bobrow, D. G.
Brown, J. E.
Bruce, J. D.
Carabateas, E. R. (Absent)
Cheng, H.
Dean, L. W., III
Dupree, T. H.
Fiocco, G.
Getty, W. D.
Goutmann, M. M. (1)(Visiting)
Gray, P. R. (1)
Hall, J. L., II (Absent)
Heiser, W. H.
Hennie, F. C., III
Hoversten, E. V. (1)
Huang, T. S.
Ingraham, J. C.
Kahn, R. E. (1)
Katona, R. G. (1)
Kennedy, R. S.
Kiparsky, R. P. V.
Klatt, D. H.
Lee, H. B.
Lenoir, W. B. (1)
Lidsky, L. M.
Oppenheim, A. V. (1)
Perry, C. H.
Pierson, E. S. (1)
Prasada, B.
Shavit, A.
Siambis, J. G. (1)
Staelin, D. H. (1)
Stickney, R. E.
Stockham, T. G., Jr.
Suzuki, R. (Visiting)
Tretiak, O. J.
Troxel, D. E.
Weiss, R.
Weiss, T. F.
Yip, S.

Lecturers

Cohen, D. (Visiting)
Ferretti, E. F.
Graham, J. W.
Whitehouse, D. R.

Instructors

Bauer, R. F.
Burns, S. K.
Crystal, T. H.
Henke, W. L.
Kuroda, S-Y.
Landsman, E. E.
Nelsen, D. E.
Parker, R. R.
Prabhu, V. K.
Sachs, M. B.
Schindall, J. E.
Schneider, H. M.
Spann, R. N.

Research Associates

Barnett, G. O.
Dupress, J. K.
Durlach, N. I.
Garrett, M. F.
Hall, R. D.
Halverson, W. D.
Kolers, P. A.
Kornacker, K.
Lettvin, J. Y.
Papert, S. A.
Pfeiffer, R. R.
Smith, T. G., Jr.
Thompson, E.
Zisk, S. H.

Guests

Beddoes, M. P.
Bullowa, Margaret
Fraser, J. B.
Gragg, G. B.
Kessler, A. R.
Peterson, P. L.
Schnabel, C. P. J.
Sezaki, N.

(1) Engineering Postdoctoral Fellow

PERSONNEL

Visiting Scholar

Moreno Diaz, R.

Research Affiliates

Barlow, J. S.
Brodey, W. M.
Brown, R. M.
Crist, A. H.
Fohl, T.
Hart, R. W.
Howland, B.
Langbein, D.
Littleboy, H. S.
McLardy, T.
Walker, D. E.

Postdoctoral Fellows

Cunningham, A. W. B. (1)
Hartman, H. (1)
Heiss, W-D. (2)
Lampis, G. (3)
Natapoff, A. (1)
Newmark, R. A. (4)
Pickard, Barbara C. (1)
Pickard, W. F. (1)
Schwartz, A. (1)
Shofer, R. J. (1)
Slawson, A. W. (2)
Songster, G. F. (1)
Taub, A. (1)

R. L. E. Research Staff

Andrews, J. M.
Badessa, R. S.
Benhaim, N.
Bergman, J. G.
Brooks, T. H.
Chung, S-H.
Clayton, R. J.
Crowther, Patricia P.
Edwards, D. J.
Fischler, H.
Fratar, Gail M.
Ingersoll, J. G.
Ingham, K. R.
Jensen, E. R.
Jordan, F. N.
Kerllenevich, N.
Kiang, N. Y. S.
Kierstead, J. D.
Levy, Rachel J.
Lontai, L. N.
Mattison, E. M.
McCarthy, J. J.
McCulloch, W. S.
McLoud, Veronica
Menyuk, Paula
Mulligan, W. J.
Nacamuli, R. M.
O'Brien, F. J.
O'Rourke, Ann M.
Pennell, Martha M.
Pitts, W. H.
Porter, R. P.
River, Eleanor C.
Rojas Carona, R. R.
Rosebury, F.
Ryan, L. W.
Shaw, Marion L.
Vidale, Eda B.
Viertel, J. J.
Wickelgren, G. L.

Research Assistants

Arnstein, D. S. (5)
Austin, M. E. (5)
Bartsch, R. R.
Brown, T. S.
Chan, S. W-C.
Chandra, A. N.
Chang, R. P. H.
Chase, D.
Citron, A. L.
Dean, Janet P.
DeRijk, R. P. E.
Dethlefson, R.
DeWolf, J. B.
Edwards, K. R.
Engelmaier, W.
Evers, W. H., Jr.
Ezekiel, S.
Flynn, R. W.
Fraim, F. W.
Gabrielian, A.
Gadzuk, J. W.
Geis, M. L.
Grams, G. W.
Gustafson, K. T.
Hamawi, J. N.
Harlem, G. S.
Heggestad, H. M.
Hill, R. A.
Hofmann, T. R.
Huang, T.
Jameson, P. W.
Kalelkar, A. S.
Kitrosser, D. F.

(1) National Institutes of Health Fellow
(2) Research Laboratory of Electronics Fellow
(3) Senior Fellow, NASA
(4) National Science Foundation Fellow
(5) Lincoln Laboratory Staff Associate

Research Assistants (continued)

Klouman, P. H. B.
Kniazzeh, A. G. F.
Koons, H. C.
Kusse, B. R.
Levy, E. K.
Liu, J-H.
Logan, R. M.
Lou, D. Y-S.
Mark, R. G.
Maul, M. K.
Max, J.
McNary, C. A.
Mendelsohn, R. L.
Meyn, J. H.
Milne, D. C.
Moir, R. W.
Molden, J. C.
Molnar, C. E.
Moran, J. M.
Moses, J.
Nahvi, M.
Pauwels, H. J. E. H.
Portner, E. M., Jr.
Poussart, D. J. M.
Pruslin, D. H.
Qualls, C. B.
Ribbeck, C. S.
Rogers, A. E. E.
Scholl, M. M.
Simon, E. M.
Snyder, D. L.
Spiridon, A.
Steinbrecher, D. H.
Sun, P. B-S.
Sutherland, W. R. (1)
Taylor, M. G.
Thome, R. J.
Tomlinson, R. S.
Wagner, C. E.
Waller, M. H.
Wang, C. H.
Williams, J. A.
Woo, J. C.
Yamamoto, S.
Young, R. A.
Zeiders, G. W., Jr.

Graduate Assistants

Andrews, M. L.
Brenner, J. F.
Cohen, A. J.
Fertel, Jeanne H.
Fukumoto, A.
Garosi, G. A.
George, E. V.
Glenn, W. H., Jr.
Golub, R.
Guttrich, G. L.
Johnston, W. D., Jr.
Kronquist, R. L.
Kukolich, S. G.
Langdon, R. M., Jr.
Llewellyn-Jones, D. T.
Macon, J. L.
Manheimer, W. M.
Martin, J. F.
McClintock, J. E.
McEnally, T. E., Jr.
Pleasance, L. D.
Reifenstein, E. C., III
Reznek, S. R.
Rogoff, G. L.
Rosen, L.
Swain, D. W.
Tse, F. Y-F.
Waletzko, J. A.
Wilheit, T. T., Jr.
Wright, B. L.
Young, E. F.

Teaching Assistants

Dum, C. T.
Fehrs, D. L.
Glaser, J.
Graham, D. N. (Absent)
Guttman, D. S.
Lazarus, M. B.
Leonardi-Cattolica, A. M.
Levin, M. I.
Metz, P. J., III
Ng, L. C.
O'Leary, G. C.
Poulo, L. R.
Samis, M. A.
Schaefer, D. W.
Smith, T. B.
Speck, C. E.
Stone, E. T.
Veneklasen, L. H.
Woodson, N. D.

Graduate Students

Allen, R. J.
Anderson, J. A. (2)
Azevedo, J. C. deA. (3)
Baggeroer, A. B.
Baker, T. H.
Bedell, G. D., IV (5)
Bever, T. G.
Braida, L. D. (4)
Browne, E. W. (5)
Bucher, E. A. (4)
Caldwell, D. (4)
Callen, J. D. (6)

(1) Lincoln Laboratory Staff Associate
(2) Public Health Service Fellow
(3) Brazilian Navy Research Grant
(4) National Science Foundation Fellow
(5) National Defense Education Act Fellow
(6) Atomic Energy Commission Fellow

Graduate Students (continued)

Carter, R. J. (1)
Cesarski, W. V. (2)
Chapin, P. G. (3)
Clarke, J. F. (1)
Collins, L. D. (4)
Cornew, R. W. (5)
Crane, D. E. (4)
Davis, J. A. (4)
Decher, R. (6)
Doane, J. L. (7)
Dougherty, R. C. (1)
Emonds, J. E. (1)
Falconer, D. D. (8)
Feldman, D. A.
Fetz, E. E. (4)
Fidelholtz, J. L. (9)
Flannery, D. L. (4)
Freeman, J. A.
Gaut, N. E. (6)
Gentle, K. W. (4)
Goldfield, R. (9)
Good, W. E., Jr. (10)
Greenspan, R. L.
Gruber, J. S. (9)
Guinan, J. J., Jr. (4)
Guldi, R. L. (11)
Harris, J. W. (3)
Hartline, D. K. (3)
Hebel, W. T., Jr.
Hoft, D. J. (12)
Houtsma, A. J. M.
Huntington, T. A.
Jackendoff, R. S. (9)
Jenkins, L.
Katyl, R. H. (4)
Kawanami, M.
Kayne, R. S. (9)
Kimball, J. P. (1)
Kinzer, T. J., III (9)
Krackauer, J. J. (4)
Lee, F. F. (7)
Lieberman, M. A. (4)
Lubin, M. D.
Martinelli, M. A. (4)
McDowell, G. Q. (4)
Merrill, E. G. (13)
Mozzi, R. L. (12)
Mueller, P. E. (14)
Myers, Amy E. (9)
Neuburger, A.
Nolan, J. J., Jr.
Offenberger, A. A. (15)
Perlmutter, D. M. (9)
Peters, P. S., Jr.
Pilc, R. (16)
Pinkston, J. T., III (4)
Portinari, J. C. (17)
Rabiner, L. R. (4)
Rezende, S. M. (18)
Richters, J. S. (4)
Riehl, J. W. (19)
Ross, J. A. (4)
Ross, J. R. (1)
Schultz, H. M., III (4)
Shupe, D. S.
Simpson, J. I. (4)
Singer, J. J. (4)
Smith, C. V., Jr. (20)
Smith, R. S. (4)
Snow, M. S. (4)
Snyder, D. D. (4)
Spielman, Carol A. (9)
Stanley, R. J. (4)
Thomae, I. H. (4)
Thornburg, C. O., Jr.
von Bismark, G. (21)
Vugrinec, Z. (22)
Wallace, R. N. (4)
Warshawsky, Florence (3)
Weiner, S. D. (4)
Wickelgren, Barbara G. (4)
Wiederhold, M. L. (3)
Wilkins, D. R. (23)
Wolaver, D. H. (4)
Woo, Nancy H. (1)

Undergraduates (Thesis or Special Problems)

Bird, P. A.
Casperson, L.
Casseday, M. W.
Cowan, M. J.
Davidoff, I. G.
DeAngelis, D. L.
Doherty, R.
Funderburg, J. C.
Harris, R. V., III
Hess, R. A.
Hildebrand, S. J.

(1) National Institutes of Health Trainee
(2) Atomic Energy Commission Fellow
(3) National Institutes of Health Fellow
(4) National Science Foundation Fellow
(5) Sperry Fellow
(6) NASA Fellow
(7) Hertz Foundation Fellow
(8) Hughes Aircraft Fellow
(9) National Defense Education Act Fellow
(10) Upjohn Pharmaceutical Fellow
(11) National Science Foundation Trainee
(12) Raytheon Fellow
(13) Public Health Service Fellow
(14) American Can Company Fellow
(15) Canadian National Research Council Fellow
(16) Bell Telephone Laboratories Fellow
(17) National Research Council Fellow
(18) Institute of International Education Act Fellow
(19) Proctor and Gamble Fellow
(20) Gerard Swope Fellow
(21) Fulbright Fellow
(22) United Nations Fellow
(23) Thompson-Remo-Wooldridge Space Technology Fellow

Undergraduates (Thesis and Special Problems) (continued)

Jukvam-Wold, H. C.
Koralek, R. W.
Leary, A. R.
McQueen, D. H.
Memishian, J., Jr.
Naqvi, A. A.
Novenski, A. F.
Patterson, J.
Rientjes, J. F.
Robbins, W. B.
Schlitt, L. G.
Schwartz, P. R.
Smith, D. P.
Strand, T. F.
Swobada, W.
Vahey, D. W.
Warshaw, A. S.
Weidner, M. Y.
Wertz, R. P.
Williams, F. K.
Wolfe, P. D.

Student Employees

Ackerman, W. B.
Granek, H.
Haney, D. L.
Hendryx, S. A.
Howatt, J. R.
Lackner, J. R.
Michel, A.
O'Lague, P. H.
Partridge, L. D.
Perkell, J. S.
Pollack, R. A.
Prahl, E. L.
Ray, J. N.
Sahagan, Judith A.
Tuttle, S. D.
Tweed, D. G.
Ward, S. A.
Waters, J. W.
Wawzonek, J. J.
Westerfeld, E. C.

R. L. E. Administrative Staff

Donald F. Duffy
Hewitt, J. H.
Keyes, R. V., Jr.
Sayers, R. A.
Smith, P. L.
Thomas, Helen L.

Administrative Assistant

Bella, C. J.

Office Clerks

Barron, Gladys G.
Chaudhari, Karin
Durrah, Ann P.
Engler, R. R.
Gregor, C. A.
Hurley, Susan
Ippolito, Dorothy A.
Panarello, D. J.
Peck, J. S.
Ruggere, P. A.
Scalleri, Mary B.
Stagliola, Eleanor E.
Toebes, Rita K.

Typists

Foley, Ruth E.
Hurley, Janet P.
Kay, Judith T.
Murphy, Mary R.
Myers, Alberta L.
Napolitano, Joan V.

Technical Typists

Barnes, R. A.
Capron, Evelyn L.
Smee, P. E.

PERSONNEL

Secretaries

Bauer, Joan C.
Cangeme, Maria G.
Carbone, Angelina
Chorba, Linda D.
Cohen, Phyllis J.
Conwicke, Vera
Cullum, Barbara G.
Cummings, Jane F.
Finer, Faith L.
Geller, Elaine J.
Gordon, Linda S.
Hamilton, Martha C.
Harlem, Rosina P.
Hoover, Jane O.
Hurvitz, Rose S.
Johnson, Barbara A.
Kaloyanides, Venetia
Lipchinsky, Cheryl A.
Loeb, Charlotte G.
Lynch, Kathy Ann
McCarthy, Barbara L.
McEntee, Doris C.
Murray, Maureen P.
O'Neil, Patricia A.
Owens, Mary E.
Parrella Cynthia A.
Petone, Rosina C.
Pierce, Marilyn A.
Ponte, Mary J
Reid, Gloria C.
Ricker, Barbara J.
Riddle, Roberta M.
Russell, Susan P.
Smith, Clare F.
Wanner, Patricia A.

Engineering Assistants

Barrett, J. W.
Berg, A. E.
Crist, F. X.
Fontaine, C. L.
McKenzie, J. A.
Papa, D. C.
Thompson, J. B.

Technical Assistants

Arnn, JoAnn
Blum, G.
Byers, F. H.
Chase, Arbella P.
Grande, Esther D.
Graustein, Diana D.
Iverson, Alice I.
Major, Diane
Rabin, Sylvia G.
Randall, J. J.
Rosenthal, Kathryn F.
Shipley, Jenot W.
Swenson, Judith E.
Yaffee, M. A.

Technicians (Assigned to Research Groups)

Babcock, E. B.
Barrows, F. W.
Bauer, T. K.
Butler, R. E., Jr.
Connolly, J. T.
Cranmer, R. E.
DiPietro, P. J.
Fitzgerald, E. W., Jr.
Gay, H. D.
Iovine, M. A.
Kaufman, D. E.
Kelly, M. A.
Lewis, R. R.
Massey, L. N.
McLean, J. J.
Neal, R. W.
North, D. K.
Owens, R. C., Jr.
Robey, H. C.
Schwabe, W. J.
Sears, A. R.
Sprague, L. E.
Stevens, J. A.
Tortolano, A. J.
Yee, F. Q.

Technicians' Shop

Lorden, G. J., Foreman
Banks, E. C.
Fownes, Marilyn R.
Hill, Roland F.
MacDonald, K. R.

Laboratory Assistants

Beaton, Catherine M.
Cardia, P. F.
Massey, Barton E.
Miller, S. A.

PERSONNEL

Drafting Room

Navedonsky, C. P., Foreman
Donohue, J. B.
Hillier, Anna M.
Porter, Jean M.
Rollins, I. E.

Photographic Shop

Aradi, M. G.
Cook, J. F.
Karas, P.

Machine Shop

Keefe, J. B., Foreman
Aalerud, R. W.
Bletzer, P. W.
Brennan, J.
Bunick, F. J.
Cabral, M., Jr.
Carter, C. E.
Harvey, A. O.
Liljeholm, F. H.
Muse, W. J.
Reimann, W.
Ridge, P. A.
Ryan, J. F.
Sanromá, J. B.
Shmid, E.
Wentworth, W. G., Jr.

Tube Laboratory

Rosebury, Fred
Aucella, Alice G.
Griffin, J. L.
Leach, G. H., Jr.
MacDonald, A. A.

Glass Shop

Ryan, L. W.
DiGiacomo, R. M.
Doucette, W. F.

Stock Clerks

Doherty, R. H.
Haggerty, R. H.
Legier, D. O.
Morris, P. L.
Sharib, G.

Utility and Maintenance

Doiron, E. J., Foreman
Audette, A. G.
Lucas, W. G.
McDermott, J. F.
Riley, J. F.
Sincuk, J., Jr.
Thibodeau, D. S.

PUBLICATIONS AND REPORTS

MEETING PAPERS PRESENTED

Sixty-ninth Meeting, Acoustical Society of America, Washington, D. C.

June 2-5, 1965

W. T. Peake and J. J. Guinan, Jr., Middle Ear Movement in Anesthetized Cats

U. Ingard, Propagation of Acoustic Waves in Plasmas (invited)

Cold Spring Harbor Symposium on Quantitative Biology, Long Island, New York

June 6-11, 1965

J. Y. Lettvin and R. C. Gesteland, Speculations on Smell (invited)

First IEEE Annual Communications Convention, Boulder, Colorado

June 7-9, 1965

R. G. Gallager, Coding Concepts for Error Control

A. V. Oppenheim, Optimum Homomorphic Filters

H. L. Van Trees, Bounds on the Accuracy Attainable in the Estimation of Continuous Random Processes

Symposium on Far Infrared Transpose Spectroscopy, Mellon Institute, Pittsburgh, Pennsylvania

June 10-11, 1965

C. H. Perry, Application of Interferometric Techniques for Solid-State Spectroscopy (invited)

20th Annual Molecular Spectroscopy Symposium, Columbus, Ohio

June 14-18, 1965

C. H. Perry and E. F. Young, The Far Infrared Spectra of Some Cubic Perovskite Fluorides

G. Rupprecht, P. H. Smakula, C. H. Perry, and R. Geick, Normal Modes in Hexagonal Boron Nitride

Lectures, Technische Universität, Berlin

June 14-July 9, 1965

W. A. Rosenblith, June 14-18, Introduction and a Historical Overview. June 21-25 (a) A Communication Scientist's View of Sensory Systems, (b) Psychophysical Thresholds: Ordering and Scaling. June 28-July 2 (a) Information in Auditory and Visual Displays, (b) Fundamentals of Neuroelectric Activity. July 5-9 (a) Neuroelectric Responses to Sensory Stimuli, (b) Coding of Sensory Information: Model-Making in Relation to Sensory Communication

The 1965 Solid-State Device Research Conference, Princeton University, Princeton, New Jersey

June 21-23, 1965

A. Bers and A. L. McWhorter, Helicon Instabilities in Drifted Plasmas

T. Musha and A. Bers, Electron-Phonon Instabilities in a Magnetic Field

American Nuclear Society Meeting, Gatlinburg, Tennessee

June 21-24, 1965

P. S. Spangler, N. C. Rasmussen, and D. J. Rose, Fusion Reactor Blanket Experiment

American Physical Society Meeting, New York

June 23-25, 1965

W. D. Getty, Wave Amplification and Plasma Heating by Electron Beam-Plasma Interaction (invited)

E. B. Hooper, Jr. and G. Bekefi, Electron Density Measurements with a Laser Interferometer

Twenty-third Annual Conference on Electron Device Research, University of Illinois, Urbana, Illinois

June 23-25, 1965

A. Bers and A. L. McWhorter, Helicon Instabilities in Drifted Plasmas

T. Musha and A. Bers, Electron-Phonon Instabilities in a Magnetic Field

1965 Conference on Quantum Electronics, San Juan, Puerto Rico

June 28-30, 1965

R. Y. Chiao, Brillouin Scattering and the Dispersion of Hypersonic Waves

C. Freed and H. A. Haus, Amplitude Noise in Gaseous Lasers below and above the Threshold of Oscillation

International Symposium on Meteor Orbits and Dust, Smithsonian Astrophysical Observatory, Harvard University, Cambridge, Massachusetts

August 9-13, 1965

G. Fiocco, Evidence of the Influx of Micrometeorites in the Earth's Atmosphere by Optical Radar (invited)

NATO Summer Institute on Plasma Waves and Instabilities, Breukelen, Netherlands

August 9-20, 1965

J. Clarke, Single-Particle Interactions with Transverse Plasma Waves

Conference on Photoelectric and Secondary Electron Emission, University of Minnesota, Minneapolis, Minnesota

August 9-10, 1965

R. E. Stickney and P. B. Sun, Temperature Dependence of Photoemission from Tungsten

VIIIth European Congress on Molecular Spectroscopy, Copenhagen, Denmark

August 14-20, 1965

C. H. Perry, R. Geick, and E. F. Young, The Infrared Spectra of Some Cubic (ABF) Perovskite Fluorides (invited)

MEETING PAPERS PRESENTED (continued)

6th International Conference on Medical Electronics and Biological Engineering, Tokyo, Japan

August 22-27, 1965

W. D. Jackson, R. F. Lercari, and G. O. Barnett, Linear System Analysis of Blood-Pressure Regulation

American Physiological Society 17th Autumn Meeting, University of California, Los Angeles, California

August 23-27, 1965

P. R. Gray, N. Y. S. Kiang, and J. W. Shipley, Probabilities Associated with Spike Discharges in Auditory Nerve Fibers

N. Y. S. Kiang and M. B. Sachs, Effects of Acoustic Stimuli on Spontaneous Spike Discharges in Auditory Nerve Fibers

Seventh International Conference on Phenomena in Ionized Gases, Belgrade, Yugoslavia

August 22-27, 1965

T. J. Fessenden and L. D. Smullin, A Simple Technique for Measuring the Density of a Plasma in a Large Metal Box

T. J. Fessenden and L. D. Smullin, Electron Production and Loss in a Plasma Produced by Pulsed Microwaves at the Electron-Cyclotron Resonant Frequency

W. H. Glenn, Jr., S. C. Brown, and D. R. Whitehouse, Ion-Cyclotron Oscillations in a Plasma

E. B. Hooper, Jr. and G. Bekefi, Electron Density Measurements with a Laser Interferometer

J. C. Ingraham, Electron-Atom Collision Cross-Section Measurements in the Afterglow of a Pulsed Cesium Plasma

R. L. Kronquist and G. Bekefi, Radiation near Electron Cyclotron Harmonics from a Beam-Generated Plasma

Boulder Millimeter Wave and Far Infrared Conference, Estes Park, Colorado

August 30-September 1, 1965

J. M. Andrews, Jr. and M. W. P. Strandberg, Thermal Microwave Phonons

R. Geick and C. H. Perry, Solid-State Studies by Means of Fourier Transpose Spectroscopy

JOURNAL PAPERS ACCEPTED FOR PUBLICATION

(Reprints, if available, may be obtained from the Document Room, 26-327, Research Laboratory of Electronics, Massachusetts Institute of Technology, Cambridge, Massachusetts 02139.)

M. A. Arbib, Hitting and Martingale Characterisations of One-Dimensional Diffusions (Z. Wahrscheinlickheitstheorie)

V. Arunasalam and S. C. Brown, Microwave Scattering Due to Acoustic-Ion-Plasma-Wave Instability (Phys. Rev.)

H. A. Baldwin, S. Frenk, and J. Y. Lettvin, Glass-Coated Tungsten Microelectrodes (Science)

J. E. Brown, Dendritic Fields of Retinal Ganglion Cells of the Rat (J. Neurophysiol.)

J. E. Brown and J. A. Rojas, Rat Retinal Ganglion Cells: Receptive Field Organization and Maintained Activity (J. Neurophysiol.)

N. Chomsky and M. Halle, Some Controversial Questions in Phonological Theory (J. Ling.)

L. S. Cutler and C. L. Searle, Some Aspects of the Theory and Measurement of Frequency Fluctuations in Frequency Standards (Proc. IEEE)

J. M. Deutch and J. S. Waugh, Correlation Functions in Nuclear Relaxation. I. Analysis of Random Motions from Field Dependence of Relaxation Times (J. Chem. Phys.)

C. F. Doggenweiler and S. Frenk, Staining Properties of Lanthanum on Cell Membranes (Proc. Natl. Acad. Sci. U.S.)

Jeanne H. Fertel and C. H. Perry, Long-Wave Infrared Spectra of Alkali Salts of Platinum Halide Complexes (J. Phys. Chem. Solids)

G. D. Forney, Jr., On Decoding BCH Codes (IEEE Trans. (IT))

J. B. Heywood, An MHD Channel Flow with Temperature-Dependent Electrical Conductivity (AIAA J.)

U. Ingard, Acoustic Wave Generation and Amplification in a Plasma (Phys. Rev.)

W. A. Jeffers, Jr. and W. M. Whitney, Temperature and Frequency Dependence of Ultrasonic Absorption in Liquid Helium below 1° K (Phys. Rev.)

J. J. Katz, The Relevance of Linguistics to Philosophy (J. Philos.)

P. A. Kolers, Review of Communication Processes, Frank A. Geldar (ed.), Pergamon Press, New York, 1965. (Psychol. Rev.)

H. C. Koons and G. Fiocco, Proton Flow into the Magnetosphere (Sky and Telescope)

R. M. Logan and R. E. Stickney, Simple Classical Model for the Scattering of Gas Atoms from a Solid Surface (J. Chem. Phys.)

R. Melzack and S. K. Burns, Neurophysiological Effects of Early Sensory Restriction (Exptl. Neurol.)

D. L. Morse, Erratum: Plasma Rotation in a Hollow-Cathode Discharge (Phys. Fluids)

P. Penfield, Jr., Circuit Theory of Periodically Driven Nonlinear Systems (Proc. IEEE)

W. F. Pickard, On the Propagation of the Nervous Impulse down Medullated and Unmedullated Fibres (J. Theoret. Biol.)

H. Putnam, Trial and Error Predicates and the Solution to a Problem of Mostowski (J. Symbolic Logic)

G. C. Theodoridis and E. P. Gyftopoulos, Cesium Ion Beam Neutralization with Energetic Electrons (AIAA J.)

JOURNAL PAPERS ACCEPTED FOR PUBLICATION (continued)

A. Taub and P. O. Bishop, The Spinocervical Tract: dorsal column linkage, conduction velocity, primary afferent spectrum (Exptl. Neurol.)

H. L. Van Trees, Analog Communication over Randomly Time-Varying Channels (IEEE Trans. (IT))

H. L. Van Trees and C. J. Boardman, Optimum Angle Modulation (IEEE Trans. (CS))

C. G. Wade and J. S. Waugh, Temperature and Pressure Dependence of Self-Diffusion in Liquid Ethane (J. Chem. Phys.)

F. M. Wiener, R. R. Pfeiffer, and A. S. N. Backus, On the Sound Pressure Transformation by the Head and Auditory Meatus of the Cat (Acta Oto-Laryngol.)

J. S. Waugh and E. L. Wei, Strong Coupling in Nuclear Resonance Spectra. V. Perturbation Theory for the Extreme Coupling Case (J. Chem. Phys.)

LETTERS TO THE EDITOR ACCEPTED FOR PUBLICATION

J. M. Deutch and J. S. Waugh, On the Detectability of the Quadratic NMR Electric Field in Liquids (J. Chem. Phys.)

T. S. Huang and A. Gabrielian, Minimizing the Maximum Signal Energy (IEEE Trans. (CS))

C. J. Johnson, Some Dielectric and Electro-optic Properties of $BaTiO_3$ Single Crystals (Appl. Phys. Letters)

E. B. Hooper, Jr. and G. Bekefi, A Laser Interferometer for Repetitively Pulsed Plasma (Appl. Phys. Letters)

B. T. Lubin, T. L. Földvári and W. D. Jackson, Nonlinear Network for the Measurement of the Relative Electrical Conductivity Between Highly Conducting Materials (Rev. Sci. Instr.)

H. B. Lee, An Additional Realization Cycle for LC Impedances (IEEE Trans. (CT))

P. Penfield, Jr., The Lorentz Force (Proc. IEEE)

D. Snyder, Some Useful Expressions for Optimum Linear Filtering in White Noise (Proc. IEEE)

D. L. Snyder, Some Useful Expressions for Optimum Filtering in White Noise. II. (Proc. IEEE)

O. J. Tretiak and T. S. Huang, Resistance of an N-Dimensional Cube (Proc. IEEE)

TECHNICAL REPORTS PUBLISHED

(These and previously published technical reports, if available, may be obtained from the Document Room, 26-327, Research Laboratory of Electronics, Massachusetts Institute of Technology, Cambridge, Massachusetts 02139.)

439 J. E. Savage, The Computation Problem with Sequential Decoding

440 G. David Forney, Jr., Concatenated Codes

SPECIAL TECHNICAL REPORT PUBLISHED

(These monographs are available from The M. I. T. Press, E19-741, Massachusetts Institute of Technology, Cambridge, Massachusetts 02142.)

Number 12 Robert R. Capranica, The Evoked Vocal Response of the Bullfrog - A Study of Communication by Sound (M. I. T. Research Monograph No. 33)

SPECIAL PUBLICATIONS

J. S. Barlow, Review of Techniques and Methods of Electroencephalography (in Russian), V. G. Kratin, N. P. Bechtereva, V. I. Gusselnikov, V. A. Kozhevinkov, B. T. Senichenkov, V. V. Ussov. (Publishing House of the Academy of Sciences of the USSR, Moscow and Leningrad, 1963, 312 p.) (EEG Clin. Neurophysiol. and Medical Electronics and Biological Engineering (J. Int. Fed. Med. Electronics))

J. S. Barlow, Review of Contemporary Methods of EEG Analysis (in Russian), V. A. Koskevnikov and R. M. Meshcharski. (State Publishing House of Medical Literature, Moscow, 1963, 325 p.) (EEG Clin. Neurophysiol. and Medical Electronics and Biological Engineering (J. Int. Fed. Med. Electronics))

J. S. Barlow, Review of Progress in Brain Research, Vol. 1: Brain Mechanism, edited by G. Moruzzi, A. Fessard and H. H. Jasper. (Elsevier Publishing Company, Amsterdam, 1963) (Am. J. Med. Electronics)

B. Liu and R. E. Kahn, Optimum Prefiltering in Sampled Data Systems with Read-in Jitter (1965 IEEE International Convention Record, Part 7, pp. 127-133)

G. H. Matthews, Hidatsa Syntax (Mouton and Co., The Hague, 1965)

W. S. McCulloch, Lekton - An Introduction to 'The Logical Structure of Mind' by Eilhard von Domarus (Proc. Symposium on Communication Theory and Research, University of Missouri in Kansas City, March 24-25, 1965)

INTRODUCTION

This report, the seventy-ninth in a series of quarterly progress reports issued by the Research Laboratory of Electronics, contains a review of the research activities of the Laboratory for the three-month period ending August 31, 1965. Since this is a report on work in progress, some of the results may not be final.

GENERAL PHYSICS

I. MOLECULAR BEAMS*

Prof. J. R. Zacharias	R. S. Badessa	S. G. Kukolich
Prof. J. G. King	J. F. Brenner	F. J. O'Brien
Prof. C. L. Searle	R. Golub	R. D. Posner
Prof. K. W. Billman	G. L. Guttrich	C. O. Thornburg, Jr.
Prof. E. F. Taylor	W. D. Johnston, Jr.	L. H. Veneklasen

A. HIGH-RESOLUTION MEASUREMENTS WITH A TWO-CAVITY MASER – ANALYSIS OF UNRESOLVED SPECTRA

The resonance pattern produced by the two-cavity maser spectrometer[1] for a single molecular resonance line is the typical "Ramsey" line shape shown in Fig. I-1, and it may be easily analyzed to determine the resonance frequency. There are many cases in the ammonia inversion spectrum, however, in which the resonance lines are so close that these patterns overlap and the lines are not completely resolved. In order to analyze such cases a computer program was written to perform a least-squares fit to the experimental spectrum by using a superposition of the known single-line resonance patterns. This program was used successfully to determine the amplitudes and frequencies of three overlapping lines.

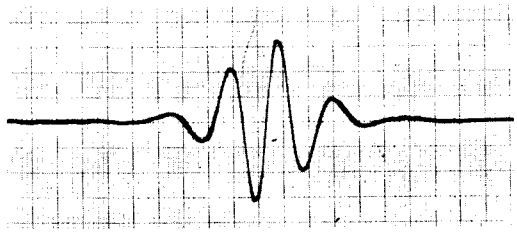

Fig. I-1. Single line Ramsey function with $\phi = 0$.

One case that was analyzed successfully is the main line ($\Delta F = \Delta F_1 = 0$) of the $J = 3$, $K = 3$ inversion transition. The signal-to-noise ratio is very good in this case (1000/1). The resonance pattern for a single line can be accurately represented by the function $A \exp\left(-b(f-f_o)^2\right) \sin\left(\pi(f-f_o)/\Delta f - \phi\right)$. This spectrum contains three overlapping functions of this form. We have assumed that these functions are linearly superposed, since the microwave receiver response is linear and the microwave power from the molecules is considerably less (20 db less in the second cavity) than the stimulating signal. The experimental spectrum (circled points in Fig. I-2) is divided into two parts, and the part containing the line that is least influenced by the others is used to determine values for the phase ϕ_1, the frequency f_1, and the amplitude A_1 which give the best fit to that part of the spectrum. We assume that the phase ϕ will be the same for all three components, so we use the value of ϕ_1 for the phase of the other components. The second part of the spectrum is then used to determine the frequencies and amplitudes of the second and third components, while the amplitude and frequency of the first component are held constant. Then the first part is corrected for the influence of the second and third

*This work was supported principally by the Joint Services Electronics Program (Contract DA36-039-AMC-03200(E).

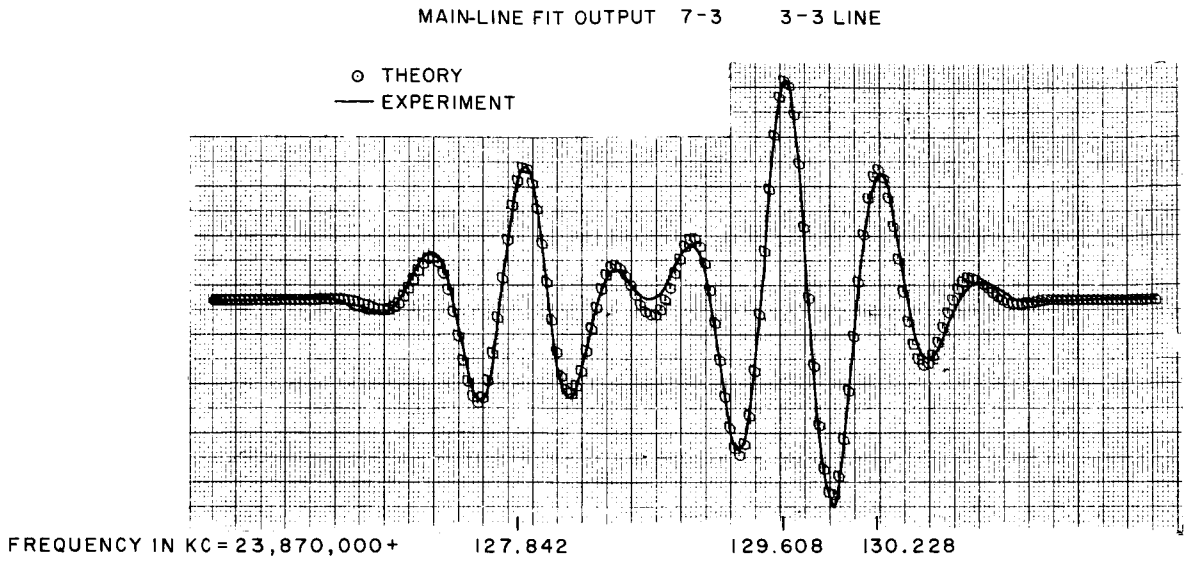

Fig. I-2. Results of the fit procedure for one set of data. Circles represent experimental points, line is theoretical curve which gives best fit.

Table I-1. Results of the fit procedure for three sets of data.

MAIN LINE FIT RESULTS 3 - 3 LINE

FREQUENCIES IN KC

FIT RESULT	AVERAGE	F1
23,870,127.842	23,870,127.88167	3
23,870,127.895	23,870,127.88167	3
23,870,127.908	23,870,127.88167	3
23,870,129.608	23,870,129.61700	4
23,870,129.608	23,870,129.61700	4
23,870,129.635	23,870,129.61700	4
23,870,130.228	23,870,130.22367	2
23,870,130.204	23,870,130.22367	2
23,870,130.239	23,870,130.22367	2

STANDARD DEVIATION = .01992

components and a better value of ϕ_1 is obtained. This procedure is repeated many times to minimize effects of interdependence of the variables.

This whole fit is then carried out for various values of b and Δf, and then the fit giving the smallest standard deviation over the whole pattern is chosen. ϕ, Δf, and b are assumed to be the same for all three components in one experimental curve. These parameters may be varied experimentally, ϕ may have any value from 0 to 2π, but Δf and b may only be varied by ±20 per cent. The typical molecular resonance linewidth, Δf, for the present device is 350 cps and $1/b \cong (2\Delta f)^2$. The result of one of the fits is shown in Fig. I-2. Table I-1 shows the results of fits to three different sets of experimental data which had different values of ϕ, Δf and b. The standard deviation of the frequencies of the component lines in these fits was 20 cps.

I wish to thank my wife, Joan Kukolich, for programming help and the Computation Center, M. I. T., for supplying the computer time.

S. G. Kukolich

II. MICROWAVE SPECTROSCOPY*

Prof. M. W. P. Strandberg
Prof. R. L. Kyhl
Dr. J. M. Andrews, Jr.
A. Fukumoto
J. G. Ingersoll
J. D. Kierstead
M. K. Maul
T. E. McEnally
S. Reznek
L. Rozen
W. J. Schwabe

A. WORK COMPLETED

1. A STUDY OF SUPERCONDUCTING DOMAIN STRUCTURES USING OPTICAL POLARIZATION TECHNIQUES

This work has been completed by Lowell Rosen and submitted as a thesis to the Department of Physics, M. I. T., August 1965, in partial fulfillment of the requirements for the degree of Master of Science. An abstract of the thesis follows.

The superconducting magnetic structures of Tantalum have been studied by using the effect of optical Faraday rotation in Cerous Metaphosphate glass. Photographs of the Tantalum specimen showing both the intermediate and mixed states of the metal are included. The sequence of magnetization pictures shows the magnetic structures as the magnetic field is first increased in one direction, decreased to zero, and then increased in the opposite direction. Part of the sequence of photographs clearly indicates the phenomenon of the flux-jumping characteristic of Type II and hard superconductors.

M. W. P. Strandberg

2. THE LOW-TEMPERATURE USE OF ELECTROLYTIC CAPACITORS AND BIFILAR PULSE TRANSFORMERS

A Master's thesis with this title has been submitted by Michael K. Maul to the Department of Electrical Engineering, M.I. T., August 1965. A summary of the thesis follows.

The use of electrolytic capacitors and bifilar pulse transformers in liquid Helium has been found to be practical if the following conditions are noted. The capacitance at 4.2°K of Sprague 150° tantalums is 15 per cent of the room-temperature value. The values measured were in the range 1 mfd-47 mfd at room temperature.

Bifilar transformers with ferrite cores were found inadequate to pass 1 μsec pulses at 4.2°K. This was due to the large decrease in permeability as the temperature decreases. YIG was found to have a sufficiently low loss of permeability to pass these pulses.

R. L. Kyhl

*This work was supported principally by the Joint Services Electronics Program (Contract DA36-039-AMC-03200(E).

B. INCOHERENT PHONON PROPAGATION IN X-CUT QUARTZ

There is some evidence to indicate that the unknown signals reported in previous experiments[1,2] are caused by ringing in the pulse circuit. At low temperatures the source impedance of our superconducting bolometer usually was decreased to values that were of the order of 0.1 Ω, a value that is somewhat lower than the series resistance in the stainless-steel transmission line and numerous coaxial adapters that were used for the video signal. These conditions can produce ringing in a pulse transformer circuit. In a series of subsequent experiments we increased the impedance of the bolometric film by removing portions of it after the leads were attached. This is shown in

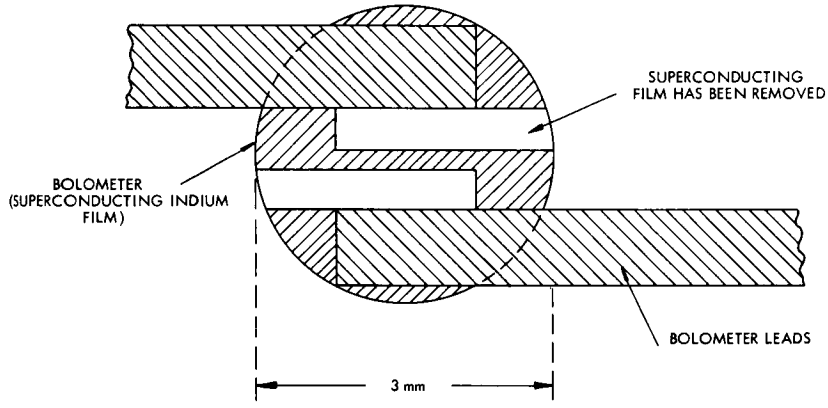

Fig. II-1. Bolometer geometry. Illustrating schematically the manner in which the low-temperature impedance of the superconducting bolometer was increased from 0.1 to 1 Ω by removing portions of the film.

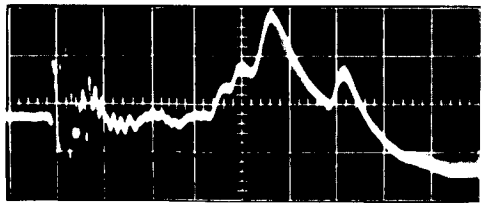

Fig. II-2.

Pulses of incoherent phonons in x-cut quartz. Four distinct pulses are resolved by the 1-Ω bolometer. All have been accounted for theoretically. The L stands for longitudinal; FT, fast-transverse; ST, slow-transverse; O, oblique. Oscilloscope sweep rate, 1 μsec/cm.

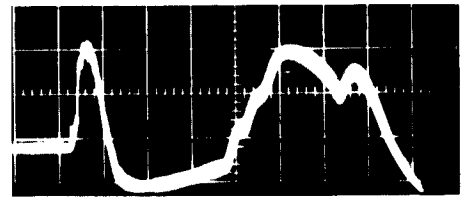

Fig. II-3.

Pulses of incoherent phonons in x-cut quartz at a power level close to breakdown in the waveguide. Elastic dispersion in the quartz is beginning to produce an observable effect on the pulsewidth. A shift in the peak of the pulse in the direction of increasing time was also observed.

detail in Fig. II-1. Signals detected by this bolometer did not reveal any more than four distinct pulses: the three pure modes and the oblique mode discussed at length in the previous report.[2] In Fig. II-2 we show a typical incoherent phonon signal in an x-cut quartz rod 19 mm long detected by the 1-Ω bolometer. The sweep rate is 1 μsec/cm.

We increased the microwave power incident upon the aluminum film that generates the heat pulse in an attempt to display the dispersion effects that we expect from the theoretical discussion of the preceeding section. At a power level extremely close to the onset of breakdown in the waveguide we were able to obtain the trace shown in Fig. II-3. Because of an intermittent breakdown problem in the waveguide, we could only estimate that the incident peak power was several kilowatts. Pulse broadening is quite evident, and a shift of the peak of the pulse in the direction of increasing time was observed. A detailed comparison of these pulse shapes with the theory presented in Sec. II-C will require a video amplifier with an increased bandwidth.

The author wishes to express his appreciation to Mr. M. C. Graham who carried out the experiments.

J. M. Andrews, Jr.

References

1. J. M. Andrews, Jr., "Observations of Incoherent Phonon Propagation in X-cut Quartz," Quarterly Progress Report No. 77, Research Laboratory of Electronics, M.I.T., April 15, 1965, pp. 7-15.

2. J. M. Andrews, Jr., "Incoherent Phonon Propagation in X-cut Quartz," Quarterly Progress Report No. 78, Research Laboratory of Electronics, M.I.T., July 15, 1965, pp. 10-15.

C. INCOHERENT PHONON PROPAGATION IN A BORN-KÁRMÁN LATTICE

The simplest model that includes dispersion in a description of the lattice dynamics of a three-dimensional crystal is that proposed originally by Born and von Kármán.[1] This model treats a crystal as an elastically isotropic continuum except that the linear dispersion relationship has been replaced by the sinusoidal dispersion function obtained from the one-dimensional linear chain model. From some of the x-ray studies of lattice vibrations[2] it would appear that a sinusoidal dispersion relation is a reasonably good representation, provided that the phase of the function can be scaled to fit the experimental data.

Phonon dispersion in crystalline quartz has recently been studied by neutron diffraction techniques.[3] There is good agreement between the experimental results obtained along the c crystallographic axis and the theory based upon a Born-Kármán model. We are interested, however, in the dispersion of the acoustic modes whose wave vectors are directed along the x axis. The results of a calculation based upon the Born-Kármán

model are shown in Fig. II-4. The frequencies of the three acoustic branches of the vibrational spectrum have been plotted as a function of the x component of the elastic

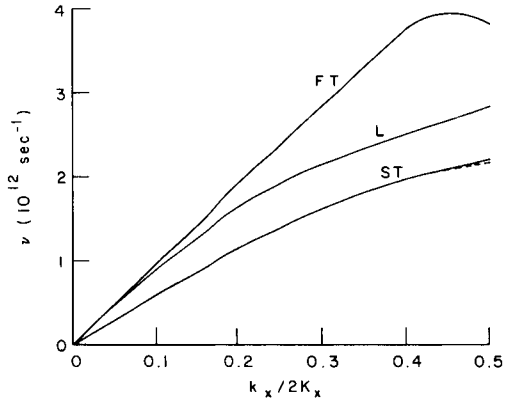

Fig. II-4.

Elastic dispersion in a Born-Kármán lattice. Solid lines were calculated by Elcombe.[4] L stands for longitudinal polarization; FT, fast-transverse; ST, slow-transverse. The dotted line is the sinusoidal function of Eq. 1.

wave vector. These are shown by the solid lines in the figure. We have attempted to approximate the dispersion of the slow-transverse mode by a sinusoidal function given by

$$\nu = \nu_o \sin\left(\frac{\epsilon \pi k_x}{2K_x}\right) \text{sec}^{-1}, \tag{1}$$

where ν is the frequency of the mode, ν_o is the maximum frequency of the mode that can be transmitted along the x axis of the crystal; ϵ is an adjustable parameter of approximately unity, k_x is the x component of the elastic wave vector, and K_x is the edge of the Brillouin zone in the x direction. We have fitted this function to the slow-transverse mode by choosing $\epsilon = 0.88$ and $\nu = 2.21 \times 10^{12}$ sec^{-1}. Equation 1 is shown by the dotted line in Fig. II-4.

We wish to examine the nature of the propagation of an incoherent superposition of fast-transverse elastic modes in α quartz whose wave vectors are all directed along the x crystallographic axis, but whose frequencies are characterized by a black-body distribution function. We seek a function P(t,x) that represents the rate of elastic energy flow at any time t and at any point x along an x-cut rod. We shall assume that the temperature of the quartz is at absolute zero and the crystal is perfect so that the frequency-dependent scattering process can be neglected. In order to represent the quantity P(0, 0) as a Dirac delta function,

$$P(t, 0) = W\delta(t) \text{ watts.} \tag{2}$$

When this function is integrated over all time, we obtain the total energy, W joules, contained in the thermal spike represented by Eq. 2. The spatial character of the function is contained in the expression

$$P(0, x) = UV\delta(x/v) \text{ watts}, \tag{3}$$

where U is the elastic energy density, and V is an arbitrary volume. Since

$$\frac{dW}{dx} = \frac{dW}{dt}\frac{dt}{dx} = \frac{P(0, x)}{v}, \tag{4}$$

the entire energy of the thermal spike at t = 0 can be obtained again by integration of Eq. 4 from $-\infty < x < +\infty$. Since this is equal to the integral of Eq. 2, we have

$$W = UV. \tag{5}$$

The physical interpretation of the volume V can be clarified by noting that a thin metallic film evaporated onto the end of a crystalline quartz rod can be excited by microwave power of extremely short duration, τ. This pulse injects energy into the elastic modes of the crystal, and for those modes whose velocity is v and whose wave vectors are directed along the axis of the rod, this energy is initially contained within a volume

$$V = Av\tau, \tag{6}$$

where A is the cross-section area of the rod. The velocity v of the modes is actually a function of their frequency ν, according to Eq. 1, but in the limit $\nu \to 0$ this has no effect on the normalization volume, V.

The elastic energy density U is assumed to be characterized by a black-body distribution

$$U = \int_0^{\nu_o} \frac{h\nu g(\nu)\, d\nu}{e^{\frac{h\nu}{k_B T}} - 1}, \tag{7}$$

where h is Planck's constant, k_B is Boltzmann's constant, T is the absolute temperature, and $g(\nu)$ is the density of states. The thermal power as a function of time and space P(t, x) of a heat pulse, whose initial form can be characterized by a Dirac delta function, is therefore given by

$$P(t, x) = Av\tau \int \frac{h\nu g(\nu)\, \delta(t - x/v)\, d\nu}{e^{\frac{h\nu}{k_B T}} - 1}, \tag{8}$$

Recall that v is the group velocity of the thermal phonons, and can be obtained by differentiating Eq. 1:

$$v = 2\pi \frac{d\nu}{dk} = \frac{\epsilon \pi^2 \nu_o}{K_x} \cos\left(\frac{\epsilon \pi k_x}{2K_x}\right) \tag{9}$$

or

$$v(\nu) = v_o\left[1-(\nu/\nu_o)^2\right]^{1/2}, \tag{10}$$

where

$$v_o = \frac{\epsilon\pi^2\nu_o}{K_x}.$$

The limiting group velocity for very low frequencies is v_o.

The usual approximation for the elastic density of states in the Born-Kármán lattice is to assume that the modes are distributed equally over a sphere in wave-vector space. This yields

$$g(\nu)\,d\nu = \frac{3k^2}{2\pi^2}\left(\frac{dk}{d\nu}\right)d\nu. \tag{11}$$

If the anisotropy of quartz is neglected, Eqs. 1 and 11 yield

$$g(\nu) = \frac{12\pi\nu_o^2}{v_o^3}\left[\sin^{-1}(\nu/\nu_o)\right]^2\left[1-(\nu/\nu_o)^2\right]^{-1/2}. \tag{12}$$

This density-of-states function has been plotted as a function of the reduced frequency parameter (ν/ν_o) in Fig. II-5. There is a singularity at $\nu/\nu_o = 1$, and the Van Hove

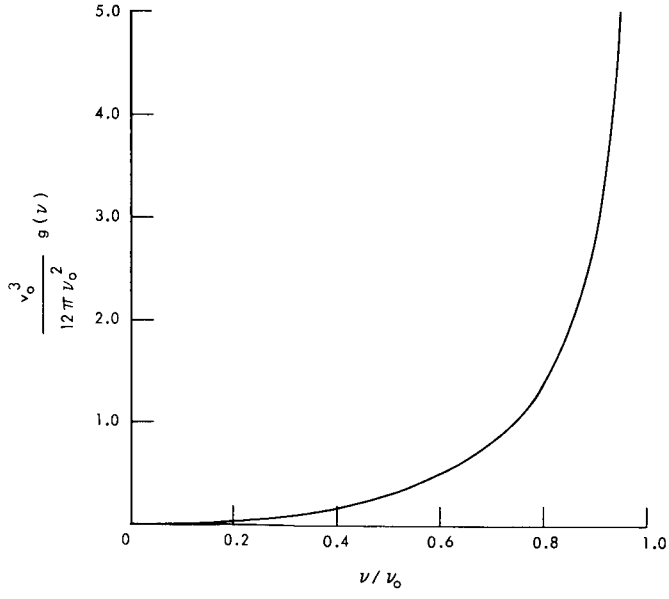

Fig. II-5.

Elastic density of states in a Born-Kármán lattice. This model produces a singularity at ν/ν_o and the Van Hove critical points[5] are absent, but the behavior of $g(\nu)$ at low frequencies is typical of some of the experimentally determined vibration spectra of solids.[2]

critical points[5] do not exist. The low-frequency portion of this function, however, reproduces the experimentally determined vibrational spectra of crystals[2] quite well. At

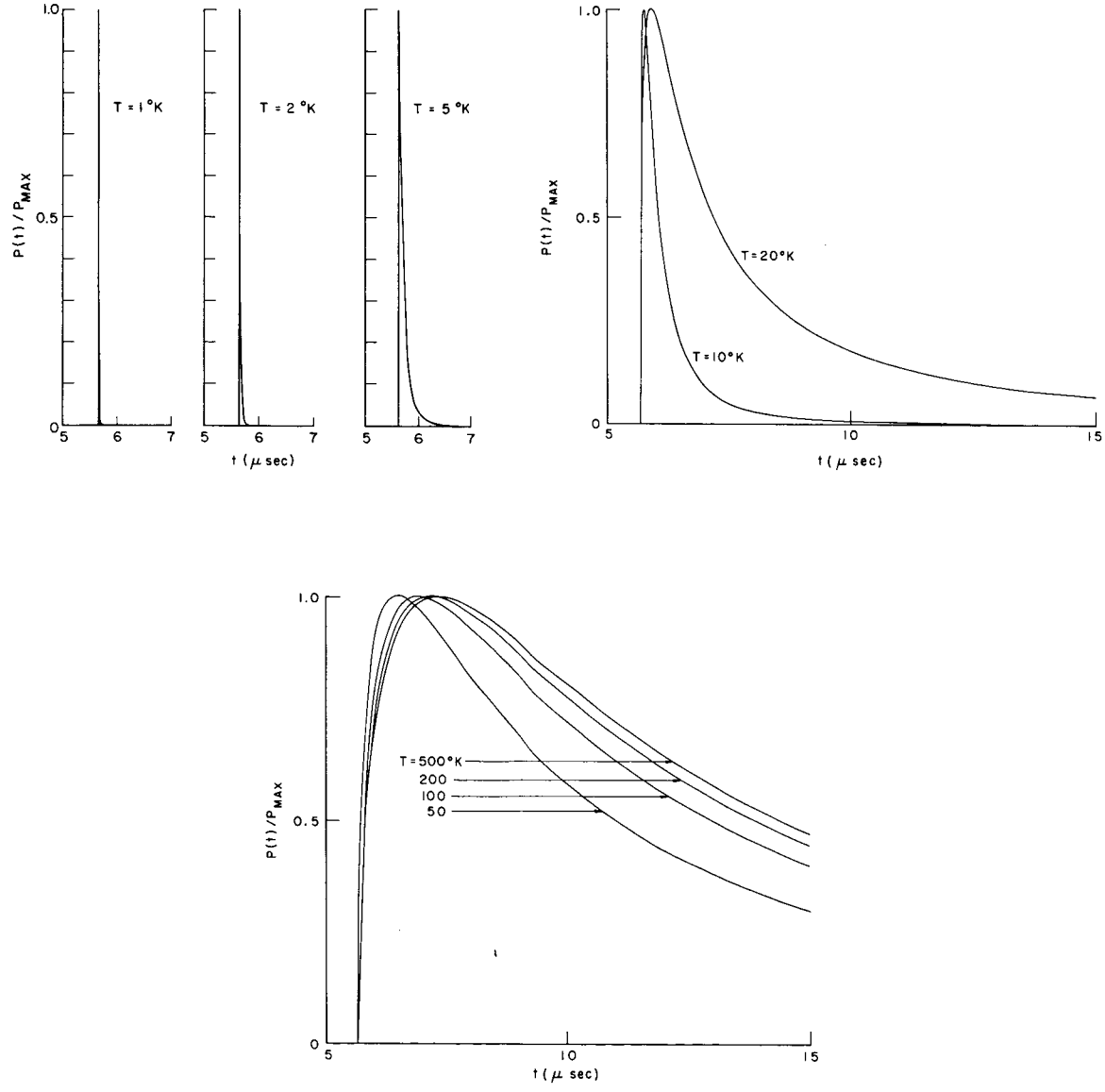

Fig. II-6. Thermal spike that has been propagated through a Born-Kármán lattice. The frequency distribution of the phonons composing the spike has been characterized by black-body distributions at varying temperatures between 1°K and 500°K. The effects of dispersion become very pronounced at the higher temperatures.

temperatures close to absolute zero, Eq. 12 can be used as an excellent approximation.

The elastic density-of-states function $g(\nu)$ given by Eq. 12 is introduced into Eq. 8. The integration variable is changed to

$$t' = \frac{}{v_o}\left[1-(\nu/\nu_o)^2\right]^{-1/2}, \tag{13}$$

and we obtain

$$P(t, x) = \frac{12\pi hA\tau\nu_o^4}{xv_o}\begin{cases}(u\cos^{-1}u)^2\left(e^{\gamma\sqrt{1-u^2}}-1\right)^{-1} & x/v_o < t < \infty \\ 0 & t \leq x/v_o\end{cases} \tag{14}$$

where

$$u = x/v_o t \qquad \gamma = h\nu_o/k_B T.$$

We have evaluated Eq. 14 for the slow-transverse mode in an x-cut quartz rod, 3 mm in diameter and 19 mm long. The value for v_o is the experimentally determined ultrasonic velocity 3.36×10^5 cm/sec, and the value for ν_o was obtained by fitting a sinusoidal,

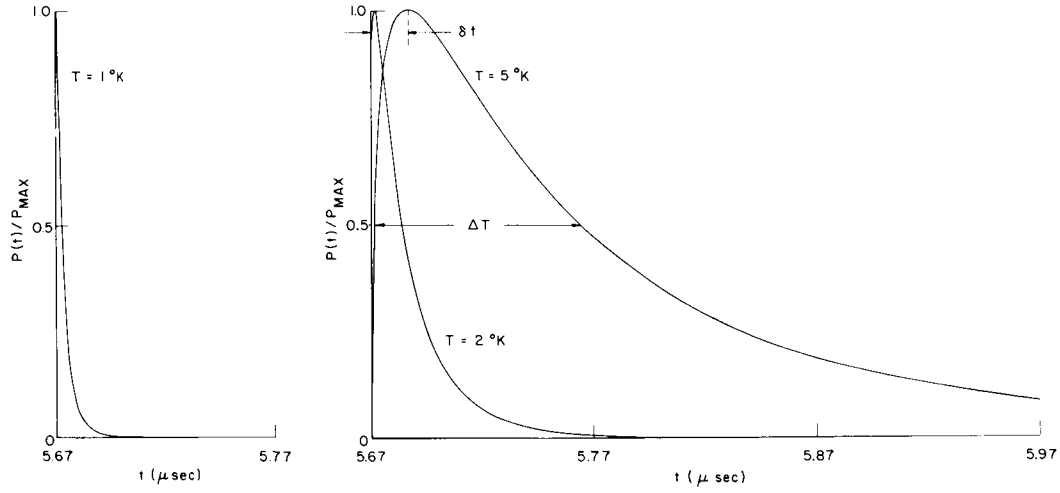

Fig. II-7. Magnified view of Fig. II-6 for T = 1°, 2°, 5°K. This shows the maximum in each curve very close to $t = x/v_o$.

function to the data of Elcombe, as shown in Fig. II-4 ($\nu_o = 2.21\times10^{12}\ \text{sec}^{-1}$). Equation 14 has been plotted in Fig. II-6 as a function of time t for various values of the absolute temperature T ranging from 1.0 to 500°K. If we recall that at very low temperatures only the lowest elastic modes are excited and that these low-lying modes

exhibit very little dispersion, it is reasonable to expect that the sharp thermal spike initiated into the crystal is very nearly reproduced at x = 19 mm when the temperature that characterizes the black-body distribution is at 1°K. Detail of the first three thermal

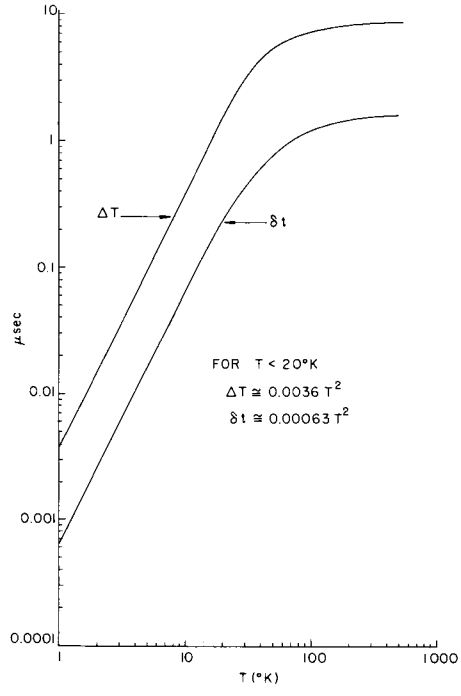

Fig. II-8.

Curve Δt shows variation in the width of the heat pulse at the half-power point ($P/P_{max}=0.5$) as a function of absolute temperature. The shift in the peak of the heat pulse away from $t = x/v_o$ is shown as a function of absolute temperature by δt. Below T = 20°K both curves are very nearly proportional to the square of the absolute temperature.

spikes is shown in Fig. II-7, where the abscissa has been expanded in order to show the maxima more clearly. This occurs very close to $t = x/v_o$ the proper time for an ultrasonic pulse exhibiting no dispersion. Returning to Fig. II-6, we can see that the effect of dispersion becomes very pronounced at higher temperatures as the thermal spike broadens out and its peak moves in the direction of increasing time. In Fig. II-6 the quantity Δt indicates the width of the heat pulse at $P/P_{max} = 0.5$. The shift of the peak of the pulse away from $t = x/v_o$ is indicated by δt. These data are plotted as a function of temperature in Fig. II-8. Up to about 20°K both of these quantities are very nearly proportional to the square of the absolute temperature. Elastic dispersion effects are most evident in the magnitude of the width Δt, which is approximately six times the shift δt in the peak.

J. M. Andrews, Jr.

References

1. M. Born and T. von Karman, Physik. Z. 13, 297 (1912); 14, 15 (1913).
2. See, for example, C. B. Walker, Phys. Rev. 103, 547 (1956).
3. M. Elcombe, Bull. Am. Phys. Soc. 10, 435 (1965).

4. M. Elcombe, private communication, 1965. Miss Elcombe very kindly provided her calculations for 5 different values of the reduced wave vector. We have taken the liberty of drawing smooth curves through these points.

5. L. Van Hove, Phys. Rev. 89, 1189 (1953).

D. FERMI SURFACES OF GALLIUM SINGLE CRYSTALS BY THE SIZE EFFECT

The Fermi surface of Gallium single crystals has been investigated by using the size effect. This is due to the small thickness of the sample which is comparable with the radius of the electronic orbit. The result has been compared with the Fermi surface derived previously by the author from the ultrasonic attenuation at microwave frequencies.[1]

The experimental arrangement is shown in Fig. II-9. Metallic Gallium of 99.9999% purity was purchased from the United Chemical and Mineral Corporation, New York.

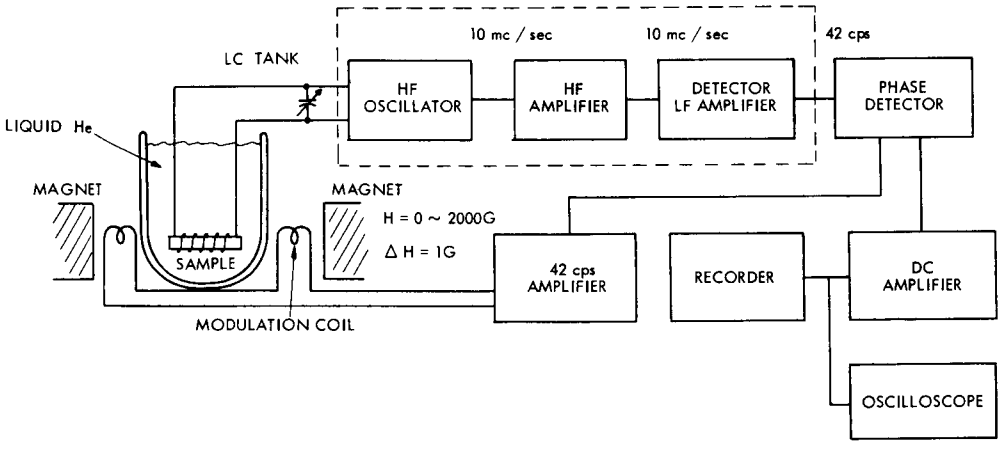

Fig. II-9. Experimental arrangement.

A Gallium crystal was grown between two lucite slabs, with a milar film used to fix the thickness of the crystal. Crystals of 0.15-1 mm thickness and 2 cm × 1 cm area have been made by this technique. The crystal axis has been checked by x-ray and the angles verified within one degree. Enamel wire No. 38 was wound directly on the sample to make a coil in an LC tank circuit in a high-frequency oscillator. The frequency of the oscillator was set to 5-10 Mc/sec which is small enough compared with the cyclotron frequency of the electron (1-3 Gc/100 gauss) and large enough, so that the skin depth of the high-frequency wave stays much less than the sample thickness.

The DC magnetic field was set parallel to the flat surfaces of the sample, and the electron then rotates in a plane perpendicular to the flat surfaces. The electronic orbit intersects both surfaces when the DC field, H, reaches

$$H_o = \frac{2\hbar c k}{de}, \tag{1}$$

where d is the sample thickness.

If the field is swept through H_o, there is a singularity in the surface impedance of the Gallium slab at H_o, hence the Q of the coil shows a singularity of this point. The change in Q appears in the amplitude of the HF oscillator output. This output is high-frequency amplified and supplied to the recorder after detection and DC amplification. To improve the signal-to-noise ratio, the DC field was modulated at 42 cps. The signal output was then proportional to the derivative, dA/dH, of the absorption with respect to the field.

The skin depth at 42 cps is larger than the sample thickness so the modulation field penetrates through the sample. The wave vector of the electron located at the extremum point in the Fermi surface can be found from H_o through Eq. 1.[2] By rotating the slab in the plane parallel to the field, the extremal cross sections of the Fermi surface were found.

Figure II-10 shows the dA/dH vs H curve for a sample, 0.335 mm thick, $\theta = 15°$ and with a modulation field strength of 1 gauss where θ is the angle between the magnetic

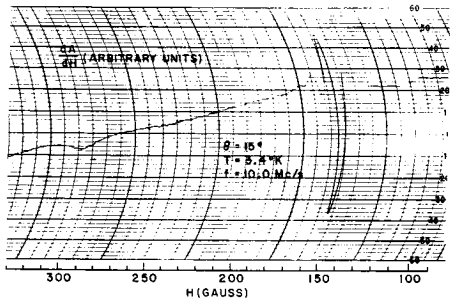

Fig. II-10. Detected signal vs magnetic field.

field direction and the b axis. A second harmonic is evident in Fig. II-10 at $H \approx 310$ gauss. Third and higher harmonics could not be identified because of the poor signal-to-noise ratio.

The wave vectors of this sample are plotted in Figs. II-11. This is the Fermi surface in the ky-kz plane, if the center of the extremum orbit coincides with the center of the Brillouin zone.

In the previous report, to find the Fermi surface by ultrasonic attenuation we used Tepley's[3] value for sound velocity, $v_a = 3.73 \times 10^5$ cm/sec which he found using an oscilloscope and sound pulses.

If we use instead $v_a = 4.62 \times 10^5$ cm/sec, which corresponds to the sound velocity along the c axis found by Tepley, then the Fermi surface found in the ultrasonic experiment becomes very close to that obtained in the present experiment. This fact suggests

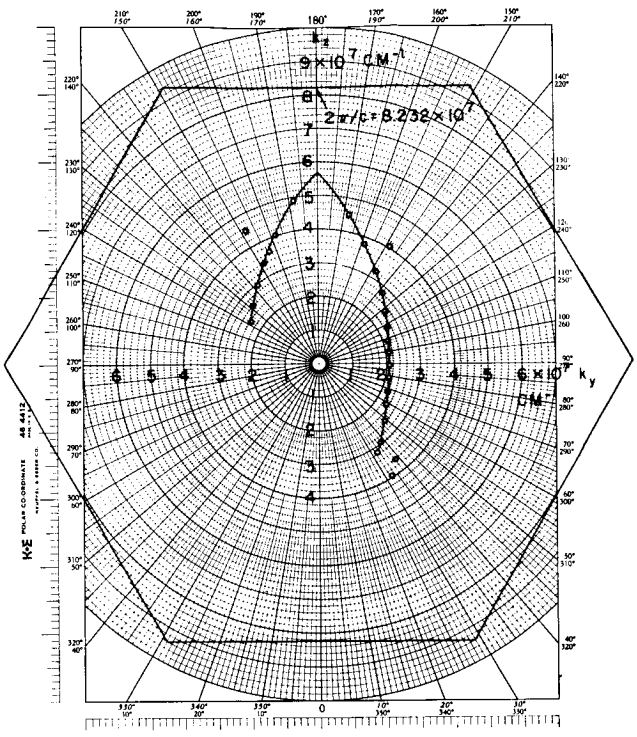

Fig. II-11. Fermi surface derived from sample No. 7/8-1.

that the size effect may provide a good method for measuring the sound velocity in metals together with the ultrasonic attenuation.

A. Fukumoto

References

1. A. Fukumoto, Quarterly Progress Report No. 78, Research Laboratory of Electronics, M.I.T., July 15, 1965, pp. 15-19.
2. T. F. Gantmakher, Soviet Phys. – JETP 17, 549 (1963).
3. N. Tepley, Ph.D. Thesis, Department of Physics, M.I.T., 1963.

III. RADIO ASTRONOMY*

Prof. A. H. Barrett
Prof. J. W. Graham
Prof. M. Loewenthal
Prof. R. P. Rafuse
Dr. W. B. Lenoir
Dr. D. H. Staelin
Dr. S. H. Zisk
R. J. Allen
R. K. Breon
Patricia P. Crowther
A. B. Hull
J. M. Moran, Jr.
M. A. Palfy
S. M. Rezende
A. E. E. Rogers
J. H. Spoor
D. H. Steinbrecher
A. Vander Vorst

A. OBSERVATIONS OF MICROWAVE EMISSION FROM ATMOSPHERIC OXYGEN

A series of four more balloon flight experiments was performed from the NCAR Balloon Base, Palestine, Texas, in July 1965.[1-3] The flight characteristics and comments on the flights are summarized in Table III-1.

Table III-1. Summary of balloon flight experiments.

Flight	Date	Duration	Float Height	Ascent	Descent	Purpose	Comments
150-P	17 July	8 hr	30 km	2 hr	2 hr	To study line shape	Data of first hour missing, otherwise successful
152-P	21 July	8 hr	39 km	2 1/2 hr	Parachute	To infer temperature profile	Successful
153-P	27 July	8 hr	39 km	2 1/2 hr	Parachute	To infer temperature profile	Successful
154-P	30 July	8 hr	30 km	2 hr	2 hr	To study line shape	Successful

The flights made to study the line shape have been previously described.[1-3]

Flights 152-P and 153-P represent the first attempt to infer the temperature profile from microwave measurements taken remotely. The only difference in the radiometer for these experiments is that the antennas are directed at 0° and 60° nadir angles (rather than 60° and 75° zenith angles as in Flights 150-P and 154-P). The resulting weighting functions are shown in Fig. III-1 under the assumptions of an altitude of 40 km and atmospheric profiles the same as those measured during Flight 55-P in July 1964. The computed brightness temperatures for the 6 channels are plotted in Fig. III-2 against height.

The data are undergoing analysis, but preliminary indications are that the results

*This work was supported principally by the National Aeronautics and Space Administration (Grant NsG-419); and in part by the Joint Services Electronics Program (Contract DA36-039-AMC-03200(E)).

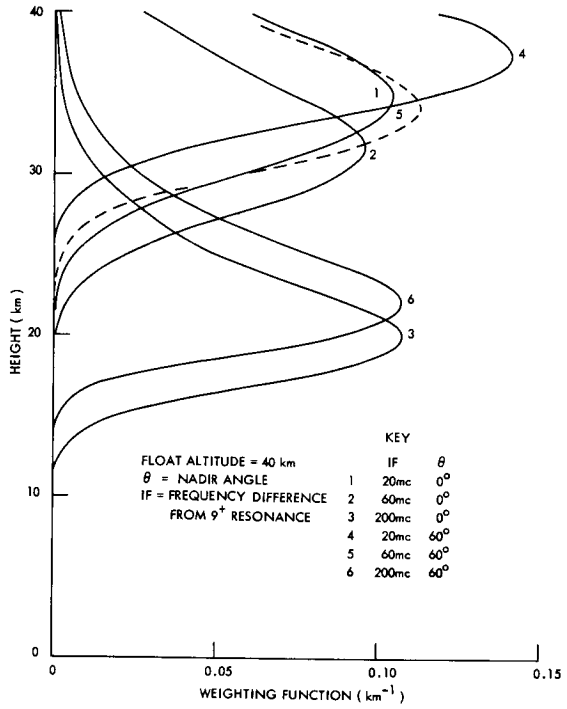

Fig. III-1. Weighting functions.

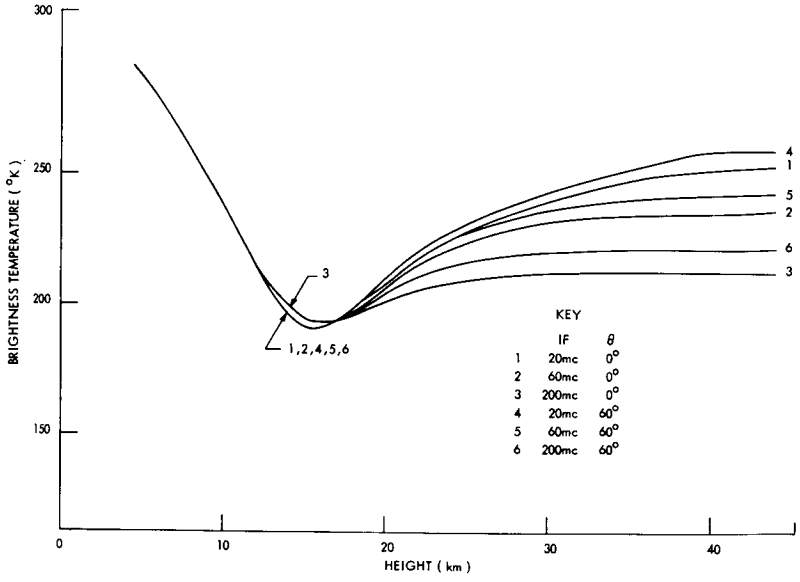

Fig. III-2. Brightness temperatures.

are very good for all flights. The PDP-1 computer is being used for partial analysis of the data for greater speed and accuracy.

W. B. Lenoir

References

1. W. B. Lenoir, Quarterly Progress Report No. 77, Research Laboratory of Electronics, M. I. T., April 15, 1965, pp. 20-23.
2. W. B. Lenoir and J. W. Kuiper, Quarterly Progress Report No. 75, Research Laboratory of Electronics, M. I. T., October 15, 1964, pp. 9-18.
3. A. H. Barrett, J. C. Blinn III, and J. W. Kuiper, Quarterly Progress Report No. 71, Research Laboratory of Electronics, M. I. T., October 15, 1963, pp. 69-76.

B. REMOTE SOUNDING OF THE UPPER ATMOSPHERE BY MICROWAVE MEASUREMENTS

1. Introduction

The Zeeman effect has been included in a rigorous analysis of the microwave spectrum of atmospheric O_2 near λ 5 mm.[1,2] On the basis of this analysis it appears possible to remotely sound the atmospheric temperature from satellite-based radiometers.

This radiometer would probably be a Dicke superheterodyne radiometer characterized by ν_o, the center frequency of the passband; BW, bandwidth; τ, post detection integration time; and T_N, effective noise temperature. The rms deviation of the receiver output expressed in temperature units would be

$$\Delta T_{rms} = \frac{2T_N}{\sqrt{BW \cdot \tau}}. \tag{1}$$

For a satellite in a polar orbit similar to that of a Nimbus satellite, an effective ground speed of 6 miles/sec is experienced. The desired horizontal spatial resolution will, therefore, limit the length of τ. Likewise, the desired vertical spatial resolution will limit BW.

2. Equations of Radiative Transfer

In considering the microwave emission from atmospheric oxygen the appropriate equation of propagation is the matrix equation of radiative transfer,[1,2]

$$\frac{d}{dz}\underline{\underline{T_B}}(\nu,z) + \underline{\underline{A}}(\nu,z)\,\underline{\underline{T_B}}(\nu,z) + \underline{\underline{T_B}}(\nu,z)\,\underline{\underline{A}}^{t*}(\nu,z) = 2t(z)\,\underline{\underline{A}}(\nu,z) \tag{2}$$

with

$\underline{\underline{T_B}}(\nu, z)$ = brightness temperature matrix

$\underline{\underline{A}}(\nu, z)$ = attenuation matrix

$t(z)$ = kinetic temperature

z = vertical distance variable.

The formulation of Eq. 2 and the derivation of $A(\nu, z)$ has been reported elsewhere.[1]

The terrestrial atmosphere was approximated as a series of constant-temperature, constant-pressure layers, each 1 km thick. One hundred such layers from the ground

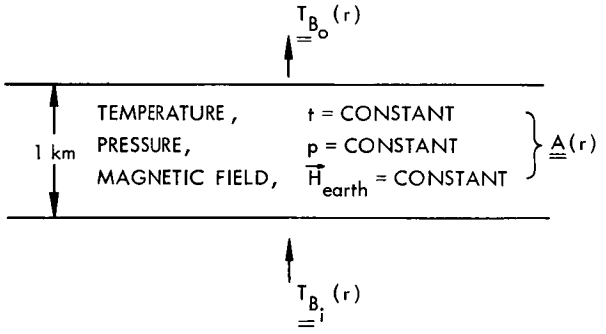

Fig. III-3. Layer geometry.

to a height of 100 km were used. (Above 100 km there is insufficient oxygen to be of importance.) See Fig. III-3.

The solution to (2) for one such layer is

$$\underline{\underline{T_B}}_o(\nu) = e^{-\underline{\underline{A}}(\nu)\Delta z}\, \underline{\underline{T_B}}_i(\nu)\, e^{-\underline{\underline{A}}(\nu)\Delta z} + t\left[\underline{\underline{I}} - e^{-2\underline{\underline{A}}(\nu)\Delta z}\right]. \tag{3}$$

The ground-atmosphere interface is not of importance here because only frequencies in the center of the resonance complex are considered. For these frequencies the attenuation from the ground to 100 km is so great that emission below 10 km does not contribute to the $\underline{\underline{T_B}}(\nu)$ at 100 km. The $\underline{\underline{T_B}}(\nu)$ observable by a satellite-based radiometer is found by continual application of (3) for each of the layers between the ground and 100 km.

A somewhat different analysis, emphasizing the contribution to $\underline{\underline{T_B}}(\nu)$ of the individual layers, was actually used. The emission from each layer is carried through all layers above it to give its contribution to the total $\underline{\underline{T_B}}(\nu)$. These contributions are then summed for the $\underline{\underline{T_B}}(\nu)$. In this manner it is convenient to define a weighting-function matrix,

$$\underline{\underline{WF}}(z, \nu) = \underline{\underline{P}}(z, \nu)\left[\underline{\underline{I}} - e^{-2\underline{\underline{A}}(\nu, z)\Delta z}\right] \underline{\underline{P}}^{t*}(z, \nu) \tag{4}$$

with

$$\underline{\underline{P}}(z,\nu) = e^{-\underline{\underline{A}}(\nu,100)}\, e^{-\underline{\underline{A}}(\nu,99)} \cdots e^{-\underline{\underline{A}}(\nu,z+1)}.$$

Thus

$$\underline{\underline{T_B}}(\nu) = \sum_{z=1}^{100} \underline{\underline{WF}}(z,\nu)\, t(z). \tag{5}$$

The polarization basis for the calculations was linear polarizations along the θ and φ directions in the geomagnetic coordinate system. The angles are defined in Fig. III-4. The 1-1 elements of the matrices represent linear polarization with the H field in the ±φ direction, while the 2-2 elements represent linear polarizations with the H field in

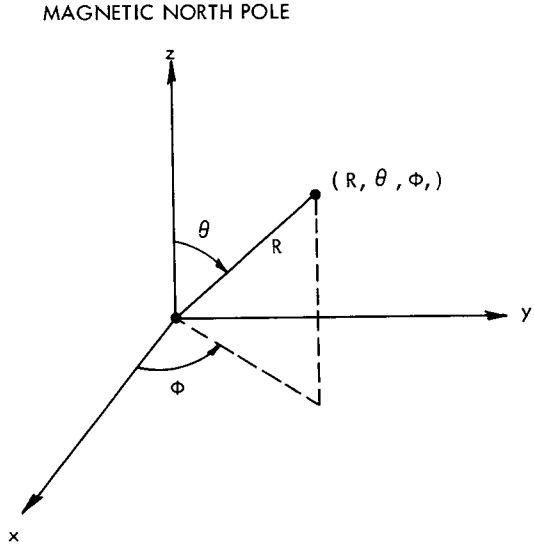

Fig. III-4. Coordinate system.

the ±θ direction.

The magnetic field model was a dipole with peak strength of 0.62 gauss at the poles. To simplify computations, the magnitude of the field at 65 km was used for all heights (i.e., the radial dependence of the field was ignored). The total variation (peak-to-peak) of the magnitude of the field over height ranges of interest was less than 2 per cent. This is negligibly small compared with probable anomalies from a true dipole field. The direction of the dipole field is independent of height, hence no further assumption was made.

The polarization from a π component of the Zeeman split resonance is θ linear, independent of the magnetic equator. It does, however, have a $\sin^2\theta$ amplitude dependence. The polarization from a σ component depends on latitude. For θ = 90° (magnetic equator) the polarization is φ linear. For θ = 0° (magnetic pole) the polarization is circular with the sense depending on which σ component is being considered. For

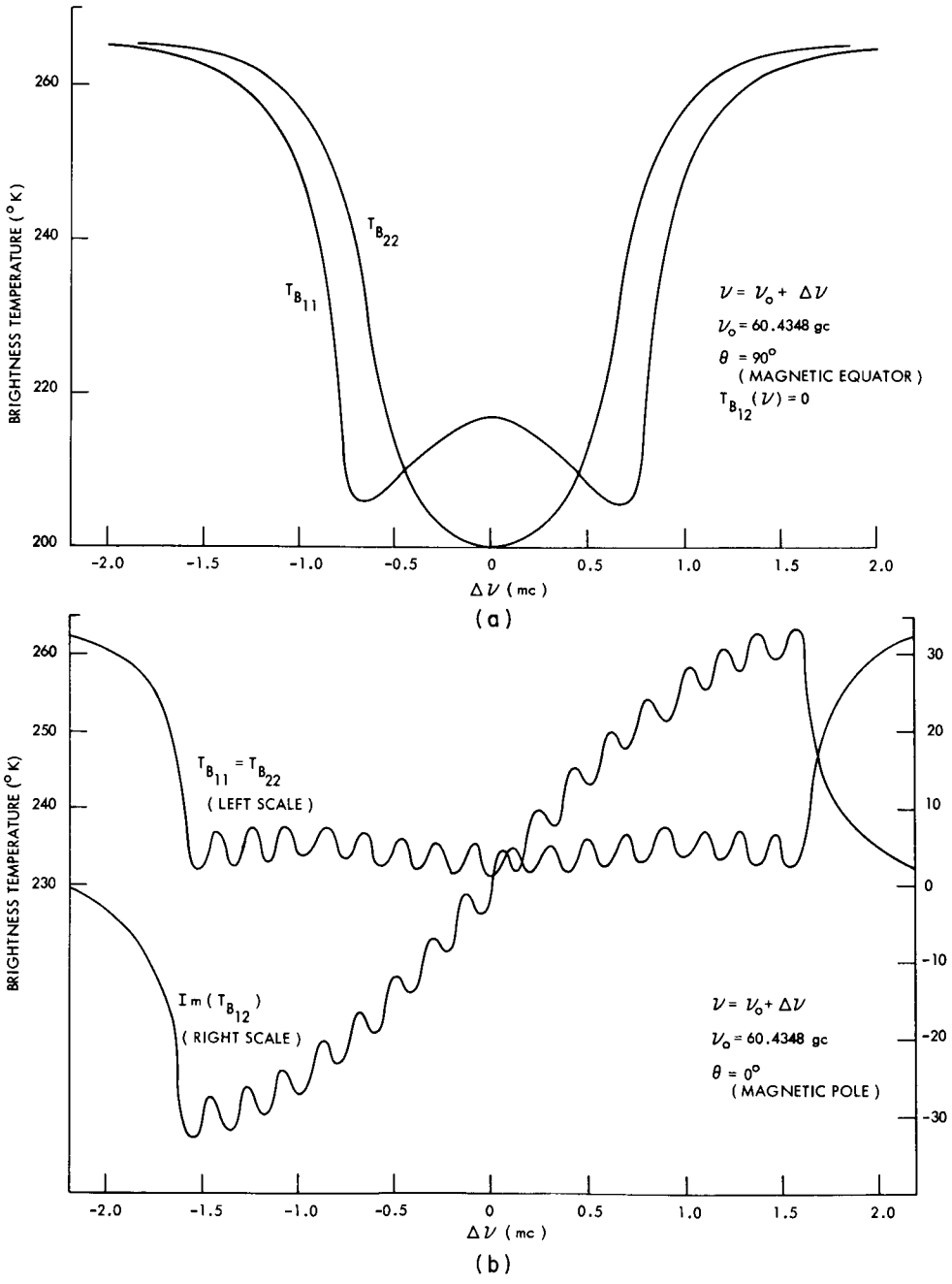

Fig. III-5. Brightness temperature spectrum, 7^+ line. (a) Magnetic equator. (b) Magnetic pole.

$0° \leq \theta \leq 90°$ the polarization is elliptical with the major axis in the $\pm\phi$ direction and the minor axis in the $\pm\theta$ direction (the sense again depending on the σ component).

Because of the choice of coordinate system, the real part of the off-diagonal terms of $\underline{\underline{T_B}}(\nu)$ will be zero for all latitudes. This means that there is no linear coherence between the 1-1 element and the 2-2 element, which can be seen above. The imaginary part of the off-diagonal terms can, however, be nonzero, being a measure of the circular coherence between the two main diagonal elements. The imaginary part is zero only along the magnetic equator.

3. Mesospheric Sounding

To sound the atmosphere as high as possible the most intense resonance lines should be used. The most intense lines for temperatures of 200-300°K are the 7^+ and 7^- lines. The 7^+ line has more Zeeman components than the 7^-, so the relative transparency (deeper probing) of frequencies between the Zeeman components is less. Using the 1962 U. S. Standard Atmosphere as an atmospheric model, we analyzed the 7^+ line as seen from a satellite.

$\underline{\underline{T_B}}(\nu)$ for the 7^+ line is plotted in Fig. III-5 for both the magnetic equator and the magnetic pole. An experiment with passband centered on the 7^+ resonance and with a 1.5-Mc bandwidth was found to be the best for global high-altitude sounding. The $\underline{\underline{WF}}(z,\nu)$'s for this bandwidth are shown in Fig. III-6. The latitude dependence of the heights of the weighting function peaks and heights at which the weighting functions are one-half of their peak values is shown in Fig. III-7. The 7^+ line experiment is summarized in Table III-2.

Table III-2. 7^+ Experiment.

ν_o = 60.4348 Gc
BW = 1.5 Mc
h_o = height of WF peaks
Δh = full width between 1/2 peak heights

	h_o	Δh
Equator, 11 polarizations	72.5 km	20 km
Equator, 22 polarizations	74 km	20 km
Pole, all polarizations	66 km	26 km

If a measurements as summarized in Table III-2 were performed with a radiometer having $T_N = 10^4$°K and τ = 10 sec (60 miles on ground), the ΔT_{rms} would be 5°K. For

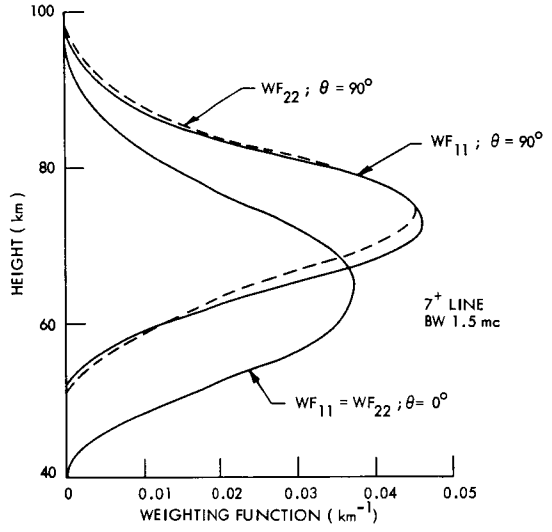

Fig. III-6. Weighting functions, 7^+ line, 1.5-Mc bandwidth.

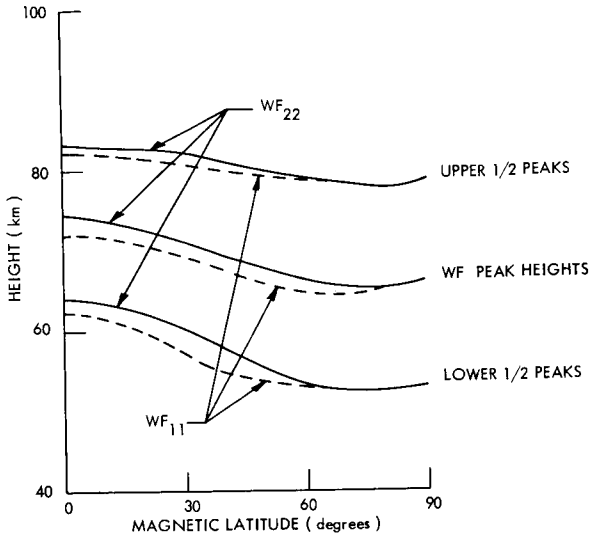

Fig. III-7. Height variation of weighting-function peaks.

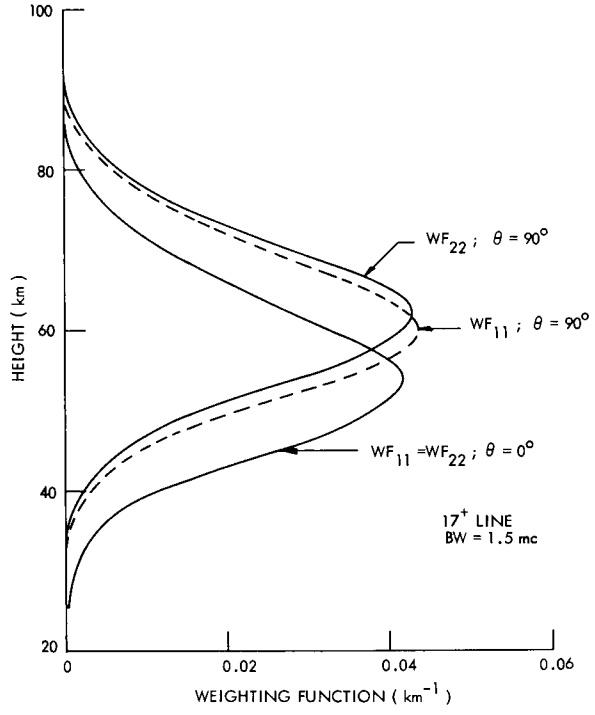

Fig. III-8. Weighting functions, 17^+ line, 1.5-Mc bandwidth.

T_N = 7000°K and τ = 30 sec (180 miles), a ΔT_{rms} = 2°K results.

4. Atmospheric Soundings at 10-80 km

A weighting function peaking at 55-60 km would be the 17^+ line with a 1.5-Mc bandwidth. The WF for this experiment are shown in Fig. III-8.

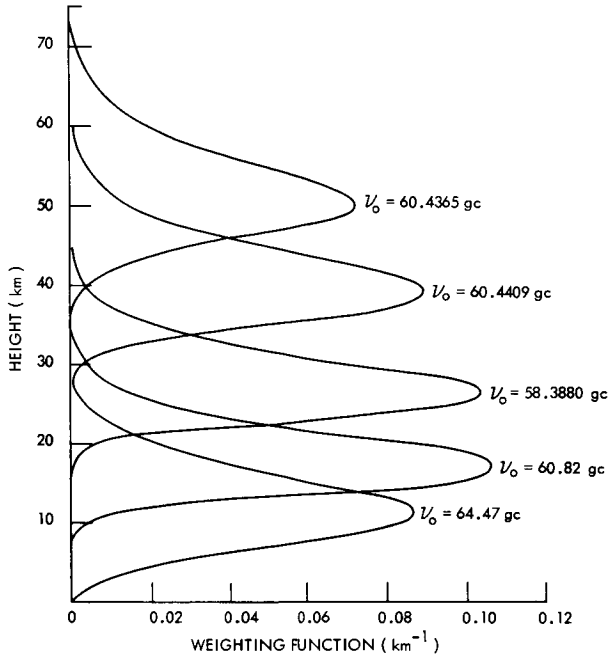

Fig. III-9. Weighting functions, 10-50 km soundings.

For WF peaking below 50 km, the Zeeman effect is not important. The pressure broadening is much larger than the Zeeman splitting and the line appears as a single, unpolarized line. Frequencies and bandwidths to cover the range 10-50 km were chosen with the bandwidth as large as possible without broadening the WF to a great extent. Table III-3 summarizes these five WF, which are plotted in Fig. III-9.

Table III-3. 10-50 km Soundings.

ν_o (gc)	BW (mc)	h_o (km)	Δh (km)
64.47	200	12	10
60.82	200	18	7
58.388	30	27	9
60.4409	2.5	40	12
60.4365	1.0	50	21

A seven-channel satellite experiment to remotely sound the atmospheric temperature could combine the seven experiments discussed above. The parameters for such an experiment are listed in Table III-4.

Table III-4. Remote sounding at 12-75 km.

$\Delta T_1 = \Delta T_{rms}$ for $T_N = 10^4$°K, $\tau = 10$ sec
$\Delta T_2 = \Delta T_{rms}$ for $T_N = 7000$°K, $\tau = 30$ sec

ν_o (Gc)	BW (Mc)	h_o (km)	Δh (km)	ΔT_1 (°K)	ΔT_2 (°K)
64.47	200	12	10	0.5	0.2
60.82	200	18	7	0.5	0.2
58.388	30	27	9	1.2	0.5
60.4409	2.5	40	12	4	1.5
60.4365	1.0	50	21	6	2.5
63.5685	1.5	60, equator 54, pole	21 26	5	2
60.4348	1.5	73, equator 66, pole	20 26	5	2

W. B. Lenoir

References

1. W. B. Lenoir, Ph. D. Thesis, Department of Electrical Engineering, M. I. T., June 1965.
2. W. B. Lenoir, Quarterly Progress Report No. 77, Research Laboratory of Electronics, M. I. T., April 15, 1965, pp. 24-40.

C. VARACTOR PARAMETERS

The barrier capacitance of a p-n junction is given by the well-known relationship

$$C_j = C_{min}\left[\frac{V_B + \phi}{V + \phi}\right]^{\gamma}, \qquad (1)$$

where ϕ is the contact potential, V is the applied voltage (positive for reverse bias), V_B is the breakdown voltage, C_{min} is the junction capacitance at breakdown, and $\gamma = 0.5$

for an abrupt junction and = 0.333 for a linearly graded junction.

The junction is not directly accessible, since the diode is mounted and packaged. The package characteristics can even be dominant at X-band. The simplest equivalent

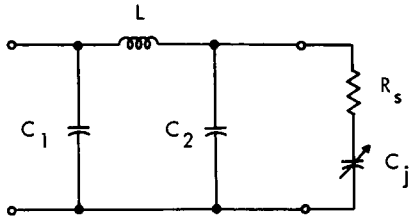

Fig. III-10. Equivalent circuit.

circuit for the packaged diode is shown in Fig. III-10, in which the following parameters are represented:

C_j, junction capacitance

R_s, junction series resistance

L, series inductance

C_2, shunt capacitance, across the junction

C_1, exterior case capacitance.

We have studied Sylvania diodes. For these varactors two mounts are available (Fig. III-11). When examining these mounts, one suspects that the series inductance is

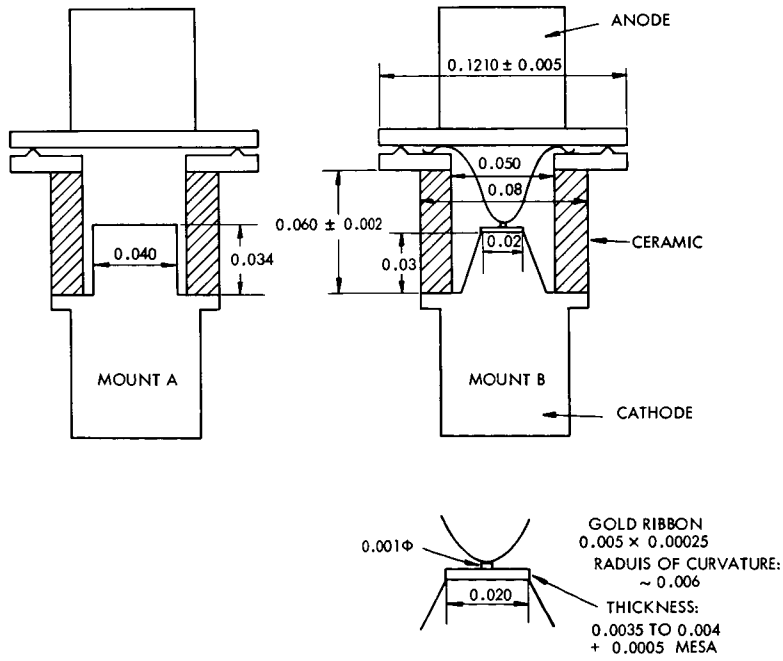

Fig. III-11. Diode mounts.

due mostly to the inductance of the Gold ribbon that makes the contact between the mesa and the anode post. One also suspects that the total case capacitance of mount A is bigger than the total case capacitance of mount B: indeed, in mount A, the ceramic cylinder is shielded by the metallic structure, along approximately three-fifths of its height. The manufacturer tells the customer that the difference between the case capacitance of mount A and of mount B is ~0.04 pf.

The capacitance C_2 as given by the manufacturer is $C_2 \approx 0.06$ pf.

On a parallel-plate basis (with the conical structure replaced by an average horizontal plane) the total case capacitance of mount B can be calculated:

$$C_{case} = C_1 + C_2 = 0.172 \text{ pf.}$$

1. Low-Frequency Measurements

At low frequency (1 MHz) the series inductance is negligible. The only "parasitic" element is the total case capacitance.

Theoretically, only three measured values of the junction capacitance are necessary to determine the case capacitance and the exponent γ. Indeed, the total measured capacitance is

$$C = C_{case} + C_{min}\left[\frac{V_B + \phi}{V + \phi}\right]^{\gamma}. \tag{2}$$

Having measured three values C_1, C_2, and C_3, one can easily eliminate C_{min}, V_B, and C_{case}:

$$\frac{C_1 - C_2}{C_1 - C_3} = \frac{1 - \left[\frac{V_1 + \phi}{V_2 + \phi}\right]^{\gamma}}{1 - \left[\frac{V_1 + \phi}{V_3 + \phi}\right]^{\gamma}}. \tag{3}$$

There are two unknowns in this equation, ϕ and γ. The problem can be solved by iteration, until a self-consistent solution is found.

We have shown that this method leads to wrong values of γ and C_{case} because C_1, C_2, and C_3 need to be known with extremely high accuracy to get the right values of γ and C_{case}.

A computer program was written,[1] which we used to handle measurements on 16 Sylvania varactors.

The measurements are performed in a special diode holder. Its principal characteristics are the following:

1. The diode is measured between two plates to make the fringing capacitance

identical to that of the diode mounted in a reduced-height waveguide.

2. The mechanical stability is very good: an experimental repeatability of ±0.002 pf has been measured.

There is no problem in determining by this method the case capacitance and the exponent γ of true abrupt junctions. Measurements on 6 diodes indicate that the total case capacitance of mount B and the corresponding standard deviation are $C_{case} = 0.165 \pm 0.002$ pf. The exponent was found to be 0.500 within a few per cent. Such an error is expected: it can be calculated from the errors caused by the capacitance bridge and the voltmeter (a potentiometer was used here).

The case capacitance of mount A has not been determined with such accuracy; we had either graded junctions in this mount or junctions for which the doping concentration was not uniform. In both cases the contact potential varies with the applied voltage, and our method is not so accurate. We found the following values for case capacitance: 0.190, 0.192, 0.205 pf.

2. X-band Measurements

X-band measurements were performed on a reduced-height waveguide, in use at Lincoln Laboratory, M.I.T. The transmitted power is measured at resonance and at the 3-db points. This allows one to determine[2] R_s, junction series resistance; L, series inductance (Fig. III-10); and C_2, shunt capacitance (Fig. III-11).

It has been pointed out[3] that the model of Fig. III-10 is not sufficient: a series inductance L_1 in front of it (Fig. III-12) takes into account the behavior of an inductive post in a waveguide. Indeed, the packaged diode behaves as a radial line; at resonance its input impedance is very small and the packaged diode is almost a short. The value of L_1 can be calculated: $L_1 = 0.256$ nH.

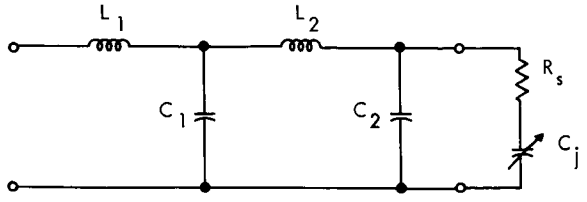

Fig. III-12. Double LC equivalent circuit.

We have verified experimentally the fact that the calculated value of the inductance L (Fig. III-10) is too large with respect to the expected value ($L_2 \approx 0.4$ nH) by an amount ≈ 0.25 nH.

The transformation of the diode impedance to the entry of the double LC circuit has been performed. It has been shown theoretically that C_1 and C_2 are almost equal at X-band (while $C_1/C_2 \approx 2$ at 1 MHz). This allows one to determine C_1 and C_2 at microwave frequencies, independently of the low-frequency value. The following results have been found at X-band for abrupt junctions in mount B:

$$L_2 = 0.496 \pm 0.01 \text{ nH}$$

$$C_1 + C_2 = 2C_1 = 2C_2 = 0.169 \pm 0.015 \text{ pf.}$$

The total case capacitance is thus frequency-independent until X-band, since the low-frequency value was $C_{case} = 0.165 \pm 0.002$ pf.

Since C_1 and C_2 have been found to be equal (within 2%), a new model is suggested for the package: a one-dimensional transmission line. The parameters of this line have been calculated: the standard deviation is smaller on these parameters than on the lumped circuit parameters. This suggests that a transmission line is a better model than a lumped circuit. The characteristic impedance is approximately 70 Ω at X-band; it increases slowly with frequency.

A. S. Vander Vorst

References

1. D. H. Stebbins, "Data Processing Technique for Evaluating Some Parameters of Packaged Varactors," S. B. Thesis, Department of Electrical Engineering, M. I. T., June 1965.
2. D. H. Steinbrecher and W. C. Schwab, "ABC's of Varactor Measurements," Internal Memorandum, Research Laboratory of Electronics, M. I. T., 1964.
3. W. J. Getsinger, "The Packaged and Mounted Diode as a Microwave Circuit," Lincoln Laboratory preprint, July 1965.

D. SPECTRAL-LINE RADIOMETER SYSTEM AT HAYSTACK

Spectral-line radio astronomy has reached a new stage in its development with the discovery of more spectral lines in addition to the well-known 21-cm line of neutral hydrogen.[1] The 18-cm lines of OH show some extremely narrow features that require resolutions of 1 kcps, or better, to fully resolve their spectral detail.

A new spectral-line radiometer has recently been completed at the Haystack Research Facility of Lincoln Laboratory, M.I.T., to meet the demands of the field. The system uses the 120 ft parabolic dish, a parametric amplifier front end, and a 100-channel digital autocorrelator[2] in conjunction with a Univac 490 real-time computer. The parametric amplifier and feeds are usable in the frequency range 1.4-1.8 Gc/sec with system temperature of 200°K, or better. The correlator in conjunction with the computer gives spectra with total bandwidths ranging from 4 Mc to 40 kc and equivalent filter resolutions from 100 kc to 1 kc respectively.

A block diagram of the system is shown in Fig. III-13. A photograph of the control room panels is shown in Fig. III-14. The correlation and computer calculate a comparison and difference spectrum. The difference spectrum can be the difference between antenna and dummy load or the difference between antenna and sky horn. Alternatively, the ferrite switch can be locked and the difference between spectra in adjacent frequency

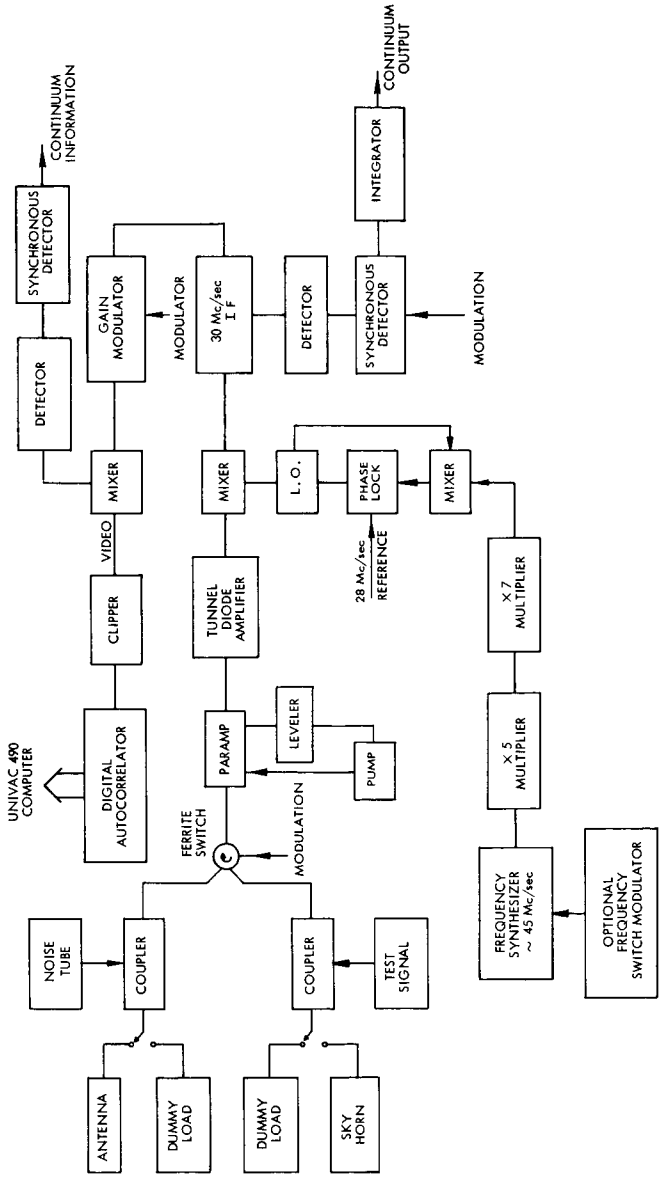

Fig. III-13. The spectral-line radiometer.

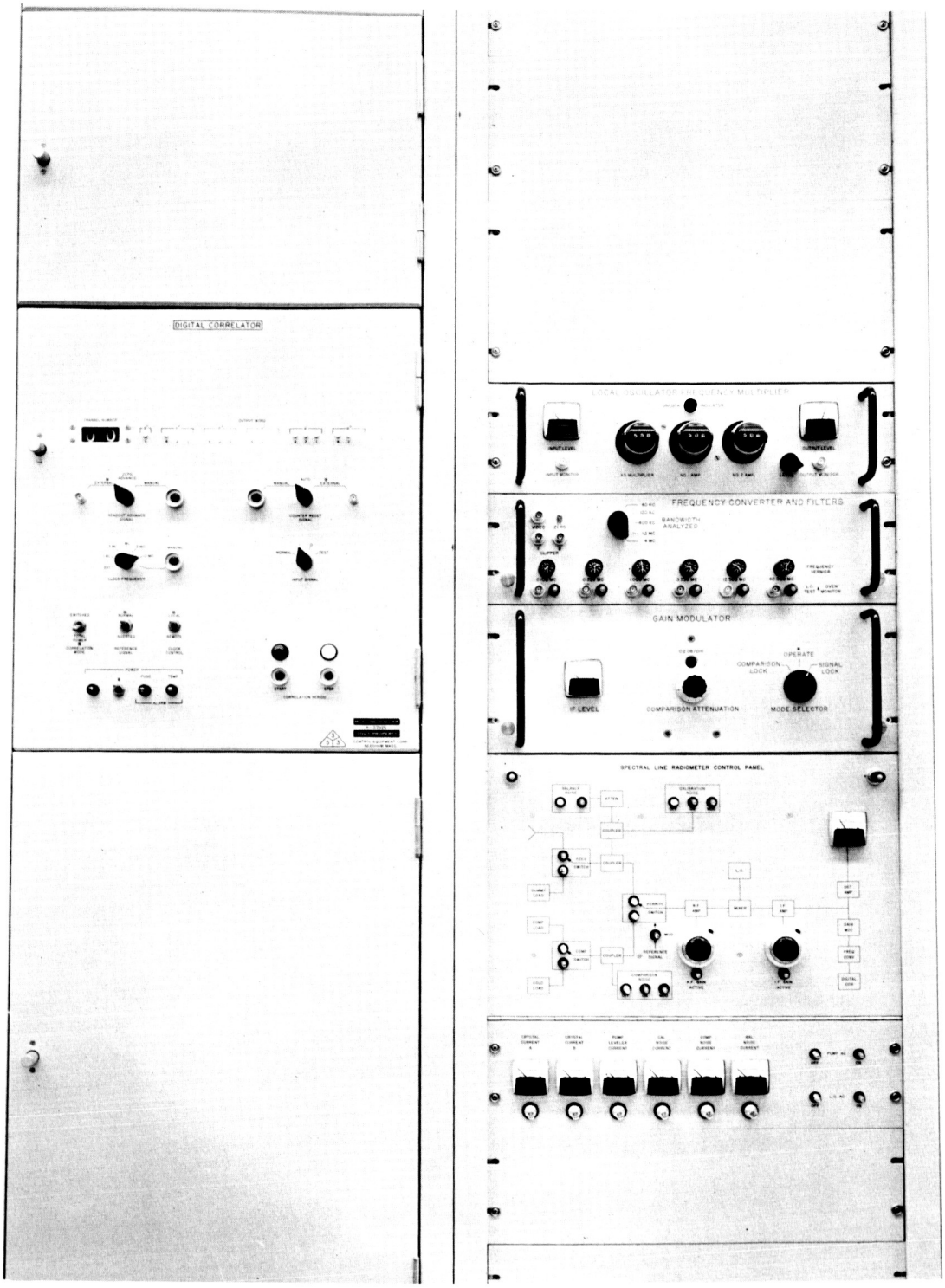

Fig. III-14. Showing portions of the spectral-line radiometer and digital correlator.

bands taken by switching the local-oscillator frequency.

The radiometer has been used to repeat the measurement of OH absorption in the spectrum of Cassiopeia A. An integration period of 20 minutes was enough to duplicate weeks of work done at Millstone.[1]

In a recent article Weaver, Williams, Dieter, and Lum[3] reported observations of strong microwave emission lines in the HII region W3. The lines, observed at approximately 1665 Mc/sec (see Fig. III-15), exhibited complex spectral structure but could

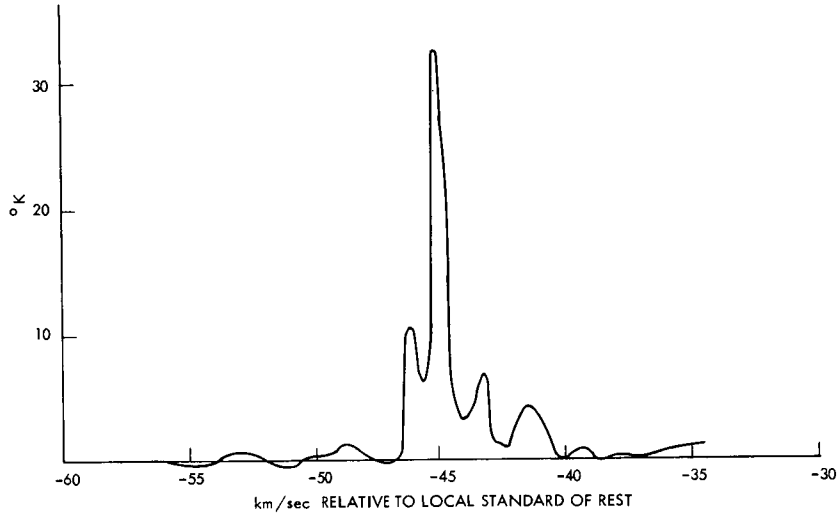

Fig. III-15. Emission spectrum in W3 at 1665 Mc.

not be detected at 1667 Mc/sec, as would be expected if the emission were attributable to OH. Weaver and his co-workers considered the lines to be unidentified and called them "mysterium." We have observed the same region and conclude that (i) emission is present not only at 1665 Mc/sec but also at 1667 Mc/sec and 1720 Mc/sec with frequency spacings as predicted from the OH spectrum; (ii) the emission at 1665 Mc/sec and 1667 Mc/sec is linearly polarized as much as 30-40 per cent; and (iii) the maximum emission is not coincident with the source W3 but displaced approximately 0.5°. These observations represent the first detection of polarized line emission in radio astronomy. Our observations are not complete but we conclude "mysterium" is really OH. The ratios of line intensities, however, are clearly anomalous. If the polarization is attributed to the Zeeman effect, the indicated magnetic fields are several orders of magnitude greater than those normally associated with the galactic interstellar medium.

A. H. Barrett, A. E. E. Rogers

References

1. A. H. Barrett, "Discovery of the Interstellar 18-cm Lines of the Hydroxyl (OH) Radical," Quarterly Progress Report No. 72, Research Laboratory of Electronics, M. I. T., January 15, 1964, pp. 28-30.
2. S. Weinreb, "A Digital Spectral Analysis Technique and its Application to Radio Astronomy," Technical Report 412, Research Laboratory of Electronics, M. I. T., August 30, 1963.
3. H. Weaver, D. R. W. Williams, N. H. Dieter, and W. T. Lum, "Observations of a Strong Unidentified Microwave Line and of Emission from the OH Molecule," Nature 208, 29-31 (1965).

E. THEORETICAL STUDIES OF RADAR ECHOES FROM THE SUN

The solar radar, near El Campo, Texas, built and originally operated by Lincoln Laboratory, M. I. T., has been operating almost continuously since April 1961. Since January 1965, the facility has been an activity of the Space Science Center, M. I. T., under the auspices of the National Aeronautics and Space Administration. The results obtained thus far have been of considerable interest, particularly since there are some very puzzling aspects in the data. In at least two areas theoretical studies should prove profitable. These have to do with explaining the great variability of the returned signal levels and the solar radar cross section deduced from them and, second, the very wide, variable, and asymmetrical Doppler spectra that have been observed.

The radar cross section computed from the data varies significantly from day to day. Most of the time the variation is from approximately 0.4 to 1.2 times the projected area of the photosphere, $\pi R_o^2 = 1.5 \times 10^8$ square meters. While this variation is difficult to account for, even harder is the large number of occasions on which the echo has been very much larger or smaller than these values. A projected area of twice πR_o^2 is not uncommon; values around $5\pi R_o^2$ have been obtained more than a dozen times, while the largest value observed was $16\pi R_o^2$. At other times, the echo has disappeared. It should be remembered that all of the solar radar observations have been made during the low part of the sunspot cycle, so that even more spectacular results might be expected as the peak period of solar activity is approached.

Characteristic of the echo spectra, which is measured at a number (~20) of range intervals, is first the large width and great variability of the spectra. Half-power widths averaging 30-40 kc/sec (the radar frequency is 38.25 Mc/sec) can vary by factors of two either way. (In fact, the spectra were much wider than anticipated so that the system had to be redesigned a number of times as the original separation of only 8 kc/sec in the frequency-shift keying of the transmitter was increased to 60 kc/sec. As a result, there are some inaccuracies in the earlier data.) The sequence of spectra shows considerable variation in both the range and range spread of the energy distribution of echoes. At the

same time, there are variations with range in the mean Doppler shift, and the peak of the Doppler spectrum. In general, but not always, the mean Doppler shift is positive and more positive for the earlier range intervals. Moreover, there is no obvious correlation between these effects and the variation of the radar cross section. Finally, the normal daily fluctuations in the echo do not correlate well with any of the other measurable effects of solar activity, K indices, and so forth. The abnormally large cross sections however, have usually occurred under disturbed conditions.

Many of these effects are difficult to explain by any model of the solar structure. Certainly, a spherically symmetric distribution of ion density hardly explains any of the facts. A somewhat more complex model, in which strong specular reflection is avoided, is obtained by allowing the reflecting surface, at least, to be rough. In addition to other troubles, such models fail in relying only on the solar rotation to produce the observed Doppler spectra; some form of motion is required. Somewhat more successful are models that introduce random scattering centers in an otherwise spherically symmetric model. Still more promising are models that introduce some systematic structure and organized mass motion. While the problem is complicated, some of the effects are so gross that something more than a casual explanation is required, and there is every assurance that concrete results should be obtainable.

Of the several models now being studied, the most promising and interesting are those involving a radial structure aligned with a radial magnetic field. Such R-rays are located in the solar corona above active areas in the photosphere and are tied in with the production of streamers and the Type II slow-drift bursts. The evidence indicates that the inhomogenieties may have longitudinal dimensions $\approx 10^5$ km. and electron densities averaging approximately 10 times those of the undisturbed solar atmosphere. The filaments may occur and re-occur at places where the magnetic structure is particularly stable. The effort involved in the study of the various propagating modes on such structures and the reflection of radio waves from them (including the effect of the solar rotation and charge motions) should prove interesting.

M. Loewenthal

References

1. J. C. James, "Radar Studies of the Sun," preprint of Chap. XI in a proposed book, Radar Astronomy, edited by J. V. Evans and Tor Hagfors (Lincoln Laboratory, M. I. T.).

2. E. R. Mustel, "On the Spatial Structure of the Solar Corona," Part I. Soviet Astronomy, A. J., Vol. 6, No. 3, pp. 333-339, 1962; Part II. Soviet Astronomy, A. J., Vol. 6, No. 4, pp. 488-496, 1963.

3. C. de Jager, "Structure and Dynamics of the Solar Atmosphere," Handbuch der Physik, Vol. 52, p. 80, 1959.

4. A. H. Maxwell and A. R. Thompson, "Spectral Observations of Radio Bursts, II. Slow-drift Bursts and Coronal Streamers," Astrophys. J. 135, 138-150 (1962).

IV. OPTICAL AND INFRARED SPECTROSCOPY*

Prof. C. H. Perry
Dr. R. Geick
D. P. Athans
W. J. Hakel
D. B. Hall
P. Lubitz
E. C. Reifenstein III
E. F. Young

A. TEMPERATURE DEPENDENCE OF THE FAR INFRARED REFLECTIVITY OF MAGNESIUM STANNIDE

Among the II-IV semiconducting compounds with the antiflourite structure, Magnesium Stannide has the smallest width of the forbidden gap with 0.33-0.36 ev.[1-5] Consequently, at room temperature and above the intrinsic conduction dominates. Measurements of the electrical properties[1-7] cover the range 60°-1000°K. At high temperatures Busch and Winkler[1,2] found a $T^{-2.5}$ law for the mobility for which explanations have been given in terms of optical mode scattering[8,9] and more phonon processes.[10] For the mixed conduction range, however, Lichter[7] reported a $T^{-1.5}$ law in agreement with the theory concerning acoustical mode scattering.[11] Similar results have been obtained for Mg_2Ge and Mg_2Si.[8,9]

With respect to lattice vibrations, Mg_2Sn has for $\vec{g} \approx 0$ an infrared active and a Raman active mode. The frequency of the infrared active mode at room temperature has been determined from the far infrared reflectivity.[12,13]

We have extended the study of the lattice vibrational properties to other temperatures and investigated the electrical properties at infrared frequencies by measuring the reflectivity of Mg_2Sn in the region from 50 cm^{-1}-370 cm^{-1} at various temperatures in the range 100°-600°K. Two samples of different origin yielded the same reflectivity within experimental error. Both were pure material, and their reflectivities at 100°K exhibited no indication of free-carrier effects (cf. Fig. IV-1). With increasing temperature the influence of the free carriers becomes more and more important, and above 400°K this is dominant. The reflection spectrum of our samples at room temperature is in good agreement with the data reported previously,[13] except that the subsidiary band in the Reststrahlenband has not been found with our samples.

The reflection spectra were analyzed by means of a classical oscillator fit including Drude terms for electrons, as well as for holes. Details of the dispersion formula and the notation used have been previously published.[14] In this analysis $\epsilon_\infty = 16.4$ was used according to the refractive index of Mg_2Sn in the near infrared,[15] and ϵ_∞ was assumed to be independent of temperature. ϵ_o, ω_o, and γ in the lattice dispersion term were determined from the reflectivity and are shown as a function of temperature in Figs. IV-2 and IV-3. At high temperatures γ is nearly proportional to T^2 which means that predominantly 3-phonon processes via quartic lattice potential terms determine the width

*This work was supported principally by the Joint Services Electronics program (Contract DA-36-039-AMC-03200(E).

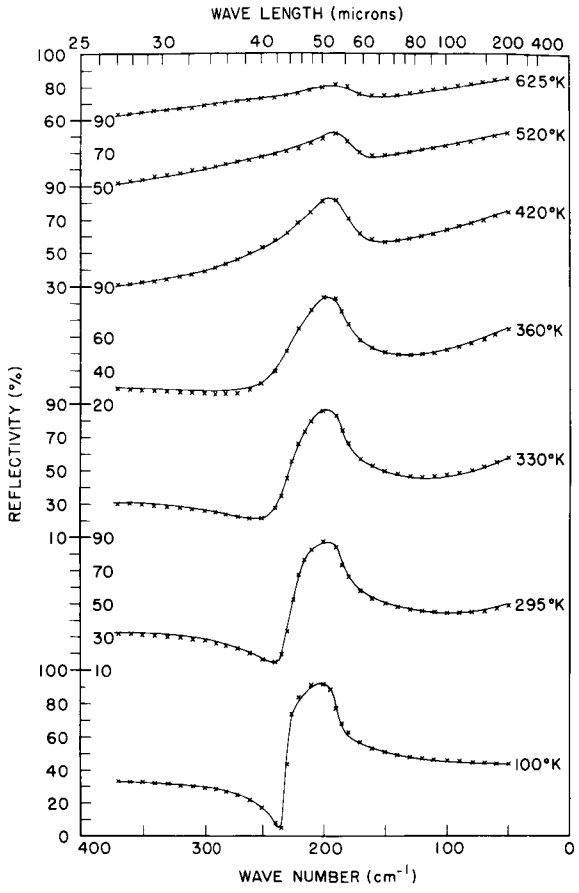

Fig. IV-1.

Reflectivity of Mg_2Sn at various temperatures, experimental data (solid line) and calculated by means of classical dispersion formula (X).

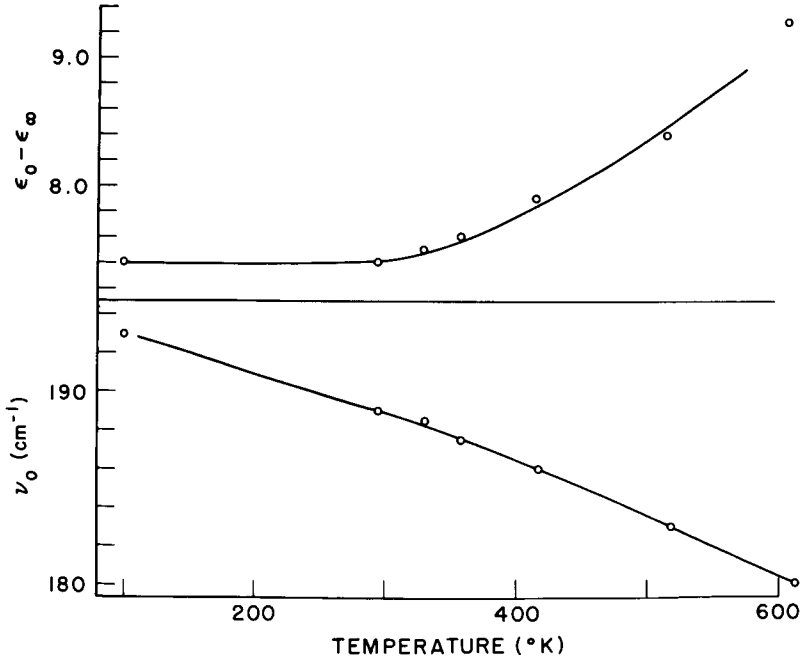

Fig. IV-2. Temperature dependence of the infrared eigenfrequency ω_o and the oscillator strength $(\epsilon_o - \epsilon_\infty)$ of Mg_2Sn.

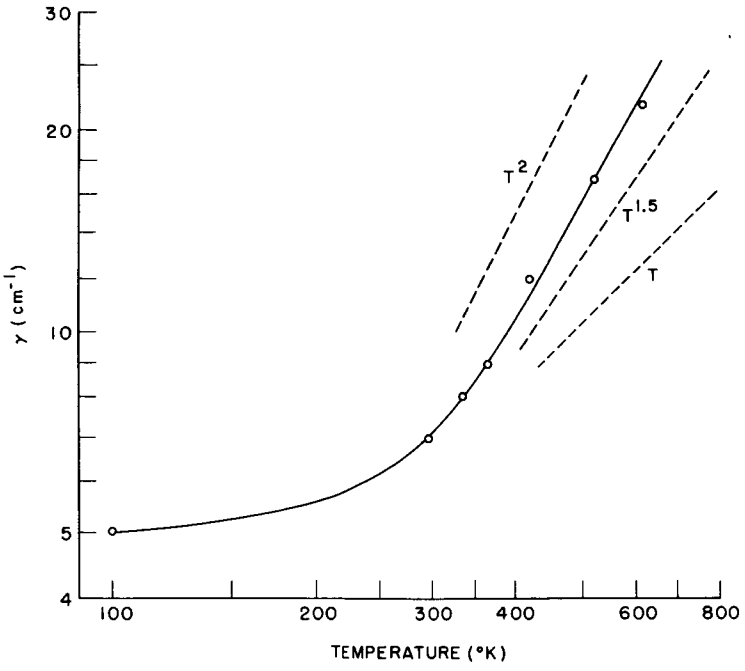

Fig. IV-3. Temperature dependence of the damping constant γ in the lattice dispersion term for Mg_2Sn.

of the fundamental lattice band.[16]

In the free-carrier part of the dispersion formula, too many parameters are involved to determine them all from the reflection spectra. For T = 100°K the free-carrier effects could be neglected completely. At room temperature a reasonable fit was obtained with the values reported from electrical measurements:

A. Intrinsic carrier concentration $N_i = 1.5 \cdot 10^{17}\ cm^{-3}$ [3]

B. Conductivity effective masses of electrons and holes, respectively, $m_e^* = 0.15 m_o$ [3] and $m_h^* = 0.10 m_o$ [3]

C. Mobilities of electrons and holes, respectively, $\mu_e = 370 \frac{cm^2}{V\ sec}$ [3,7] and $\mu_h = 300 \frac{cm^2}{V\ sec}$ [3,7].

No attempt was made to vary the effective masses with temperature, and the room temperature values were used for all temperatures. The mobilities were assumed varying proportional to $T^{-2.5}$ according to the results of Busch and Winkler.[1,2] The mobility ratio used was $\mu_e/\mu_h = 1.23$ independent of temperature.[3,7] The carrier concentration was determined from the reflectivity (cf. Fig. IV-4). For comparison N_i was calculated using the values $m_e^* = 1.20 m_o$ [3] and $m_h^* = 1.30 m_o$ [3] for the density of states effective masses and the value of the band gap energy $Eg = (0.36 - 2.8\ 10^{-4} T)\ ev$ [1-3] (cf. Fig. IV-4).

The agreement of the experimental data with the calculated values is reasonable.

An attempt was also made to fit the reflectivity with mobilities proportional to $T^{-1.5}$ according to the results of Lichter[7] in the mixed conduction range. The calculated

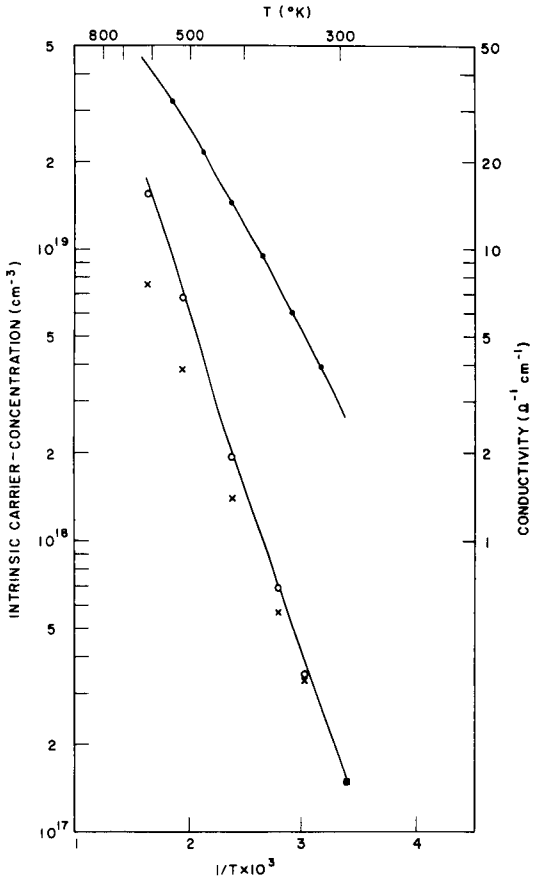

Fig. IV-4.
Intrinsic carrier concentration N_i versus 1/T as determined from reflection spectra with $\mu \sim T^{-2.5}$(O) and with $\mu \sim T^{-1.5}$(X), calculated values of N_i (————) and total static conductivity (————·————).

reflectivity is the same as in the former case within 2-3% for all temperatures and consequently, only one calculated value is shown in Fig. IV-1. The carrier concentration deviates systematically from the calculated values, and the ratio of the calculated to the experimental values is proportional to T. The resulting total static conductivity σ_o is the same in both cases and thus the reflectivity is sensitive to the conductivity only. Furthermore, the plot log σ_o versus 1/T is not a straight line, which indicates once more a $T^{-2.5}$ law for the mobilities (cf. Fig. IV-4). This means that already in the temperature range covered by our measurements the temperature dependence of the mobility cannot be explained by acoustical mode scattering only,[11] and that optical mode scattering or more phonon processes have to be considered.[8-10]

Because of the relatively low mobility in Mg_2Sn, the free-carrier effects produce no sharp plasma edge in the reflectivity which would have provided additional information.

Such a minimum and a steep vise of the reflectivity always occur when the real part of the dielectric constant changes from positive to negative values with increasing wavelength and the imaginary part is sufficiently small. The corresponding condition is for a lattice dispersion term

$$\frac{(\sqrt{\epsilon_o}-\sqrt{\epsilon_\infty})\omega_o}{\sqrt{\epsilon_\infty}\,\gamma} \gg 1, \tag{1}$$

and for a Drude term

$$\frac{Nm^*\mu^2}{\epsilon_{Lattice}} \gg 1. \tag{2}$$

For Mg_2Sn, condition 1 is fulfilled, but $\frac{Nm^*\mu^2}{\epsilon_{Lattice}} < 1$ for electrons, as well as for holes. Therefore no plasma edge has been found in the spectra.

We wish to thank Professor D. W. Lynch, of Iowa State University, for providing one of the Mg_2Sn samples. All computations were performed on the IBM 7094 computer at the Computation Center, M. I. T.

R. Geick

References

1. G. Busch and U. Winkler, Physica 20, 1067 (1954).
2. U. Winkler, Helv. Phys. Acta 28, 633 (1955).
3. H. G. Lipson and A. Kahan, Phys. Rev. 133, A800 (1964).
4. R. F. Blunt, H. P. R. Frederikse, and W. R. Hosler, Phys. Rev. 100, 663 (1955).
5. W. D. Lawson, S. Neilson, E. H. Putley, and W. Roberts, J. Electronics 1, 203 (1955).
6. H. P. R. Frederikse, W. R. Hosler, and D. E. Roberts, Phys. Rev. 103, 67 (1955).
7. B. D. Lichter, J. Electrochem. Soc. 109, 819 (1962).
8. R. D. Redin, R. G. Morris, and G. C. Danielson, Phys. Rev. 109, 1916 (1958).
9. R. G. Morris, R. D. Redin, and G. C. Danielson, Phys. Rev. 109, 1909 (1958).
10. Ch. Entz, Physica 20, 983 (1954); Helvetia Phys. Acta 27, 199 (1954).
11. F. Seitz, Phys. Rev. 73, 549 (1948).
12. D. McWilliams and D. W. Lynch, Phys. Rev. 130, 2248 (1963).
13. A. Kahan, H. G. Lipson, and E. V. Loewenstein, Physics of Semiconductors, Proceedings of the 7th International Conference, Paris, 1964, p. 1067.
14. R. Geick and C. H. Perry, Quarterly Progress Report No. 77, Research Laboratory of Electronics, M. I. T., April 15, 1965, pp. 41-48.
15. D. McWilliams and D. W. Lynch, J. Opt. Soc. Am. 53, 298 (1963).
16. D. W. Jepsen and R. F. Wallis, Phys. Rev. 125, 1496 (1962).

V. GEOPHYSICS*

Prof. F. Bitter	Dr. J. F. Waymouth	J. B. DeWolf
Prof. G. Fiocco	R. J. Breeding	G. W. Grams
Dr. T. Fohl	J. C. Chapman	H. C. Koons
Dr. W. D. Halverson	A. J. Cohen	K. Urbanek

A. ABSORPTION OF λ = 4880 Å LASER BEAM BY ARGON IONS

The absorption of the output beam of a steady-state argon ion laser (λ = 4880 Å) by excited argon ions in a low-pressure arc discharge has been observed. The argon ions, excited to the $4s^2P_{3/2}$ state, strongly absorb the laser beam that is produced by the Ar II transition $4p^2D^o_{5/2} \rightarrow 4s^2P_{3/2}$.

The ultimate purpose of this work is to develop a technique to measure the temperature of ions in moderate temperature plasmas by determining the Doppler width of an ion absorption line. The steady-state ion laser provides a series of extremely sharp emission lines corresponding to the optical resonant cavity modes of the laser. The ratios of the intensities of the laser modes, determined with and without the absorbing ions, can be related to the Doppler width of the ion absorption line. For excited argon ions absorbing energy corresponding to the $4s^2P_{3/2} \rightarrow 4p^2D^o_{5/2}$ transition, the relation between the Doppler width of the absorption line and the ion temperature is shown in Fig. V-1. The density of the excited ions can also be determined if the total absorbed power from the beam and the oscillator strength of the absorption line are known. The

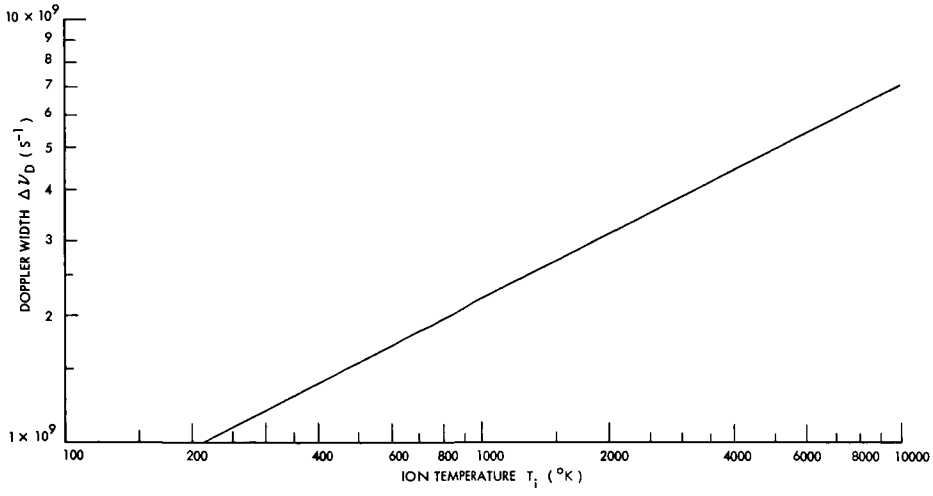

Fig. V-1. Absorption linewidth resulting from Doppler broadening of Ar II transition $4s^2P_{3/2} \rightarrow 4p^2D^o_{5/2}$ (λ = 4880 Å).

*This work was supported principally by the Joint Services Electronics Program (Contract DA36-039-AMC-03200(E).

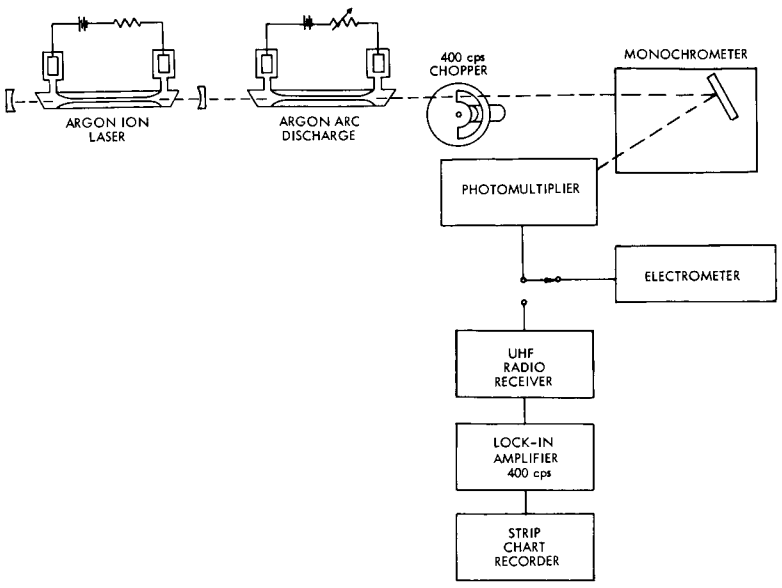

Fig. V-2. Experimental arrangement.

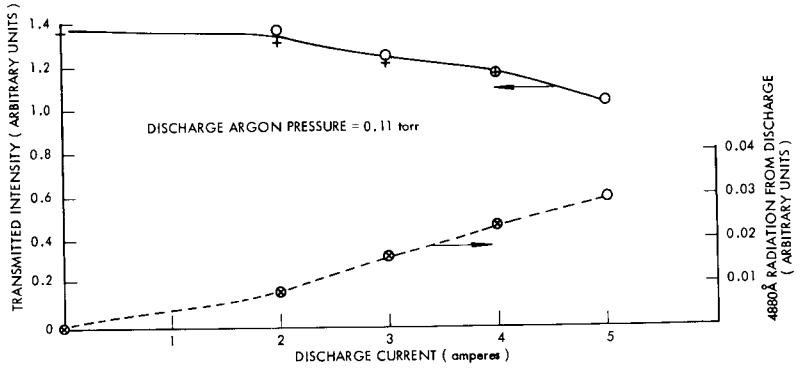

Fig. V-3. Laser beam intensity transmitted through argon discharge and background radiation at λ = 4880 Å vs discharge current.

oscillator strengths of important argon ion lines have been measured by Olsen.[1]

For preliminary evaluation of this technique, the experimental arrangement of Fig. V-2 was set up. A steady-state argon ion laser (λ = 4880 Å) sends a beam through a second argon discharge in a capillary, 2-mm in diameter and 49 cm long. The beam is then sent into a Jarrell-Ash monochromator and the λ = 4880 Å component is detected by a photomultiplier. The transmitted laser beam intensity and the argon discharge background radiation at 4880 Å, monitored directly at the photomultiplier output by a high-impedance electrometer, are shown in Fig. V-3 as a function of discharge current. The beam intensity decreases by 24 per cent as the absorbing discharge current is

increased from 0 to 5 amps.

In order to have a preliminary idea of the absorption of the individual laser modes, the radiofrequency beats between the modes were detected by a UHF radio receiver. The signal-to-noise ratio of the receiver output is increased by chopping the transmitted laser beam at 400 sec^{-1} and amplifying the audio output with a Princeton Applied Research lock-in amplifier tuned to 400 sec^{-1}. The laser modes are separated in frequency by approximately 150 Mc/sec.

Preliminary measurements of the laser beat frequencies up to 1 Gc/sec have been made, but problems in obtaining reproducible data have been encountered because the laser output power had not been adequately stabilized. Modifications of the experimental arrangement are now under way which should correct this problem and extend the frequency spectrum.

G. Fiocco, W. D. Halverson

References

1. H. N. Olsen, J. Quant. Spectroscopy and Rad. Transfer 3, 59-76 (1963).

B. OPTICAL DOPPLER RADAR I

Preliminary experiments to demonstrate the feasibility of developing an optical radar capable of measuring the velocity of moving reflectors are being carried out. Our aim

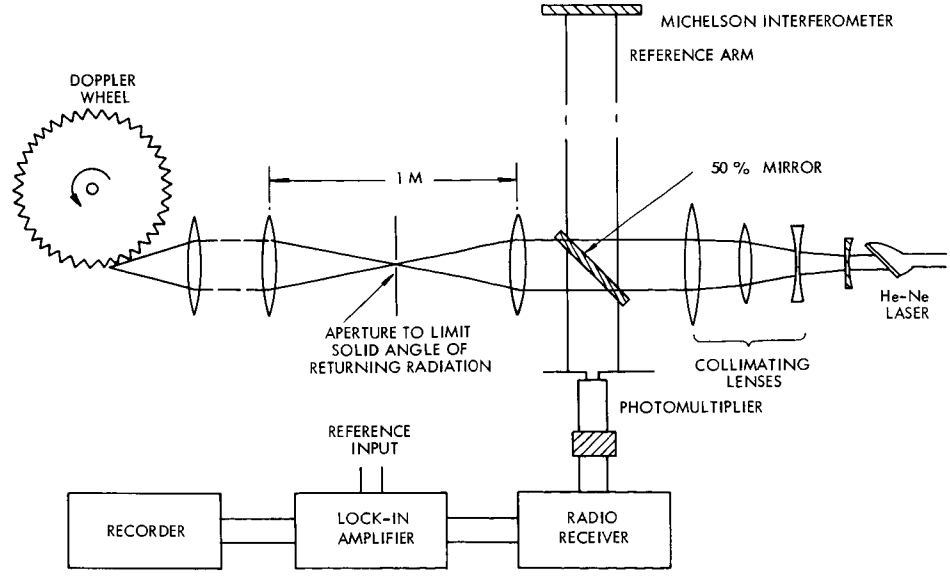

Fig. V-4. Detection system for an optical Doppler radar.

is to construct a device capable of measuring velocity distributions of atmospheric gases at a distance, by the detection of the broadening and shifting of a laser-emitted line.

For this purpose, we have assembled in the laboratory the device illustrated in Fig. V-4. This is basically a Michelson interferometer in which the signal in one of the arms is reflected from a moving surface. The moving surface simulates the motion of a real target; in the present case it consists of a wheel, 25 cm in diameter, with 180 teeth that can be rotated at various speeds. The wheel is contained in an enclosure that can be evacuated in order to achieve high speeds. At present, however, the wheel rotates at 1800 rpm which results in a peripheral speed of 24 m/sec^{-1}. Taking into account the geometry of the encounter, the frequency shift is calculated to be approximately 45 Mc.

The signal from the wheel is mixed with the signal from the reference arm of the interferometer and both are detected by a photomultiplier. Frequency analysis is carried out with a radio receiver with a bandwidth of 13 kc. To improve the signal-to-noise ratio, synchronous detection methods in which a lock-in amplifier is used in conjunction with a beam chopper placed in the wheel arm have been employed.

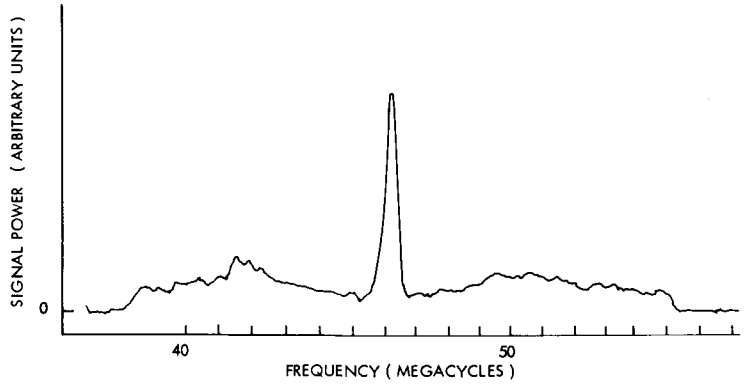

Fig. V-5. Power spectrum after detection.

Figure V-5 is a reproduction of the power spectrum after detection showing the beat signal at 46.6 Mc. The line has a width of approximately 1 Mc which is caused by the fact that the reflection occurs over the surface of a tooth which moves faster on the inside edge than on the outside edge. In obtaining this beat signal, a number of the conditions necessary for successful detection have been clarified.

G. Fiocco, J. B. DeWolf

C. INVESTIGATION OF A REFLEX DISCHARGE

Electron gyro frequency or cyclotron harmonic radiation has been observed from a hot-cathode reflex or Penning discharge. Probe measurements have been made and the density determined from the ion saturation currents. No change in radiometer output maxima near the harmonics was observed for densities between 2 and 20×10^{18} m^{-3}.

The discharge cavity was a water-cooled, stainless-steel cylinder, 19.7 cm in diameter and 15.2 cm high. The anodes, also water-cooled, were hollow copper annuli, 10.2 cm apart. Spirals of 25-mil tungsten wire were used for cathodes (see Fig. V-6). These cathodes emitted tungsten copiously and soon developed hot spots that resulted in copious, but localized, emission of tungsten and electrons, and a bright pencil in the discharge.

Magnetic fields of up to 0.15 Wb/m^2 were used. The field was uniform 1 per cent within 3 cm of the axis of the cavity. The X-band radiometer had no filter before the mixer and so was sensitive to two 20 Mc/sec bands 120 Mc/sec apart. The IF amplifier detected output was fed through a P.A.R. lock-in amplifier to an X-Y recorder. A

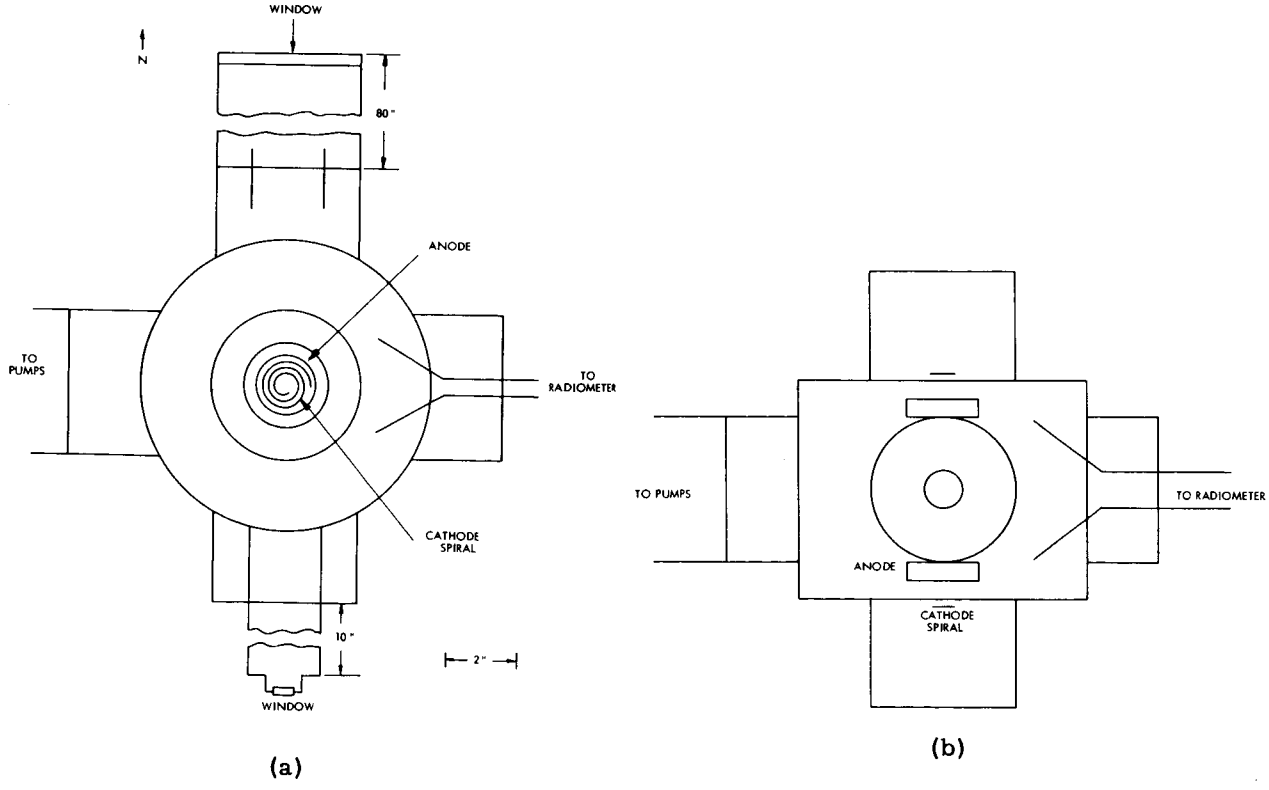

Fig. V-6. (a) Cavity seen from above.
(b) Cavity seen from the North.

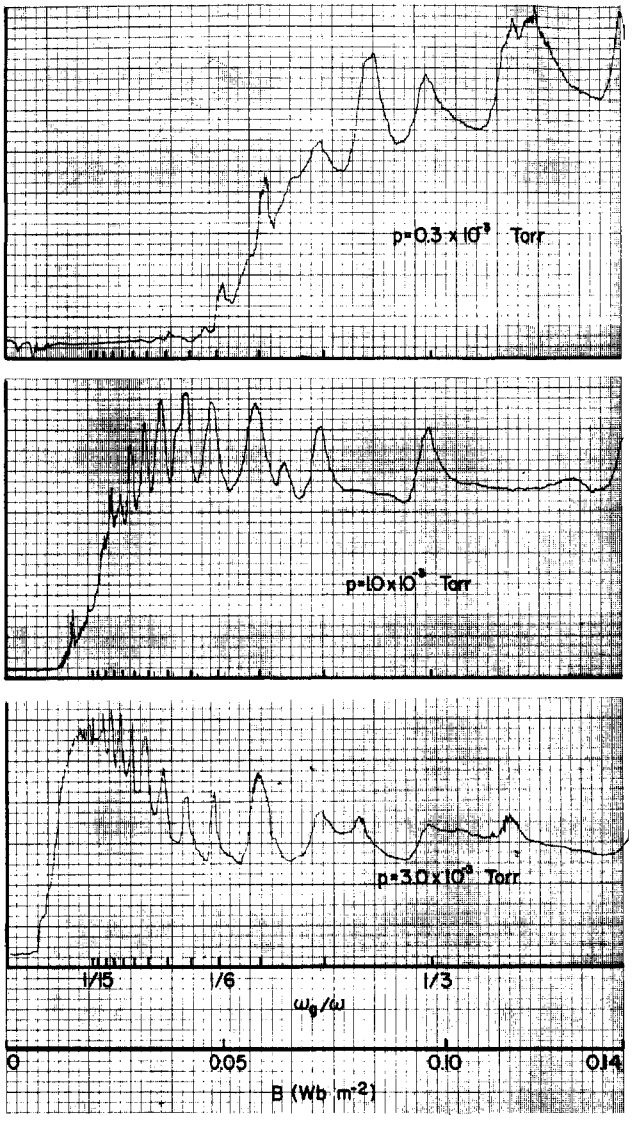

Fig. V-7.

Radiometer output as a function of magnetic field; I_{DC} = 0.8 amp. The vertical scale is arbitrary, except that the lowest curve has been amplified by a factor of 100 with respect to the others.

signal proportional to the current through the magnet coils was fed to the other axis of the recorder.

Densities were calculated from the ion saturation current by using the small-sheath approximation. Sheath radii calculated from the $V^{3/2}$ law were found to be between 1.2 and 1.4 times the probe radius which was 3 mil. The effect of the magnetic field on these results should be negligible because the probe radius was an order of magnitude smaller than the minimum ion gyro radius. The density could be changed by varying the neutral pressure in the cavity and/or the discharge current. Densities between 2 and 20×10^{18} m^{-3} were obtained. The electron thermal energy was found to be approximately 3 ev.

Figure V-7 shows some typical results for three different pressures. Peaks near the gyro-frequency harmonics were usually observed for harmonic numbers 3-10 and occasionally as high as 25. Within the accuracy of the system, the peaks were located right at the harmonics and no change with density could be found. Peaks not near the harmonics were also present, but their occurrence and intensity were directly related to the prominence of the pencil in the plasma. When the plasma was uniform these maxima were either greatly diminished or absent. The intensity of the peaks at the harmonics was also dependent on the strength of the pencil.

In our future plans we envision improvement of the discharge by the use of other cathodes that will provide a uniform plasma. A filter and an IF amplifier with a narrower bandwidth will give narrower peaks and improved accuracy. Improvements in

probe design should extend the range and increase the accuracy of the density determinations.

R. J. Breeding

VI. NOISE IN ELECTRON DEVICES*

Prof. H. A. Haus
Prof. P. L. Penfield, Jr.
Prof. R. P. Rafuse
J. L. Doane
H. J. E. H. Pauwels
V. K. Prabhu

A. SIGNAL-TO-NOISE RATIO OF PHOTOMULTIPLIER SPECTRUM MEASUREMENT AND COUNTING EXPERIMENT

Intensity fluctuations of a narrow-band light source such as an optical maser can be observed experimentally by letting the light emitted from the source impinge upon a photomultiplier.[1-4] One may either observe the spectrum of the photomultiplier anode current or connect the anode to a counter and record the photoelectron counts in a set of fixed time intervals of duration T. The spectral density of the photomultiplier anode current is given[5] by

$$\Phi(\omega) = \frac{AeI_o}{2\pi}\left[\Gamma + 2\pi\frac{\xi}{h\nu}\frac{\Phi_p(\omega)}{\bar{p}}\right] \tag{1}$$

where A is the photomultiplier gain; e, the electron charge; I_o, the anode current; Γ, the secondary-emission shot-noise enhancement factor; ξ, the quantum efficiency; h, Planck's constant; ν, the frequency of the light; $\Phi_p(\omega)$, the spectral density of the light power (intensity); and $\bar{p}$, the average power. The first term is the enhanced shot noise. The second term gives the excess noise resulting from time variation of the light intensity and contains the information on the spectral density of the incident light power.

The second-order factorial moment $\overline{n(n-1)}$ of the photoelectron count n in a time interval of duration T contains the same information as the spectral measurement. One can show[2,6] that

$$\frac{\overline{n(n-1)} - \bar{n}^2}{\bar{n}} = 2\frac{n}{T^2}\int_0^T (T-\tau)\,\rho_p(\tau)\,d\tau, \tag{2}$$

where $\rho_p(\tau)$ is the normalized time-dependent part of the autocorrelation function of the light power p(t)

$$\overline{p(t)\,p(t+\tau)} = \bar{p}^2[1+\rho_p(\tau)]. \tag{3}$$

Because $\Phi_p(\omega)/\bar{p}^2$ and $\rho_p(\tau)$ are related by a Fourier transform, the second factorial moment indeed yields the same information as the spectral measurement.[7]

The purpose of this report is to evaluate the signal-to-noise ratio of these two

*This work was supported principally by the Joint Services Electronics Program (Contract DA36-039-AMC-03200(E).

experiments and compare them with the Brown and Twiss correlation measurement[8] and coincidence counting experiment.[9] Before we do this, we shall consider briefly the advantages and disadvantages of these various methods – aside from their respective signal-to-noise ratios (which will be found to be comparable to each other except for the coincidence counting experiment). In order to obtain the full spectral information in the Brown and Twiss correlation measurement and the coincidence experiment, it is necessary to introduce delays into one of the two photomultiplier outputs used in the experiments. The delays must be of the order of the inverse bandwidth of the incident light. If the light is of narrow bandwidth, such as the light from a gaseous laser, the delays required are prohibitively long. Thus, the Brown and Twiss experiments are suited for the measurement of light spectra of bandwidths greater than, say, 1 Mc. The spectral measurement and counting experiment discussed here take preference for bandwidths less than that.

The counting experiment, as opposed to the spectral measurement, gives more information. Indeed, if enough samples are taken, it is possible to find the complete probability distribution P(n) of counting exactly n photoelectrons within a time interval of duration T; however, it is more laborious. Furthermore, the photoelectron rate cannot exceed the resolution rate of single photoelectron pulses, whereas the spectral measurement does not impose the same stringent restriction. Thus, if the source used is capable of producing a photoelectron rate higher than the rate that can be resolved, attenuation must be used at the expense of signal-to-noise ratio.

1. Signal-to-Noise Ratio of the Spectral Measurement

In the experiments on the fluctuations of the light emitted by a gaseous maser,[1-4] the operation was sufficiently near threshold, so that the modulation of the light was strong and it was not difficult to distinguish the excess noise from the shot noise. In experiments farther away from threshold, this becomes increasingly more difficult and it is necessary to study the question of signal-to-noise ratio.

If it were possible to determine experimentally the shot-noise term in Eq. 1 with perfect accuracy, one could subtract it from the observed total spectrum $\Phi(\omega)$, and thus it would be possible to discern the signal with no attendant uncertainties. In fact, however, the shot-noise level cannot be determined with certainty by a spectral measurement of finite bandwidth B and observation time T_o. We shall define the signal-to-noise ratio of the spectral measurement by the ratio of the excess noise observed in a bandwidth B to the uncertainty in the shot-noise level[7]

$$\frac{\text{Signal}}{\text{Noise}} = \frac{2AeI_oB\frac{\xi}{h\nu}\,2\pi\Phi_p(\omega)/\bar{p}}{\text{Uncertainty of shot-noise level}}. \tag{4}$$

Here, the uncertainty of shot-noise level is

$$\left\{\overline{\left[\frac{1}{T_o}\int_0^{T_o} i^2(t)\,dt\right]^2} - \overline{\left[\frac{1}{T_o}\int_0^{T_o} i^2(t)\,dt\right]}^2\right\}^{1/2}, \tag{5}$$

where i(t) is the current passing the filter of bandwidth B. We shall evaluate the uncertainty of the shot-noise level in the limit of a negligible signal, an assumption that is legitimate in the limit of a small signal-to-noise ratio. In this case the current i(t) in (5) is a random time function with a Gaussian amplitude distribution. Assuming that the filter characteristic is square, one may represent i(t) as a superposition of sinusoids of random amplitudes, N in number:

$$i(t) = \sum_{i=1}^{N} (a_i \sin \omega_i t + b_i \cos \omega_i t), \tag{6}$$

in which, according to the sampling theorem, N is given by

$$N = BT_o. \tag{7}$$

The random amplitudes of the sinusoids satisfy the conditions

$$\overline{a_i b_i} = 0$$

$$\overline{a_i a_j} = \overline{a^2}\delta_{ij} = \overline{b_i b_j} \tag{8}$$

where we have assumed stationarity and symmetry of the current spectrum. The ratio of the uncertainty of the experimental determination of the shot-noise level normalized to shot noise is given by

$$\frac{\text{Uncertainty of shot-noise level}}{\text{Shot noise}} = \frac{\left\{\overline{\left[\frac{1}{T_o}\int_0^{T_o} i^2(t)\,dt\right]^2} - \overline{\left[\frac{1}{T_o}\int_0^{T_o} i^2(t)\,dt\right]}^2\right\}^{1/2}}{\frac{1}{T_o}\int_0^{T_o} \overline{i^2(t)}\,dt} \tag{9}$$

The shot-noise level in terms of N and a^2 may be found immediately by using (6), (7), and (8):

$$\frac{1}{T_o}\int_0^{T_o} \overline{i^2(t)}\,dt = N\overline{a^2}. \tag{10}$$

On the other hand, we know that

$$\frac{1}{T}\int_0^T \overline{i^2(t)}\,dt = 2BAeI_o\Gamma. \tag{11}$$

The numerator of (9)

$$\overline{\left[\frac{1}{T_o}\int_0^{T_o} i^2(t)\,dt\right]^2} - \overline{\left[\frac{1}{T_o}\int i^2(t)\,dt\right]}^2 = \overline{\left[\sum_{i=1}^{N}\frac{1}{2}\left(a_i^2+b_i^2\right)\right]^2} - (N\overline{a^2})^2$$

$$= \frac{1}{4}\left(\sum_i \overline{a_i^4} + \sum_i \overline{b_i^4} + 2\sum_{i,j}\overline{a_i^2}\,\overline{b_j^2} + \sum_{i\neq j}\overline{a_i^2}\,\overline{a_j^2} + \sum_{i\neq j}\overline{b_i^2}\,\overline{b_j^2}\right) - N^2\,\overline{a^2}^2$$

$$= N(N+1)\,\overline{a^2}^2 - N^2\,\overline{a^2}^2 = N\,\overline{a^2}^2. \tag{12}$$

The second expression in (12) is obtained by introducing (6) and integrating over the time interval T_o. The third expression is obtained by replacing the square of the sum by a double summation and using the statistical independence of a_i and a_j, $j\neq i$, and a_i and b_j; the fourth expression results by noting that the single summations contain N terms and the summations over unequal indices contain N(N−1) terms, and further using the relationship applicable to the Gaussian variables a_i and b_i:

$$\overline{a_i^4} = 3\overline{a^2}^2 = \overline{b_i^4}. \tag{13}$$

Using (11) and (12) in (9), one finally obtains

$$\frac{\text{Uncertainty of shot-noise level}}{\text{Shot noise}} = \frac{1}{\sqrt{N}} = \frac{1}{\sqrt{BT_o}}. \tag{14}$$

Assuming that the spectral density of the light power, $\Phi_p(\omega)$, is that of Gaussian light with a Lorentzian line shape of bandwidth $\Delta\omega$, so that

$$\frac{\Phi_p(\omega)}{\overline{p}^2} = \frac{1}{\pi\Delta\omega}\,\frac{1}{1+\frac{\omega^2}{\Delta\omega^2}},$$

one finally obtains from (4), (9), (11), and (14) for the maximum signal-to-noise ratio at $\omega \to 0$:

$$\frac{\text{Signal}}{\text{Noise}} = \frac{2\overline{r}}{\Gamma\Delta\omega}\sqrt{BT_o}, \tag{15}$$

in which we have used the fact that the photoelectron rate $\overline{r}$ is related to $\overline{p}$ by

$$\overline{r} = \frac{\xi}{h\nu}\,\overline{p}.$$

The signal-to-noise ratio increases with the square root of the bandwidth and of the observation time, with the photoelectron rate, and decreases with increasing bandwidth of the incident light. A correction factor would have to be included in (15) to account for other than Gaussian light.

2. Signal-to-Noise Ratio for the Counting Experiment

The signal of the counting experiment may be defined as

$$\text{Signal} = \frac{\overline{n(n-1)} - \overline{n}^2}{\overline{n}} \tag{16}$$

This quantity would vanish if the process were Poisson and an infinite number of samples were taken so that the ensemble averages may be equated to the experimental averages. Because of the finite number of samples taken in an experiment, however, (16) would not yield zero even for a Poisson process. It is meaningful to define as the "noise" in this experiment the mean-square deviation (from zero) of (16) for a pure Poisson process, because of the finite number of samples taken. In this case one may evaluate the noise by using Poisson statistics for the photoelectron counts. Assuming that N samples are taken, we have

$$\text{Noise} = \frac{1}{\overline{n}} \left\{ \overline{\left[\frac{1}{N} \sum_{i=1}^{N} n_i(n_i-1) - \left(\frac{1}{N} \sum_{i=1}^{N} n_i \right)^2 \right]^2} \right\}^{1/2} . \tag{17}$$

Replacing the higher powers of the sums in (17) by multiple sums, one obtains

$$\text{Noise} = \frac{1}{\overline{n}} \left\{ \frac{1}{N^2} \sum_{i,j} \overline{n_i(n_i-1)\, n_j(n_j-1)} + \frac{1}{N^4} \sum_{i,j,k,\ell} \overline{n_i n_j n_k n_\ell} - 2\,\frac{1}{N^3} \sum_{i,j,k} \overline{n_i(n_i-1)\, n_j n_k} \right\}^{1/2} . \tag{18}$$

In the first sum we have to be concerned with terms of equal indices i and j, and with terms of unequal indices. There are N terms of the former type, and N(N-1) terms of the latter type. In the second summation, there are N terms in which all subscripts are the same, 4N(N-1) terms in which three subscripts are the same and one is different; 3N(N-1) terms in which two pairs have equal subscripts; 6N(N-1)(N-2) terms in which

two subscripts are the same and the others are different; and N(N-1)(N-2)(N-3) terms in which all subscripts are different. A similar study of the third summation in (18) gives N terms in which all subscripts are alike, N(N-1) terms in which j = k, but j ≠ i, 2N(N-1) for which j = i or k = i, but j ≠ k, and N(N-1)(N-2) for which all subscripts are different. Further, using the expressions for the moments n^k for a Poisson process, one may calculate (18) retaining only terms of 0^{th} and 1^{st} order 1/N: this is legitimate because in all experiments, the number of samples N would be large. One finds that the

$$\text{Noise} = \sqrt{\frac{2}{N}} \tag{19}$$

Again, assuming that the "signal" is produced by Gaussian light of Lorentzian line shape and bandwidth $\Delta\omega$, one has

$$\rho_p(\tau) = e^{-\Delta\omega\tau}$$

and therefore, from (2) and (16) for the maximum signal attained in the limit $T \gg \Delta\omega$

$$\text{Signal} = \frac{2\bar{r}}{\Delta\omega}. \tag{20}$$

Introducing this expression for the signal, one obtains with the aid of (20)

$$\frac{\text{Signal}}{\text{Noise}} = \sqrt{2}\,\frac{\bar{r}}{\Delta\omega}\sqrt{N}. \tag{21}$$

This expression has to be multiplied by the same correction factor as (15) to account for other than Gaussian light. Note the similarity of the signal-to-noise ratio of this experiment and the signal-to-noise ratio of the spectrum measurement, (15), which is even enhanced by the fact that the product $T_o B$ stands for the number of samples necessary to describe the time function i(t) of bandwidth B in the observation time T.

3. Comparison with Brown and Twiss Experiments

We shall now compare the results obtained here with the corresponding expressions obtained by Brown and Twiss.[8,9] The correlation experiment yields in their case, for a square filter characteristic, the result [Eq. (3.62) of Brown and Twiss[7]]

$$\frac{S}{N} = \frac{\sqrt{2}}{\Gamma}\,\frac{\bar{r}}{\Delta\nu}\sqrt{BT_o} = \frac{2\sqrt{2}\pi\bar{r}}{\Gamma\Delta\omega}\sqrt{BT_o}, \tag{22}$$

where we have set

$$\frac{1}{\Gamma} = \left(1-\frac{1}{\mu}\right),\ \eta \tilde{=} 1,\ A = A_1 = A_2$$

and

$$\frac{A\int_0^\infty a^2(\nu)\, n^2(\nu)\, d\nu}{\int_0^\infty a(\nu)\, n(\nu)\, d\nu} = \frac{\bar{r}}{\Delta\nu}.$$

Except for the factor $\sqrt{2}\,\pi$, this is the same expression as (15).

Next, compare the signal-to-noise ratio of the coincidence experiment with the expression obtained thus far. Brown and Twiss point out[8] that the signal-to-noise ratio for the coincidence experiment is given by (22) as well, if one interprets $B = 1/4\,\tau_c$, where τ_c is the resolving time of the counter. But their analysis applies to the case for which the inverse resolving time of the counter is much smaller that the light bandwidth $\Delta\omega$. If one develops an expression for the signal-to-noise ratio for the case $\Delta\omega \ll 1/\tau_c$, one finds[10] [Eq. (5.23) of Brown and Twiss[9]]

$$\frac{\text{Signal}}{\text{Noise}} = \bar{r}\sqrt{T_o\tau_c}$$

$$= \frac{\bar{r}}{\Delta\omega}\sqrt{T_o\Delta\omega}\sqrt{\Delta\omega\tau_c}.$$

Insofar as the bandwidth of the spectral measurement can be made comparable to the light bandwidth (say, $2\pi B \sim \Delta\omega/4$), the expression above looks like the signal-to-noise ratio of the spectral experiment, except for the factor $\sqrt{\Delta\omega\tau_c}$. The resolving time must be made short enough to accommodate the rate $\bar{r}$. Thus $\Delta\omega\tau_c$ is usually much less than unity; and, accordingly, the signal-to-noise ratio of the coincidence counting experiment is smaller than that of the other measurements discussed here.

H. A. Haus

References

1. H. A. Haus, Quarterly Progress Report No. 76, Research Laboratory of Electronics, M. I. T., January 15, 1965, pp. 47-51.
2. H. A. Haus, Quarterly Progress Report No. 78, Research Laboratory of Electronics, July 15, 1965, pp. 71-73.
3. C. Freed, H. A. Haus, Appl. Phys. Lett. 6, 85 (March, 1965).
4. C. Freed and H. A. Haus, a paper presented at the Conference on Physics of Quantum Electronics, San Juan, Puerto Rico, June 28-30, 1965 (to be published).
5. This is an extension of an expression derived by C. T. J. Alkemade, Physica 25, 1145 (1959). See also appendix to C. Freed and H. A. Haus, "Photocurrent Spectrum and Photoelectron Counts Produced by a Gaseous Laser" (submitted to the Physical Review).
6. L. Mandel, Proc. Phys. Soc. (London) 72, 1037 (1958).
7. The mean-square fluctuations of the current in a narrow bandwidth B are related to the spectrum by $4\pi B\,\Phi(\omega)$.

8. R. H. Brown, and R. Q. Twiss, Proc. Roy. Soc. (London) A242, 300 (1957).

9. R. H. Brown, and R. Q. Twiss, Proc. Roy. Soc. (London) A243, 291 (1958).

10. H. A. Haus, "Theory of Brown and Twiss Experiment as Applied to Noise Measurements on Optical Masers," Internal Memorandum No. 131, January 7, 1964.

B. QUANTUM ANALYSIS OF NOISE IN THE LASER OSCILLATOR

1. Introduction and Summary

Spontaneous emission noise is essentially a quantum phenomenon. It can only be described by an analysis in which the field is quantized. For the laser amplifier and the laser oscillator below threshold, which are both linear devices, such an analysis is known.[1] In this report we shall give the general outline[2] of a quantum analysis of the nonlinear laser oscillator above threshold. We make use of the concept of quantum noise sources. These are operators whose first-order moments are zero and whose second-order moments are nonzero. They drive Van der Pol equations whose variables are operators. We linearize these equations in the noise, and solve for the first- and second-order Glauber functions,[3] $G^{(1)}$ and $G^{(2)}$, and for the expectation value of the commutator of the field variables. These three results refer to the field inside the cavity.

These results will be compared with the results of an earlier theory[4] in which the semiclassical equations are considered to be driven by the linear noise sources. We shall call this theory "semiclassical." Our results contain "saturation corrections" caused by the fact that the correlation functions of our quantum noise sources differ slightly from the corresponding quantities in the "semiclassical" theory. Our results also contain "quantum corrections" caused by the fact that our variables are operators. Both of these corrections are small. Because our results refer to the fields inside the cavity, and because experiments[5] are performed on the fields of the laser beam outside the cavity, we cannot yet give an exact discussion of the experimental meaning of these corrections.

Furthermore, it can be shown that any particular moment of the field can be rederived from an equivalent classical problem consisting of the semiclassical equations driven by appropriate noise sources. For different field moments one needs different noise sources. It turns out that $G^{(1)}$ and $G^{(2)}$ need the same noise sources. These noise sources differ slightly from the linear sources of the "semiclassical" theory.

2. Fundamental Equations

We shall consider one field mode in interaction with N two-level systems (particles, material) in resonance with the field mode. The particles undergo collisions and we restrict ourselves in this report to one type with collision time T. The field also

interacts with a loss system consisting of an infinite set of harmonic oscillators, originally in thermal equilibrium at temperature T_L, and with a flat spectral distribution. We shall concentrate here on the interaction between field and material; the effect of the loss will be mentioned without proof.[1,2] In between collisions the system is described by the Hamiltonian

$$H = \hbar\omega_o a^+ a + \sum_j \hbar\omega_o w_j + \sum_j i\hbar\kappa_j (a^+ p_j^- - p_j^+ a) + \text{Loss} \tag{1}$$

in which a, a^+ are the annihilation and creation operators of the field mode, and w_j, p_j^-, p_j^+ are the energy operator and the negative and positive frequency components of the polarization operator of the j^{th} two-level system. They are adequately normalized so that

$$\left[p_j^+, p_j^-\right] = 2w_j; \quad \left[w_j, p_j^+\right] = p_j^+; \quad \left[p_j^-, w_j\right] = p_j^- \tag{2}$$

This Hamiltonian leads to the following equations of motion:

$$\frac{da(t)}{dt} = \sum_j \kappa_j p_j^-(t) + \text{Loss}; \quad \text{and Hermitian conjugate (h. c.)} \tag{3}$$

$$\frac{dp_j^-(t)}{dt} = 2\kappa_j w_j(t)\, a(t); \quad \text{and h. c.} \tag{4}$$

$$\frac{dw_j(t)}{dt} = -\kappa_j\left[p_j^+(t)\, a(t) + a^+(t)\, p_j^-(t)\right]. \tag{5}$$

We adopt the following model for collision. When there is no field in the cavity, the material is in a randomized equilibrium state characterized by a given inversion $\rho_+ - \rho_-$ (or, equivalently, a given negative temperature $-T_m$). When the field is excited, a particle j interacts for some time t_j with the field, whereby both field and particle develop components in each other's Hilbert space. At the collision the interaction stops, the field retains its components in the j^{th} particle Hilbert space, but the j^{th} particle is kicked back to its original randomized equilibrium state and becomes independent of all of its previous states. It is now in fact a "new" j^{th} particle with a new Hilbert space, and during the next interaction the field will develop additional components in this new space. The material operators immediately after such a collision will be denoted by $p_j^{\pm}(0)$, $w_j(0)$. They have the properties

$$\left\langle p_j^+(0)\, p_k^-(0)\right\rangle = 2\left\langle w_j(0)\right\rangle (1+\beta_m)\, \delta_{jk}; \quad \left\langle p_j^-(0)\, p_k^+(0)\right\rangle = 2\left\langle w_j(0)\right\rangle \beta_m \delta_{jk}$$

$$\left\langle p_j^{\pm n}(0)\right\rangle = 0; \quad 2\left\langle w_j(0)\right\rangle = \rho_+ - \rho_- \tag{6}$$

in which $j \neq k$ for a different particle or collision, and $\beta_m = [(\rho_+/\rho_-)-1]^{-1} = [\exp(\hbar\omega_o/kT_m)-1]^{-1}$.

3. Solution

Consider a time interval $t_i, t_i + \tau$ of order a few times T, and a particular interaction of particle j with duration t_j, somewhere in that interval. We put $a^{\pm}(t) = a^{\pm}(t_i)$ in Eqs. 4 and 5 during τ. These equations are then solved during this interaction for $p_j^{\pm}(t)$ in terms of $p_j^{\pm}(0)$, $w_j(0)$ and $a^{\pm}(t_i)$ to third order in $\kappa_j t$. These solutions are then used to integrate Eq. 3 in the interval $t_i, t_i + \tau$ to fourth order in $\kappa_j t_j$. If τ is considered a differential dt, one may cast the result in the form of a differential equation

$$\frac{da}{dt} - (\gamma - \mu - \alpha\gamma a^+ a)\, a = x^-(t); \qquad \frac{da^+}{dt} - a^+(\gamma - \mu - \alpha\gamma a^+ a) = x^+(t) \tag{7}$$

in which $\gamma\, dt = \sum_j \sum_c \kappa_j^2 t_j^2 w_j$, $\alpha\gamma\, dt = \sum_j \sum_c (1/3)\, \kappa_j^4 t_j^4 w_j$, $\langle\gamma\rangle = 2N\kappa^2 T\langle w\rangle$, $\langle\alpha\gamma\rangle = 8N\kappa^4 T^4\langle w\rangle$ ($\sum_j$ means summation over the particle index, $\sum_c$ summation over the collisions in dt, the argument (0) has been dropped), $x^-(t) = x_L^-(t) + x_m^-(t)$, and h.c. The quantities μ and x_L are caused by the loss.[1,2] The loss noise sources x_L are independent of the material noise sources x_m and for $t_1 = t_2$

$$\left\langle x_L^+(t_1)\, x_L^-(t_2)\right\rangle = 2\mu\beta_L(1/dt); \qquad \left[x_L^-(t_1),\, x_L^+(t_2)\right] = 2\mu/dt, \tag{8}$$

where $\beta_L = [\exp(\hbar\omega_o/kT_L)-1]^{-1}$; for $|t_1 - t_2| > dt$ these expressions are zero. The material noise sources are given by

$$x_m^-(t)\, dt = \sum_j \sum_c \left\{\kappa_j t_j p_j^- - (1/3)\, \kappa_j^3 t_j^3 \left[p_j^+ a^2 + p_j^- a^+ a\right]\right\}$$

$$x_m^+(t)\, dt = \sum_j \sum_c \left\{n_j t_j p_j^+ - (1/3)\, n_j^3 t_j^3 \left[p_j^- a^{+2} + p_j^+ a^+ a\right]\right\}. \tag{9}$$

It can be shown that these noise sources are Gaussian (operators u, v, w, x, ... are defined to be Gaussian in some ensemble if $\langle uvwx\rangle = \langle uv\rangle\langle wx\rangle + \langle uw\rangle\langle vx\rangle + \langle ux\rangle\langle vw\rangle$); the errors made in Eq. 7 by replacing τ by a differential are negligible if $\gamma T < 1$ or, in experimental terms, if the cold-cavity bandwidth is smaller than the collision-broadened linewidth; Eq. 7 conserves the field comutator $[a, a^+] = 1$; if we consider the field operators in $x_m^{\pm}$ as c-numbers, we must consider γ as a c-number (because of the large number of particles and collisions in dt, this c-number is obviously $\langle\gamma\rangle$).

We use the substitution

$$a(t) = [R_o+\Delta(t)]\, e^{-i\theta_t}; \quad a^+(t) = [R_o+\Delta^+(t)]\, e^{i\theta_t} \tag{10}$$

in which Δ, Δ^+ are operators with $[\Delta,\Delta^+] = 1$, and R_o and θ_t are c-numbers. By putting $\alpha\gamma R_o^2 = \gamma - \mu$, we have adjusted R_o^2 so that it is equal to the steady-state photon number in the cavity, n_o, as predicted by the semiclassical theory without noise sources. We linearize Eqs. 7 in Δ, Δ^+, and θ_t; we replace the field operators in $x_m^{\pm}$ by their main terms, which are c-numbers; and consistently consider γ as a c-number. Furthermore, defining $2in_s = x^- \exp(i\theta_t) - x^+ \exp(-i\theta_t)$, $2n_c = x^- \exp(i\theta_t) + x^+ \exp(-i\theta_t)$, we obtain

$$i\theta_t 2R_o + \frac{d(\Delta^+-\Delta)}{dt} = -2in_s; \quad \frac{d(\Delta^++\Delta)}{dt} + 2(\gamma-\mu)(\Delta^++\Delta) = 2n_c. \tag{11}$$

Equations 11 can now be solved for the correlation functions of θ_t, Δ, and Δ^+. The third unknown, θ_t, can be chosen freely as an independent Gaussian, but its correlation function is uniquely defined by the condition that the correlation function of $(\Delta^+-\Delta)$ should stay finite. These correlation functions are then used to calculate the moments of the field. Consistency with the linearization approximation requires that all moments of $\Delta^{\pm}$ higher than the second be neglected.

From Eqs. 6, 8, and 9 we obtain

$$\left\langle n_s(t+\tau)\, n_s(t)\right\rangle = A_s\delta(\tau) = \left[\gamma\left(\frac{1}{2}+\beta_m\right) + \mu\left(\frac{1}{2}+\beta_L\right)\right]\delta(\tau)$$

$$\left\langle n_c(t+\tau)\, n_c(t)\right\rangle = A_c\delta(\tau) = \left[A_s - 4(\gamma-\mu)\left(\frac{1}{2}+\beta_m\right)\right]\delta(\tau)$$

$$i\left\langle [n_c(t+\tau), n_s(t)]\right\rangle = (\gamma-\mu)\,\delta(\tau). \tag{12}$$

This leads to the following results for $G^{(1)} = \langle a^+(t+\tau)\, a(t)\rangle$, $G^{(2)} = \langle T^+(a^+(t)\, a^+(t+\tau))\, T(a(t+\tau)\, a(t))\rangle$ and the field commutator, respectively.

$$G^{(1)} = \exp\left[-\frac{A_s}{2n_o}|\tau|\right]\left[n_o + \frac{1}{4}\frac{A}{\gamma-\mu}\, e^{-2(\gamma-\mu)|\tau|}\right] \tag{13a}$$

$$\frac{G^{(2)} - n_o^2}{n_o} = \frac{A}{(\gamma-\mu)}\, e^{-2(\gamma-\mu)|\tau|} \tag{13b}$$

$$\left\langle [a(t+\tau), a^+(t)]\right\rangle = \exp\left[-\frac{A_s}{2n_o}|\tau|\right]\left[\frac{1}{2}+\frac{1}{2}e^{-2(\gamma-\mu)|\tau|}\right]. \tag{14}$$

Here, we have introduced the time-ordering operators T (which puts the later time first) and T^+ (which puts the earlier time first); these were needed in the definition of $G^{(2)}$ because $[a(t-\tau), a(t)] \neq 0$. We have also introduced the average number of photons in the

cavity $\langle n(t)\rangle \approx R_o^2 = n_o$, and the parameter A, defined by

$$A = A_c - (\gamma-\mu) = A_s - (\gamma-\mu)(3+4\beta_m). \tag{15}$$

We note that all parameters in Eqs. 12-15 have experimental meaning: 2μ is the cold-cavity bandwidth ($\Delta\omega_o$ in Haus[5]), $2(\gamma-\mu)$ is the hot-cavity bandwidth ($\Delta\omega$ in Haus[5]), $2\gamma = \omega_o/|Q_m^o|$ with Q_m^o the negative cavity Q,[5] and n_o is related to the power, P_o, transmitted in the laser beam by $P_o = 2\mu n_o \hbar\omega_o$.

The field commutator (Eq. 14) is 1 for $\tau = 0$, decays to 1/2 with time constant $(1/2(\gamma-\mu))$ for $|\tau|$ small, and to zero with the time constant $(2n_o|A_s)$ for $|\tau|$ large. The terms having A in $G^{(1)}$ and $G^{(2)}$ describe the influence of the amplitude fluctuations on $G^{(1)}$ and $G^{(2)}$. The influence on $G^{(1)}$ is small and if we neglect it, the spectrum of $G^{(1)}$ becomes Lorentzian with full half-power width, $\Delta\omega_1$,

$$\Delta\omega_1 = \frac{A_s}{n_o} = \frac{\hbar\omega_o}{2P_o}(2\mu)^2\left[\frac{\gamma}{\mu}\left(\frac{1}{2}+\beta_m\right) + \left(\frac{1}{2}+\beta_L\right)\right]. \tag{16}$$

Apart from the factor [ ], this is the double of the Townes width.[7] The influence on $G^{(2)}$ is essential: the semiclassical meaning of $G^{(2)}$ tells us that Eq. 13b gives us the relative correlation function of the photon number, and for $\tau = 0$ it is

$$\frac{A}{\gamma-\mu} = \frac{\mu}{\gamma-\mu}\left[\frac{\gamma}{\mu}\left(\frac{1}{2}+\beta_m\right) + \left(\frac{1}{2}+\beta_L\right)\right] - (3+4\beta_m). \tag{17}$$

As we have mentioned, we still cannot translate this result into the experimentally important power correlation in the laser beam.

We shall now interpret the quantities A and A_s in Eqs. 13 in the light of an equivalent classical problem. In Fig. VI-1 we put $G_m = G_m^o - (\alpha C|2\hbar\omega_o)\, G_m^o |V(t)|^2$, $\omega_o^2 = 1/LC$, $V = |V(t)|\cos(\omega_o t+\theta_t)$. The noise source i_n has positive and negative frequency components i_n^+ and i_n^- such that $i_n = i_n^+ \exp(i\omega_o t) + i_n^- \exp(-i\omega_o t)$. From these we derive the in-phase component $i_c = (1/2)[i_n^- \exp(i\theta_t) + i_n^+ \exp(-i\theta_t)]$ and the quadrature component $i_s = (1/2)[i_n^- \exp(i\theta_t) - i_n^+ \exp(-i\theta_t)]$, so that $i_n = 2i_c \cos(\omega_o t+\theta_t) + 2i_s \sin(\omega_o t+\theta_t)$. The components i_c and i_s are supposed to be independent, stationary processes, "white" with respect to the "hot" cavity bandwidth but narrow-band with respect to ω_o. One can show that the circuit of Fig. VI-1 gives rise to the equations

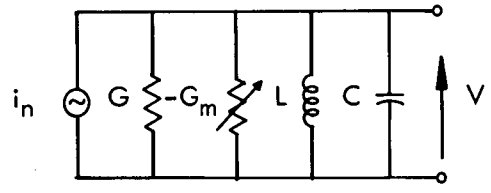

Fig. VI-1. Equivalent circuit of the noisy laser oscillator.

$$\frac{dV^+}{dt} + \frac{G - G_m}{2C} V^+ = \frac{i_n^+}{2C}; \quad \frac{dV^-}{dt} + \frac{G - G_m}{2C} V^- = \frac{i_n^-}{2C}. \tag{18}$$

The correspondence with our analysis is made by taking the following scaling factors into account: $V^+ = (\hbar\omega_o/2C)^{1/2}\, a^+$, $G/2C = \mu$, $G_m^o/2C = \gamma$, $(\alpha C/2\hbar\omega_o)\, G_m^o |V(t)|^2 = \alpha\gamma a^+ a$, $i_n^+ = (2\hbar\omega_o C)^{1/2} x_{eq}^+$, $i_c = (2\hbar\omega_o C)^{1/2} n_{ceq}$. By putting $\Delta = \Delta^+ = R_1 =$ c-number in Eq. 10, we obtain from Eq. 18

$$R_o \theta_t' = -n_{seq}; \quad \frac{dR_1}{dt} + 2(\gamma-\mu) R_1 = n_{ceq} \tag{19}$$

The "semiclassical" circuit[4] is obtained by postulating $\langle n_{seq}(t+\tau)\, n_{seq}(t)\rangle = \langle n_{ceq}(t+\tau)\, n_{ceq}(t)\rangle = A_s\delta(\tau)$ and $\langle n_{ceq}(t+\tau)\, n_{seq}(t)\rangle = 0$, where $\delta(\tau)$ is a delta function on time scales of the inverse "hot" cavity bandwidth, but certainly not on time scales of $1/\omega_o$. This leads to a stationary i_n with spectrum $S_{i_n}(f)$ around ω_o: $\overline{i_n^2} = 2S_{i_n}(f)\, df = 4S_{i_c}(f)\, df = 4A_s(2\hbar\omega_o C)\, df = \left[4G_m^o\left(\frac{1}{2}+\beta_m\right) + 4G\left(\frac{1}{2}+\beta_L\right)\right]\hbar\omega_o\, df$. This is the well-known "linear voltage source" (i.e., it predicts the exact voltage fluctuations below threshold[7]). These noise sources would follow from our theory if we dropped the nonlinear terms in Eqs. 9 for x_m^- and x_m^+. Equation 19 now leads to the results (13) but with A replaced by A_s. Therefore, in the "semiclassical" theory one predicts correctly the width $\Delta\omega_1$ (Eq. 16) but because A_s differs from A (Eq. 15), one makes an error of $(3+4\beta_m)$ photons in the relative photon number fluctuations at $\tau = 0$ (Eq. 17). Close to the threshold ($\gamma \approx \mu$), $\mu/(\gamma-\mu)$ is large, so that this error is relatively small compared with the main term of Eq. 17. Higher above threshold $\gamma - \mu$ increases and the error becomes relatively more important, but absolutely it is independent of $\gamma - \mu$ and is always small.

The exact equivalent problem instead is obtained by postulating $\langle n_{seq}(t+\tau) n_{seq}(t)\rangle = A_s\delta(\tau)$, $\langle n_{ceq}(t+\tau)\, n_{ceq}(t)\rangle = A\delta(\tau)$ and $\langle n_{ceq}(t+\tau)\, n_{seq}(t)\rangle = 0$. This leads then to the exact results (13). Because $A \neq A_s$ the new source i_n is nonstationary. It is interesting to investigate the cause of $A \neq A_s$. First, A is different from A_c (Eq. 15). This is a "pure quantum" effect because it is caused by the operator character of Δ and Δ^+, and by $\langle [n_c, n_s]\rangle \neq 0$. This effect corrects the relative photon number fluctuation by exactly 1 photon. It is also interesting to note that it is not present in the exact expression for $\langle a^+(t)\, a(t)\, a^+(t+\tau)\, a(t+\tau)\rangle$, which for $\tau = 0$ equals $G^{(2)} + n_o$. Second, A_c is different from A_s (Eq. 12). This is a "saturation" effect and can be explained classically. This difference is indeed caused by the terms containing a^2 and a^{+2} in Eqs. 9. These terms are phase-dependent and they make x^- and x^+ nonstationary, although n_s and n_c are stationary. This corresponds to the classical statement that i_n is nonstationary if $\langle i_c^2\rangle \neq \langle i_s^2\rangle$. This effect corrects the relative photon number fluctuation by $(2+4\beta_m)$

photons. These two effects add and that leads ultimately to $A \neq A_s$, and the correction $(3+4\beta_m)$ in Eq. 17.

H. J. Pauwels

References

1. W. H. Louisell, Radiation and Noise in Quantum Electronics (McGraw-Hill Book Company, New York, 1964).
2. H. J. Pauwels, "Phase and Amplitude Fluctuations of the Laser Oscillator" (submitted to IEEE Transactions on Quantum Electronics) contains more details.
3. R. J. Glauber, "The Quantum Theory of Optical Coherence," Phys. Rev. 130, 2529 (June 15, 1963).
4. H. A. Haus, "Amplitude Noise in Laser Oscillators," IEEE J. Quantum Electronics, Vol. 1, No. 4, pp. 179-180, July 1965.
5. H. A. Haus, Quarterly Progress Report No. 76, Research Laboratory of Electronics, M.I.T., January 15, pp. 47-51.
6. C. H. Townes, "Some Applications of Optical and Infrared Masers," in Advances in Quantum Electronics (Columbia University Press, New York, 1961).
7. H. A. Haus and J. A. Mullen, "Noise in Optical Maser Amplifiers," Proc. Symposium on Optical Masers, Polytechnic Institute of Brooklyn, April 16-19, 1963, pp. 131-155.

C. SPECTRAL ANALYSIS OF LASER OSCILLATOR BY MEANS OF HIGHER AUTOCORRELATION FUNCTIONS

Reported here is the theoretical basis for an experimental confirmation of the supposed Gaussian property of the noise caused by spontaneous emission in a cavity-type laser oscillator. This noise in the semiclassical analysis appears as a random source in a van der Pol equation describing the oscillation of the electric field of a laser operating somewhat above threshold.[1] It has been shown experimentally that in that region the noise is due mainly to spontaneous emission.[2]

The variation $R_1(t)$ in the electric field amplitude about its steady-state value R_o above threshold is assumed to satisfy a linearized equation derivable from the van der Pol equation. In this region of operation, it is found that information about the third-order autocorrelation function $\overline{R_1(t)\,R_1(t+\tau_1)\,R_1(t+\tau_2)\,R_1(t+\tau_3)}$ can be extracted from the spectrum of the square of the anode current in a photomultiplier placed in the laser beam. This is accomplished with the aid of a direct current and lowpass filter before squaring.

We assume that the effect of the filters is to produce the following form for the transform of the deterministic current pulse:

$$F_i(\omega) = \begin{cases} \frac{eA}{2\pi}, & 0 < |\omega| < \omega_f \\ 0, & \omega = 0 \text{ or } |\omega| \geq \omega_f \end{cases} \tag{1}$$

where ω_f is the filter bandwidth, A is the photomultiplier gain, and e is the unit of electronic charge. Each pulse is the result of the emission of one photoelectron, if the effect of secondary emission is neglected. With no lowpass filter present, ω_f can be interpreted as the photomultiplier bandwidth, which can be 10^8-10^9 rad/sec.

In the region where the linearized theory is valid, the modulation coefficient $m \equiv R_1^2(t)/R_o^2$ is much less than unity. Furthermore, if the noise source is Gaussian, then $R_1(t)$ must be Gaussian in this region. Using these facts and the assumptions of the preceding paragraphs, we obtain for the squared current spectrum $S_{I^2}(\omega)$ when $\omega \ll \omega_f$, and when the modulation process bandwidth ω_o is much less than ω_f

$$S_{I^2}(\omega) = \frac{8A^4e^4}{\pi^3}\,\omega_f^2 r^2 m\,\frac{\omega_o}{\omega_o^2+\omega^2} + \frac{128A^4e^4}{\pi}\,r^4m^2\,\frac{\omega_o}{4\omega_o^2+\omega^2}. \tag{2}$$

Here, r is the average rate of emission of photoelectrons, which ranged around 10^{10} sec^{-1} in the measurements made above threshold on the ordinary spectrum as reported by Haus.[2] The first term in Eq. 2 arises from the first-order autocorrelation $\overline{R_1(t)\,R_1(t+\tau)}$ and is basically the same as the term measured in the unsquared spectrum. The second term arises from the third-order autocorrelation of $R_1(t)$. All other terms, including shot-noise terms and contributions from even higher autocorrelation functions of $R_1(t)$, are negligible in the region where the linearized theory is valid, and not too far above threshold.

By increasing the attenuation in front of the photomultiplier, r is decreased and the first term of (2) will predominate. Increasing r or decreasing ω_f will make the second term predominate. It is shown elsewhere[3] that the assumption of typical realizable DC and lowpass filters instead of the ideal filter represented by (1) only increases the first term of (2) by $\pi^2/4$. The second term, which is independent of ω_f, remains unchanged as long as ω lies within the passband of the filter.

If the predictions of (2) are verified by experiment, then we may conclude that the spontaneous emission noise source of the semiclassical analysis is Gaussian. This assumption could not be checked with measurements of the ordinary spectrum. Furthermore, as m increases and threshold is approached, the linearized theory will become invalid. Measurements of the squared current spectrum with the filters used as discussed above should show deviations from the linearized theory before measurements of the ordinary spectrum. Because of the possibility of using filters and operating with a higher photoelectron emission rate, we also conclude that measurements of the squared current spectrum could yield more information about the third-order autocorrelation of $R_1(t)$ than could counting experiments. Higher speed and thus less sensitivity to drift in laser operation would also be achieved.

J. L. Doane

References

1. H. A. Haus, IEEE J. Quantum Electronics, Vol. 1, No. 4, pp. 179-180, July 1965.
2. H. A. Haus, Quarterly Progress Report No. 76, Research Laboratory of Electronics, M.I.T., January 15, 1965, pp. 47-51.
3. J. L. Doane, S.M. Thesis, Department of Electrical Engineering, M.I.T., August 26, 1965.

VII. PHYSICAL ELECTRONICS AND SURFACE PHYSICS*

Prof. R. E. Stickney
R. M. Logan
P. B. Sun

A. SIMPLE CLASSICAL MODEL FOR THE SCATTERING OF GAS ATOMS FROM SOLID SURFACES

1. Introduction

For the case of gases of extremely low density (i.e., for free molecule flow), the transfer of momentum and energy between the gas and a solid surface depends entirely upon the nature of the collisions of individual gas atoms with surface atoms. A satisfactory theory of this interaction has not yet been established. The principal objective of the present study is to formulate a simple model whose behavior agrees qualitatively with the experimental data for the scattering of a beam of gas particles from a solid surface.

The following symbols are used:

u = velocity of gas particle

u_n = component of velocity of gas particle in direction normal to surface plane

u_t = component of velocity of gas particle in direction tangential to surface plane

v = velocity of surface atom (assumed to be in direction normal to surface plane)

M = mass of gas particle

m = mass of surface atom

μ = mass ratio, M/m

T_g = temperature of gas beam

T_s = temperature of surface

θ_o = incident angle (measured from surface normal)

θ_1 = outgoing angle (measured from surface normal)

η = angular deviation of the maximum of the angular distribution of the scattered particles from the specular direction.

(All angles are measured in the plane containing both the incident beam and the surface normal.)

*This work was supported principally by the Joint Services Electronics Program (Contract DA36-039-AMC-03200(E).

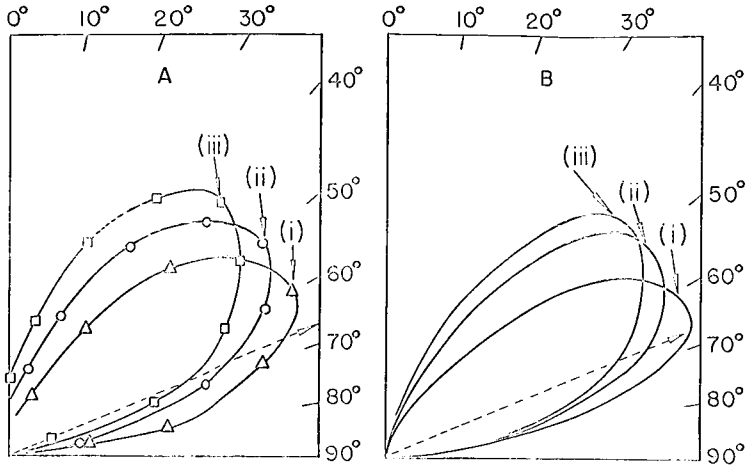

Fig. VII-1.

Temperature dependence of scattering patterns.
(A) Experimental results for Ar on Pt.[1]
(B) Analytical results.
In both cases, $\theta_o = 67.5°$ and $\mu = 0.2$
Curve (i): $T_s/T_g = 1.24$;
Curve (ii): $T_s/T_g = 2.57$;
Curve (iii): $T_s/T_g = 3.68$.

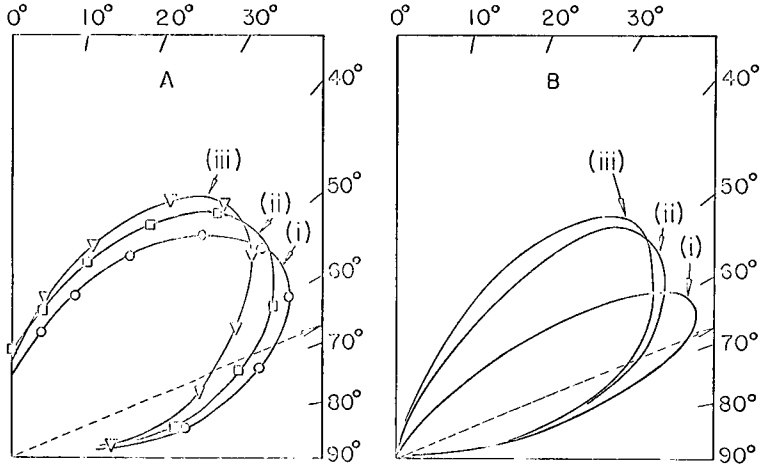

Fig. VII-2.

Mass dependence of scattering patterns.
(A) Experimental results for He, Ne, and Ar on Pt.[1]
(B) Analytical results.
In both cases, $\theta_o = 67.5°$ and $T_s/T_g = 3.60$
Curve (i): $\mu = 0.02$ (He on Pt)
Curve (ii): $\mu = 0.1$ (Ne on Pt)
Curve (iii): $\mu = 0.2$ (Ar on Pt).

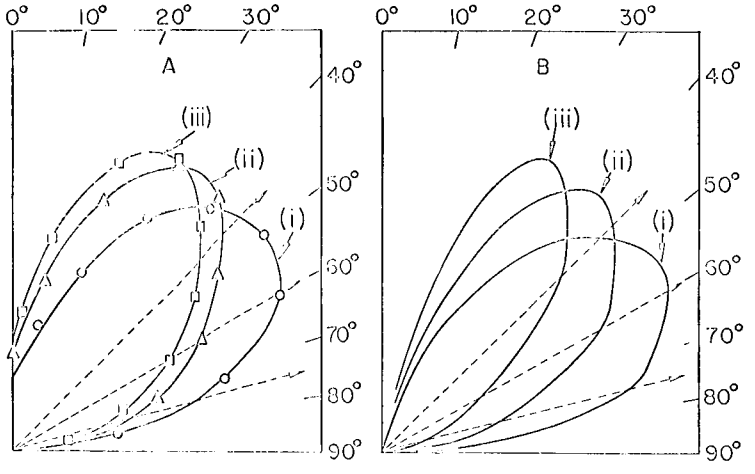

Fig. VII-3.

Incident angle dependence of scattering patterns.
(A) Experimental results for Ar on Pt.[1]
(B) Analytical results.
In both cases, $\mu = 0.2$ and $T_s/T_g = 3.67$
Curve (i): $\theta_o = 75°$;
Curve (ii): $\theta_o = 60°$;
Curve (iii): $\theta_o = 45°$.

The experimental results which are relevant to the present study are the lobular scattering patterns, examples[1] of which are shown in Figs. VII-1A, VII-2A, and VII-3A. Most of the available experimental results, for a variety of different gases on a variety of different surfaces, may be described by the following characteristics:

1. $\frac{\partial \eta}{\partial T_s}$ is positive
2. $\frac{\partial \eta}{\partial T_g}$ is negative
3. $\frac{\partial \eta}{\partial M}$ is positive
4. $\frac{\partial \eta}{\partial \theta_o}$ may be positive or negative

Characteristics 1, 3, and 4 are illustrated in Figs. VII-1A, VII-2A, and VII-3A, respectively. One further characteristic which seems to hold is $\eta \to 0$ as $\theta_o \to 0$.

2. The Model

The simple classical model which is used is based upon the following principal assumptions: (i) the interaction of a gas atom with a surface atom may be represented

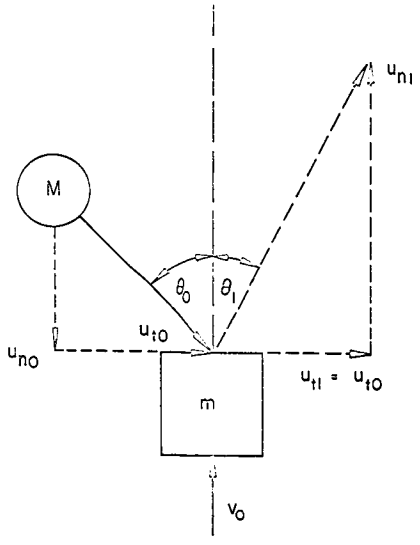

Fig. VII-4. The "Hard-Cube" model.

by an impulsive force of repulsion; (ii) the gas-surface intermolecular potential is uniform in the plane of the surface (hence the interaction does not change the tangential velocity of the gas particle); (iii) the surface atoms are represented by independent particles confined by square-well potentials; (iv) the surface atoms have a Maxwellian velocity distribution. The model incorporates many of the same features as that proposed

by Goodman.[2] As a result of these assumptions, the model is simplified to the extent that it contains no adjustable constants. In order to combine assumptions 1 and 2, it is convenient to think of the surface atoms as cubes oriented with one face parallel to the surface plane and with motion only in the direction normal to the surface plane. Each gas particle interacts with just one of these cubes (Fig. VII-4).

3. Summary of the Analysis

Since the details of the analysis require considerable space, we have chosen to omit them here. A more complete report has been submitted for publication in the Journal of Chemical Physics.

The analysis has been carried out in two stages. In the first stage, the analysis is simplified by representing the velocities of the gas and surface particles by mean values instead of considering the velocity distributions of each. In the second stage, the velocity distributions are considered.

The first stage analysis yields only the approximate angular position of the maximum of the scattering pattern, and hence η, as given by the following expression:

$$\eta = \theta_o - \cot^{-1}\left\{\cot\theta_o\left[\left(\frac{1-\mu}{1+\mu}\right) + \frac{16}{9\pi}\left(\frac{\mu}{1+\mu}\right)\frac{T_s}{T_g}\frac{1}{\cos^2\theta_o}\right]\right\} \qquad (1)$$

An indication of the behavior of Eq. 1 is given in Figs. VII-5 and VII-6.

The full analysis involves integration over the distribution functions of the gas and surface atoms, and this has been done partly by numerical computation. Some of the

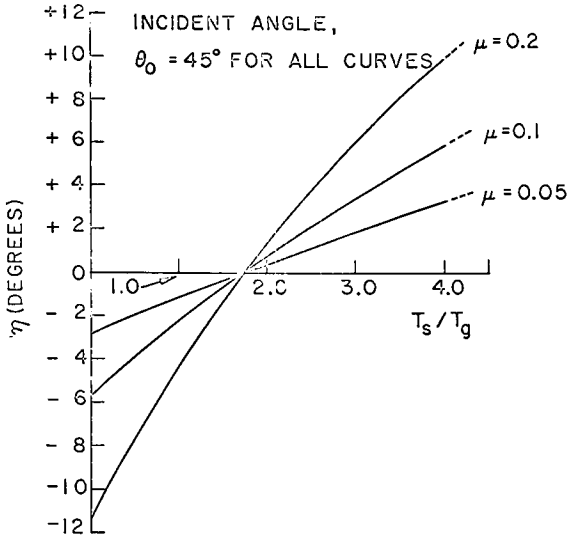

Fig. VII-5. Characteristics of the approximate analysis: The temperature dependence of η, the angular deviation from the specular direction, for several values of the mass ratio μ.

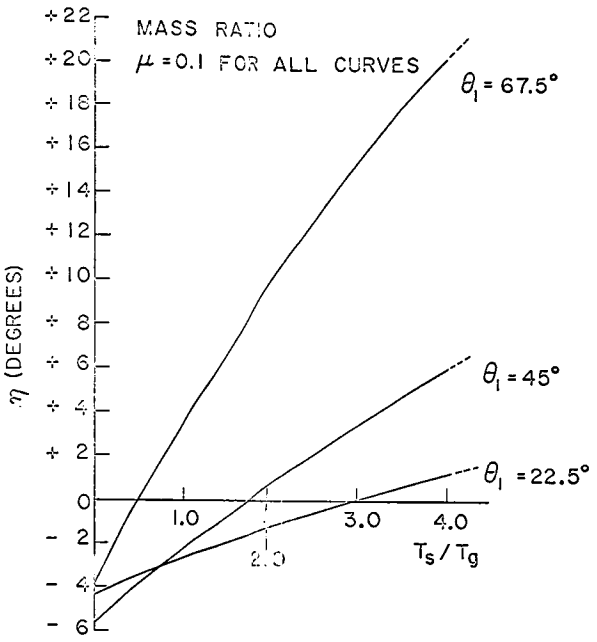

Fig. VII-6. Characteristics of the approximate analysis: The temperature dependence of η, the angular deviation from the specular direction, for several values of the angle of incidence, θ_o.

results are shown in Figs. VII-1B, VII-2B, and VII-3B so that they may be compared with the corresponding experimental results.

4. Conclusions

It is found that the results for η given by Eq. 1 are in resonable agreement with the results from the full analysis. The results from the full analysis are in good qualitative agreement with the experimental results as illustrated in Figs. VII-1, VII-2, and VII-3. Significant quantitative results are not expected from such a simplified model. The good qualitative agreement does indicate, however, that this model may contain the principal mechanisms of the interaction. The results may also be considered as some indication that the general nature of the experimentally observed scattering patterns is not dominated by the precise form of the intermolecular potential or by the topographical form of the atomic surface.

R. M. Logan, R. E. Stickney

References

1. J. J. Hinchen and W. M. Foley, "Scattering of Molecular Beams by Metallic Surfaces," in Rarefied Gas Dynamics, Proceedings of the Fourth International Symposium, edited by J. H. deLeeuw (Academic Press, Inc., New York, 1965).

2. F. O. Goodman, J. Phys. Chem. Solids 26, 85-105 (1965).

VIII. PHYSICAL ACOUSTICS*

Prof. K. U. Ingard
Prof. L. W. Dean III
Dr. G. C. Maling, Jr.
Dr. M. A. Martinelli
Dr. H. L. Willke, Jr.
C. T. Dum
P. A. Fleury
W. M. Manheimer
J. A. Ross
S. D. Weiner

A. INSTABILITY IN PARALLEL HYDRODYNAMIC AND MAGNETO-HYDRODYNAMIC FLOWS

In Quarterly Progress Report No. 77 (pages 76-79) we showed that the stationary parallel flows of lossless fluids and plasmas – with one peculiarly unphysical exception – are constant along streamlines, and demonstrated the instability of nontrivial hydrodynamic flows in three dimensions under small perturbations. This result contradicts neither Rayleigh's demonstration that two-dimensional plane parallel flows without inflected profiles have only stable normal modes nor Squire's proof that for such flows three-dimensional normal modes are "more stable" than two-dimensional modes, since the perturbations in question are not represented among the generally incomplete normal modes considered by Rayleigh and Squire. Using the more comprehensive Laplace-transform approach, Case found stability for such flows, but considered only two-dimensional disturbances.

This report demonstrates the instability of the magnetohydrodynamic, as well as hydrodynamic, cases of lossless stationary parallel flow. We first assume periodic boundary conditions along the flow.

As in the hydrodynamic case, in this instance it suffices to perturb initially only the velocity field, and to consider only perturbations preserving the constancy along streamlines of the given unperturbed flow $(\underline{1}W(x_2, x_3), \rho_o(x_2, x_3), S_o(x_2, x_3), \underline{1}B_o(x_2, x_3))$, in which $p(\rho_o(x_2, x_3), S_o(x_2, x_3)) + \frac{B_o^2(x_2, x_3)}{8\pi} = p_o$ = constant. With $\underline{V}^{(0)}(x_2, x_3) = \underline{1}W(x_2, x_3) + u^{(0)}(x_2, x_3)$, the magnetohydrodynamic equations become

$$\frac{dV}{dt} = 0 \tag{1a}$$

$$\frac{du_2}{dt} + \frac{\partial_2\left(p + \frac{B^2}{8\pi}\right)}{\rho} = 0 \tag{1b}$$

$$\frac{du_3}{dt} + \frac{\partial_3\left(p + \frac{B^2}{8\pi}\right)}{\rho} = 0 \tag{1c}$$

*This work was supported principally by the U.S. Navy (Office of Naval Research) under Contract Nonr-1841(42).

$$\frac{d\rho}{dt} = -\rho(\underline{\nabla}\cdot\underline{u}) \tag{1d}$$

$$\frac{dS}{dt} = \frac{d\,\frac{B}{\rho}}{dt} = 0, \tag{1e}$$

in which $\frac{d}{dt} = \frac{\partial}{\partial t} + u_2\partial_2 + u_3\partial_3$. In terms of the Lagrangian coordinates $\underline{X}(\underline{x}, t)$ (i.e., the solution of $d\underline{X}/dt = 0$ with the property that $\underline{X}(\underline{x}, 0) = \underline{x}$) we have at once

$$S(\underline{X}, t) = S_o(X_2, X_3) \tag{2a}$$

$$\frac{B}{\rho}(\underline{X}, t) = \frac{B_o}{\rho_o}(X_2, X_3) \tag{2b}$$

$$\rho(\underline{X}, t) = \rho_o(X_2, X_3)\exp\left(-\int_0^t (\underline{\nabla}\cdot\underline{u})(\underline{X}, t')\,dt'\right). \tag{2c}$$

Let us restrict our attention to perturbations $u^{(0)}(x_2, x_3)$ such that $\nabla \cdot u^{(0)} = 0$. Then if we neglect in Eq. 2c the change of $\underline{\nabla} \cdot \underline{u}$ from its initial value with the passage of time, we get

$$p(\underline{X}, t) + \frac{B^2(\underline{X}, t)}{8\pi} \approx p(\rho_o(X_2, X_3), S_o(X_2, X_3)) + \frac{B_o^{(2)}(X_2, X_3)}{8\pi}$$

$$= p_o = \text{constant},$$

so that Eqs. 1a, 1b, and 1c become

$$\frac{dV}{dt} = \frac{du_2}{dt} = \frac{du_3}{dt} = 0,$$

so that

$$V(X, t) = V^{(0)}(X_2, X_3) = W(X_2, X_3) + u_1^{(0)}(X_2, X_3) \tag{4a}$$

$$u_2(\underline{X}, t) = u_2^{(0)}(\underline{X}) \tag{4b}$$

$$u_3(\underline{X}, t) = u_3^{(0)}(\underline{X}). \tag{4c}$$

With the aid of the well-known inversion formula

$$\underline{x}(\underline{X}, t) = \underline{X} + \int_0^t V(\underline{X}, t')\,dt', \tag{5}$$

we find that in this approximation

$$\underline{\nabla} \cdot \underline{u} \approx \partial_i u_i^{(0)}(X_2, X_3) = \left(\partial_i u_i^{(0)}\right)(X_2, X_3) - \frac{\partial \int_0^t u_j^{(0)}(\underline{X}(\underline{x}, t))\, dt'}{\partial x_i} \left(\frac{\partial u_i^{(0)}}{\partial x_j}\right)(X_2, X_3).$$

Roughly speaking, then, Eqs. 4b and 4c approximate the solutions to Eqs. 1b and 1c to second order in certain derivatives of the $u_i^{(0)}$ (Eq. 4a is exact in terms of X).

The instability is now at hand, for

$$u_1(\underline{x}, t) = V_1(\underline{X}(\underline{x}, t), t) - W(\underline{x})$$

$$= u_1^{(0)}(\underline{X}, (\underline{x}, t)) + [W(\underline{X}(\underline{x}, t)) - W(\underline{x})]. \tag{6}$$

The first term in Eq. 6 will remain small if it is so initially. We can always make the bracketted term approach $\left|\sup_{\underline{x}} W(\underline{x}) - \inf_{\underline{x}} W(\underline{x})\right|$ by choosing $u^{(0)}$ so that streamlines starting sufficiently near the location of one extremum of W(x) pass at some later time sufficiently close to the location of the other extremum. Initially small perturbations are thus amplified by this mechanism up to the level of the spatial variation of the unperturbed flow. The latter will be small only if the unperturbed flow is essentially a Galilean translate of the null flow W = 0.

Although Eq. 6 is not an exact solution, it is better than a linearized solution in that it rounds off instead of growing indefinitely large with time. For comparison with Eq. 6, and to better exhibit the initial growth of the perturbation, we write the linearized solution corresponding to Eq. 6. Such a solution will not exist if W has large jump discontinuities, since in that case the more accurate solution (Eq. 6) will immediately jump from small to macroscopic levels at arbitrarily small $t > 0$. We extract the linearized solution from Eq. 6 by treating $\underline{X}(\underline{x}, t) - \underline{x}$ as a small parameter and keeping lowest order terms. If W is differentiable, we obtain with the aid of Eq. 5

$$u_1(\underline{x}, t) \approx u_1^{(0)}(\underline{x}) + (\underline{X}(\underline{x}, t) - \underline{x}) \cdot \nabla W(\underline{x}) + \ldots$$

$$= u_1^{(0)}(\underline{x}) - \int_0^t \underline{u}^{(0)}(\underline{x})\, dt' \cdot \nabla W(\underline{x}) + \ldots$$

$$u_1^{(0)}(\underline{x}) - t(\underline{u}^{(0)}(\underline{x}) \cdot \nabla)\, W(\underline{x}),$$

so that u_1 exhibits linear growth with time in the linearized approximation.

H. L. Willke, Jr.

PLASMA DYNAMICS

IX. PLASMA PHYSICS*

Prof. S. C. Brown
Prof. W. P. Allis
Prof. G. Bekefi
Prof. D. R. Whitehouse
Dr. J. C. Ingraham
Dr. G. Lampis
M. L. Andrews
F. X. Crist
J. K. Domen
E. W. Fitzgerald, Jr.
D. L. Flannery
E. V. George
W. H. Glenn, Jr.
E. B. Hooper, Jr.
P. W. Jameson
R. L. Kronquist
D. T. Llewellyn-Jones
E. M. Mattison
J. J. McCarthy
W. J. Mulligan
J. J. Nolan, Jr.
R. C. Owen
L. D. Pleasance
G. L. Rogoff
D. W. Swain
F. Y-F. Tse

A. ELECTRON DENSITY MEASUREMENTS WITH A LASER INTERFEROMETER

A laser interferometer has been used to study the time and spatial decay of a pulsed P.I.G. discharge.[1] The electron density decay is studied in a range from above 10^{14} cm^{-3} to below 10^{13} cm^{-3}. It is concluded from the dependence of the decay on gas pressure and magnetic field that the electron density and temperature both decay initially by radial diffusion. After a time of 100-200 microseconds, electron-ion collisions become an important cooling mechanism, and the electron temperature drops rapidly. The decay rates after 200 microseconds are consistent with the radiative-collision calculations of Bates, et al.[2]

The interferometer used in the study has been described elsewhere.[3] Briefly, it can measure phase shifts in the optical and near infrared of less than $2\pi \times 10^{-3}$ radians. In the present plasma, electron densities are thus measured with an accuracy of 10^{12} cm^{-3}. The time response of the interferometer was measured to be less than 5 microseconds.

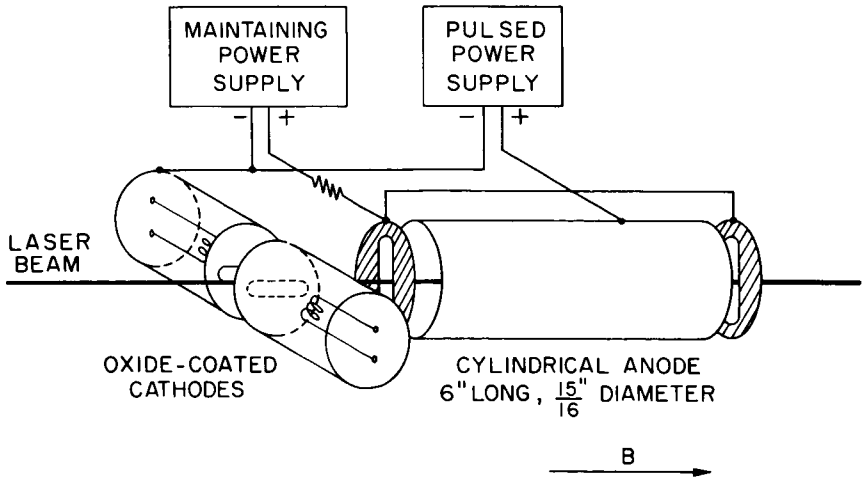

Fig. IX-1. The P.I.G. discharge.

*This work was supported principally by the U.S. Atomic Energy Commission under Contract AT(30-1)-1842.

The discharge tube is shown in Fig. IX-1. Cathodes have been placed outside the discharge region so that the laser beam can pass along the axis of the tube. A current pulse containing approximately one joule was fired 100 times per second by means of a delay line. To make the pulse reproducible the gas was pre-ionized by running a weak (10 ma) DC discharge.

Examples of the time and spatial dependence of the electron density are shown in Fig. IX-2. As can be seen the density closely follows the Bessel function predicted by elementary diffusion theory.

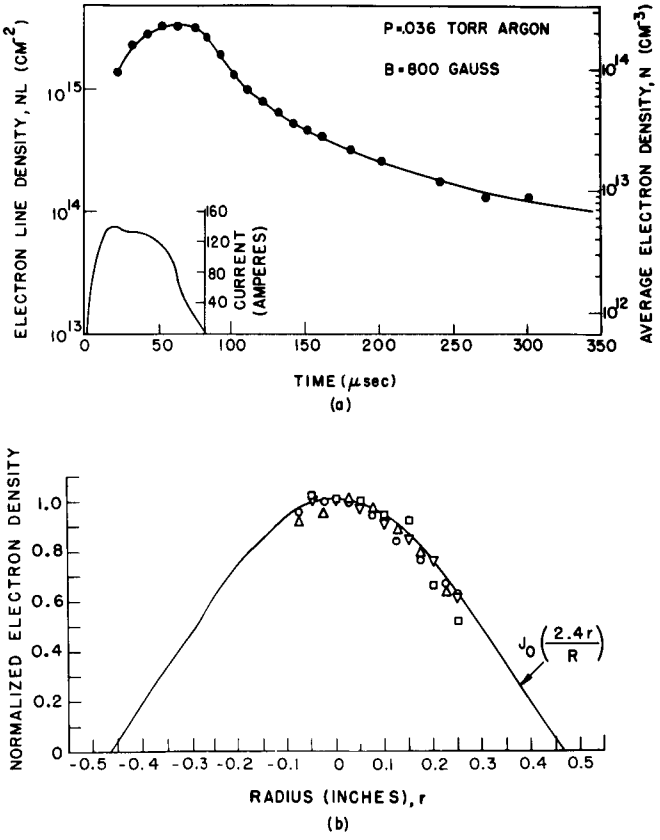

Fig. IX-2.

(a) Time decay of the axial electron density. The discharge current is shown in the lower left-hand corner.

(b) Radial distribution of the electron density. The data is compared with the zero-order Bessel function. The magnetic field is 800 gauss, and the time t = 80 μsec; similar data were obtained at other fields and times in the afterglow. The symbols correspond to different pressures: □, p = 0.22 Torr; ○, p = 0.044 Torr; △, p = 0.104 Torr; ▽, p = 0.160 Torr.

The rate of change of the electron density is plotted in Fig. IX-3 for several pressures. It is clear from this figure that in the early afterglow the decay is most rapid for low pressures. This fact and the spatial dependence (Fig. IX-2b) are strong indications that the initial decay is by diffusion. In addition, the magnetic field dependence (not shown) indicates that diffusion across the field dominates diffusion along the field, a conclusion which is supported by numerical estimates of decay rates.

To obtain a detailed picture of the decay of the plasma, it is necessary to consider both temperature and density decay. As the density decay in the early afterglow is

primarily due to diffusion, the density decay equation is

$$\frac{\partial \ln n}{\partial t} = -\frac{D_{am}}{\Lambda^2} \tag{1}$$

Here D_{am} is the coefficient for ambipolar diffusion across the magnetic field:

$$D_{am} = \frac{D_a}{1 + \frac{\omega_e \omega_i}{\nu_{ei} \nu_{ia}}} \tag{2}$$

where ω_e and ω_i are the electron and ion cyclotron frequencies, ν_{ia} is the ion-atom collision frequency, and ν_{ei} is a spatially averaged electron-ion collision frequency.

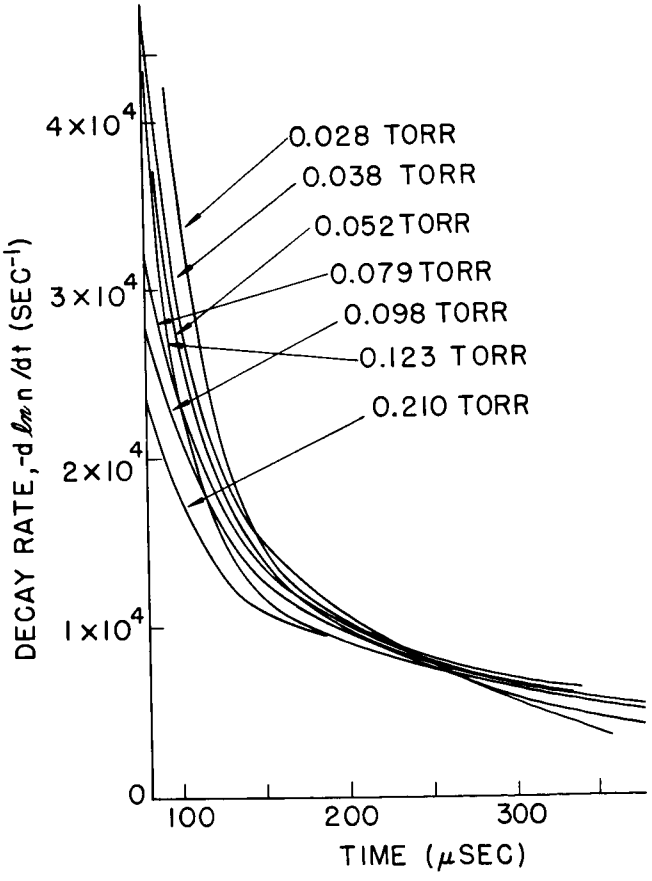

Fig. IX-3.

Plasma decay rates as a function of time. The magnetic field is 800 gauss. The experimental points are not shown because of lack of space, instead smooth curves have been drawn through the data.

Following Golant and Zhilinskii,[4] ν_{ei} is found to be 0.38 times the collision frequency at the center of the discharge tube.

Calculations of the electron and ion cooling rates were made.[1] It was found that the

ion-atom collision frequency is so high that the ions are at practically the atom temperature. The important electron cooling mechanisms are diffusion and electron-ion collisions. Recombination plays no part at these densities and temperatures. The rate of electron temperature decay is given by

$$\frac{\partial \ln T}{\partial t} = -\frac{D_{am}}{\Lambda^2}\left[\frac{2}{3} + \frac{1 - (\omega_e/\nu_{ei})^2}{1 + (\omega_e/\nu_{ei})^2} + \frac{2}{3}\,\frac{a}{1 + \dfrac{\omega_e\omega_i}{\nu_{ei}\nu_{ia}}} + \frac{2}{3}\,b\right] - g\nu_{ei}. \tag{3}$$

The terms in the brackets on the right-hand side of Eq. 3 arise in the order presented from (a) the temperature dependence of the ambipolar diffusion coefficient; (b) the temperature dependence of the electron mobility; and (c) the flow of diffusion currents in the space-charge fields. The term containing "a" arises from the volume field and that containing "b" arises from sheath fields. Both "a" and "b" are weak functions of the plasma parameters; for the present plasma they are about 2.1 and 0.16 respectively. The collisional cooling term is proportional to $g = 2m_e/M_A$.

As diffusion is important for both the density and the temperature decays, it is convenient to combine Eqs. 2 and 3:

$$\frac{\partial \ln (T^{3/2}/n)}{\partial t} = -\frac{D_{am}}{\Lambda^2}\left[\frac{3}{2}\,\frac{1 - (\omega_e/\nu_{ei})^2}{1 + (\omega_e/\nu_{ei})^2} + \frac{a}{1 + \dfrac{\omega_e\omega_i}{\nu_{ei}\nu_{ia}}} + b\right] - \frac{3}{2}\,g\nu_{ei}. \tag{4}$$

The right-hand side of this equation can be either positive or negative. In the limiting case that it is zero, $T^{3/2}/n$ is a constant during the decay. In this case, the density decay equation becomes

$$\frac{\partial \ln n}{\partial t} = -\left(\frac{D_{am}}{\Lambda^2}\right)\left(\frac{n}{n_o}\right)^{2/3} \tag{5}$$

where the subscript zero indicates initial conditions.

Examples of the decay rates of the plasma are plotted in Fig. IX-4 for a magnetic field of 800 gauss. It is observed that the initial decay of the plasma follows Eq. 5, indicating that the right-hand side of Eq. 4 is indeed approximately zero. This conclusion will be verified numerically below.

Because the initial decay follows Eq. 5, it is possible to determine the electron temperature. The value of $(D_{am})_o$ can be obtained from plots such as Fig. IX-4. If the initial temperature is independent of pressure, one obtains

$$(D_{am})_o = \frac{(D_a)_o p}{p + \dfrac{\omega_e\ \omega_i}{\nu_{ei}\ \nu_{ia}/p}}. \tag{6}$$

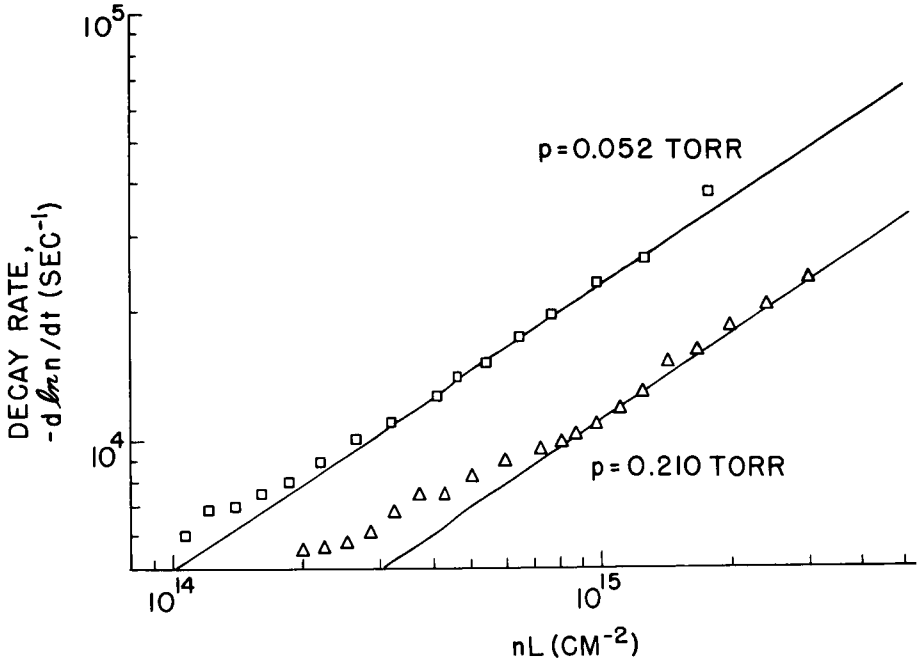

Fig. IX-4. Plasma decay rates at a magnetic field of 800 gauss. The data are fitted to lines for which $T^{3/2}/n$ is constant.

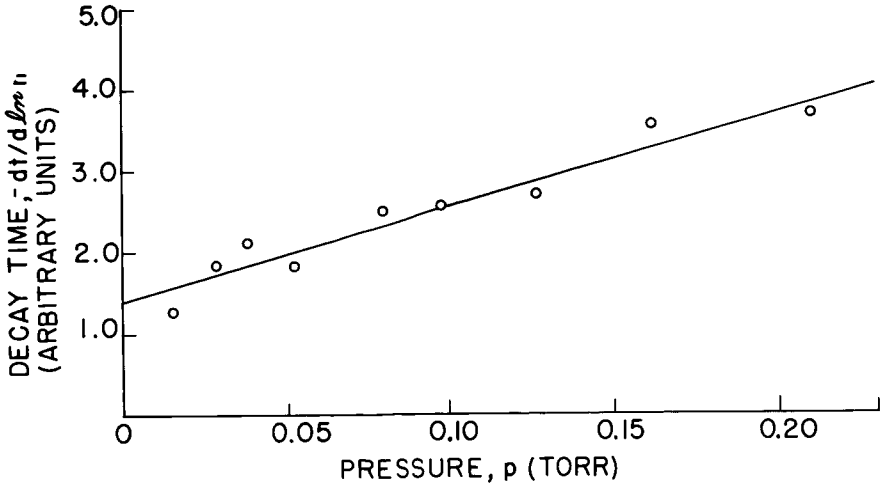

Fig. IX-5. Pressure dependence of the decay.

As the initial decay is such that ν_{ei} is constant, a plot of $(D_{am})_o^{-1}$ against p yields a straight line, as shown in Fig. IX-5. The value of ν_{ei} (and hence of T) can be obtained from this figure; it is found that at a density of 2×10^{14} cm^{-3} the temperature is 1.4 ev. The absolute diffusion rate at this density and temperature, and at a pressure

of 0.1 Torr, is 3.6×10^4 sec^{-1}, in excellent agreement with the measured decay rate (see Fig. IX-4).

Once the electron temperature is determined, it is possible to check the consistency of the approximation that Eq. 4 is zero. One finds (for example) at a pressure of 0.1 Torr, $n = 2 \times 10^{14}$ cm^{-3}, and T = 1.4 ev, that the set of terms arising from diffusion has a value $+1.0 \times 10^4$ sec^{-1}, and that the electron-ion collision term has the value -1.7×10^4 sec^{-1}. These terms thus add up to a net cooling rate of 0.7×10^4 sec^{-1}, considerably less than the initial diffusion rate. The approximation was indeed a good one. This cancellation is a fortuitous one for the experimental conditions discussed, and does not hold, for example, at a magnetic field of 400 gauss.

As the decay proceeds, the diffusion terms decrease and the collisional term remains approximately constant. Thus, after a short while the collisional term dominates the diffusion terms; in such a case the temperature can be shown[1] to drop much more rapidly than the density. Once this occurs, radiative-collisional recombination becomes important because of the strong temperature dependence of the recombination coefficient.[2] It is found that for times later than 200-300 microseconds after the start of the afterglow, the decay rates are consistent with the recombination calculations of Bates et al.[2] The bending of the decay curves of Fig. IX-4 away from the straight lines is thus apparently an indication of the onset of recombination.

Similar data was obtained at 400 gauss, although the initial temperature decay was more rapid than at 800 gauss; otherwise, the decay was qualitatively the same. At 0 gauss the temperature decays very rapidly by diffusion, and recombination becomes important almost immediately.

Detailed verification of above conclusions requires time resolved measurements of the electron temperature in addition to the electron density measurements which have been described. Temperature measurements have not been made.

E. B. Hooper, Jr.

References

1. E. B. Hooper, Jr., Ph.D. Thesis, Department of Physics, M.I.T., September 1965.

2. D. R. Bates, A. E. Kingston, and R. W. P. McWhirter, Proc. Roy. Soc. (London) A (GB), 267, 297 (1962); D. R. Bates and A. Delgarno in D. R. Bates (ed.), Atomic and Molecular Processes (Academic Press, New York, 1962).

3. E. B. Hooper, Jr. and G. Bekefi, Appl. Phys. Letters (to be published); E. B. Hooper, Jr., "Laser Interferometer," Quarterly Progress Report, No. 75, Research Laboratory of Electronics, M.I.T., October 15, 1964, p. 55; E. B. Hooper, Jr., "Electron Density Measurements with a Laser Interferometer," Quarterly Progress Report No. 78, Research Laboratory of Electronics, M.I.T., July 15, 1965, pp. 85-89.

4. V. E. Golant and A. P. Zhilinskii, Zhur. Tekh. Fiz. 32, 1313 (1962); translated in Soviet Phys. – Tech. Phys. 7, 970 (1963).

B. ION CYCLOTRON RESONANCE IN A RADIOFREQUENCY DISCHARGE – HIGH Q MODE

The ion cyclotron experiment described previously[1] has been altered slightly and, as a result, now operates in a high Q mode. This mode is strongly influenced by impurities and, thus far, has only been observed when the electrode is not oxide-coated. Alignment of the magnetic pickup probe with the electrode is another factor strongly influencing operation in this mode. The best resonance curves are obtained when the pickup is in such a position that it interferes least with the streaming of electrons along lines of $\underset{\sim}{B}_o$ from points on the electrode.

Signals from the pickup are detected by a radio receiver tuned to the applied frequency (4 Mc). The automatic volume control (AVC) voltage of the receiver is traced, as a function of B_o, on an oscilloscope face. Within experimental accuracy, the resonance occurs exactly at the ion cyclotron point

$$\beta_+ = \frac{eB_o}{M_+\omega} = 1.$$

The discharge gas is always hydrogen and only resonance of the atomic ion (proton) has been investigated.

A model has been developed[2] which accounts for a majority of effects observed. Two of the more interesting features, which are still unexplained, are:

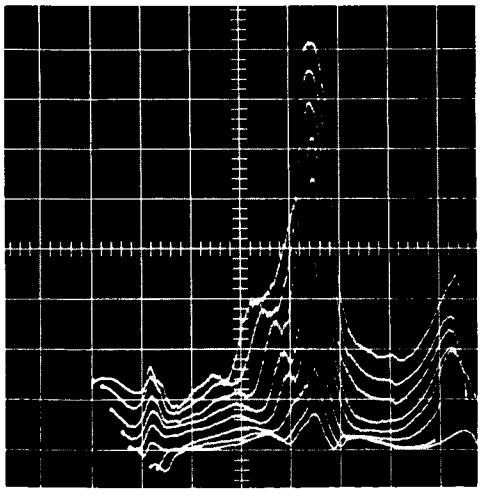

Fig. IX-6. Resonance curves at different applied voltages. Peak-to-peak applied voltage of 600 → 425 volts in steps of 25 volts. Hydrogen pressure, 18 μ.

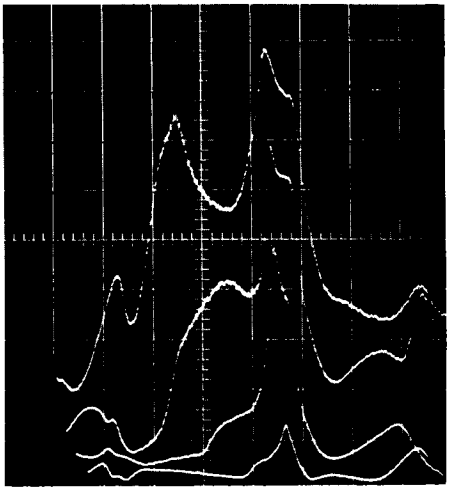

Fig. IX-7. Resonance curves at different applied voltages; 1000, 800, 600, and 500 volts peak-to-peak. Hydrogen pressure, 16 1/2 μ.

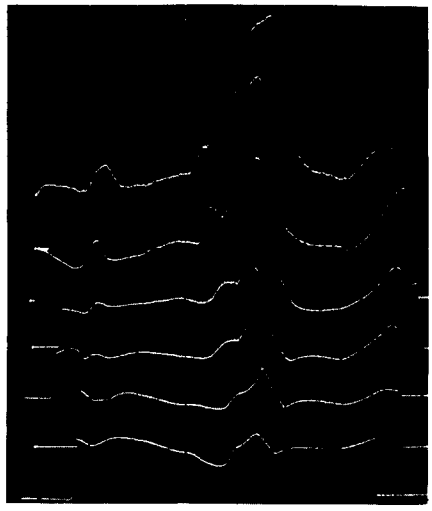

Fig. IX-8. Resonance curves at different hydrogen pressures. Pressure decreased 19 μ → 14 μ in steps of 1 μ, top to bottom. Applied voltage, 500 volts peak-to-peak.

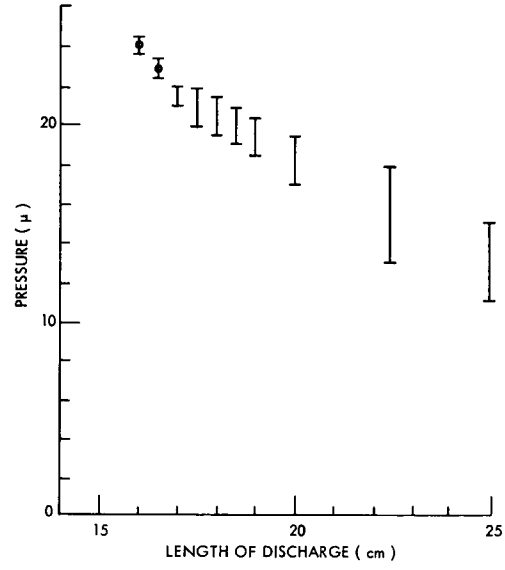

Fig. IX-9. Pressure required for observation of a sharp resonance vs length of discharge. Applied voltage, 500 volts peak-to-peak.

1. This mode is observed only when the applied RF voltage is above a certain threshold. Resonance curves are sharpest ($Q \approx 30$) just above this threshold. This is illustrated in Figs. IX-6 and IX-7.

2. This mode is observed only for a rather narrow pressure range. This pressure range is determined by the position of the (electrically insulating) end wall which limits the length of the discharge. This is illustrated in Figs. IX-8 and IX-9.

A possible explanation of these two effects is the varying percentages of atomic versus molecular ions and neutral particles. This matter requires further investigation.

J. J. Nolan, Jr.

References

1. J. J. Nolan, Jr., "Ion Cyclotron Resonance in a Radiofrequency Discharge," Quarterly Progress Report No. 77, Research Laboratory of Electronics, M. I. T., April 15, 1965, pp. 109-112.

2. J. J. Nolan, Jr., "'Direct Coupling' to a Plasma in the Vicinity of Ion Cyclotron Resonance," Ph. D. Thesis, Department of Electrical Engineering, Massachusetts Institute of Technology, September 1965.

X. GASEOUS ELECTRONICS*

Prof. S. C. Brown	J. C. de Almeida Azevedo	J. J. McCarthy
Prof. W. P. Allis	A. J. Cohen	W. J. Mulligan
Prof. G. Bekefi	F. X. Crist	R. C. Owen
Prof. D. R. Whitehouse	E. W. Fitzgerald, Jr.	J. A. Waletzko
Dr. J. C. Ingraham	G. A. Garosi	B. L. Wright

A. OSCILLATIONS OF AN INHOMOGENEOUS PLASMA

This report indicates the usefulness of operator methods for dealing with problems involving Vlasov's equation in its more general linearized form, that is, when applied to inhomogeneous bounded anisotropic plasmas. Although these operator methods have been successfully applied by Laplace (in working with diffusion theory), their use seems almost to have been restricted only to quantum theory where they are used in full detail. The first application of operational techniques to plasma physics is probably the work of Buchsbaum and Hasegawa (B. H.).[1] In the present report we shall derive some generalizations of their work and indicate how to generalize their theory to one that is correct to all orders of temperature. First, we shall indicate how to derive the fundamental equation; second, we shall use this equation to explain the structure of the Tonks-Dattner resonances and those recently observed in microwave emission by Mitani, Kubo, and Tanaka[2] and in microwave absorption by Buchsbaum and Hasegawa[1]; and third, we shall explain the rules for obtaining partial differential equations that are correct to all orders of temperature. Important extensions such as damping and coupling to outside waves are in progress.

1. Derivation of the Fundamental Equation

We start with the Vlasov equation $\frac{\partial f}{\partial t}+\vec{v}\cdot\frac{\partial f}{\partial \vec{x}}-\frac{e}{m}\left(\vec{E}+\frac{\vec{v}}{c}\times\vec{B}\right)\cdot\frac{\partial f}{\partial \vec{v}}=0$ which we linearize according to the usual Landau prescription $f(\vec{x},\vec{v},t) = g(\vec{x})\, f_o(\vec{v}) + f_1(\vec{x},\vec{v},t)$, in which we have assumed that the unperturbed distribution function separates into a spatial part $g(\vec{x})$, and a Maxwell-Boltzmann distribution function $f_o(\vec{v})$. The particle density of the inhomogeneous plasma is given by $N(\vec{x}) = N_o g(\vec{x})$. The fields are given by

$$\vec{E}(\vec{x},t) = 0 + \vec{E}_1(\vec{x},t); \quad \vec{B}(\vec{x},t) = \vec{B}_o + \vec{B}_1(\vec{x},t). \tag{1}$$

Setting the zero-order electric field equal to zero has been discussed but physically meaningful results appear to be obtained; probably the best justification is that we arrive at correct results by so doing. We choose the z axis along the constant external magnetic field $\vec{B}_o$ and cylindrical coordinates in velocity space $\vec{v} = (v_\perp \cos\phi, v_\perp \sin\phi, v_\parallel)$. If we consider one component in the Fourier time spectrum we find that, using the above simplifications, we can write the Vlasov equation in the linearized form

*This work was supported principally by the Joint Services Electronics Program (Contract DA36-039-AMC-03200(E).

$$\left(\frac{\partial}{\partial\phi} + i\alpha - \beta\cos\phi\frac{\partial}{\partial x} - \beta\sin\phi\frac{\partial}{\partial y}\right) f_1 = Av_\perp \hat{f} g(\vec{x})\,(\cos\phi E_x + \sin\phi E_y), \tag{2}$$

where

$$\alpha = -\frac{\omega}{\omega_b}, \quad \beta = -\frac{v_\perp}{\omega_b}; \quad A = \frac{(1/2\pi)^{3/2}\,\omega_p/\omega_b}{4\pi e L_D V_T^4}; \quad \hat{f} = \exp -\frac{v_\perp^2 + v_\parallel^2}{2v_T^2}.$$

Here, ω_b is the cyclotron frequency; L_D, ω_p, and V_T are the Debye length, plasma frequency, and thermal velocity; $L_D\omega_p = V_T$; $\omega_p^2 = 4\pi N_o e^2/m$, etc. Equation 2 is formally identical to an equation found in Allis, Buchsbaum and Bers[4, 3] and can also be considered a kind of "inhomogeneous Schrödinger equation" with the Hamiltonian

$$H = i\alpha - \beta\cos\phi\frac{\partial}{\partial x} - \beta\sin\phi\frac{\partial}{\partial y}. \tag{3}$$

Then we can formally integrate Eq. 2 and (after imposing the condition that the perturbed distribution function be axially symmetric in velocity space) obtain the expression

$$f_1(\vec{x}, \vec{v}, \omega) = Av_\perp \hat{f} \exp\left(\beta\sin\phi\frac{\partial}{\partial x} - \beta\cos\phi\frac{\partial}{\partial y}\right) \sum_{\substack{n,m\\-\infty}}^{+\infty} i^{m-1} J_n\left(i\beta\frac{\partial}{\partial x}\right) J_m\left(\frac{\beta}{i}\frac{\partial}{\partial y}\right)$$

$$\cdot\left\{\frac{G(\vec{x})\, e^{i(m+n+1)\phi}}{m+n+\alpha+1} + \frac{F(\vec{x})\, e^{i(m+n+1)\phi}}{m+n-1+\alpha}\right\} \tag{4}$$

where J_k stands for Bessel functions of first kind and order k and

$$F(\vec{x}) = g(\vec{x})\, E_+(\vec{x}); \quad G(\vec{x}) = g(\vec{x})\, E_-(\vec{x}); \quad E_\pm(\vec{x}) = \tfrac{1}{2}\left(E_x(\vec{x}) \pm iE_y(\vec{x})\right). \tag{5}$$

Since $\frac{\partial}{\partial x}$ and $\frac{\partial}{\partial y}$ are commuting operators, we see that Glauber's lemma allows us to write

$$\exp\left(\beta\sin\phi\frac{\partial}{\partial x} - \beta\cos\phi\frac{\partial}{\partial y}\right) J_n\left(i\beta\frac{\partial}{\partial x}\right) J_m\left(\frac{\beta}{i}\frac{\partial}{\partial y}\right)$$

$$= J_n\left(i\beta\frac{\partial}{\partial x}\right) J_m\left(\frac{\beta}{i}\frac{\partial}{\partial y}\right) \exp\left(\beta\sin\phi\frac{\partial}{\partial x}\right) \exp\left(-\beta\cos\phi\frac{\partial}{\partial y}\right). \tag{6}$$

If we recall the property of the displacement operator $\exp(\vec{x}_o\cdot\vec{\nabla})\, M(\vec{x}) = M(\vec{x}+\vec{x}_o)$, we can write the exact integral of the linearized Vlasov equation in the form

$$f_1 = Av_\perp \hat{f} \sum_{\substack{n,m\\-\infty}}^{+\infty} i^{m-1} J_n\left(i\beta\frac{\partial}{\partial x}\right) J_m\left(\frac{\beta}{i}\frac{\partial}{\partial y}\right)\left\{\frac{e^{i(m+n+1)\phi}}{m+n+\alpha+1} G(x+\beta\sin\phi, y-\beta\cos\phi)\right.$$

$$\left. + \frac{e^{i(m+n+1)\phi}}{m+n+\alpha-1} F(x+\beta\sin\phi, y-\beta\cos\phi)\right\}. \tag{7}$$

Heretofore no approximations have been made: Eq. 7 is the exact integral of the

linearized Vlasov equation. Since we have an infinite series, we have to limit the number of terms to be kept in the expansion and we choose to keep those terms that are linear in temperature. This greatly simplifies the algebra and also, from the structure of the differential equations so obtained, permits their extension when all powers of temperature are taken into account. Keeping terms linear in temperature means that only terms in β^0, β^1, β^2, and β^3 need be kept in the expansion. When we do this the equations obtained have denominators of the form $\omega \pm n\omega_b$, with only n = 0, 1, 2. The expansion is valid when the Larmor radius is small compared with the wavelength, or the scale length of the density gradient, and it is clear that dropping terms above β^3 makes the solution invalid in the neighborhood of cyclotron harmonics above the second. The solution is found to be correct for $\omega_b = 0$. The exact criterion of validity in terms of the frequency is not yet understood, but in terms of temperature the equations are valid up to linear terms only.

To calculate the charge density $-e \int d^3v f_1$, we have to perform integrals of the perturbed distribution function in velocity space.

The ϕ integrals are easily performed because of well-known orthogonality relations. The $v_{\parallel}$ integral is also easily done and amount to multiplication by $\sqrt{2\pi}\, V_T$ and changing $\hat{f}$ into $\exp\left(-v_\perp^2/2v_T^2\right)$. The $v_\perp$ integrals amount to evaluating integrals of the sort[5]

$$\int_0^\infty (dx)\, x^{s-1}\, e^{\alpha' x^2 - \gamma x} = (2\alpha')^{-3/2}\, \Gamma(s)\, \exp\left(\frac{\gamma^2}{8\alpha'}\right) D_{-s}\left[\gamma(2\alpha')^{-1/2}\alpha'\right],$$

where Γ is the gamma function, and D_{-s} is a parabolic cylinder function of order -s.

If we perform all of the tediously lengthy algebra of the expansions, we arrive at an expression for Poisson's equation div E = $4\pi\rho$ in the form

$$\operatorname{div} \vec{E} = \left(\epsilon_1 + \lambda_1^2 \nabla^2\right) \operatorname{div} g\vec{E} + i\left(\epsilon_2 + \lambda_2^2 \nabla^2\right) (\operatorname{rot} g\vec{E}) \cdot \vec{e}_3, \tag{8}$$

where $\vec{e}_3$ is a unit vector along $\vec{B}_o$, div, ∇^2, and rot are the usual divergence, Laplacian, and curl operators and also

$$\epsilon_2 = \frac{\omega_b}{\omega}\epsilon_1 = \frac{\omega_b}{\omega}\,\frac{\omega_p^2}{\omega^2 - \omega_b^2}$$

$$\lambda_2^2 = 2\,\frac{\omega_b}{\omega}\,\lambda_1^2 = 2\,\frac{\omega_b}{\omega}\,\frac{3V_T^2\omega_p^2}{\left(\omega^2-\omega_b^2\right)\left(4\omega_b^2-\omega^2\right)}, \qquad V_T = L_D\omega_p. \tag{9}$$

This equation has already been obtained by Buchsbaum[6] and Hasegawa; in their paper they were restricted to one dimension in which the curl term was absent. For the case

$\omega_b \to 0$, Eq. 8 becomes

$$\operatorname{div} \vec{E} = \left(\epsilon_o - \lambda_o^2 \nabla^2\right) \operatorname{div} g\vec{E}, \quad \lambda_o^2 = 3L_D^2\left(\frac{\omega_p}{\omega}\right)^4, \quad \epsilon_o = \left(\frac{\omega_p}{\omega}\right)^2. \tag{10}$$

Equation 8 will be called the fundamental second-order equation. It is simply a kinetic interpretation of Poisson's equation. The calculation of the conductivity current and use of the full set of Maxwell's equation will be carried out. We shall now be concerned with some consequences and generalizations of Eq. 8.

2. Consequences of the Fundamental Second-Order Equation

We now show that Eq. 8 duplicates the results of other existing theories whenever these are based on Vlasov's equation, but find some disagreement when they are based on the method of moments, with their chain broken with some ad hoc assumption.

We compare therefore our fundamental equation with results from the theory of the cold, homogeneous, and unbounded plasma as derived by Allis, Buchsbaum, and Bers[4]; with Bohm-Gross[7] dispersion relation which applies to the hot homogeneous and unbounded plasma (which is also correct to order T); and with some of Bernstein's[8] result. The last comparison involves the eigenfrequency spectrum that is still to be derived.

To compare with Allis, Buchsbaum, and Bers we first set T = 0 and also g = 1. Equation 8 becomes

$$\operatorname{div} E = \epsilon_1 \operatorname{div} gE + i\epsilon_2 (\operatorname{rot} gE) \cdot \vec{e}_3 \tag{11}$$

which can be written

$$\frac{\partial}{\partial x}\left[(1-\epsilon_1 g)E_x - i\epsilon_2 g E_y\right] + \frac{\partial}{\partial y}\left[(1-\epsilon_1 g)E_y + i\epsilon_2 g E_x\right] = 0. \tag{12}$$

This can be written $\operatorname{div} \vec{D} = 0$, where $D_i = \epsilon_{ij} E_j$, $\epsilon_{xx} = \epsilon_{yy} = 1 - \epsilon_1 g$, and $\epsilon_{xy} = -\epsilon_{yx} = -i\epsilon_2 g$. These according to Eq. 9 can be written

$$\epsilon_{xx} = \epsilon_{yy} = 1 - \frac{\omega_p^2 g(\vec{x})}{\omega^2 - \omega_b^2}; \quad \epsilon_{xy} = -\epsilon_{yx} = -i\left(\frac{\omega_c}{\omega}\right)\frac{\omega_p^2 g(\vec{x})}{\omega^2 - \omega_b^2}, \tag{13}$$

which, apart from notation, are the same as Allis' Eqs. 2.20 when we set g(x) = 1; and as might be expected $g(\vec{x})$ multiplies ω_p^2 when the plasma is inhomogeneous. We also confirm Allis, Buchsbaum, and Bers' statement[10] concerning the validity of cold-plasma theory to the first cyclotron frequency interval only: to obtain the second harmonic we have to give up the cold-plasma assumption.

Bohm and Gross' well-known dispersion relation is $\omega^2 = \omega_p^2 + 3k^2 V_T^2$. This formula is

a consequence of magnetohydrodynamic theory. If we evaluate the singular integral $k^2 = \omega_p^2 \int_{-\infty}^{+\infty} dv \frac{G(v)}{v - \omega/k}$, $G(v) = -(2\pi)^{-1/2} v_T^{-3/2} \exp\left(-v^2/2v_T^2\right)$ in the sense of a principal value integral (If G(x) does not vanish at $x = x_o$ and x_o is in the range of integration then $P \int_a^b dx\, G(x)(x-x_o)^{-1} = \lim_{\epsilon \to 0} \left(\int_a^{x_o - \xi} + \int_{x_o+\xi}^b \right) dx\, G(x)(x-x_o)^{-1}$, where $\epsilon > 0$,) $k^2 = \omega_p^2 P \int_{-\infty}^{-\infty} dv\, G(v)(v-\omega/k)^{-1}$, then it can be seen that the correct Bohm-Gross formula is $\omega^2 = \omega_p^2 + 3k^2 V_T^2 (\omega_p/\omega)^2$. This result is easily obtained by Fourier-analyzing the electric field in Eq. 10 which then becomes simply

$$1 = \epsilon_o + \lambda_o^2 k^2 \tag{14}$$

which agrees with the correct Bohm and Gross formula.

We consider next the solutions of Eq. 8 when applied to the slab geometry $-L \leq x \leq L$ and for the infinite cylinder geometry under the situations $\omega_c = 0$ and $\omega_c \neq 0$ and for the homogeneous plasma ($g(\vec{x})=1$) and the inhomogeneous plasma, where $g^{-1}(\vec{x}) = 1 + \gamma \vec{x}^2/\vec{x}_o^2$. This profile is in reasonable agreement with experiment and leads to analytical solutions in closed form. The partial differential equations for the homogeneous plasma are quite simple and only the results will be stated. (The eigenfrequencies are obtained by setting the electric field (current) equal to zero at the boundary wall.)

For $g(x) = 1$ and $\omega_c = 0$ no eigenfrequency exists when $\omega < \omega_p$. The eigenfunctions are sines and cosines of argument kx, $k^2 = (1-\epsilon_o)/\lambda_o^2$. For $\omega > \omega_p$ these are given by

$$\omega^2 = \frac{\omega_p^2}{2}\left\{1 + \sqrt{1 + 12\left(\frac{L_D}{L}\right)^2 (2n+1)^2 \frac{\pi^2}{4}}\right\}, \quad n = 0, \pm 1, \pm 2 \ldots \tag{15}$$

or by the same expression with $(2n+1)\,\pi/2$ replaced by $n\pi$. For small L_D/L Eq. 15 reduces to $\omega^2 = \omega_p^2 + 3(2n+1)^2 \frac{\pi^2}{4} \frac{V_T^2}{L^2}$ which apart from the factor of 3 on the right-hand side is a formula previously obtained by Weissglas. The case $\omega_b \neq 0$ does not present further complications. Then it is seen that the resonances exist only when $\omega^2 > \omega_p^2 + \omega_c^2$. These are extraordinary waves.[4] The eigenfunctions are sines and cosines of argument kx, $k^2 = \frac{L^2}{\lambda_1^2}(\epsilon_1 - 1)$. Their resonances are given by

$$\omega^2 = \frac{1}{2}\left\{\omega_p^2 + 5\omega_b^2 + \sqrt{\left(\omega_p^2 - 3\omega_b^2\right)^2 + 12\left(\frac{L_D}{L}\right)^2 \omega_p^4 (2n+1)^2 \frac{\pi^2}{4}}\right\}, \tag{16}$$

where $n = 0, \pm 1$, etc. and we could also have $n\pi$ instead of $(2n+1)\,\pi/2$; apart from

notation, Eq. 16 agrees with an equation previously derived by Bernstein.[8] It is important to notice that for $\omega_b = 0$ the resonances exist only for $\omega > \omega_p$, whereas for $\omega_b \neq 0$ these waves exist only for $\omega^2 > \omega_p^2 + \omega_b^2$ which corresponds to the experimentally observed fact that the Tonks-Dattner ($\omega_b=0$) waves are trapped between the wall and the high-density regions, whereas the Buchsbaum-Hasegawa waves exist in the other region, that is, they are trapped in the high-density regions.

The inhomogeneous case $g^{-1}(x) = 1 + \gamma x^2/L^2$ has been treated by Buchsbaum and Hasegawa,[1] but only for $\omega_c < \omega < 2\omega_c$. The eigenfunctions are parabolic cylinder functions:

$$\frac{d^2G}{dZ^2} + \left(n+\frac{1}{2}-\frac{1}{4}Z^2\right)G = 0,$$

where $G(Z) = g(Z)\,E(Z)$, and

$$n = \frac{1}{2}\left[\frac{L(\epsilon_1-1)}{\lambda_1\sqrt{\gamma}} - 1\right], \qquad x = \left(\frac{L^2\lambda_1^2}{4\gamma}\right)^{1/4} Z. \tag{17}$$

Therefore

$$G = A[D_n(Z)+D_n(-Z)], \tag{18}$$

Here, D_n is a parabolic cylinder function of order n. The condition that the total electrostatic energy in the plasma be finite restricts the solution to a parabolic cylinder function of integral order, in which case a dispersion relation of the form of Eq. 16 can be derived and is given by

$$\omega^2 = \frac{1}{2}\left(\omega_p^2 + 5\omega_b^2 + \sqrt{\left(\omega_p^2-3\omega_b^2\right)^2 + 36\gamma\omega_p^4\left(\frac{L_D}{L}\right)^2 (2n+1)^2}\right). \tag{19}$$

The two formulas would give the same results if γ were equal to $\pi^2/12 = 0.82$; however, γ is by far smaller, approximately 0.02 for a cylinder of 2.5-cm radius, T = 4.9 ev, and this alters the spacing of the resonances significantly, thereby making the agreement with experiment much better.

The proper treatment of the cylinder problems with the curl term included is very complicated and we shall limit ourselves to cases in which $g(\vec{x})$ depends only on r and the electric field is purely radial. In this case the curl term drops out and we can write

$$\frac{d^2G}{dr^2} + \frac{1}{r}\frac{dG}{dr} + \left(\frac{\epsilon_1 - 1}{\lambda_1^2} - \frac{1}{r^2} - \frac{\gamma r^2}{\lambda_1^2 r_o^2}\right)G = 0,$$

where $G(r) = g(r)\,E_r(r)$. By setting $r^2 = \lambda_1 r_o \gamma^{-1/2} Z$ and $G = Z^{-1/2}v$, Eq. 18 reduces

to a Whittaker equation; proper behavior at the origin gives the solution in terms of a transformed Whittaker function:

$$\vec{E}(r) = \vec{e}_1 \left(1 + \gamma \frac{r^2}{r_o^2}\right) \frac{\gamma^{1/2}}{\lambda_1 r_o} Ar \exp\left(-\frac{\gamma^{1/2} r^2}{2\lambda_1 r_o}\right) {}_1F_1\left(1-k, 2; \frac{\gamma^{1/2} r^2}{\lambda_1 r_o}\right), \tag{21}$$

where ${}_1F_1$ is a confluent hypergeometric function, $k = \frac{r_o}{\lambda_1} \frac{\epsilon_1 - 1}{4\sqrt{\gamma}}$. Equation 19 was carefully compared with experimental measurements by Gruber and Bekefi.[9] They actually measured the electric fields inside the plasma and the agreement between theory and

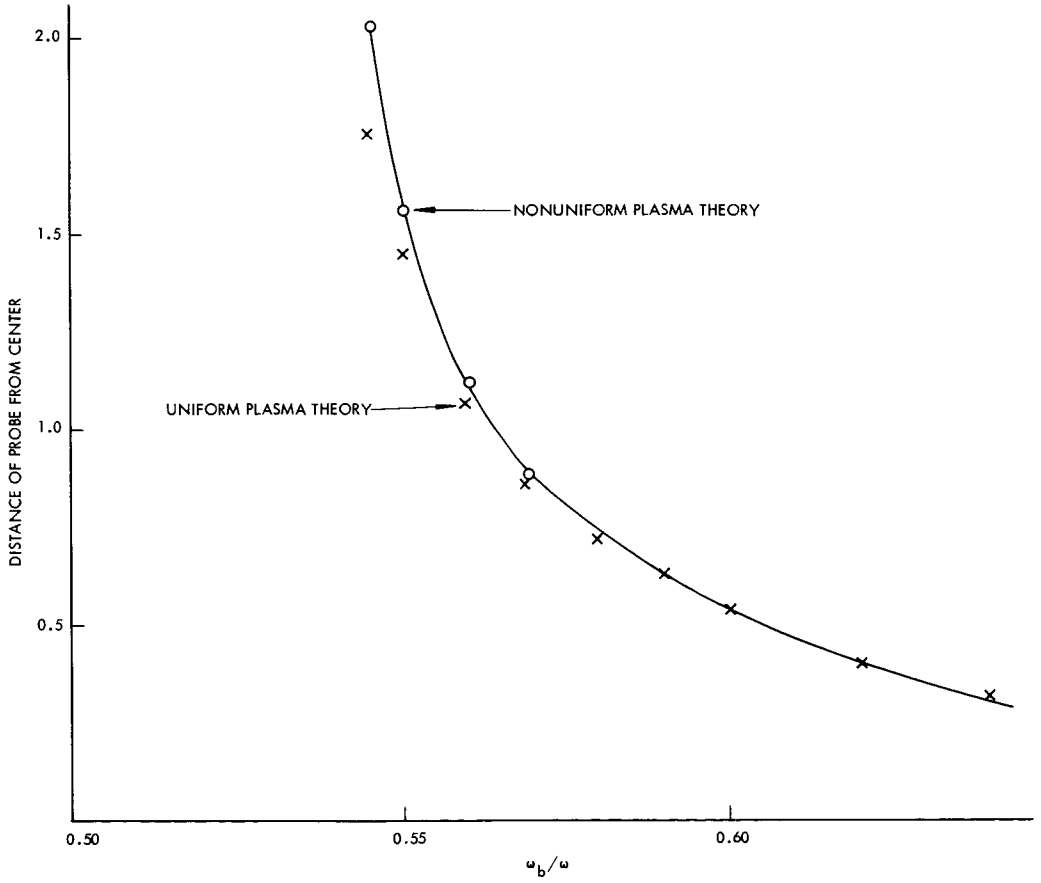

Fig. X-1. Solid line shows the locus of the first zero of the electric field (after Gruber and Bekefi[9]) oscillations as function of ω_b/ω. Open circles represent the first zero of the hypergeometric function; crosses are computed under the assumption of a uniform plasma $\gamma = 0$, $g(x) \equiv 1$. Agreement with experiment is very good even for the uniform plasma. It can be seen that the uniform plasma predictions deviate from the experimental results when the zero falls near the wall.

experiment is good. Their results will be published elsewhere[9] (see Fig. X-1 for the result of one of their measurements). In some limiting cases asymptotic expansions of

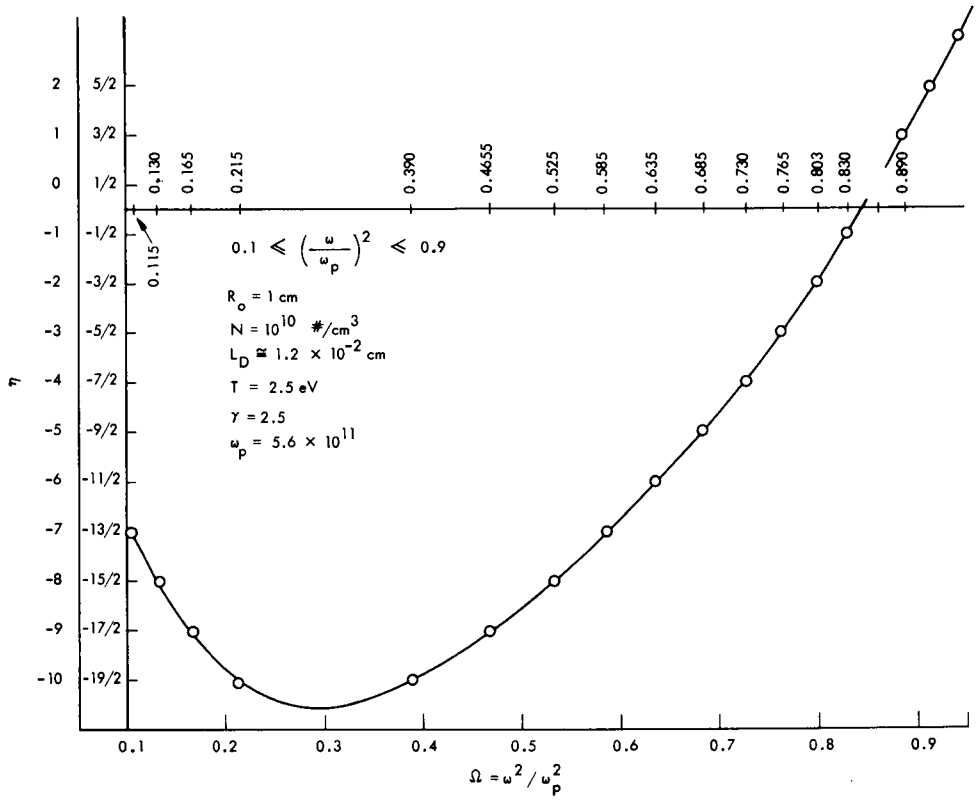

Fig. X-2. Frequency spectrum of the Tonks-Dattner resonance.

transformed Whitaker functions can be used; if we perform this expansion and match the conditions at the wall, we obtain an expression similar to Eq. 16, except that $(2n+1)\,\pi/2$ is replaced by $1/12 + (n+1)\pi$.

The Tonks-Dattner case is also solved along similar lines. In this case we set G = gE in div $\vec{E} = \left(\epsilon_o - \lambda_o^2 \nabla^2\right)$ div $g\vec{E}$, set $r^2 = x$ and $G = x^{-1/2}R$ and obtain

$$\frac{d^2R}{dx^2} + \left(\frac{\gamma}{4r_o^2\lambda_o^2} - \frac{(1-\epsilon_o)/4\lambda_o^2}{x}\right) R = 0 \tag{22}$$

which is the equation for the Rutherford scattering of S-waves whose solutions are known.

$$R = A\,\frac{\sqrt{\gamma}}{\Gamma_o\lambda_o}\,(ix)\,\Gamma\left(1 + i\left(\frac{r_o}{\lambda_o}\right)\frac{1-\epsilon_o}{4\sqrt{\gamma}}\right)\exp\left(-i\,\frac{\sqrt{\gamma}\,r^2}{2r_o\lambda_o}\right)\,{}_1F_1\left(1 + i\left(\frac{r_o}{\lambda_o}\right)\frac{1-\epsilon_o}{4\sqrt{\gamma}}, 2, \frac{i\sqrt{\gamma}\,r^2}{r_o\lambda_o}\right) \tag{23}$$

which also has an asymptotic expansion

$$\lim_{\substack{\sqrt{\gamma}\, r^2 \\ \overline{2r_o\lambda_o} \to \infty}} R = \frac{2r_o\lambda_o}{\sqrt{\gamma}\, r^2} \sin\left(\frac{r^2\sqrt{\gamma}}{2r_o\lambda_o} + \frac{r_o}{\lambda_o}\frac{1-\epsilon_o}{4\sqrt{\gamma}} \ln\frac{r^2\sqrt{\gamma}}{r_o\lambda_o} - \Omega_{ko}\right),$$

where $\Omega_{ko} = \arg \Gamma\left(1 + i\frac{r_o}{\lambda_o}\frac{1-\epsilon_o}{4\sqrt{\gamma}}\right)$. We evaluate Ω_{ko} and set $R(r_o) = 0$ to obtain

$$\frac{1}{2\pi}\left(\frac{\omega}{\omega_p}\right)^2 \frac{r_o}{L_D}\left(\frac{\gamma}{3}\right)^{1/2} + \frac{r_o}{\pi L_D}\frac{(\omega/\omega_p)^2 - 1}{4\sqrt{3\gamma}} \ln\left[\frac{r_o}{L_D}\left(\frac{\gamma}{3}\right)^{1/2}\frac{\omega^2}{\omega_p^2}\right] = n + \frac{1}{2}, \qquad n = 0, \pm 1, \pm 2, \ldots \tag{24}$$

This equation can be solved numerically by plotting the left-hand side versus ω^2/ω_p^2. The abscissa of the intersection of this curve with the straight lines $n + 1/2$ are the resonances looked for. Part of this plot for $0.1 < (\omega/\omega_p)^2 < 0.9$ is found in Fig. X-2.

3. Partial Differential Equations Correct to All Orders of Temperature

Our theory has been hampered by two restrictions, one which we tacitly imposed when we restricted to two dimensions having propagation across B_o: $k_z = 0$. The other consisted in keeping only terms of order less than T^2. It is important to get rid of these restrictions, principally the first one. Both of them, however, will be lifted simultaneously. To achieve this we rewrite Eq. 8 in the form

$$\frac{\partial}{\partial x}\left\{\left(\frac{1}{g} - \epsilon_1 - \lambda_1^2\nabla^2\right) gE_x - i\left(\epsilon_2 + \lambda_2^2\nabla^2\right) gE_y\right\}$$
$$+ \frac{\partial}{\partial y}\left\{\left(\frac{1}{g} - \epsilon_1 - \lambda_1^2\nabla^2\right) gE_y + i\left(\epsilon_2 + \lambda_2^2\nabla^2\right) gE_x\right\} = 0. \tag{25}$$

If in this equation we set $g(\vec{x}) = 1$ and assume that the plasma is infinite, we can set according to Fourier analysis $\nabla^2 = -k^2 = -\left(k_x^2 + k_y^2\right)$. So that Eq. 25 really reduces to the proper components of the dielectric tensor of the homogeneous unbounded medium like

$$\epsilon_{xx} = 1 - \frac{\omega_p^2}{\omega^2 - \omega_b^2} + \frac{3L_D^2\omega_p^4 k^2}{\left(\omega^2 - \omega_b^2\right)\left(4\omega_b^2 - \omega^2\right)}. \tag{26}$$

These are correct to order T. Equation 26 and other similar equations for ϵ_{yx}, ϵ_{xy}, etc., are an important check on the validity of the theory developed thus far; but this means much more. For, if we keep in mind the operator procedures used above, we

see that the physical interpretation of the terms $g^{-1} - \epsilon_1 - \lambda_1^2\nabla^2, \pm i\left(\epsilon_2+\lambda_2^2\nabla^2\right)$ is that they are the components of the dielectric tensor operators of the bounded plasma, that is,

$$\hat{\epsilon}_{xx} = \frac{1}{g(\vec{x})} - \frac{\omega_p^2}{\omega^2 - \omega_b^2} - \frac{3L_D^2\omega_p^4\nabla^2}{\left(\omega^2-\omega_b^2\right)\left(4\omega_b^2-\omega^2\right)}, \text{ etc.} \tag{27}$$

Therefore we propose the following rules:

The solution of the linearized Vlasov equation and substitution of the distribution function in Poisson's equation gives rise to a partial differential equation which when correct to order T^n is of order $2^n + 1$. This equation can be written down as well as the conductivity current by use of the following four rules.

RULE ONE: Take the dielectric tensor derived for the infinite homogeneous medium and change the unit term into $1/g(\vec{x})$; at the same time change the wave vector $\vec{k}$ into $-i\vec{\nabla}$; to obtain the dielectric tensor operator

$$\epsilon^{ij}\left(1, \frac{\omega_b}{\omega}, \frac{\omega_p}{\omega}, L_D\vec{k}\right) \rightarrow \hat{\epsilon}^{ij}\left(\frac{1}{g}, \frac{\omega_b}{\omega}, \frac{\omega_p}{\omega}, -iL_D\vec{\nabla}\right).$$

RULE TWO: Construct the vector $T_j(\vec{x}) = g(\vec{x})\, E_j(\vec{x})$, where $E_j(\vec{x})$ is the j component of the electric field at point $\vec{x}$ and $g(\vec{x}) = N(\vec{x})/N_o$.

RULE THREE: Contract both tensors obtained in one and two to obtain the displacement vector $D^i(\vec{x}) = \epsilon^{ij}g(\vec{x})\, E_j(\vec{x})$. The equation D^i, i = 0 or div $\vec{D} = 0$ corresponds to Poisson's equation.

In order to obtain the electromagnetic fields inside the plasma, we still have to calculate $\vec{J}(\vec{x})$, the conductivity current. We can infer from the structure of the kinetic equations, as well as Maxwell's, that all that we have to do is to take the dielectric tensor operator and construct from it the conductivity tensor operator $\hat{\sigma}^{ij}$ as given by

RULE FOUR: $\hat{\sigma}^{ij} = \frac{i\omega}{4\pi}(\delta^{ij}-\hat{\epsilon}^{ij})$ from which the conductivity current is given by

$$J^l(\vec{x}) = \hat{\sigma}^{lm}g(\vec{x})\, E_m(\vec{x}).$$

The author would like to thank Dr. S. Gruber and Professor G. Bekefi for making their results available before publication. He would like also to express appreciation to Professor W. P. Allis and Dr. S. J. Buchsbaum for their encouragement and advice, as well as for having suggested this problem.

J. C. de Almeida Azevedo

References

1. S. J. Buchsbaum and A. Hasegawa, Phys. Rev. Letters 12, 25, 685 (1964).
2. K. Mitani, H. Kubo, and S. Tanaka, J. Phys. Soc. Japan 19, 211 (1964).

3. Y. Furutani and G. Kalman, Rapport LP. 35, Laboratoire des Hautes Energies, University of Paris, Avril 1964.

4. W. P. Allis, S. J. Buchsbaum, and A. Bers, Waves in Anisotropic Plasmas (The M. I. T. Press, Cambridge, Mass., 1963).

5. H. Bateman, Tables of Integral Transforms, Higher Transcendental Functions, E'rdelyi, Magnus, Oberhettinger and Tricomi.

6. S. J. Buchsbaum (private communication).

7. D. Bohm, E. P. Gross, Phys. Rev. 75, 1851 (1949).

8. I. Bernstein, Phys. Rev. 109, 10 (1958).

9. S. Gruber and G. Bekefi, Proceedings of the VII International Conference on Ionization Phenomena in Gases, Beograd, Yugoslavia, September 1965.

10. W. P. Allis, S. J. Buchsbaum, and A. Bers, op. cit., p. 91.

B. RADIOFREQUENCY DIPOLE RESONANCE PROBE

In Quarterly Progress Report No. 74 (pages 91-98) Bekefi and Smith presented a theory for the dipole resonance probe. They derived an expression for the complex susceptance, B (= j×complex admittance), for a probe-plasma system in which the sheath region around the conducting dipole sphere was taken to be a vacuum and the surrounding plasma extended to infinity. By using a computer, their solution for the susceptance has been evaluated for several values of the parameters f and ν_c, f is the ratio of the radius of the sheath cavity to the probe radius, and ν_c is the collision frequency normalized to plasma frequency. Figure X-3 shows the first two multipole contributions to the probe admittance for f = 1.2 and ν_c = 0.1. The octopole contribution (ℓ=3) is ~0.2 of the dipole contribution (ℓ=1). Also, the octopole resonance occurs at a higher frequency than the dipole resonance and the octopole antiresonance occurs at a lower frequency than the dipole antiresonance. The half-width of the conductance peak is approximately equal to ν_c for the dipole mode. Contributions from the monopole mode and the octopole mode will tend to broaden the observed half-width because their resonant frequencies differ from that of the dipole. It is found that, by increasing the value of f, the magnitude of the admittance decreases and the susceptance curve moves upward and remains positive except at the resonant frequency where it dips down to touch the zero axis. This happens because of the assumption of a vacuum sheath around the probe. As the sheath size increases (f increases), the probe response will approach the free-space value of a capacitor.

Measurements are being made with the apparatus shown in Fig. X-4 to determine the actual behavior of the complex admittance of spherical dipole probes. By allowing gas to flow into the side arms while the pumping mechanism is left open to the sphere, the gas pressure in the sphere can be maintained a factor of 30-40 below the pressure in the side arms. The gas is broken down in the side arms at a pressure of ~30 microns

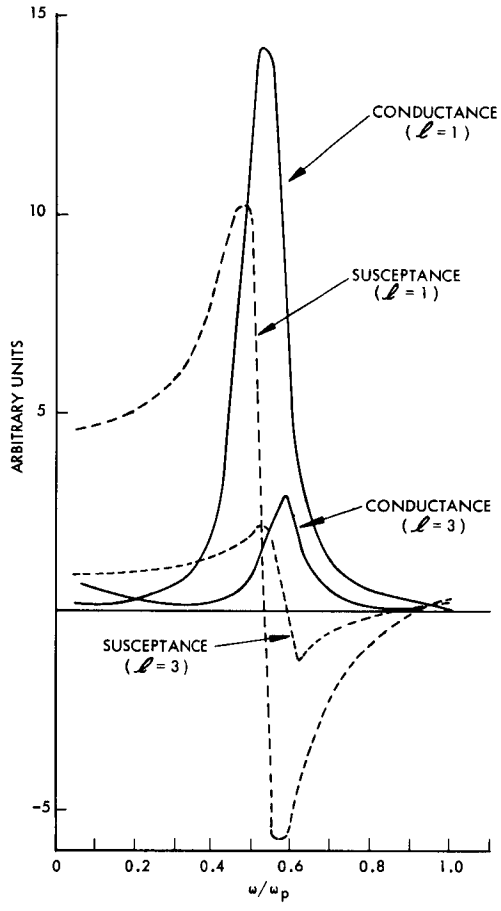

Fig. X-3. Real and imaginary parts of the admittance of a spherical dipole as a function of frequency for f = 1, 2 and ν_c = 0, 1.

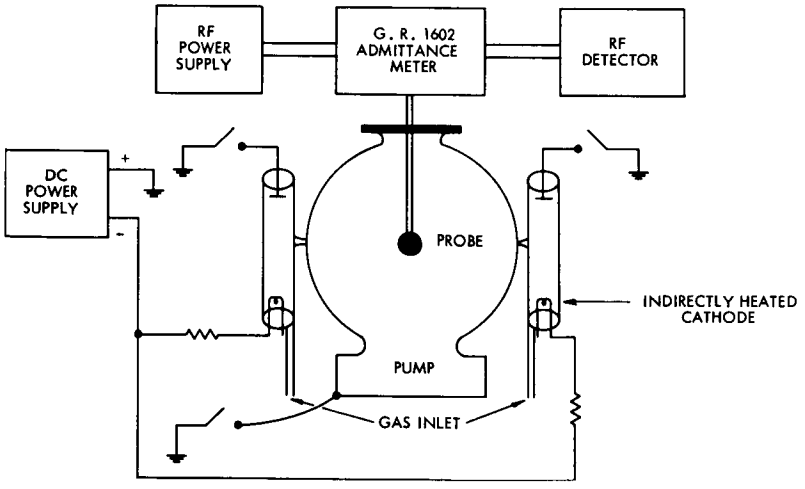

Fig. X-4. Schematic diagram of the experiment.

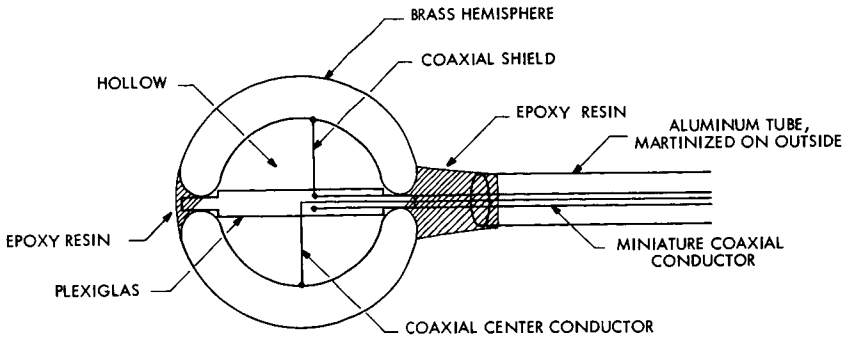

Fig. X-5. Schematic diagram of the probe construction.

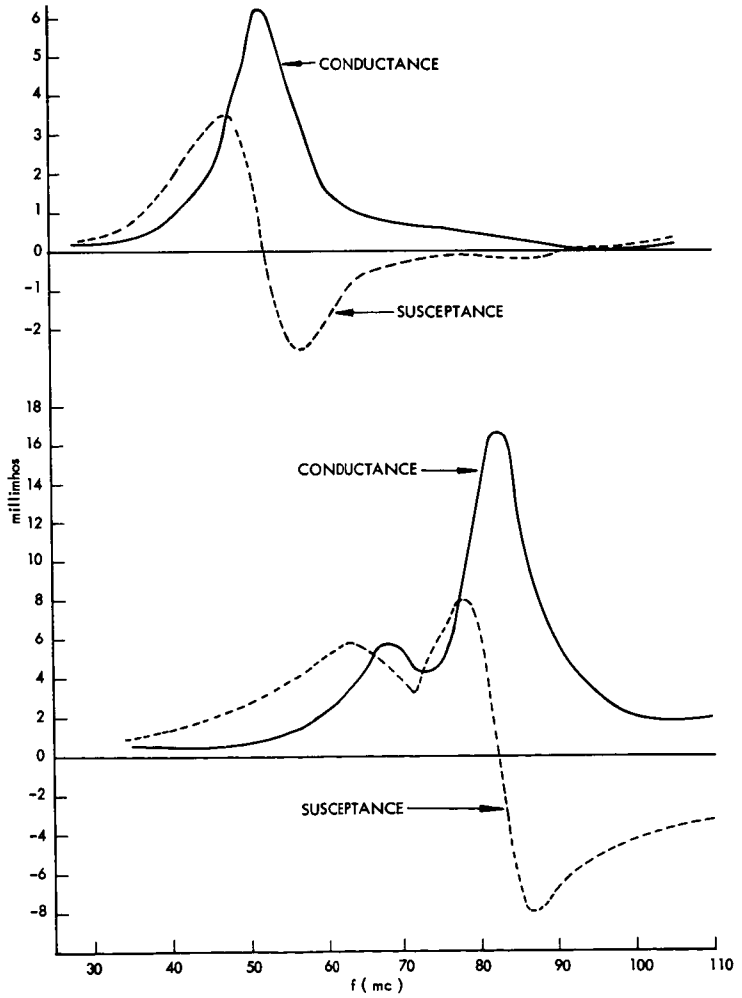

Fig. X-6. Measured real and imaginary parts of the admittance for a 1. 75-inch probe.

and the resulting plasma is made to enter the low-pressure region of the sphere by making the pump the anode. Plasma densities of 10^{+8}/cc with electron temperatures of ~4 ev at a background gas pressure of a fraction of a micron are typical using argon.

The probes used (Fig. X-5) consist of two brass hemispheres separated by a plexiglas wafer and vacuum-sealed with an epoxy resin. The edge of each hemisphere has been rounded to reduce the effect of fringing fields. The probes are coated with a thin coating of Insl-X to prevent DC current from flowing.

Two representative plots of the conductance and susceptance for a 1.75-inch diameter probe are shown in Fig. X-6. For Fig. X-6a the plasma density and electron temperature as measured by a guard-ring Langmuir probe are

$$n = 1.38 \times 10^{+8}/\text{cc} \text{ and } T_e = 3.41 \text{ ev.}$$

The admittance plot shows a resonance at 57.5 Mc and an antiresonance at 96 Mc. Assuming that the dipole mode is the dominant mode in this case, we can solve the equations given by Bekefi and Smith[1] for the resonant and antiresonant frequencies and arrive at values for ω_p and f. The result is $\omega_p = 2\pi \times 104$ Mc and f = 1.22; ω_p as measured by the Langmuir probe is $2\pi \times 105$ Mc. Using the measured value of 3.41 ev for the electron temperature, one finds that the sheath thickness in this case is 4.2 λ_D.

For Fig. X-6b the plasma density and electron temperature are $3.28 \times 10^{+8}$/cc and 4.21 ev, respectively. Figure X-6b has a double peak which indicates that in this case a monopole mode in addition to the dipole mode was probably excited. Using the Langmuir probe value for the density and assuming that the resonance at 82.5 Mc is due to the dipole mode, one gets f = 1.18. The sheath thickness in this case is 4.78 λ_D.

More data are being taken to determine the relationship between sheath thickness, probe size, and Debye length. The resonance probe can then be used to determine the electron density and temperature and the collision frequency in low-density plasmas.

J. A. Waletzko

References

1. D. F. Smith and G. Bekefi, "Radiofrequency Probe," Quarterly Progress Report No. 74, Research Laboratory of Electronics, M. I. T., July 15, 1964, pp. 91-98.

XI. PLASMA ELECTRONICS*

Prof. H. A. Haus
Prof. A. Bers
Prof. W. D. Getty
Prof. G. D. Bernard
Prof. D. J. Rose
Prof. T. H. Dupree
Prof. L. M. Lidsky
Prof. E. P. Gyftopoulos
Dr. T. Musha
R. R. Bartsch
T. S. Brown
J. F. Clarke
D. E. Crane
J. A. Davis
R. W. Flynn
J. N. Hamawi
W. T. Hebel, Jr.
C-F. G. Hsi
B. R. Kusse
S. H. Kyong
M. A. Lieberman
M. D. Lubin
R. W. Moir
A. A. Offenberger
R. R. Parker
C. S. Ribbeck
E. A. Robertson
M. A. Samis
H. M. Schneider
C. E. Speck
C. E. Wagner
R. N. Wallace
J. C. Woo
N. D. Woodson

A. ACTIVE SOLID-STATE PLASMAS

1. STIMULATED EMISSION OF PHONONS BY ELECTRONS DRIFTING ALONG THE MAGNETIC FIELD

In this report we present the results of a quantum-mechanical analysis of the interaction between acoustic phonons and electrons drifting along an external magnetic field, and show the possible relation to recent experiments.[1,2] The coupling between the electrons and phonons is taken through the deformation potential. We find that stimulated emission of phonons, with electrons making transitions between Landau levels, has a threshold magnetic field.

We neglect electron-electron interactions, which is valid for high-frequency phonons in semiconductors ($q\ell_s \gg 1$, where q is the phonon wave number, and ℓ_s is the screening length for the electrons). The interaction Hamiltonian for the deformation potential in terms of electron and phonon operators is $H' = \int \Psi^+ C\Delta(x)\, \Psi\, d^3x$, where Ψ is the field operator for electrons in the Landau gauge,[3] Δ is the dilation,[4] and C is the deformation potential coefficient. Assuming that the gyration radius of the electron is small compared with the phonon wavelength (dipole approximation), we expand H' up to first order in $\vec{q} \cdot \vec{x}$ and obtain

$$
\begin{aligned}
H' = & \sum_{\vec{q}, n, \vec{k}} iC(\hbar/2\rho V\omega_q)^{1/2}\, q\xi_n c^+_{\vec{k}+\vec{q}, n}\, c_{\vec{k}, n}\left(a_{\vec{q}} - a^+_{-\vec{q}}\right) \\
& - \sum_{\vec{q}, n, \vec{k}} \Bigg\{ iC(\hbar/2\rho V\omega_q)^{1/2}\, q(\hbar/2m\omega_c)^{1/2}\, qx \\
& \times \left[n^{1/2}\xi_{n-1} c^+_{\vec{k}+\vec{q}, n-1} - (n+1)^{1/2}\xi_{n+1} c^+_{\vec{k}+\vec{q}, n+1} \right] c_{\vec{k}, n}\left(a_{\vec{q}} - a^+_{-\vec{q}}\right) \Bigg\} \qquad (1)
\end{aligned}
$$

---

*The work reported in Sections XI-A, -B, -C, and -D was supported principally by the National Science Foundation (Grant GK-524).

where ρ is the mass density; V, the volume; ω_q, the angular frequency of the phonon with wave number $\vec{q}$; $a_{\vec{q}}$ and $a^+_{\vec{q}}$, the phonon operators; $c_{\vec{k},n} = c(k_y, k_z, n)$ and $c^+_{\vec{k},n}$, the electron Fermi operators; m, the effective mass which has been set equal to the electron cyclotron mass; and $\omega_c = eB_o/m$, the electron cyclotron frequency. In (1) ξ_n is given by

$$\xi_n(q_y) = \int \eta_n(x)\, \eta(x-\hbar q_y/m\omega_c)\, dx \tag{2}$$

and represents an overlap integral of two harmonic oscillator states in the interaction. These two states have different equilibrium positions, separated by $\delta = \hbar q_y/m\omega_c$ caused by the recoil of emitted or absorbed phonons. The overlap integral (2) becomes very small if the separation is larger than the first zero of the harmonic oscillator function[5] given by $F_n(\hbar/m\omega_c)^{1/2}$, where F_n is approximately unity. Hence, in order to get appreciable interaction we require

$$B_o > \frac{\hbar q_y^2}{F_n^2 e}. \tag{3}$$

Diagrams for the zeroth-order terms of H' are shown in Fig. XI-1b. Here the

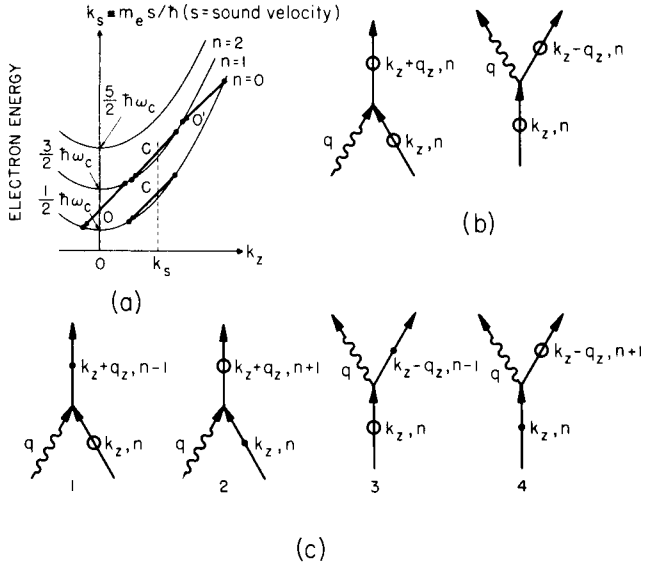

Fig. XI-1. (a) Landau-level diagram and examples of the two types of transitions.
(b) Diagrams for phonon emission and absorption resulting from the intra-Landau level.
(c) Diagrams for phonon emission and absorption resulting from the inter-Landau level transitions. Circles and dots indicate changes in the electron radius of gyration.

electron makes transitions within a Landau level without changing its radius of gyration. This is shown by arrows "C" in Fig. XI-1a and is essentially the same as the (stimulated) Cherenkov process. In this process the magnetic field does not play an important role, except for the effect of the overlap integral ξ_n, and in the classical limit $\hbar \to 0$ the interaction is independent of the magnetic field. The first-order terms in H' are shown in Fig. XI-1c, where circles and dots represent the change in radius of gyration. Diagram 3 in this figure shows emission of a phonon by electron transitions from a higher to a lower Landau level, which decreases its radius of gyration ("O" in Fig. XI-1a). Diagram 4 shows emission of a phonon by electron transitions from a lower to a higher Landau level, which increases its radius of gyration (O' in Fig. XI-1a). These processes are essentially the interaction between waves and moving oscillators.[6,7] In the classical limit they correspond to the Doppler-shifted cyclotron resonance interaction.[8]

The time rate of generation of stimulated phonons $\left(n_q^{-1}\, dn_q/dt \equiv \gamma\right)$ is obtained from time-dependent perturbation theory. The results may be summarized as follows.

For intra-Landau level (Cherenkov) processes

$$\gamma_C = \frac{C^2 m^2 \omega_c q}{2\pi\rho\hbar^3 \omega_q |\cos\theta|} \sum_n \left[(f_n(K_+) - f(K_-)\right] \frac{2}{\pi} \int_0^{\pi/2} \left[\xi_n\{q \sin\theta \sin\phi\}\right]^2 d\phi, \tag{4}$$

where

$$K_\pm = (m/\hbar)(s/\cos\theta - v) \pm (1/2)\, q \cos\theta, \tag{5}$$

θ is the angle between the magnetic field B_o and the phonon wave vector, s is the sound velocity, and v is the electron drift velocity.

For inter-Landau level (oscillator-wave) processes

$$\gamma_{OW} = \left(\frac{C^2 m^2 \omega_c q}{2\pi\rho\hbar^3 \omega_q |\cos\theta|}\right)\left(\frac{\hbar q^2 \sin^2\theta}{2m\omega_c}\right)$$

$$\times \sum_n (n+1)\{f_n(K'_+) - f_{n+1}(K'_-) + f_{n+1}(K''_+) - f_n(K''_-)\}$$

$$\times \frac{2}{\pi} \int_0^{\pi/2} \cos^2\phi\, \xi_n(q \sin\theta \sin\phi)\, \xi_{n+1}(q \sin\theta \sin\phi)\, d\phi, \tag{6}$$

where

$$K'_\pm = K_\pm + m\omega_c/\hbar q \cos\theta \tag{7}$$

$$K''_\pm = K_\pm - m\omega_c/\hbar q \cos\theta \tag{8}$$

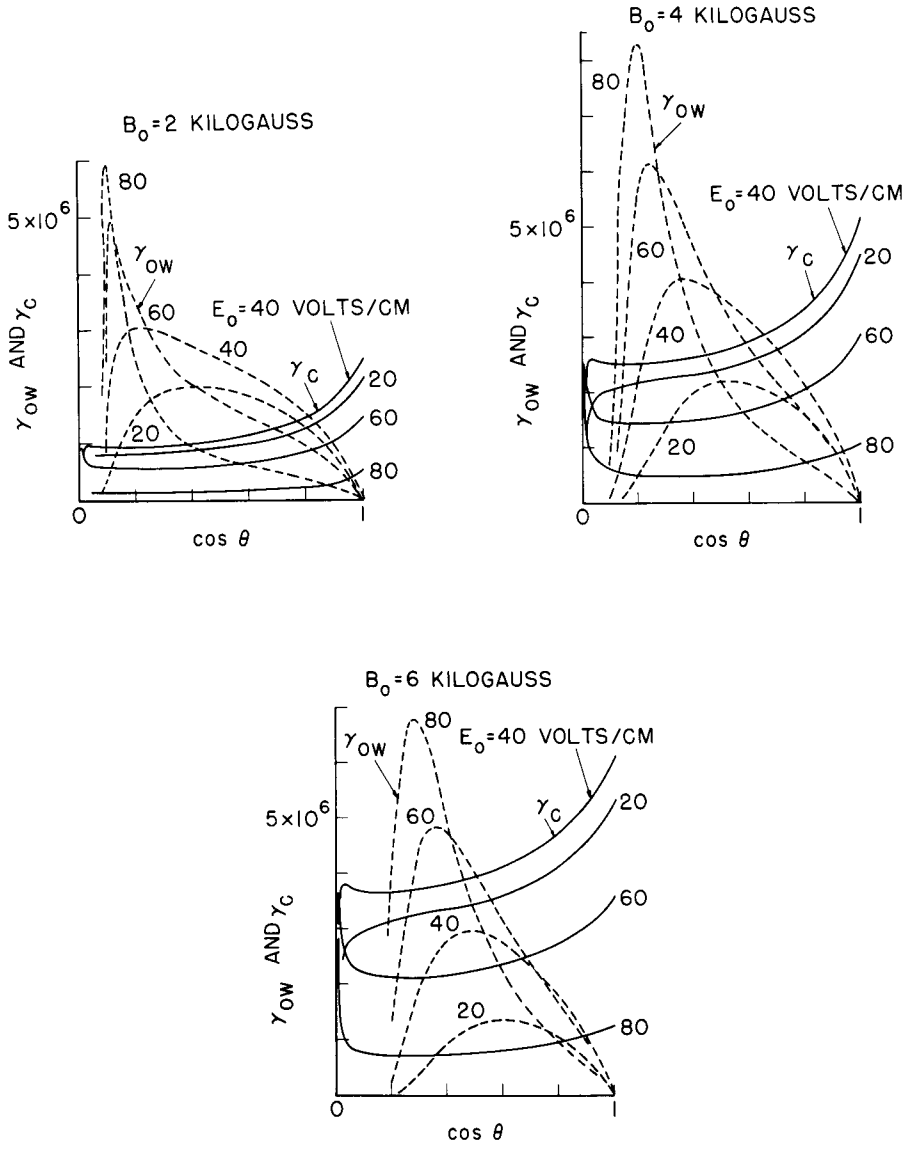

Fig. XI-2. Time rate (γ) of generation of stimulated phonons as a function of angle of emission (θ) with respect to the applied magnetic field, and for various values of B_o and E_o.

In (4) and (6) f is the Fermi distribution function,

$$f_n(K) = \{1 + \exp[\hbar^2K^2/2m+(n+1/2)\hbar\omega_c-\epsilon_F]/kT\}^{-1}. \quad (9)$$

Net stimulated emission of phonons ($\gamma>0$) is obtained when the electrons have sufficient drift, and γ exceeds the decay rate of phonons because of other processes.

Our analysis was stimulated by recent experiments[1,2] that show microwave emission from an n-type InSb bar in parallel electric and magnetic fields. For our experiments[2] at 9.3 kmc we used n-type InSb at 77°K with electron concentration of 2×10^{14} cm^{-3}, mobility 10^6 cm^2/volt sec, and the results were $q \times$ (electron mean-free path) ≈ 15, $q \times$ (Debye length) ≈ 15, and at 5 kgauss $\omega_c\tau \approx 60$, $\hbar\omega_c \approx kT_e$ (T_e=100°K), and $q \times$ (electron gyration radius) < 1 for $n < 8$. Hence, by using C = 30 ev,[9] (4) and (6) can be used to evaluate γ as a function of θ. The results are shown in Fig. XI-2. We note that for certain angles θ the inter-Landau level process can dominate. The sharp decrease in γ for small cos θ is due to the integrals of $\xi_n\xi_{n+1}$ and is approximately predicted by (3). Figure XI-3 shows the maximum growth rate for the inter-Landau level process as a function of magnetic field B_o. The threshold magnetic field corresponds closely to the magnetic field at which we observe the onset of enhanced microwave emission. The threshold electric field, which is also observed experimentally, would be determined from the condition that γ exceed the phonon decay rate resulting from other processes. At present, there are no data available on the lifetime of 10-kmc phonons in InSb at 77°K. The coupling of the phonons to the microwave field in the waveguide must be assumed to occur at the boundary of the InSb bar.

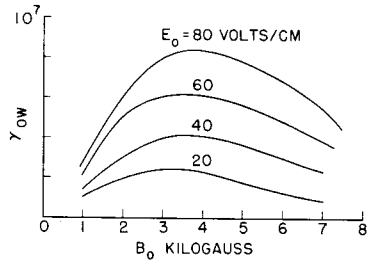

Fig. XI-3. Maximum (with respect to θ) time rate of generation of phonons as a function of the applied magnetic field, for various values of the applied electric field.

T. Musha, A. Bers

References

1. S. J. Buchsbaum, A. G. Chynoweth, and W. L. Feldmann, Appl. Phys. Letters 6, 67 (1965).

2. T. Musha and A. Bers, "Electron-Phonon Instabilities in a Magnetic Field," a paper presented at the Solid-State Device Research Conference, Princeton University, Princeton, New Jersey, June 21-23, 1965; the experiments reported in this paper are the same as those of Buchsbaum, Chynoweth, and Feldmann,[1] except at 10 kmc.

3. C. Kittell, Quantum Theory of Solids (John Wiley and Sons, Inc., New York and London, 1963), Chap. 11.

4. Ibid., pp. 23 and 132.

5. L. I. Schiff, Quantum Mechanics (McGraw-Hill Book Company, Inc., New York, Toronto, and London, 2d edition, 1955), Chap. 4.

6. V. L. Ginzburg, Soviet Phys. – Usp. 2, 874 (1960).

7. T. Musha, J. Appl. Phys. 35, 3273 (1964).

8. Doppler-shifted cyclotron resonance interaction between electrons and phonons for crossed electric and magnetic fields has been treated by H. N. Spector, Phys. Rev. 131, 2512 (1963).

9. E. Haga and H. Kimura, J. Phys. Soc. Japan 18, 777 (1963).

2. LONGITUDINAL INTERACTION OF ELECTRONS WITH PHONONS IN A MAGNETIC FIELD

In order to gain a more complete picture of electron-phonon interactions we shall attempt to formulate it in terms of a dispersion relation that contains the interactions self-consistently. In the future we shall analyze the nature of the stability of these interactions. First, we give our results of a classical self-consistent field analysis, and then the quantum-mechanical analysis. Both analyses will be for longitudinal acoustic and electron-plasma waves ($\bar{q} \parallel \bar{E}$), at an arbitrary angle to the applied magnetic field, and coupled through the deformation potential.

Classical Formulation

The equation of motion for the lattice displacement, $\bar{\xi}$, is

$$\rho \ddot{\bar{\xi}} = \nabla \cdot \bar{\bar{T}} + C\nabla n - m^* n(\dot{\bar{\xi}} - \bar{v})\,\nu, \tag{1}$$

where ρ is the mass density, $\bar{\bar{T}}$ is the stress tensor, C is the deformation potential coupling constant, n is the electron density, m^* is the electron effective mass, $\bar{v}$ is the electron velocity, and ν is the effective electron-lattice collision frequency. The electron distribution function f is taken to satisfy the Boltzmann equation and is assumed to relax to the local equilibrium function

$$\frac{\partial f}{\partial t} + \bar{w} \cdot \frac{\partial f}{\partial \bar{r}} - \frac{e}{m}\left(\bar{E} - \frac{m\nu}{e}\dot{\bar{\xi}} + \bar{w} \times \bar{B}_o\right) \cdot \frac{\partial f}{\partial \bar{w}} = -\nu\left(f - f_o - \frac{n}{n_o} f_o - \dot{\bar{\xi}} \cdot \frac{\partial f_o}{\partial \bar{w}}\right), \tag{2}$$

where f_o is the unperturbed electron distribution function, n_o is the unperturbed electron density, and $\bar{B}_o$ is the applied magnetic field.

We linearize Eqs. 1 and 2 and solve them together with Poisson's equation. Assuming a dependence $\exp(-i\omega t + i\bar{q} \cdot \bar{r})$, we find that the resultant dispersion relation is

$$K_p + K_e - 1 = 0, \tag{3}$$

where

$$K_p = \frac{\omega^2 - q^2 s^2 + i\omega\nu \dfrac{m^* n_o}{\rho}}{\omega^2 - q^2 s^2 + i\omega\nu \dfrac{m^* n_o}{\rho} + \dfrac{C^2 \epsilon_L}{\rho e^2} q^4 \left(1 - i\omega\nu \dfrac{m^*}{Cq^2}\right)^2} \tag{4}$$

$$K_e = 1 - \frac{\dfrac{\omega_p^2}{q^2} \displaystyle\int_{-\infty}^{\infty} dw_{\parallel} \int_0^{\infty} dw_{\perp}\, w_{\perp} 2\pi \sum_n \frac{J_n^2(p)\left(\dfrac{n\omega_c}{w_{\perp}} \dfrac{\partial f_o}{\partial w_{\perp}} - q_{\parallel} \dfrac{\partial f_o}{\partial w_{\parallel}}\right)}{(\omega + i\nu - q_{\parallel} w_{\parallel} - n\omega_c)}}{1 + i\nu \displaystyle\int_{-\infty}^{\infty} dw_{\parallel} \int_0^{\infty} dw_{\perp}\, w_{\perp}\, 2\pi f_o \sum_n \frac{J_n^2(p)}{(\omega + i\nu - q_{\parallel} w_{\parallel} - n\omega_c)}} . \tag{5}$$

Here, s is the sound velocity, ω_p is the electron plasma frequency, ω_c is the electron cyclotron frequency, $q_{\parallel}$ is the wave number component along B_o, $q_{\perp}$ is the wave number component across B_o, and $p = q_{\perp} w_{\perp}/\omega_c$.

If the unperturbed electron distribution function is taken as a Maxwellian with thermal velocity $v_T = \kappa T/m$, and shifted along the magnetic field with drift velocity v_D, Eq. 5 may be written in terms of the plasma dispersion function $Z(\zeta)$,[1]

$$K_e = 1 + \frac{\dfrac{\omega_p^2}{q^2 v_T^2}\left[1 + \displaystyle\sum_n I_n(\lambda)\, e^{-\lambda}\, \zeta_o Z(\zeta_n)\right]}{1 + \dfrac{i\nu}{q_{\parallel} v_T \sqrt{2}} \displaystyle\sum_n I_n(\lambda)\, e^{-\lambda}\, Z(\zeta_n)}, \tag{6}$$

where

$$\zeta_n = \frac{\omega + i\nu - q_{\parallel} v_D - n\omega_c}{q_{\parallel} v_T \sqrt{2}} \tag{7}$$

$$\lambda = \left(\frac{q_{\perp} v_T}{\omega_c}\right)^2 . \tag{8}$$

Computations on instabilities contained in Eqs. 3-8 are in progress.

Quantum-Mechanical Formulation

To account for quantum-mechanical effects in the interaction we formulate the electron part of the dispersion relation, K_e, in terms of the single-particle density matrix ρ,

including a phenomenological damping term. Previous formulations either do not account for collisions,[2] or include collisions but with relaxation to an equilibrium that has no density fluctuations.[3] For our interests in longitudinal oscillations we choose a collision description with relaxation to local equilibrium, that is, with a perturbed density.

$$\frac{\partial \rho}{\partial t} + \frac{i}{\hbar}[H, \rho] = -\frac{1}{\tau}\left\{\rho - \left(1 + \frac{n_1}{n_o} I\right) \rho_o\right\}, \tag{9}$$

where I is a matrix, each element of which is unity, H is the Hamiltonian, ρ_o is the density matrix for the steady state, n_1 and n_o are, respectively, fluctuating and averaged electron densities, and [,] is the commutation bracket. The relaxation terms on the right-hand side of (9) imply that ρ is relaxing with the time constant τ to the local equilibrium, which to first order is given by $(1+n_1 I/n_o)\rho_o$. For longitudinal waves with dependence $\exp(i\omega t - i\bar{q}\cdot\bar{r})$, we obtain

$$K_e = 1 - \frac{\dfrac{m\omega_p^2}{q^2 n_o} \displaystyle\sum_{\nu,\nu'} \frac{\rho_o(E_\nu) - \rho_o(E_{\nu'})}{E_\nu - E_{\nu'} - \hbar(\omega - i/\tau)} \xi^2_{\nu',\nu}}{1 - i\dfrac{\hbar}{\tau}\dfrac{1}{n_o} \displaystyle\sum_{\nu,\nu'} \frac{\rho_o(E_\nu)}{E_\nu - E_{\nu'} - \hbar(\omega - i/\tau)} \xi^2_{\nu',\nu}}, \tag{10}$$

where E_ν is the electron energy of the state ν specified by (k_y, k_z, n), and $\xi_{\nu',\nu}$ is the overlap integral as used in Sec. XI-A.1.

Assuming that the unperturbed electron velocity distribution is Maxwellian with thermal velocity v_T and drift velocity v_D, we obtain

$$K = 1 - \frac{\dfrac{m\omega_p^2}{q^2} \displaystyle\sum_{N,\mu} \frac{1 - e^{-\hbar\omega_c/mv_T^2}}{\sqrt{2}\,\hbar v_T q_\parallel} \left\{ Z\left(\zeta_\mu + \frac{\hbar q_\parallel}{2\sqrt{2}\, mv_T}\right) e^{-\mu\hbar\omega_c/mv_T^2} - Z\left(\zeta_\mu - \frac{\hbar q_\parallel}{2\sqrt{2}\, mv_T}\right)\right\} \xi^2_{N+\mu,N}\, e^{-N\hbar\omega_c/mv_T^2}}{1 - i\dfrac{\hbar}{t} \displaystyle\sum_{N,\mu} \frac{1 - e^{-\hbar\omega_c/mv_T^2}}{\sqrt{2}\,\hbar v_T q_\parallel} Z\left(\zeta_\mu + \frac{\hbar q_\parallel}{2\sqrt{2}\, mv_T}\right) \xi^2_{N+\mu,N}\, e^{-N\hbar\omega_c/mv_T^2}} \tag{11}$$

Here, ξ is as defined in Eq. 7. In the classical limit $\hbar \to 0$, the quantum-mechanical formulation (11) agrees exactly with the classical formulation (6). Computations on electron-phonon interactions using Eqs. 3, 4, and 11 are also in progress.

A. Bers, T. Musha

References

1. B. D. Fried and S. D. Conte, The Plasma Dispersion Function (Academic Press, Inc., New York, 1961).

2. J. J. Quinn and S. Rodriguez, "Electrodynamic Properties of a Quantum Plasma in a Uniform Magnetic Field," Phys. Rev. 128, 2487 (1962).

3. S. Tosima, J. J. Quinn, and M. A. Lampert, "Effect of Collisions on the Magneto-conductivity Tensor of a Quantum Plasma," Phys. Rev. 137, A883 (1965).

B. INSTABILITIES OF WAVES ACROSS THE MAGNETIC FIELD

1. INSTABILITIES IN TRANSVERSE WAVES ALONG B_0

In previous reports we have discussed instabilities in transelectromagnetic waves that propagate along an applied magnetic field in a plasma with anisotropic velocity distribution of electrons.[1,2] In this report we consider the extent of the damping of the instabilities arising from finite electron temperature along the magnetic field. We also show that the plasma dispersion equation contains a negative energy wave associated with the zero-order transverse energy. The instabilities are interpreted in terms of the coupling between this wave and the well-known passive right circularly polarized waves in the plasma. Further details may be found in Robertson's thesis.[3]

Damping of the Instabilities

For an electron velocity distribution of the form

$$f_0(v_\perp, v_\parallel) = \frac{1}{2\pi v_\perp}\,\delta(v_\perp - v_{0\perp})\,\delta(v_\parallel - v_{0\parallel}) \tag{1}$$

a simultaneous solution of the relativistic Vlasov equation and Maxwell's equation yields the dispersion relation[2]

$$\frac{C^2k^2}{\omega^2} = 1 - \frac{\omega_p^2(\omega - kv_{0\parallel})}{\omega^2(\omega - kv_{0\parallel} - \omega_b)} - \frac{\omega_p^2 v_{0\perp}^2(k^2 - \omega^2/c^2)}{2(\omega - kv_{0\parallel} - \omega_b)^2} \tag{2}$$

for right circularly polarized waves with dependence $e^{j(\omega t - kz)}$. Following the Bers-Briggs criterion for instability, we plot the real k locus in the complex ω-plane. The

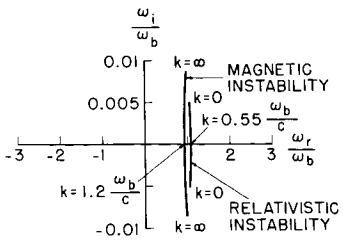

Fig. XI-4. Real k locus for $v_{0\parallel} = 0$.

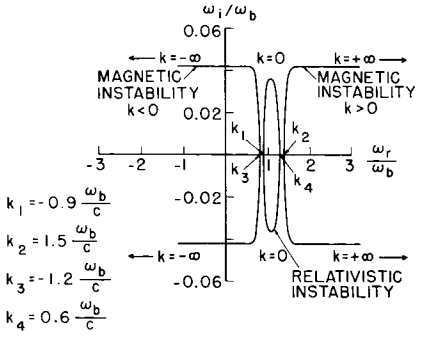

Fig. XI-5. Real k locus for finite $v_{0\parallel}$.

locus for $v_{0\parallel} = 0$ is given in Fig. XI-4, and for finite $v_{0\parallel}$ in Fig. XI-5. Two unstable branches are distinguished. A "magnetic instability," caused by first-order forces on the electron exerted by the first-order magnetic field of the wave, is found for wave numbers with magnitude greater than ω_b/c. A "relativistic instability," caused by the relativistic change in the cyclotron frequency of the electrons as they interact with the wave is found at wave numbers with magnitude less than ω_b/c.

For an electron distribution of the form

$$f_0(v_\perp, v_\parallel) = \frac{1}{(2\pi)^{3/2} v_{T\parallel} v_\perp} \delta(v_\perp - v_{0\perp}) \exp\left[-\frac{(v_\parallel - v_{0\parallel})^2}{2v_{T\parallel}^2}\right], \tag{3}$$

where $v_{T\parallel}$ is the electron temperature along B_0, the dispersion relation is

$$\frac{C^2k^2}{\omega^2} = 1 - \frac{\omega_p^2}{\omega^2}\left[1 - \frac{\omega_b}{\sqrt{2}\,kv_{T\parallel}} H(\zeta)\right] + \frac{\omega_p^2}{\omega^2} \frac{v_{0\perp}^2}{2v_{T\parallel}^2 k^2}\left(k^2 - \frac{\omega^2}{c^2}\right)(1+\zeta H(f)), \tag{4}$$

where

$$H(\zeta) = \frac{1}{\sqrt{\pi}} \int_{-\infty}^{\infty} \frac{e^{-x^2}}{x - \zeta} dx; \qquad I_m \zeta < 0 \tag{5}$$

and

$$\xi = \frac{\omega - kv_{0\parallel} - \omega_b}{\sqrt{2}\,kv_{T\parallel}}. \tag{6}$$

The real k locus obtained from (4) is given in Fig. XI-6 for $v_{0\parallel} = 0$, and in Fig. XI-7 for finite $v_{0\parallel}$. (The scale in Fig. XI-6 is expanded to show the details.) As is evident from the figures, the magnetic instabilities for large wave numbers are damped by the longitudinal temperature. As the temperature is increased, the damping of the magnetic instabilities extends to lower and lower wave numbers. From Fig. XI-7 it is evident that there are 6 wave numbers at which the plasma experiences a transition from stable to unstable. These wave numbers are defined as k_1-k_6 in Fig. XI-8. The relativistic instability exists for wave numbers between k_3 and k_4. The negative wave number branch of the magnetic instability exists between wave numbers k_1 and k_2, and the positive wave number branch between k_5 and k_6.

There is a physical reason why the magnetic instability is not found at wave numbers less than ω_b/c. The magnetic instability requires that there be some electrons in resonance with the wave. No electrons can have velocities along the magnetic field greater than c. Thus the upper limit on the phase velocity of an unstable wave is c. Since the

instability occurs near $\omega \cong \omega_b$, the lower limit on the wave number of the magnetic instability is near ω_b/c. Note that the relativistic instability that does not arise from such a wave resonance condition can have waves with phase velocities greater than c.

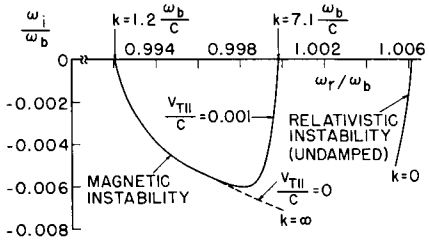

Fig. XI-6.
Zero drift real k locus for finite temperature.

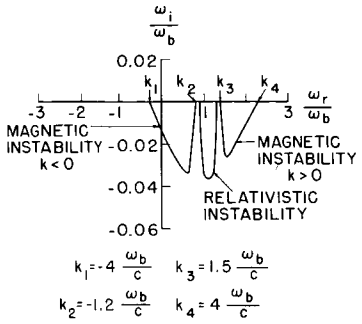

Fig. XI-7.
Finite drift real k locus with finite temperature.

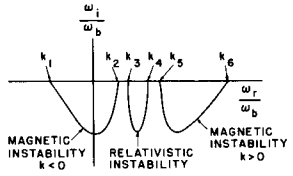

Fig. XI-8.
Characteristic shape of real k locus defining transition wave.

The temperature at which the magnetic instability disappears is found by obtaining the temperature at which $k_1 = k_2$ or $k_6 = k_5$. The transition wave numbers k_2 and k_5 can be found from the zero temperature dispersion relation (Eq. 2). The plasma becomes unstable near $\omega \approx \omega_d + kv_{0\parallel} = \omega_d$. Setting $\omega = \omega_d$ and solving the quadratic in Eq. 2 for $\omega - \omega_d$ yields

$$\omega - \omega_d = -\frac{\omega_p^2 \omega_b}{2\left(c^2k^2-\omega_d^2\right)} \pm \left\{\left[\frac{\omega_p^2 \omega_b}{2\left(c^2k^2-\omega_d^2\right)}\right]^2 - \frac{\omega_p^2 v_{0\perp}^2}{2c^2}\right\}^{1/2} . \tag{7}$$

The instabilities set in when the radical in Eq. 7 is zero. Setting the radical to zero yields for the transition wave numbers

$$\frac{k_2 c}{\omega_b} = \frac{\dfrac{v_{0\parallel}}{c} - \left[1 + \dfrac{\omega_p c}{\sqrt{2}\,\omega_b v_{0\perp}}\left(1 - \dfrac{v_{0\parallel}^2}{c^2}\right)\right]^{1/2}}{1 - \dfrac{v_{0\parallel}^2}{c^2}} \tag{8}$$

and

$$\frac{k_5 c}{\omega_b} = \frac{\frac{v_{0\parallel}}{c} + \left[1 + \frac{\omega_p c}{\sqrt{2}\,\omega_b v_{0\perp}}\left(1 - \frac{v_{0\parallel}^2}{c^2}\right)\right]^{1/2}}{1 - \frac{v_{0\parallel}^2}{c^2}}. \tag{9}$$

The transition wave numbers k_1 and k_6 are found by a method that is due to Sudan.[4] The dispersion relation is written as

$$k^2 = \frac{\pi\omega_p^2}{c^2 - \frac{\omega^2}{k^2}} \int_0^\infty dv_\perp \int_{-\infty}^\infty dv_\parallel \left[\frac{v_\perp^2 \left(v_\parallel - \frac{\omega}{k}\right) \frac{\partial f_o}{\partial v_\perp}}{v_\parallel - \left(\frac{\omega}{k} - \frac{\omega_b}{k}\right)} - \frac{v_\perp^3 \frac{\partial f_o}{\partial v_\parallel}}{v_\parallel - \left(\frac{\omega}{k} - \frac{\omega_b}{k}\right)} \right] = R\left(\frac{\omega}{k}\right). \tag{10}$$

At the transition wave numbers ω and k are pure real. The Cauchy type of integral in Eq. 10, split into its real and imaginary parts, yields the equation for the transition wave numbers k_1 and k_6:

$$k^2 c^2 \left(1 - \frac{v_{0\parallel}^2}{c^2}\right) + 2k v_{0\parallel} \omega_b \left(\frac{2v_{T\parallel}^2}{v_{0\perp}^2} - 1\right) - \omega_b^2 \left(\frac{2v_{T\parallel}^2}{v_{0\perp}^2} - 1\right)^2 - \omega_p^2 \frac{\left(1 - \frac{2v_{T\parallel}^2}{v_{0\perp}^2}\right)}{\frac{2v_{T\parallel}^2}{v_{0\perp}^2}} = 0. \tag{11}$$

The solutions from (11) are set equal to the solutions from (8) and (9), thereby resulting in the solution for the thermal velocity at which the magnetic instability disappears. The

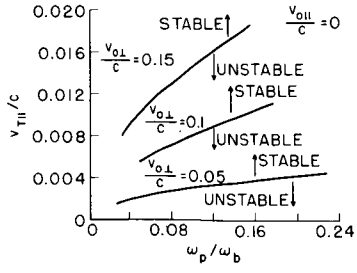

Fig. XI-9. Temperature at which magnetic instability disappears.

numerical solution for $v_{T\parallel}/c$ is shown in Fig. XI-9 as a function of ω_p/ω_b for several values of $v_{0\perp}/c$, for the case $v_{0\parallel} = 0$. From Fig. XI-9 it is evident that $\left(2v_{T\parallel}^2/v_{0\perp}^2\right) \ll 1$, for which an approximate solution for the thermal velocity at which the magnetic instability is damped as

$$\frac{v_{T\parallel}}{c} \approx \left[\frac{\omega_p v_{0\perp}^3}{\sqrt{2}\,\omega_b c^3}\right]^{1/2}. \tag{12}$$

The relativistic instability was found undamped for the nonrelativistic temperatures considered.

Mode-Coupling Picture of the Instabilities

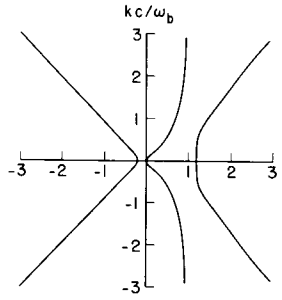

Fig. XI-10. Dispersion diagram for a cold plasma.

In Fig. XI-10 the k - vs - ω dispersion diagram is plotted for a cold plasma (Eq. 2 with $v_{0\perp}=0$). In Fig. XI-11 the dispersion diagram is plotted for finite $v_{0\perp}$. Conditions have been chosen in Fig. XI-11 such that the relativistic instability does not exist. The region of the magnetic instability where ω is complex for real k is shown as a dashed line. From Fig. XI-11 it is evident that the plasma with finite transverse energy contains a new wave branch. This wave branch satisfies the approximate relation

$$\omega \cong \omega_b + kv_{0\parallel} \tag{13}$$

The small-signal, time-averaged energy in the plasma can be calculated[5,6] from

$$\langle w_r \rangle = \tfrac{1}{4}\mu_0 |H|^2 + \tfrac{1}{4}\epsilon_0 |E|^2 \frac{\partial(\omega K_r)}{\partial\omega}, \tag{14}$$

where K_r is the right-hand element of the dielectric tensor in rotating coordinates. From the dispersion relation the small-signal energy is calculated to be

$$\frac{\langle w_r \rangle}{\frac{1}{4}\epsilon_0 |E|^2} = 2 + \frac{\omega_p^2 \omega_b}{\omega(\omega - kv_{0\parallel} - \omega_b)} - \frac{\omega_p^2 v_{0\perp}^2}{\omega c^2} \frac{[\omega(\omega_b + kv_{0\parallel}) - c^2k^2]}{(\omega - kv_{0\parallel} - \omega_b)^3}. \tag{15}$$

For the cold ($v_{0\perp}=0$) plasma of Fig. XI-10 all waves have positive energy and the plasma supports only passive waves. For the plasma with transverse energy ($v_{0\perp}\neq 0$) of Fig. XI-11 the new wave branch represented by Eq. 13 has been found to carry negative energy. The small-signal energy of this wave branch is plotted as a function of wave

number in Fig. XI-12.

The large wave number instability (magnetic instability) can be seen (Fig. XI-11) to

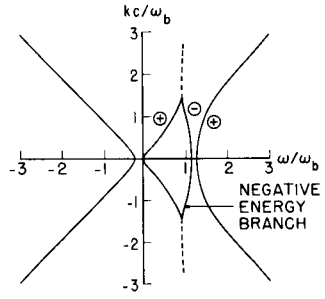

Fig. XI-11. Dispersion diagram for a plasma with zero-order energy transverse to B_0; ⊕ indicates a positive energy branch; ⊖ indicates a negative energy branch.

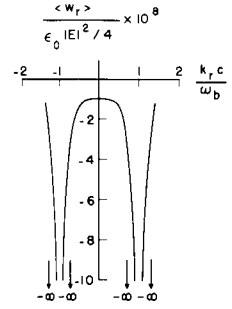

Fig. XI-12. Small signal energy of active wave branch.

arise from coupling of the negative energy branch with the right circularly polarized branch below ω_b. Since both branches have $k \to \infty$ for $\omega \to \omega_b$, this instability exists for any finite $v_{0\perp}$. The relativistic instability, which occurs for small wave numbers, arises because of coupling between the negative energy branch and the right circularly polarized branch above ω_b. For the parameters of Fig. XI-11 there is no such coupling. But, if either (ω_p/ω_b) is decreased (which moves the passive branch to lower frequencies) or $(v_{0\perp}/c)$ is increased (which moves the active branch to higher frequencies), the coupling will set in. As can be seen from Fig. XI-11, the waves that then couple have opposite group velocities, and we would expect absolute (nonconvective) instabilities to arise. We have determined that the absolute instabilities, which we have previously found from our exact computations,[1, 2] are indeed predicted by the coupling described here. Furthermore, the coupling picture clearly shows how the relativistic instability may disappear with increasing (ω_p/ω_b).

E. A. Robertson, A. Bers

References

1. A. Bers, J. K. Hoag, and E. A. Robertson, "Instabilities in Transverse Waves along B_0 for Beam-type Distributions," Quarterly Progress Report No. 77, Research Laboratory of Electronics, M. I. T., April 15, 1965, pp. 149-152.

2. E. A. Robertson and A. Bers, "Instabilities of Transverse Waves along the Magnetic Field," Quarterly Progress Report No. 78, Research Laboratory of Electronics, M.I.T., July 15, 1965, pp. 105-110.

3. E. A. Robertson, "Plasma Instabilities in Transverse Waves along the Magnetic Field," S.M. Thesis, Department of Electrical Engineering, M.I.T., Cambridge, Mass., August 24, 1965.

4. R. N. Sudan, "Plasma Electromagnetic Instabilities," Phys. Fluids 6, 57 (1963).

5. A. Bers, "Properties of Waves in Time- and Space-Dispersive Media," Quarterly Progress Report No. 65, Research Laboratory of Electronics, M.I.T., April 15, 1962, pp. 89-93.

6. A. Bers, "Energy and Power in Media with Temporal and Spacial Dispersion," Quarterly Progress Report No. 66, Research Laboratory of Electronics, M.I.T., July 15, 1962, pp. 111-116.

2. INSTABILITIES IN QUASI-STATIC WAVES ACROSS B_0

We have continued[1] the study of instabilities of quasi-static waves ($\bar{k}$ parallel to $\bar{E}$) propagating perpendicular to a static uniform magnetic field in an infinite plasma composed of stationary ions and electrons with an unperturbed distribution function

$$f_0 = \frac{1}{2\pi p_{\perp 0}} \delta(p_\perp - p_{\perp 0})\, \delta(p_\parallel) \tag{1}$$

Here, $p_\perp$ is the magnitude of the momentum across the magnetic field, and $p_\parallel$ is the momentum along the field. The dispersion relation for quasi-static waves propagating across the field has been shown[1, 2] to be

$$K_L(\omega, k_\perp) = 1 - \frac{\omega_p^2}{k^2} \sum_{n=-\infty}^{\infty} \left\{ \frac{k^2 \left(J_{m-1}^2 - J_{m+1}^2\right)}{2\omega_b(\omega - m\omega_b)} - \frac{m^2 \omega_b^2 J_m^2}{c^2(\omega - m\omega_b)^2} \right\} = 0. \tag{2}$$

This was obtained from a dielectric tensor description of the plasma that is consistent with the complete set of Maxwell's equations and the relativistic Vlasov equation.[3] Here, ω_p and ω_b are the (relativistic) electron plasma and cyclotron frequencies, respectively, c is the velocity of light, and J_m is the n^{th}-order Bessel function of the first kind and argument $(k_\perp p_{\perp 0}/M\omega_b)$.

The dispersion relation has been solved numerically for the roots $\omega = \omega(k_\perp)$. In our work an instability is said to exist when ω has a negative imaginary part for a real $k_\perp$. The criteria for classifying the type of instability (convective or absolute) has not been applied. Two distinct types of instabilities have been found.

The first type of instability had been predicted previously by a nonrelativistic analysis performed by Harris, Dory, and Guest,[4] although they did not determine the form of the dispersion characteristics. Their dispersion relation is obtained from (2) by

letting $c \to \infty$ and interpreting ω_p and ω_b as the nonrelativistic quantities. The "zero-frequency" instability that we reported also is an example of this kind of instability.[1] The study has now been extended to higher frequencies. Figure XI-13 is the dispersion diagram obtained from the nonrelativistic equation for a plasma whose density is such that $\omega_p/\omega_b = 1.5$. Note that there is a single passband at the cyclotron frequency and at each of its harmonics. The dispersion characteristics display an oscillatory behavior about the harmonic frequency. All passbands but the fundamental begin at $\omega = m\omega_b$. The fundamental begins at the hybrid frequency, $\omega = \left(\omega_b^2 + \omega_p^2\right)^{1/2}$. Figure XI-14 shows a higher density plasma with $\omega_p = 2.1\ \omega_b$. This plasma is similar to the one just discussed in that the waves are still purely propagating. But the branch of the dispersion characteristics which may be associated with the cyclotron fundamental at large values of $k_\perp$ now starts at $\omega = 2\omega_b$. It is the first harmonic that begins at the hybrid frequency. Note also that the amplitude of the oscillation of the root locus about each harmonic has increased. Figure XI-15 illustrates the dispersion characteristics of a still higher density plasma. With $\omega_p = 2.75\ \omega_b$, bands of unstable wavelengths are observed. By comparing Figs. XI-14 and XI-15 it can be seen that the amplitude of the oscillations of the root locus has become great enough for neighboring modes to overlap. This appears to happen for all modes studied at a density such that $\omega_p = 2.5\ \omega_b$. Figure XI-16, which has been drawn for a still higher density plasma, $\omega_p = 4.25\ \omega_b$, shows that increasing the density also increases the widths of the unstable bands. Also, we observe the onset of the "zero-frequency" instability. Figure XI-17 illustrates the growth rates (ω_c/ω_b) for the two unstable cases discussed above. The magnitude of the growth rate is seen to increase with increasing density. These two cases indicate, however, that it is not always the fundamental that has the maximum growth. Although more data should be taken to confirm this view, we feel that for a fixed plasma density the growth maximizes at a particular harmonic.

The small-signal time-averaged energy density for quasi-static waves in a dispersive medium[5] is given by

$$\langle \omega \rangle = \frac{1}{4}\epsilon_0 |E|^2 \left[\omega \frac{\partial K_L}{\partial \omega}\right]_{K_L=0}. \tag{3}$$

In Figs. XI-18 and XI-19 we plot the energy density of the fundamental and first harmonic when $\omega_p = 2.1\ \omega_b$. Note that at the points where the two modes are closest in Fig. XI-14, one wave (the harmonic) carries negative small-signal energy, while the other carries positive. This behavior is observed in all of the modes. When the frequency is above the harmonic the small-signal energy is positive, and it is negative when below. Thus, the high-density instabilities may be interpreted in terms of an internal coupling of an active wave (negative small-signal energy) with a passive one. The "zero-frequency"

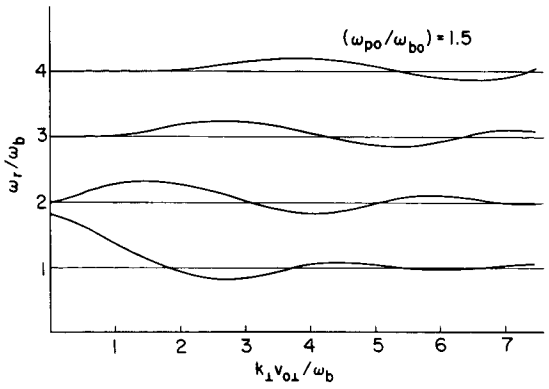

Fig. XI-13.

Nonrelativistic dispersion diagram for $(\omega_{p0}/\omega_{b0}) = 1.5$.

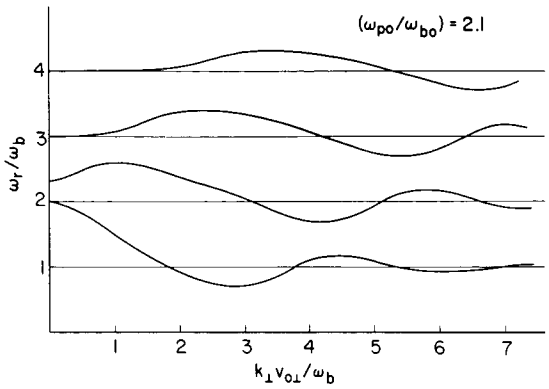

Fig. XI-14.

Nonrelativistic dispersion diagram for $(\omega_{p0}/\omega_{b0}) = 2.1$.

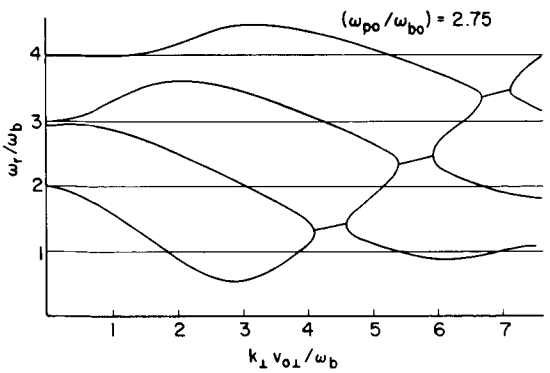

Fig. XI-15.

Nonrelativistic dispersion diagram for $(\omega_{p0}/\omega_{b0}) = 2.75$.

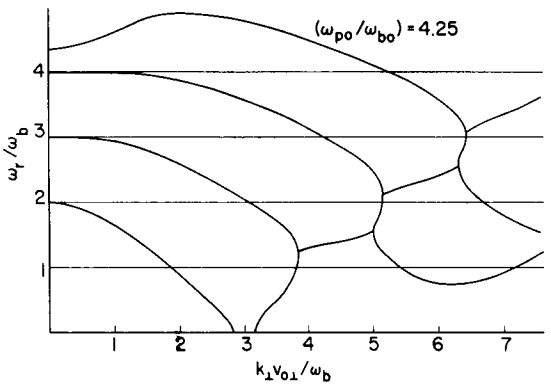

Fig. XI-16.

Nonrelativistic dispersion diagram for $(\omega_{p0}/\omega_{b0}) = 4.25$.

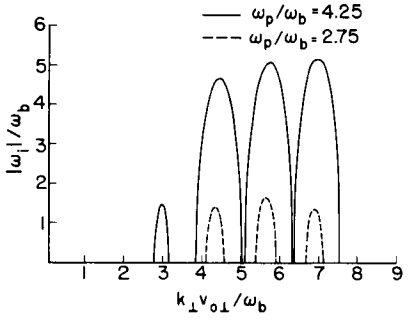

Fig. XI-17.

Growth rates for the high density instability.

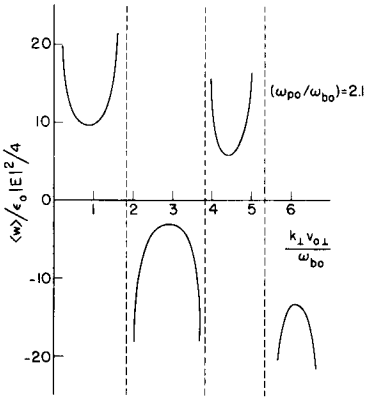

Fig. XI-18.

Small-signal energy of the fundamental. $(\omega_{p0}/\omega_{b0}) = 2.1$.

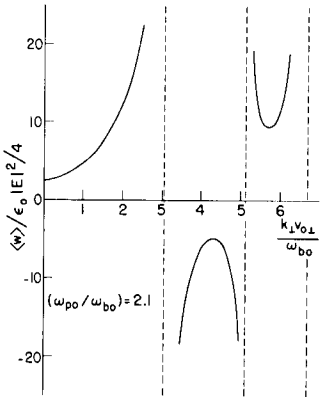

Fig. XI-19.

Small-signal energy of the first harmonic. $(\omega_{p0}/\omega_{b0}) = 2.1$.

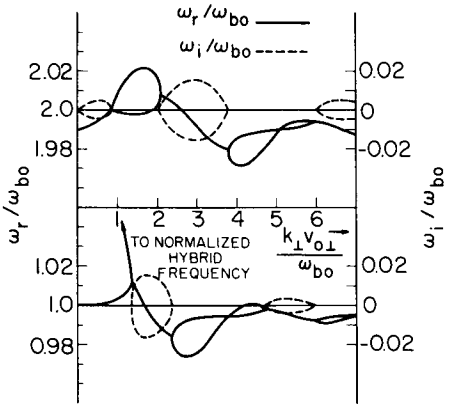

Fig. XI-20.

Relativistic dispersion of the fundamental and first harmonic. $(\omega_{p0}/\omega_{b0}) = 0.5$.

instability is interpreted as a coupling of the mode starting at $\omega = 2\omega_b$ (see Figs. XI-15 and XI-16) with the one that would start at $\omega = -2\omega_b$. (The dispersion relation is symmetrical in ω.) A numerical calculation has shown, however, that both waves carry negative small-signal energy.

The second type of instability observed in this plasma appears only in a relativistic analysis. The relativistic dispersion relation predicts two roots near each harmonic, while the nonrelativistic equation predicts only one. Figure XI-20 shows the root locus of the fundamental and first harmonic of a plasma in which $\omega_p = 0.5\,\omega_b$. The nonrelativistic analysis predicted no unstable waves at this low density; however, here we see bands of unstable wavelengths. Expanding Eq. 2 near the m^{th} harmonic and keeping terms only to second order in $(p_{\perp 0}/Mc)$, we find that the plasma is unstable at the m^{th} harmonic if

$$\frac{\omega_p/\omega_b}{p_{\perp 0}/Mc} < \frac{1}{|J'_m|}, \tag{4}$$

where the prime indicates the derivative with respect to the argument of the Bessel function. Since J'_m vanishes at discrete values of its argument $(k_\perp p_{\perp 0}/M\omega_b)$, the plasma is always unstable in bands of wavelengths about these points. The widths of these bands are always nonzero for finite (ω_p/ω_b). It is possible that this relativistic instability is more important than the high-density instabilities discussed earlier because they appear at such low densities. Note, however, that the new roots of the relativistic equation lie extremely close to the cyclotron harmonic frequencies. The validity of the quasi-static approximation used in obtaining Eq. 2 from the dielectric tensor may be in question for these roots. Further study requires that this approximation be checked. We are at present doing this.

C. E. Speck, A. Bers

References

1. C. Speck and A. Bers, Quarterly Progress Report No. 78, Research Laboratory of Electronics, M.I.T., July 15, 1965, pp. 110-114.
2. C. E. Speck, "Quasi-Static Theory of Plasma Instabilities at Cyclotron Harmonics," S.M. Thesis, Department of Electrical Engineering, M.I.T., Cambridge, Mass., September 1965.
3. A. Bers, "Dispersion Relations for Plasmas in a Magnetic Field, III," Internal Memorandum, Research Laboratory of Electronics, M.I.T., Cambridge, Mass., August 1964.
4. E. G. Harris, R. A. Dory, and G. E. Guest, "Unstable Plasma Waves Propagating Perpendicular to a Magnetic Field," Phys. Rev. Letters 5, 131-133 (1965).
5. A. Bers and S. Gruber, "Negative-Energy Plasma Waves and Instabilities at Cyclotron Harmonics," Appl. Phys. Letters 6, 27-28 (1965).
6. A. Bers, "Instabilities in Plasmas with Beam-type Distributions" (Abstract to appear in Bull. Am. Phys. Soc.)

C. QUASI-LINEAR INTERACTION OF A FILAMENTARY ELECTRON BEAM WITH A PLASMA-FILLED WAVEGUIDE

1. Introduction

In the last few years, a number of authors have examined the nonlinear aspects of the beam-plasma interaction using the methods of quasi-linear theory.[1-3] Several have considered the development of instabilities in an infinite plasma resulting from a "single-shot" injection of a beam. That is, the initial distribution function is taken as that of a plasma and a monoenergetic beam, and this distribution function is allowed to relax in time because of the development of the instability. This situation is shown in Fig. XI-21a. Because of spatial symmetry, these nonlinear solutions are independent of all spatial coordinates. While these studies provide some insight into the behavior of beam-plasma systems, they have little relevance to those beam-plasma experiments in which the beam is continuously injected into the plasma region.

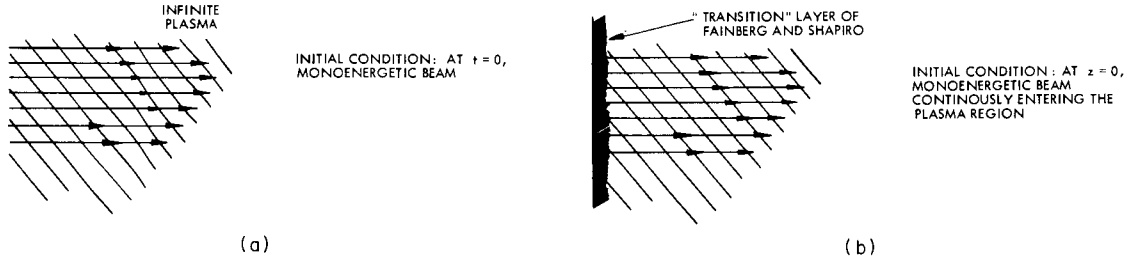

Fig. XI-21. (a) Single-shot injection of a beam into an infinite plasma.
(b) Continuous injection of a beam into a semi-infinite plasma.

Recently, Fainberg and Shapiro[3] have studied a semi-infinite plasma into which a monoenergetic electron beam is continuously injected. This is illustrated in Fig. XI-21b. They find that a "transition" layer is formed at the plasma boundary, z = 0, because of the instabilities that develop. This layer is a region of large and highly inhomogeneous electric field strength. Most of the beam energy is lost in passing through this layer, and the beam itself emerges from the layer highly diffused in velocity space. These authors find that the thickness of this layer tends to zero on a time scale of a few tenths of a microsecond for typical beam and plasma parameters. To keep the layer thickness finite, one must postulate a loss mechanism to remove energy from the boundary layer. Fainberg and Shapiro assume that the energy is transported away at the group velocity of the propagating plasma wave.

In this report we have analyzed a problem in which a monoenergetic electron beam of finite transverse dimensions in continuously injected into a circular plasma waveguide.

The beam velocity v_o at the entrance plane z = 0 is taken to be much greater than the plasma thermal velocity, v_T. The ratio of beam to plasma radius, b/a, is taken to be «1, and the plasma frequency ω_p, beam plasma frequency ω_{pb}, and electron cyclotron frequency ω_{ce} are assumed to satisfy the condition $\omega_{ce} \ll \omega_{pb} \ll \omega_p$. Only circularly symmetric solutions of the nonlinear equations will be considered. Under these assumptions, the beam-plasma system supports only a convective instability, and the electric field strength according to linear theory increases exponentially away from the beam entrance plane. Figure XI-22 shows the geometry of the system that we analyze.

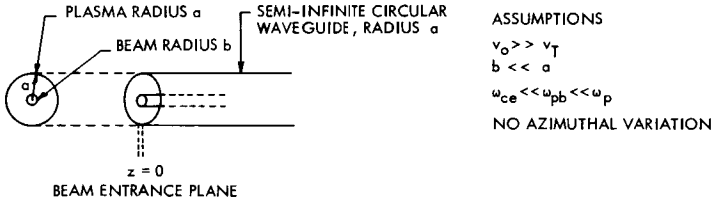

Fig. XI-22. Geometry of the beam-plasma system.

Since the beam density n_b is much less than the plasma density n_p, the important nonlinear effects occur in the beam alone. Therefore we treat the plasma as linear and solve for the beam distribution function in the steady-state limit $t \to \infty$. From this function we obtain the average beam velocity $\overline{v_o(z)}$ and the beam temperature $T_b(z)$ in the steady state.

2. Linear Theory of the Interaction between a Filamentary Electron Beam and a Plasma Waveguide

The dispersion equation of the beam-plasma system shown in Fig. XI-22 is

$$\beta(\omega) = \frac{\omega}{v_o} \frac{1}{1 \mp j\sqrt{-\dfrac{F(q)\,\omega_{pb}^2 b^2}{2v_o^2 K_\perp(\omega)}}} \tag{1}$$

where

$$F(q) = \ln \frac{1}{qb} + \frac{\pi}{2} \frac{N_o(qa)}{J_o(qa)} \tag{2}$$

and p and q are the transverse wave numbers in the beam and plasma regions, respectively. The transverse dielectric constant $K_\perp$ is given by

$$K_\perp = \frac{\omega^2 - \omega_+^2}{\omega^2 - \omega_{ce}^2}, \tag{3}$$

where

$$\omega_+^2 = \omega_p^2 + \omega_{ce}^2. \tag{4}$$

Figure XI-23 is a sketch of the dispersion function (1). It is seen from (1) that complex roots of β for real ω are obtained when $K_\perp$ is negative. The complex root with

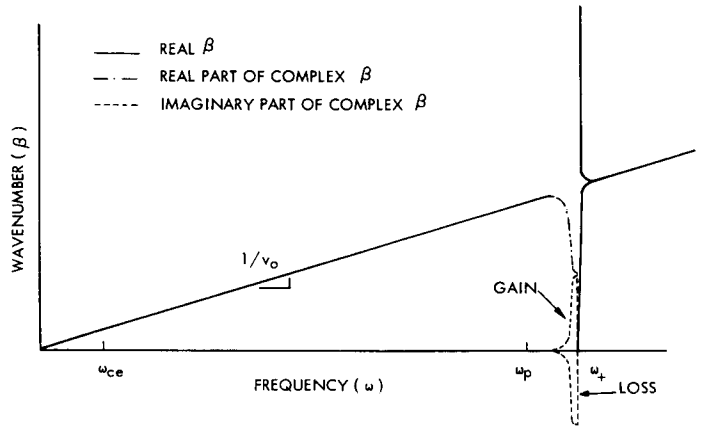

Fig. XI-23. Reactive-medium dispersion function for the n = 0 mode.

$\beta_i > 0$ is an amplifying wave, since for $\omega_i \to -\infty$ both roots of β from (1) are in the lower half β-plane. The amplification rate β_i is given by

$$\beta_i = \frac{\omega}{v_o} \frac{Q(\omega)}{1 + Q^2(\omega)}, \tag{5}$$

where

$$Q(\omega) = \sqrt{-\frac{F(q)\,\omega_{pb}^2 b^2}{2v_o^2 K_\perp(\omega)}} \tag{6}$$

provided Q is real. The condition of maximum gain is given by $Q^2 = 1$, for which the maximum gain is

$$\beta_{iMAX} = \frac{\omega_{MAX}}{2v_o} \tag{7}$$

and the frequency of maximum gain is

$$\omega_{MAX} = \omega_+ \sqrt{1 - \frac{1}{2}\frac{\omega_{pb}^2}{v_o^2} F(q)\, b^2} \tag{8}$$

The "half-power" width of the gain curve is

$$\Delta\omega = \sqrt{2}\,\omega_+ F(q)\,\frac{\omega_{pb}^2}{v_o^2}\, b^2 \tag{9}$$

in the limit $\frac{\omega_{pb}}{v_o} b \ll 1$. We shall use (7) and (9) below where a nonlinear equation describing the filamentary beam-plasma waveguide system is formulated.

It can be shown that for the system of Fig. XI-23 the filamentary beam approximation is valid, provided that $b\omega_p/2v_o \lesssim 0.1$. Furthermore, although this system supports an absolute instability at beam synchronism with the propagating plasma wave, it can be shown that the growth rate in time, ω_i, of this absolute instability is very small compared with the frequency of the oscillations, ω_p. The addition of even a small amount of collisional damping in the plasma would serve to supress the absolute instability, since the growth rate, ω_i, is so very small. Such damping would reduce the large reactive medium amplification rate (7) but slightly. Accordingly, we assume that the absolute instability is suppressed, and ignore it in the rest of this report.

3. Quasilinear Theory of the Filamentary Beam Distribution Function

We shall study the distribution function of the electron beam using the methods of quasi-linear theory. The beam distribution function $f(\bar{r}, \bar{v}, t)$ is described by the nonlinear Vlasov equation:

$$\frac{\partial f}{\partial t} + \bar{v} \cdot \frac{\partial f}{\partial \bar{r}} + \frac{q}{m}(\bar{E} + \bar{v} \times \bar{B}_o) \cdot \frac{\partial f}{\partial \bar{v}} = 0, \tag{10}$$

where $\bar{B}_o = \bar{i}_z B_o$ is the static magnetic field. The nonlinearity arises because $\bar{E}$ is itself a function of f.

$$\frac{\partial}{\partial \bar{r}} \cdot \bar{E}(\bar{r}, t) = \frac{q}{\epsilon_o}\left[n_b \int f\, d\bar{v} + n_p \int f_p\, d\bar{v} - n_b - n_p\right]. \tag{11}$$

Usually, (10) is linearized about a known "operating point" or steady-state distribution $f_o(\bar{v})$ by assuming that

$$f(\bar{r}, \bar{v}, t) = f_o(\bar{v}) + f_1(\bar{r}, \bar{v}, t). \tag{12}$$

In quasi-linear theory, the linearized solutions are used to evaluate the nonlinear term of (10) and the Vlasov equation is resolved. Provided the linear solution f_1 is much smaller than the exact (and unknown) nonlinear solution f, the separation of f into a zero and first-order distribution function is still useful. The zero-order distribution function f_o must now be considered to vary with r and t. Thus we write for the system of Fig. XI-23:

$$f(\bar{r}, \bar{v}, t) = f_o(\bar{r}, \bar{v}, t) + f_1(\bar{r}, \bar{v}, t), \tag{13}$$

where

$$f_1(\bar{r}, \bar{v}, t) = \sum_{n=1}^{2} \int_{-\infty}^{\infty} d\omega\, f_{n\omega}(\bar{v})\, J_o(p_n(\omega) r)\, \exp[j(\omega t - \beta_n(\omega) z)] \tag{14}$$

In (14), the summation over n represents a sum over the plus and minus signs of the reactive medium dispersion equation (1). Both roots must be included in f_1. The ω integration extends over negative, as well as positive, frequencies. The quantity $f_{n\omega}(\bar{v})$ represents the "Fourier coefficient" of the linearized solution at the real frequency ω. The wave numbers $p_n(\omega)$ and $\beta_n(\omega)$ are in general complex. It should be apparent that the significant contribution to the ω integral comes from the small ω regions where the reactive medium gain in high.

We also write

$$\bar{E}(\bar{r}, t) = \bar{E}_1(\bar{r}, t) = -\frac{\partial \Phi_1(\bar{r}, t)}{\partial \bar{r}}, \tag{15}$$

where

$$\Phi_1(\bar{r}, t) = \sum_{n=1}^{2} \int_{-\infty}^{\infty} d\omega\, \Phi_\omega J_o(p_n(\omega) r)\, \exp[j(\omega t - \beta_n(\omega))]. \tag{16}$$

Now Φ_ω and $f_{n\omega}(\bar{v})$ are related by the linearized Vlasov equation. In the filamentary beam limit, we obtain

$$f_{n\omega}(\bar{v}) = -\frac{q}{m} \frac{\beta_n(\omega) \frac{\partial f_o}{\partial v_z}}{\omega - \beta_n(\omega) v_z} \Phi_\omega. \tag{17}$$

The nonlinear equation describing the rate of change of the zero-order beam distribution function $f_o(\bar{r}, \bar{v}, t)$ will now be derived. We first insert the linear solutions (14-16) into the nonlinear Vlasov equation (10). Now in the linear theory, f_o is independent of time. Accordingly, in the quasi-linear theory, we assume $f_o(\bar{r}, \bar{v}, t)$ to be a weakly

varying function of time, and we average Eq. 10 over a time, T, satisfying the following inequality

$$\frac{2\pi}{\omega_{MAX}} \ll T \ll \frac{2\pi}{\Delta\omega}, \tag{18}$$

where ω_{MAX} and $\Delta\omega$ are given by (8) and (9), respectively. The time-average equation becomes

$$\frac{\partial f_o}{\partial t} + \bar{v} \cdot \frac{\partial f_o}{\partial \bar{r}} + \frac{q}{m} \bar{v} \times \bar{B}_o \cdot \frac{\partial f_o}{\partial \bar{v}} + 2 \frac{q}{m} \Delta\omega \sum_{n=1}^{2} \sum_{n'=1}^{2} \int d\omega \, \Phi_\omega \left[\left(-\frac{\partial}{\partial \bar{r}} \right) J_o(p_n(\omega) r) \, e^{-j\beta_n(\omega) z} \right]$$

$$\cdot \frac{\partial f_{n'\omega}(\bar{v})}{\partial \bar{v}} J_o(p_{n'}(-\omega) r) \, e^{-j\beta_{n'}(-\omega) z} = 0 \tag{19}$$

Taking the filamentary beam limit, performing the summations and integration, and using (17), (7), (8), and (9), we find

$$\frac{\partial f_o}{\partial t} + v_z \frac{\partial f_o}{\partial z} + 2(\Delta\omega)^2 |\Phi_\omega|^2 \frac{q^2 \omega_+}{m^2 v_o} e^{\frac{\omega_+}{v_o} z} \frac{\partial}{\partial v_z} \frac{\partial f_o}{\partial v_z} \frac{v_z}{-v_z^2 - 2v_o^2 + 2v_o v_z} = 0. \tag{20}$$

This is the equation we sought. It is a real, linear equation describing the change in the zero-order beam distribution function $f_o(\bar{r}, \bar{v}, t)$. We now solve (20) in the steady state $\frac{\partial f_o}{\partial t} = 0$. The equation is then separable. We normalize (21) by the substitutions

$$\epsilon_o = \frac{q^2}{m^2} \frac{2(\Delta\omega)^2}{v_o^4} |\Phi_\omega|^2$$

$$z' = \frac{\omega_+}{v_o} z$$

$$v' = \frac{v_z}{v_o}.$$

Then (20) becomes

$$\frac{\partial f_o}{\partial z'} e^{-z'} + \epsilon_o \frac{1}{v'} \frac{\partial}{\partial v'} \left(\frac{\partial f_o}{\partial v'} \frac{v'}{-v'^2 + 2v' - 2} \right) = 0. \tag{21}$$

Assuming a separation $f_o(z', v') = g(z') h(v')$, we obtain

$$g(z') = \exp[K(1 - e^{z'})] \tag{22}$$

and

$$\frac{d}{dv'}\left(\frac{dh(v')}{dv'}\,\frac{v'}{-v'^2+2v'-2}\right)-Kv'h(v')=0, \tag{23}$$

where K is the separation constant. Let $v' = u + 1$ and assume that h(u) is small unless $u \approx 0$. Since at the beam entrance plane $h(u) = \delta(u)$, a delta function in velocity space, this limit should prove interesting. Letting $u \to 0$ in (23) yields

$$\frac{d^2h}{du^2}+\frac{dh}{du}+\frac{K}{\epsilon_o}h=0. \tag{24}$$

Equation 24 has exponential solutions $e^{j\gamma u}$, where $K = \epsilon_o(\gamma^2-j\gamma)$. Superposing these solutions with (22) and matching the boundary condition $f_o(u, z'=0) = \delta(u)$, we find

$$f_o(u,z')=\frac{1}{\sqrt{2\pi}\,v_T(z')}\exp\left[-\frac{(u+v_d(z))^2}{2V_T^2(z)}\right], \tag{25}$$

where

$$v_T^2(z')=2\epsilon_o(e^{z'}-1) \tag{26}$$

$$v_d(z')=\epsilon_o(e^{z'}-1). \tag{27}$$

The energy density U(z') of the beam is

$$U(z')=1+\epsilon_o^2(e^{z'}-1)^2, \tag{28}$$

and the beam electron density n_b is constant. The solution is plotted in Fig. XI-24a.

Summarizing these results, we have found that

1. The zero-order beam density n_b does not vary along the length of the beam.

2. The average velocity of the beam $\overline{v_o(z')} = v_o - v_d(z')$ decreases with increasing z according to (27). At first, $\overline{v_o(z')}$ decreases linearly with z', but after a distance ≈ 1, the decrease is exponential with z'. This decrease represents a loss of DC beam energy.

3. The beam acquires a longitudinal temperature, $\frac{kT_b(z')}{m} = v_T^2$, given by Eq. 26. The thermal velocity $v_T(z')$ increases initially as the square root of z'.

4. The DC energy density of the beam <u>increases</u> as z' is increased. This surprising result indicates that the beam extracts energy from the plasma.

5. The solution (25) does not obey the conservation laws. For example, electrons are not concerned, since

$$\frac{d}{dz}(n_o v_o(z)) \neq 0.$$

These results were obtained by approximating the velocity equation (23) by a second-order linear equation with constant coefficients (24). We might expect that if (23) were solved exactly, these results would be modified. In particular, the solution of (20) should obey the conservation laws, and the DC energy density of the beam should probably decrease with increasing z'.

Since the analytical solutions (25) do not satisfy the conservation laws and lead to an increasing DC beam energy density, the exact solution of the diffusion equation (20) is of some interest. This equation has therefore been numerically integrated for $\epsilon_o = 0.01$ and z' in the range $0.4 < z' < 2.8$. The preliminary results of this numerical integration are presented in Fig. XI-24b. This figure should be carefully examined.

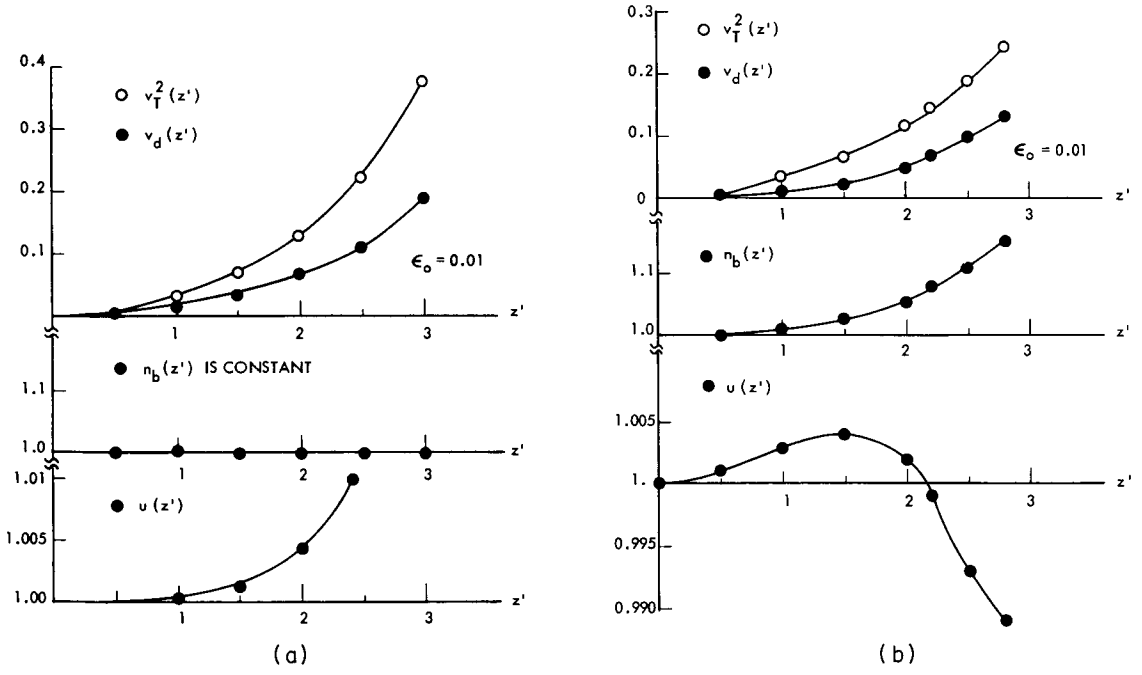

Fig. XI-24. Normalized thermal velocity v_T, velocity decrease of the beam v_d, beam density n_b, and beam energy density u as functions of z' (a) in the limit $f_o(v_z) \to 0$ unless $v_z \approx v_o$ and (b) computed exactly by numerical integration of Eq. 21.

First, note that the exact solution of (20) conserves electrons. The product $n_b(z')\overline{v_o(z')}$ is constant within one part in 10^4 over the range of z'. The beam density n_b is now an increasing function of z'. The velocities v_T and v_d are roughly similar to the approximate solutions in Fig. XI-24a; however, the DC energy density of the beam at first increases as in Fig. XI-24a, but then decreases as z' is increased. For

$z' > 2.1$, the average beam electron has lost energy. This energy must have been absorbed by the plasma; that is, the plasma has been heated by the beam.

M. A. Lieberman

References

1. Ya. A. Romanov and G. F. Filippov, Soviet Phys. – JETP 13, 87 (1961).
2. V. D. Shapiro, Soviet Phys. – JETP 17, 416 (1963).
3. Ya. B. Fainberg and V. D. Shapiro, Soviet Phys. – JETP 20, 4 (1965).

D. DISPERSION DIAGRAMS FOR HOT-ELECTRON PLASMAS

Computer solutions have been obtained for several beam-plasma dispersion equations. The computer program was described in Quarterly Progress Report No. 77 (pages 141-144). This program finds the zeros of a transcendental dispersion function $\underline{D}(\underline{\omega}, \underline{k}, \ldots)$ in the complex $\underline{\omega}$ or $\underline{k}$ plane.

1. Longitudinal Waves in an Infinite Maxwellian Plasma

Consider an electron beam of density n_b and velocity v_o immersed in an infinite, hot-electron plasma. The beam flows in the positive z direction, and all particle motion is assumed to be along z. The plasma electrons have a Maxwellian velocity distribution with thermal velocity v_T, while the plasma ions are assumed to be infinitely heavy. The dispersion equation for longitudinal (z-directed) waves in this system is

$$1 - \frac{\omega_{pb}^2}{(\omega - kv_o)^2} + \frac{1}{k^2\lambda_D^2}\left[1 + \frac{1}{\sqrt{2}\,k\lambda_D}\,\frac{\omega}{\omega_{pe}}\,Z\left(\frac{1}{\sqrt{2}\,k\lambda_D}\,\frac{\omega}{\omega_{pe}}\right)\right] = 0, \tag{1}$$

Where ω_{pb} and ω_{pe} are the beam and plasma frequencies, $\lambda_D = v_T/\omega_{pe}$ is the Debye wavelength, and $Z(\xi)$ is the plasma dispersion function tabulated by Fried and Conte.[1]

Three solutions of this dispersion equation are shown in Fig. XI-25. The dispersion equation (1) is solved under the assumption that the frequency $\underline{\omega}$ is pure real. Complex values of the wave number $\underline{k} = k_r + jk_i$ are thus obtained. The quantity k_i is the growth rate of the convective instability which this beam-plasma system supports. It is plotted as a dotted line in Fig. XI-25. The real wave number k_r is plotted as a solid line.

When the plasma thermal velocity v_T is zero, the dispersion equation can be solved exactly to yield

$$\underline{k} = \frac{\omega}{v_o} - \frac{\omega_{pb}}{v_o}\,\frac{\omega}{\sqrt{\omega^2 - \omega_{pe}^2}}. \tag{2}$$

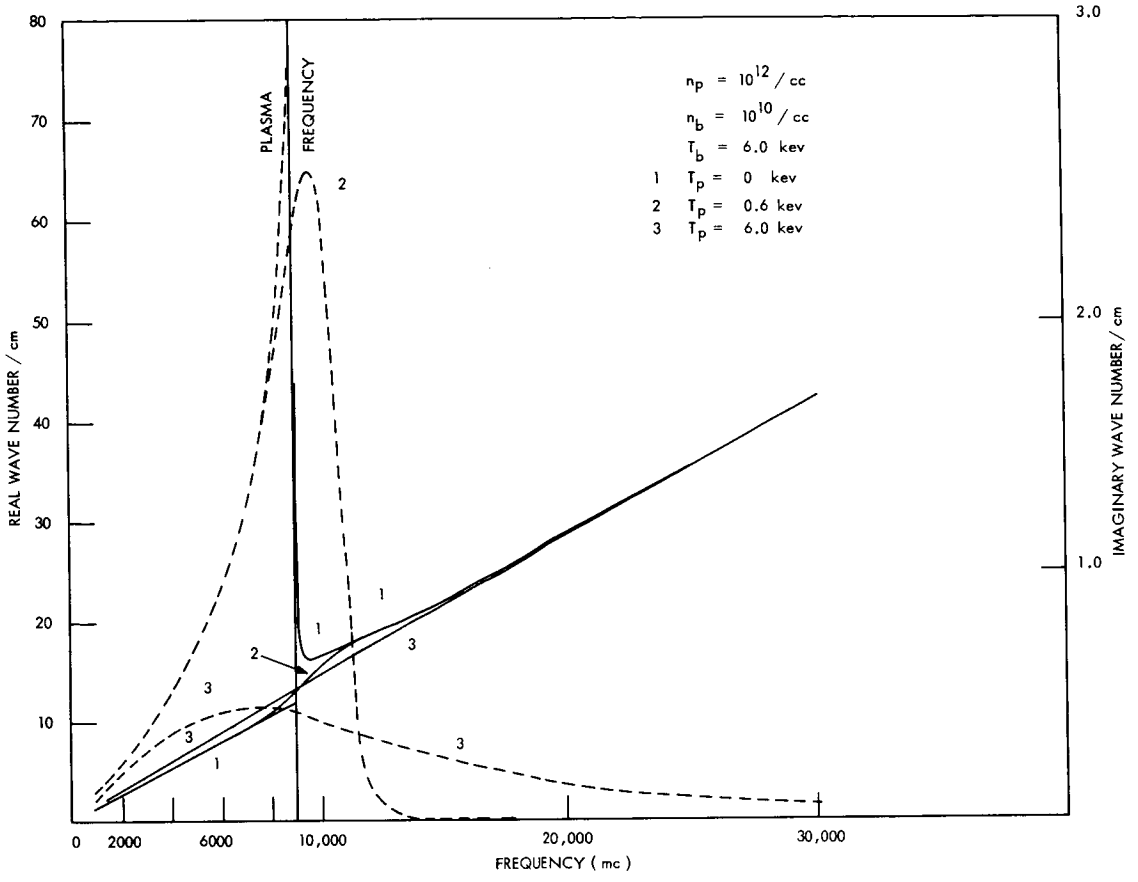

Fig. XI-25. Beam-plasma dispersion equation for longitudinal waves – Landau damping.

This well-known solution has an infinite growth rate k_i near $\omega = \omega_{pe}$. It is labeled (1) in Fig. XI-25.

The dotted curves labeled (2) and (3) in Fig. XI-25 are the corresponding growth rates when the electron thermal velocity v_T is finite. As v_T is increased, the gain k_i peaks at a finite value that decreases as v_T is increased. The frequency of maximum gain at first increases as v_T is initially increased from zero (curve (2)), but then decreases to fall below ω_{pe} for $v_T \gtrsim v_o$ (curve (3)). At the same time, the gain curve broadens as v_T is increased from zero. Physically, this broadening represents a kind of resistive medium amplification, in which the original "inductive" character of the plasma is diluted by a resistive component caused by the Landau damping in the plasma. As the thermal velocity v_T is increased above v_o, the peak gain $k_{i_{max}}$ must decrease, since the Landau damping of those plasma waves whose phase velocities coincide with v_o continually decreases.

2. Longitudinal Waves in a Cold-Ion, Hot-Electron Plasma

Consider now the dispersion equation

$$1 - \frac{\omega_{pi}^2}{\omega^2} - \frac{\omega_{pb}^2}{(\omega-\beta v_o)^2} + \frac{1}{k^2\lambda_D^2}\left[1 + \frac{1}{\sqrt{2}\,k\lambda_D}\frac{\omega}{\omega_{pe}} Z\left(\frac{1}{\sqrt{2}\,k\lambda_D}\frac{\omega}{\omega_{pe}}\right)\right] = 0 \tag{3}$$

in which the ions are now allowed to participate in the motion of the plasma. In the limit that the electron thermal velocity v_T is zero, this dispersion equation reduces to

$$1 - \frac{\omega_+^2}{\omega^2} - \frac{\omega_{pb}^2}{(\omega-\beta v_o)^2} = 0 \tag{4}$$

in which $\omega_+^2 = \omega_{pe}^2 + \omega_{pi}^2$, and ω_{pi} is the ion plasma frequency. Equation 4 has as its solution (2), in which ω_{pe}^2 is everywhere replaced by ω_+^2. Therefore, in the limit $v_T \to 0$, the gain is infinite for frequencies ω just below ω_+.

Consider now the limit $v_T \to \infty$. In this limit the dispersion equation (3) reduces to

$$1 - \frac{\omega_{pi}^2}{\omega^2} - \frac{\omega_{pb}^2}{(\omega-\beta v_o)^2} = 0 \tag{5}$$

which again has as its solution (2), in which ω_{pe}^2 is everywhere replaced by ω_{pi}^2. Therefore in the limit $v_T \to \infty$, the gain is infinite for frequencies ω just below ω_{pi}.

It is apparent from these considerations that a transition from a strong electron interaction to a strong ion interaction must occur as v_T is increased from zero. Briggs[2] considers this transition in a hot-electron plasma in which the electrons have a rectangular velocity distribution. He finds that an abrupt transition occurs when the parameter

$$\eta = \frac{n_b}{n_p}\frac{v_T^2}{2v_o^2} \tag{6}$$

is unity. For $\eta > 1$, a strong ion interaction occurs in which the gain is infinite for frequencies just below ω_{pi}. For $\eta < 1$, the ion interaction disappears, although the gain near the ion plasma frequency may still be finite.

In the weak beam limit $n_b \ll n_p$, the condition $\eta = 1$ requires $v_T \gg v_o$. Landau damping is small in this limit, so Briggs' results should hold for a Maxwellian hot-electron plasma. Figure XI-26 shows the exact solution of (3) in the weak beam limit. In Fig. XI-26a, $\eta = 1/2$ and no evidence of a strong ion interaction is apparent. Figure XI-26a is very similar to curve (3) of Fig. XI-25; that is, the gain mechanism in both curves is a resistive medium amplification.

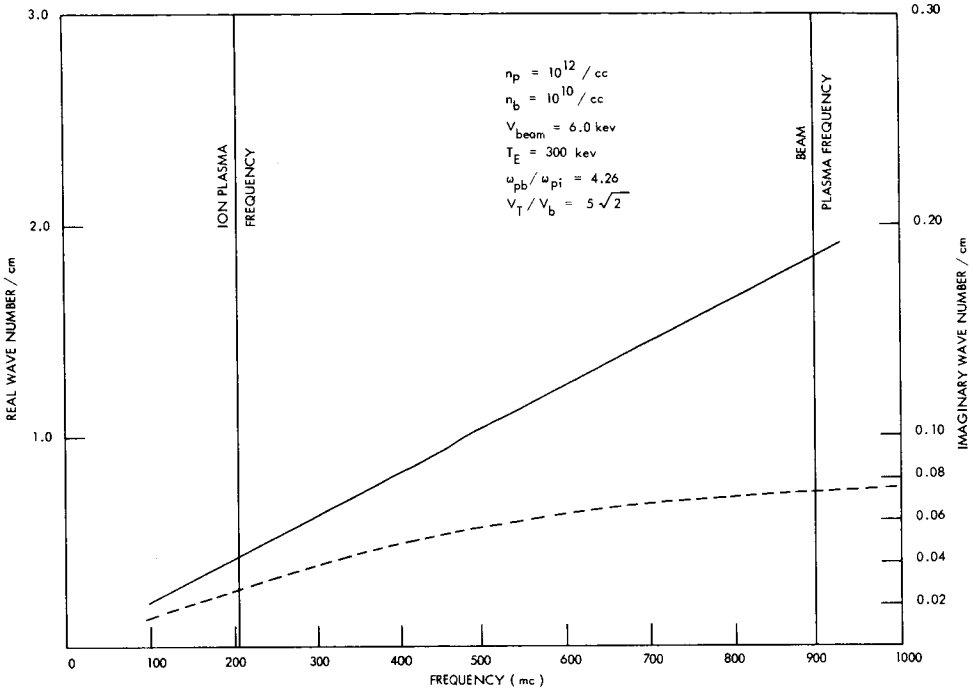

(a)

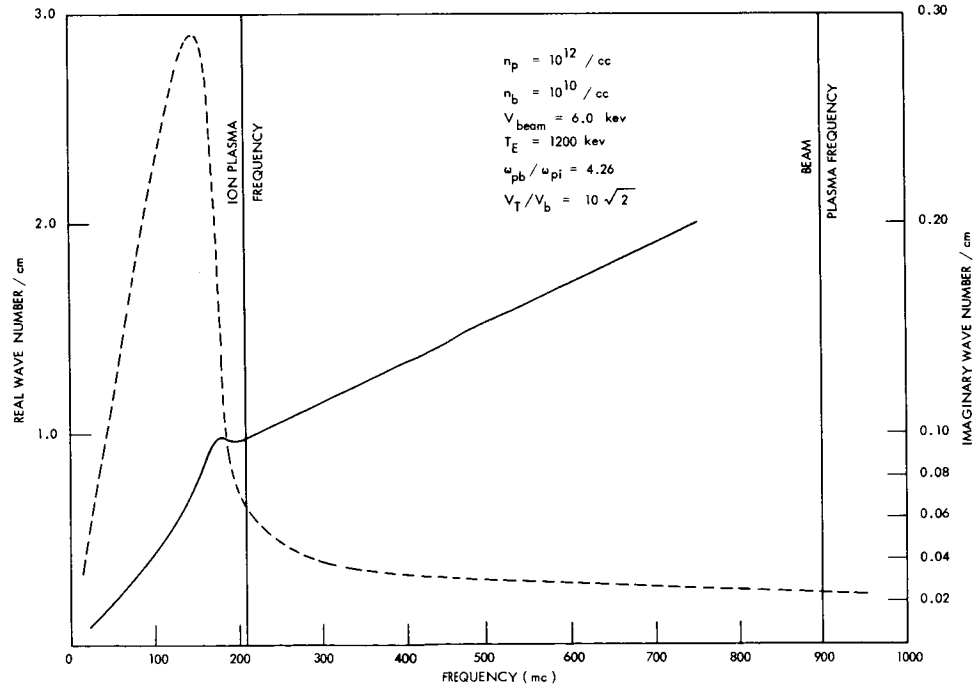

(b)

Fig. XV-26. Beam-plasma dispersion equation for longitudinal waves — Landau damping and ion motions included. (a) $\eta = 1/2$. (b) $\eta = 2$.

Figure XI-26b shows the case $\eta = 2$, for which Briggs' condition predicts a strong ion interaction. Such an interaction is indeed observed, although the gain is not infinite near the ion plasma frequency. The gain mechanism is clearly an interaction of the beam with the inductive plasma ions, degraded by the slight amount of Landau damping still present in the plasma. As η is further increased, the maximum gain near the ion plasma frequency must rapidly increase and tend to infinity as $\eta \to \infty$.

M. A. Lieberman

References

1. B. Fried and S. Conte, The Plasma Dispersion Function (Academic Press, New York, 1961).
2. R. J. Briggs, Electron-Stream Interaction with Plasmas (The M. I. T. Press, Cambridge, Mass., 1964).

E. NONADIABATIC DIFFUSION IN TOROIDAL GEOMETRY*

Construction of the toroidal device discussed in Quarterly Progress Reports No. 77 (pages 164-167) and No. 78 (pages 126-127) is nearly complete and tests are under way

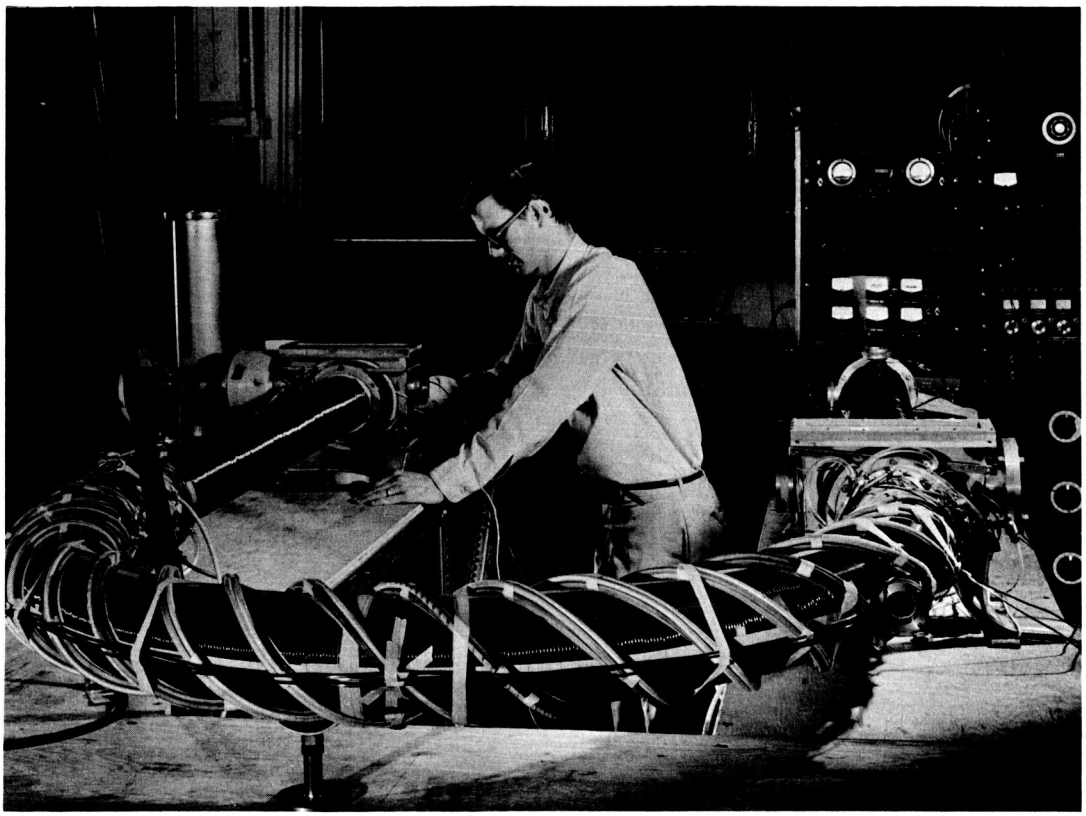

Fig. XI-27. Device for trapping an electron beam.

to determine the performance of one section of the device.

Figure XI-27 shows the device with one U bend removed for performance tests of the other U bend. These tests are performed by injecting an electron beam parallel to the field in the first straight section and observing visually the beam location at the entrance to the U bend by means of a fluorescent coated wire mesh that intercepts approximately 25 per cent of the beam. The beam is detected at the other end of the U bend by a fluorescent coated glass screen.

*This work was supported principally by the U.S. Atomic Energy Commission under Contract AT(30-1)-3285.

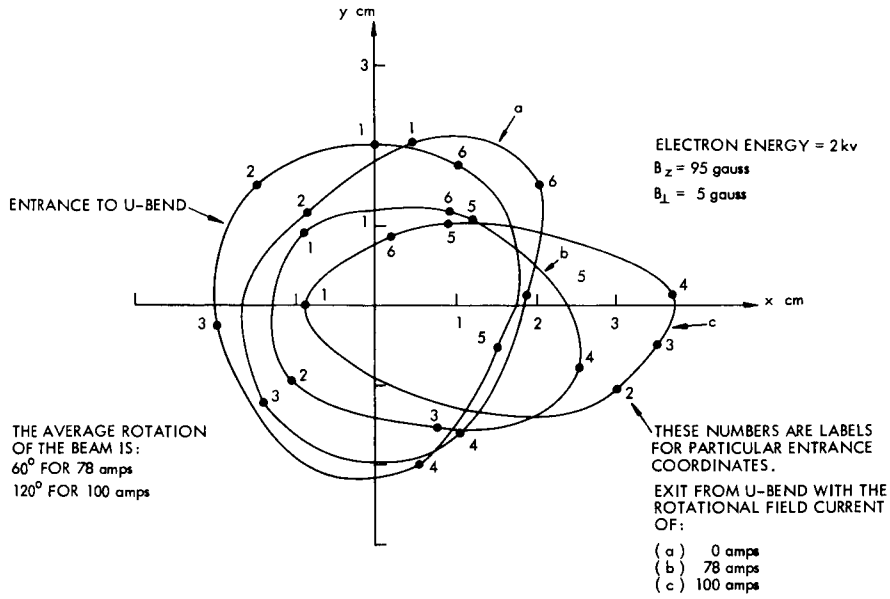

Fig. XI-28. Measured location of the input and output of the beam.

Figure XI-28 shows the location of the input and exit beams for various values of the rotational field. A vertical field, $B_\perp$, was produced on the U bend to just cancel the centripetal drift.

R. W. Moir, L. M. Lidsky

F. MEASUREMENT OF OPTICAL GAIN OF THE HOLLOW-CATHODE DISCHARGE*

Attempts by Edmonds, Gerry, and Lidsky[1] to observe laser action in a suitably configured argon hollow-cathode discharge (HCD) met with no success.

An experiment is in progress to measure directly the optical gain of the argon HCD at various wavelengths, including 4880Å and 5150Å. Our method is to direct a modulated light beam of the wavelength to be measured so that it passes axially through the HCD. The HCD is also modulated, but at a different frequency. Optical gain or absorption is manifested by an alternating component in the emergent light beam at frequencies equal to the sum and difference of the modulation frequencies of the HCD and incident light.

Preliminary results at 4880Å and 5150Å, obtained with the HCD of Edmonds, Gerry, and Lidsky, show no gain in excess of 0.1 per cent. The method indicates absorptions of 7 per cent 4804Å and 3 per cent at 4734Å.

M. D. Lubin

References

1. P. H. Edmonds, E. T. Gerry, and L. M. Lidsky, "The Hollow-Cathode Discharge as a Laser," Quarterly Progress Report No. 76, Research Laboratory of Electronics, M.I.T., January 15, 1965, pp. 129-130.

*This work was supported principally by the U.S. Atomic Energy Commission under Contract AT(30-1)-3285.

G. INTERACTION OF PARTICLES WITH CIRCULARLY POLARIZED WAVES IN PLASMAS*

The waves under discussion in this report are the right- and left-hand polarized waves moving with phase velocities very much less than that of light that appear in regions 8, 10, and 12 of the Allis diagram.[1] These are the regions in which one would expect the maximum wave activity in galactic plasmas on the basis of present density and magnetic field data. For such waves the ordinary linear dispersion relation can be written[2]

$$D_{LR} = k^2c^2 - \omega^2 - \frac{\omega_p^2 \omega \pi}{n_s} \int_{-\infty}^{\infty} dv_{||} \int_0^{\infty} v_\perp^2 \, dv_\perp \frac{\left\{ \frac{\partial F}{\partial v} - \frac{v_{||}}{v_p} \frac{\partial F}{\partial v_\perp} + \frac{v_\perp}{v} \frac{\partial F}{\partial v_{||}} \right\}}{(\omega - \omega_o - kv_{||})} = 0, \tag{1}$$

where v_p is the wave phase velocity, and ω_o is the gyro frequency.

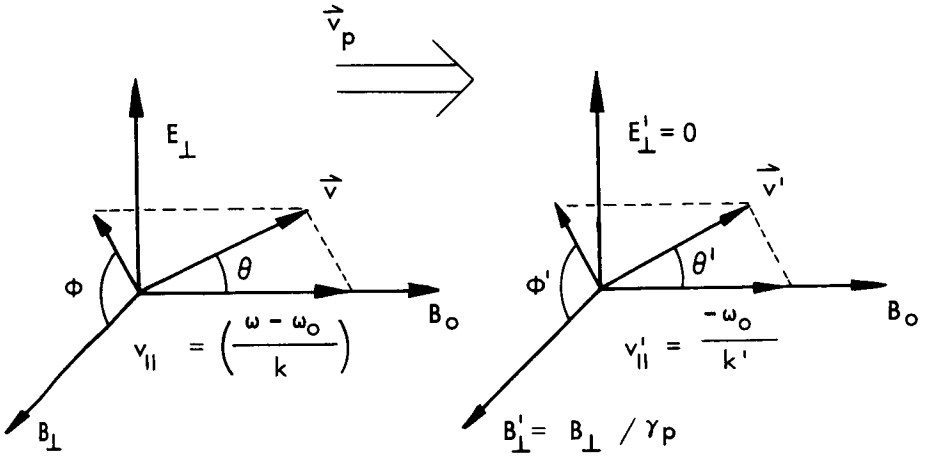

Fig. XI-29. Phase frame transform.

It is apparent that the growth or damping of such a wave depends on a group of resonant particles whose velocity parallel to the main magnetic field is

*This work was supported principally by the U.S. Atomic Energy Commission under Contract AT(30-1)-3285.

$$v_{\parallel} = \frac{(\omega-\omega_o)}{k}. \tag{2}$$

This is usually explained by observing that these particles see a Doppler-shifted local cyclotron resonance frequency and experience a cyclotron acceleration or deceleration. This is intuitively satisfying, since it presents an image of an efficient energy-transfer mechanism between the waves and the resonant particles. As a matter of fact, this picture is misleading because in the actual case the energy transfer is small, bounded, and periodic. This is easily seen by noting that for these waves propagating principally along the main magnetic field a velocity transformation exists which eliminates the wave electric field and reduces the wave to a periodic spatial magnetic field perturbation.[3] This transformation to the frame moving with the phase velocity of the wave is shown in Fig. XI-29, along with the resonant velocities in the two frames. It is seen that the resonance condition in the laboratory frame reduces to the condition for nonadiabatic motion in the phase frame.

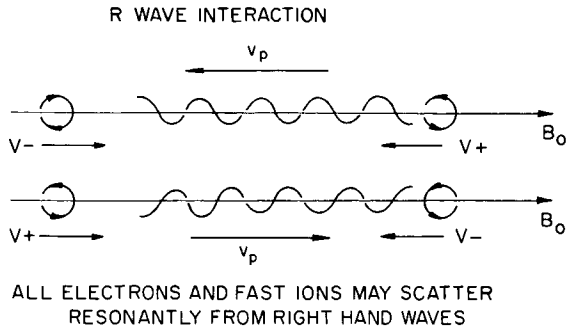

Fig. XI-30. Right-hand wave interaction.

Figure XI-30 represents two oppositely propagating right-hand polarized waves in the phase frame. The spiral line represents the locus of the end of the wave's magnetic field vector. It is also the orbit of a resonant particle. The only possible interaction in this frame is a rotation of the particle's total velocity vector. Consequently, we can represent the laboratory energy transfer in terms of the angular scattering in the variable θ' (defined in Fig. XI-29).

The laboratory energy change is

$$\frac{\Delta W}{W} \approx 2\beta\beta_p \Delta(\cos\theta'), \tag{3}$$

where $\beta = v/c$, and $\beta_p = \omega/kc$. That the energy transfer is small is seen from the fact that $\beta_p \ll 1$. That the energy transfer is periodic is seen from the equations of motion. Roberts and Buchsbaum[4] have shown that

$$W(t) = W(0) + mv_p(v(t)-v(0)), \tag{4}$$

where m is the relativistic mass, and the equation is relativistically correct. Physically, the wave magnetic field accelerates the resonant particles along the main field direction. Thus the resonant particles gain energy only while they are approaching the wave phase velocity. Resonant particles at the phase velocity interact only by virtue of

their perpendicular velocities and are decelerated in the direction of the main field, thereby reversing the energy transfer.

Another way of looking at the interaction is to notice that the ratio of wave magnetic force to wave electric force for the resonant particles is

$$(F_B/F_E) = \left(1 - \frac{\omega_o}{\omega}\right) \gg 1. \tag{5}$$

The wave magnetic field destroys the particle's phase correlation with the wave electric field.

Let us now consider the change in the particle's distribution function because of the passage of one wave. To do so, we first calculate the average change in the perpendicular velocity of a particle interacting with the wave in the phase frame. We can write Newton's equation in the form

$$\frac{dv'_+}{dz} - j\left(\frac{\omega_o}{v'_z}\right) v'_+ = j\omega_+(z), \tag{6}$$

where $v_+ = v_x + jv_y$, and $\omega_+ = \frac{q}{mc}(B_x + jB_y)$. The prime refers to the moving frame (Fig. XI-29).

If we assume that for the great majority of particles the change in z velocity is small, we find the immediate solution

$$\Delta v'_+ = j \int_{-L}^{L} \omega_+(z') \exp\left(-j \frac{\omega_o z'}{v'_z}\right) dz', \tag{7}$$

where $\Delta v'_+$ is the wave induced change in the perpendicular velocity of the particle between L and -L. Since all initial phases are assumed to be present, the average change in this quantity is

$$\left\langle \Delta v'_+ \right\rangle = \frac{1}{2\pi} \int_0^{2\pi} d\phi'_o \, (\Delta v'_+) = 0. \tag{8}$$

The mean-square change

$$\left\langle (\Delta v'_\perp)^2 \right\rangle = \left| \int_{-L}^{L} \omega_+(z') \exp\left(j \frac{\omega_o z'}{v'_z}\right) dz' \right|^2 \tag{9}$$

is finite, however, and constitutes a diffusion coefficient for the particle's perpendicular velocity. Since the total velocity is constant in the phase frame, this can easily be related to the diffusion coefficient in θ'.

Equation 9 can be written in terms of the wave spectra by Fourier-transforming $\omega_+(z)$. We find

$$\left\langle (\Delta v_\perp')^2 \right\rangle = \frac{2}{\pi} \left| \int_{-\infty}^{\infty} dk\, \omega_+^F(k) \frac{\sin\left(k - \frac{\omega_o}{v_z'}\right) L}{\left(k - \frac{\omega_o}{v_z'}\right)} \right|^2 . \tag{10}$$

If L is large, the second factor in the integral oscillates rapidly, and we may replace it by a delta function in $\left(k - \frac{\omega_o}{v_z'}\right)$. Thus we arrive at the final result for the diffusion coefficient as a function of the wave spectra

$$\left\langle (\Delta v_\perp')^2 \right\rangle = \frac{2}{\pi} \left| \omega_+^F \left(\frac{\omega_o}{v_z'}\right) \right|^2 . \tag{11}$$

This coefficient has broad application. The change in the particle's distribution function resulting from the passage of a wave is given by

$$\Delta f = \frac{1}{v_\perp} \frac{\partial}{\partial v_\perp} v_\perp \left\langle \frac{(\Delta v_\perp)^2}{v^2} \right\rangle \frac{\partial}{\partial v_\perp} f. \tag{12}$$

This shows the relaxation effect that the waves produce in the particle distribution. It is interesting to note that Eq. 12 is identical with the result of a quasi-linear calculation by Engel.[2]

We have already shown how the energy transferred in a wave-particle collision can be expressed in terms of the angular scattering in the phase frame. The mean-square energy transfer is

$$\left\langle \left(\frac{\Delta W}{W}\right)^2 \right\rangle = \frac{8}{\pi} \beta^2 \beta_p^2 \left(\frac{v_\perp'}{v_z'}\right)^2 \frac{\left| \omega_+^F \left(\frac{\omega_o}{v_z'}\right) \right|^2}{v^2} . \tag{13}$$

Employing Eq. 13, one can obtain a statistical acceleration mechanism for cosmic rays. One can also obtain a diffusion coefficient for the guiding centers of cosmic ray particles. Assuming that the wave size is small compared with the Larmor radius of the cosmic ray, one can write this coefficient

$$\left\langle (\Delta r_g)^2 \right\rangle \approx r_L \left\langle (\Delta\theta)^2 \right\rangle$$

or

$$\left\langle (\Delta r_g)^2 \right\rangle \approx \frac{v^2}{\omega_o^2} \left(\frac{v_\perp}{v_z}\right)^2 \left\langle \left(\frac{\Delta v_\perp}{v}\right)^2 \right\rangle .$$

Such guiding-center diffusion has been invoked by Davis[5] to explain the isotropy of cosmic rays.

Finally, a number of authors have suggested wave-particle scattering to explain the form of the radiation belts.[6-9] The diffusion coefficients obtained here should also apply to the description of the dynamics of this region.

Report XI-H summarizes an application of the diffusion coefficient to the confinement of particles in static nonadiabatic magnetic fields. By bearing in mind the analogy established above between motion in a static nonadiabatic field and wave-particle interaction, the results given in Sec. XI-H have relevance to the subject of the present report.

J. F. Clarke

References

1. W. P. Allis, S. J. Buchsbaum, and A. Bers, Waves in Anisotropic Plasmas (The M. I. T. Press, Cambridge, Mass., 1963), p. 38.
2. R. Engel, Phys. Fluids 8, 939 (1965).
3. J. F. Clarke, Quarterly Progress Report No. 78, Research Laboratory of Electronics, M. I. T., July 15, 1965, pp. 128-130.
4. L. J. Roberts and S. J. Buchsbaum, Phys. Rev. 135, A381 (1964).
5. L. Davis, Phys. Rev. 101, 351 (1956).
6. D. Wentzel, J. Geophys. Res. 66, 359 (1961).
7. A. J. Dragt, J. Geophys. Res. 66, 1641 (1961).
8. E. N. Parker, J. Geophys. Res. 66, 2673 (1961).
9. J. W. Dungey, Planet Space Sci. II, 591 (1963).

H. NONADIABATIC MAGNETIC TRAPS*

The diffusion coefficient developed in Sec. XI-G can be applied to a study of the relative efficiency of the nonadiabatic traps that are proposed for accumulating a thermonuclear plasma. Three basic types of nonadiabatic fields have been proposed.[1-3] In the complex notation $A+ = A_x + jA_y$, these fields can be represented by

$$\omega_+(z) = \omega_\perp \cos k_o z \qquad -L < z < +L \tag{1a}$$

$$\omega_+(z) = \frac{\omega_\perp}{2} e^{jk_o z} \qquad -L < z < +L \tag{1b}$$

$$\omega_+(z) = \omega_\perp \delta(k_o z), \tag{1c}$$

where k_o satisfies the resonance condition $k_o = \omega_o / v_z^0$ for some resonant velocity v_z^0.

Perturbation (1a) constitutes an axially symmetric field, (1b) a helically symmetric field, and (1c) an impulsive change in the field equivalent to a standing shock wave. This group can be extended by requiring that the resonance condition be satisfied at every point on the particle's orbit. That is, the trap is designed to have a variable wavelength. Each of these variations can be compared in terms of the mean-square step in magnetic moment, which a trapped particle makes on traversing the perturbation. This mean-square step is simply related to the diffusion coefficient given in Sec. XI-G.

Consider the Fourier transforms of the perturbations

$$\omega_+^F(k) = \frac{\omega_\perp}{\sqrt{2\pi}} \left\{ \frac{\sin (k_o - k)L}{(k_o - k)} + \frac{\sin (k_o + k)L}{(k_o + k)} \right\} \tag{2a}$$

$$\omega_+^F(k) = \frac{\omega_\perp}{\sqrt{2\pi}} \frac{\sin (k_o - k)L}{(k_o - k)} \tag{2b}$$

$$\omega_+^F(k) = \frac{1}{\sqrt{2\pi}} \frac{\omega_\perp}{k_o}. \tag{2c}$$

From the diffusion coefficient

$$\left\langle \left(\frac{\Delta v_\perp}{v} \right)^2 \right\rangle = \left| \int_{-\infty}^{+\infty} dk\, \omega_+^F(k) \frac{\sin \left(k - \frac{\omega_o}{v_z} \right) L}{\left(k - \frac{\omega_o}{v_z} \right)} \right|^2 \tag{3}$$

---

*This work was supported principally by the U.S. Atomic Energy Commission under Contract AT(30-1)-3285.

we see that the magnetic moments of the particles will have large changes only when the two factors in the integral overlap appreciably.

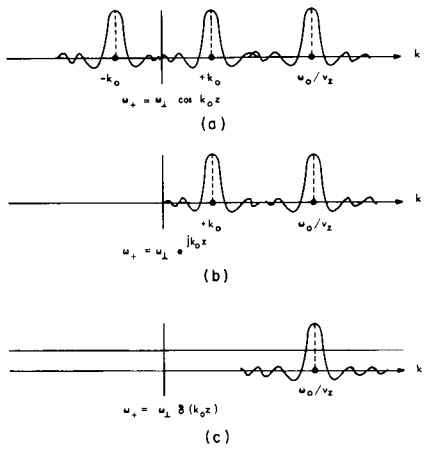

Fig. XI-31. Diffusion coefficient factors in k space.

Figure XI-31 shows graphically the situation for the three perturbations. The initial trapping occurs when $v_z = v_z^0$, and the functions on the positive k axis merge. For trapped particles, there can never be a complete superposition, since some of their initial axial velocity, v_z^0, has been transformed to perpendicular velocity. The net scattering comes from the overlapping of the wings of the peaks. It becomes immediately clear that on the reverse transit through the perturbation, when the ω_o/v_z peak lies on the negative k axis, the rotating perturbation is far superior to the axial symmetric one. Furthermore, the resonant nonadiabatic systems are superior to the nonresonant because in the latter case all velocities interact by the same amount and independently of their direction of motion.

It is also interesting to note the height and breadth of the k_o resonance peaks in Fig. XI-31. The peak height is $\omega_\perp L/2\pi$ and its width is $2\pi/L$. Now, considering the fact that for an untuned system $k_o = 2\pi N/L$, we see that as the system becomes longer and the particle interacts with more periods of the perturbation, the peaks grow in height and become narrower. All of this is in agreement with the physical argument presented by Wingerson, Dupree, and Rose[4] and the numerical calculations of Laing and Robson.[5]

We turn now to a final example of the use of the diffusion coefficient. Wingerson, Dupree, and Rose conclude that a long highly tuned system, in which the perturbation field goes gradually to zero at both ends, would constitute the optimum trap. We can examine such a trap analytically.

Let us consider a trap in which the perturbation wavelength lengthens as z decreases. For simplicity, choose a wave number

$$k_{eff} = k_o + k_1^2 z \tag{4}$$

and a Gaussian envelope to damp the perturbations away from the origin

$$\omega_+(z) = \frac{\omega_\perp}{2} e^{-\gamma^2 z^2} \exp\left[\left(k_o + k_1^2 z\right) z\right] \tag{5}$$

In the light of Sec. XI-G, this is the phase-frame form of a wave packet. The Fourier transform of this function is

$$\omega_+^F(k) = \frac{\omega_\perp}{8} \frac{\exp\left[-\gamma^2 \frac{(k_o-k)^2}{4\left(\gamma^4+k_1^4\right)} + j \frac{k_1^2(k_o-k)^2}{4\left(\gamma^4+k_1^4\right)}\right]}{\left(\gamma^2-jk_1^2\right)^{1/4}}. \tag{6}$$

Since our Gaussian envelope damps the wave, we can take $L \to \infty$ in the integration of the diffusion coefficient. This is equivalent to replacing the sine factor by a delta function. Then the diffusion coefficient reduces to a term proportional to the square of Eq. 6 with k replaced by ω_o/v_z. Note that the damping coefficient and the increasing wavelength coefficient appear in "parallel" in this expression. This illustrates the physical point that both damping and tuning decrease the scatter of nonresonant particles. These particles rotate faster or slower than the perturbation field, and the scattering from each field peak tends to be cancelled by the next peak. Only the last peak scatter has full effect, and the damping reduces this to a low level. Tuning reduces the resonance volume in phase space which is available to particles. In terms of Fig. XI-31, the central peak is narrowed.

To simplify the expression, let us assume that the damping length is large compared as with a wavelength, and that the change in wavelength is small compared with a wavelength. Choosing N wavelengths in our perturbation, we can set

$$\gamma = \frac{k_o}{N} \tag{7a}$$

and

$$k_1 = \frac{k_o}{N}. \tag{7b}$$

The diffusion coefficient simplifies to

$$\left\langle \left(\frac{\Delta v_\perp}{v}\right)^2 \right\rangle = \frac{1}{2} \frac{v_z^{0^2}}{v^2} \left|\left(\frac{\omega_+}{\omega_o}\right)\right|^2 \frac{N^2}{4} \exp\left[-\frac{N^2}{8}\left(1-\frac{v_z^0}{v_z}\right)^2\right]. \tag{8}$$

This expression illustrates the sharpness of the resonance peak.

In conclusion, we find that the physical arguments presented by Wingerson, Dupree, and Rose are in full agreement with calculations performed with the simplified diffusion coefficient derived in Sec. XI-G. An experimental study of this nonadiabatic scattering phenomenon is underway.

J. F. Clarke

References

1. K. D. Sinenikov et al., Soviet Phys. – Tech. Phys. 5, 236 (1960A).
2. R. C. Wingerson, Phys. Rev. Letters 6, 446 (1961).
3. R. C. Wingerson, T. H. Dupree, and D. J. Rose, Phys. Fluids 7, 1475 (1964).
4. E. W. Laing and A. E. Robson, J. Nucl. Energy (Part C, Plasma Phys.) 3, 146 (1961).

I. STUDY OF LASER RADIATION THOMSON-SCATTERED BY AN ELECTRON BEAM*

The present experiment is concerned with the dependence on angle of the frequency of laser light that is Thomson-scattered by a relativistic electron beam. Preliminary calculations had led us to believe that if the laser beam intersects the electron beam at 90° and the angle of observation from the electron beam is 90°, then the relativistic transformations from the laboratory frame of the laser beam to the moving frame of the electron beam and back to the laboratory frame of the observation system would result in a factor of γ^2 $\left(\gamma = \left(1 - \frac{v^2}{c^2}\right)^{-1/2}\right)$ in the frequency relation. Thus even when the Doppler shift that is associated with advancing sources (the "normal" shift) is absent, there will be a shift from the laser wavelength of 2 per cent if the beam voltage is 5 kilovolts. An exact examination of the relativistic and normal Doppler transformations shows that, instead of γ^2, the correct factor is unity when the normal shift is zero. Furthermore, the total relativistic transformation from the laboratory frame of the laser to the beam frame and then into the laboratory frame of the observation system is identical to the normal Doppler transformation.

Straightforward calculations of the number of photons scattered by the electron beam, with the Thomson scattering cross section used and the radiation treated as if it were in the form of particles colliding with the electrons and then scattered in all directions, show that in order to have reasonably good statistics the electron beam must have a density greater than 5×10^{10} electrons/cm^3. This value is true for the 50-joule ruby laser used in the experiment when it has been focussed to make a beam of 1 mm diameter. A density such as this corresponds to a beam current of 200 ma at 3 kv if the beam diameter is 1 mm. The number of photons in the incident laser beam is $\approx 10^{20}$, and the number scattered is only 10^5, while the number collected by the observation system is ≈ 500. These 500 photons pass through an interference filter that will pass only radiation whose wavelength lies in a 5Å interval. From there they hit the cathode of a very sensitive photomultiplier and produce photoelectrons with an efficiency of only 2 per cent. With only 10 photoelectrons in each laser shot it is plain that several shots are necessary at each angle and frequency to get good results.

Thus far, an electron gun of the Pierce type has been constructed and after experiencing difficulties in design it eventually evolved to the point where it produces a well-defined beam of about 1 mm in diameter at 200 ma and 3 kv. The gun has a microperveance of 3, and can be operated so that there is no power dissipated in the anode. The

*This work was supported principally by the U.S. Atomic Energy Commission under Contract AT(30-1)-3285.

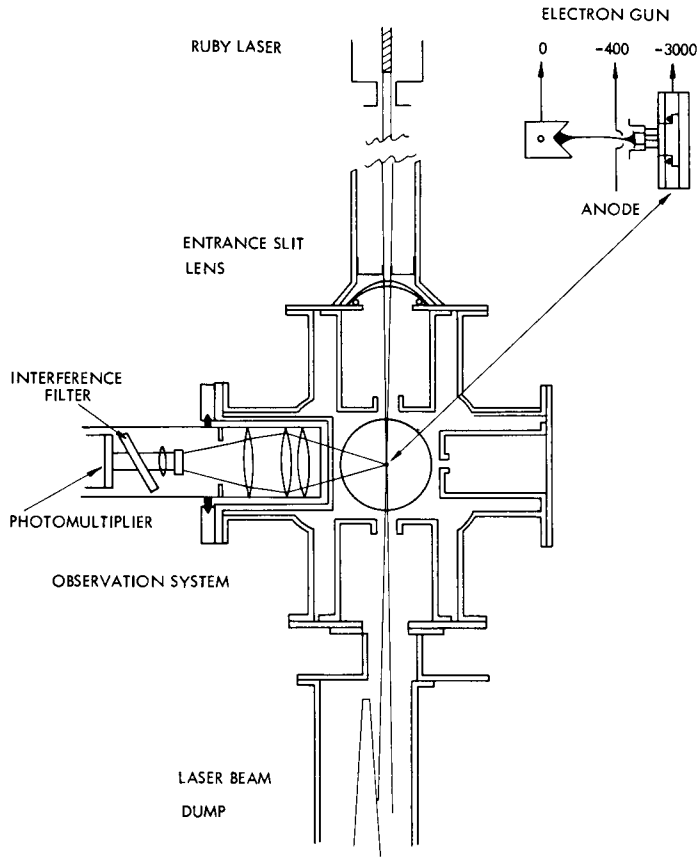

Fig. XI-32. Illustrating the experimental arrangement.

operating pressure is 1×10^{-6} torr, and beam operation is very stable. Also, an observation system was designed and built to cover as large a solid angle as was compatible with frequency spread and vacuum can space requirements. The system can be scanned from an angle of 90° to 70° from the electron beam direction of motion. The arrangement of the various parts of the experiment is shown in Fig. XI-32.

The problem of the reflection of laser light into the observation system has been overcome by the use of special light dumps and aperture stops. The experiment is now under way and it is anticipated that it will be almost completed by December 31, 1965. The electron beam, laser beam, and viewing system have all been operated separately, and trial results are now being obtained and the signal-to-noise in the experiment (the crucial problem here) appears to be satisfactorily low.

M. A. Samis

J. INCOHERENT SCATTERING OF LIGHT FROM A PLASMA. II.*

In Quarterly Progress Report No. 78 (pages 131-135) we reported signal-to-noise calculations for the cooperative scattering effects at small scattering angles of visible laser light from a plasma discharge.[1] Noise measurements of the light emission from the plasma indicated that by using an Argon ion laser of sufficient optical power (tens of watts) one could experimentally undertake the measurement of the weak scattered-light spectrum. Nominal integration times would suffice for signal-to-noise, but the expected spectral width would be small, thereby limiting the attainable resolution. Also, the question of diffracted or otherwise stray laser light at small angles interfering with the scattered, Doppler-shifted wavelength was posed but not answered. Fortunately, this question will no longer arise with the new technique presented in this report.

We wish to report the adoption of a new laser, which was unknown at the time of submitting the last report. The modified experiment will now use an infrared laser developed by Patel of Bell Telephone Laboratories, Inc.[1] It is a nitrogen, carbon-dioxide laser yielding very high power output at 10.6 microns, utilizing closely coupled vibrational levels in N_2 and CO_2. A discharge of 4 kv/m and 50 ma DC, in a tube, ~8 ft long and 1 inch in diameter, with continuous gas flow (CO_2 pressure 0.4 torr, N_2 pressure 2 torr), reported by Patel has yielded up to 16 watts cw of 10.6-micron radiation, coupled out through a hole in one of the end mirrors. The intracavity power was several hundred watts.

An indication of benefits from adopting this laser can be seen from the following discussion. Analogous to the noise calculations of our previous report, we may calculate the equivalent noise powers for an experiment, using 10.6-micron radiation. Note that since the spectral width varies as $\lambda \sin\frac{\theta}{2}$, and that for observation of coherent effects $\frac{\lambda}{4\pi\lambda_D \sin\frac{\theta}{2}} \sim 1$, an increased wavelength (10.6 μ versus 0.5 μ) allows observation at very much larger angles, where λ is the incident wavelength, λ_D is the plasma Debye length, and θ is the scattering angle with respect to incident direction. At 0.5 μ one need work at $\theta = 2°$, leaving no latitude for angular scan, whereas at 10.6 μ one can scan to $\theta = 90°$. Two important features result: (i) a larger solid angle in the detector optics can be used, and (ii) a larger optical bandpass filter can be employed. Note also that detector efficiencies at 10.6 μ versus 0.5 μ (mercury doped germanium and photomultiplier, respectively) are ~100 per cent and ~10 per cent. Since signal-to-noise varies as $\sqrt{\Delta\Omega\Delta\lambda\epsilon}$, where $\Delta\Omega$ is the solid angle, $\Delta\lambda$ is the bandpass, ϵ is the quantum efficiency of the detector, a large increase is to be gained. In fact, the use of 10.6-μ radiation will yield a factor of

*This work was supported principally by the U.S. Atomic Energy Commission under Contract AT(30-1)-3285.

100 increase in signal-to-noise for scattered light versus plasma emission; consequently, the plasma itself will be essentially noise-free for an optical power input of

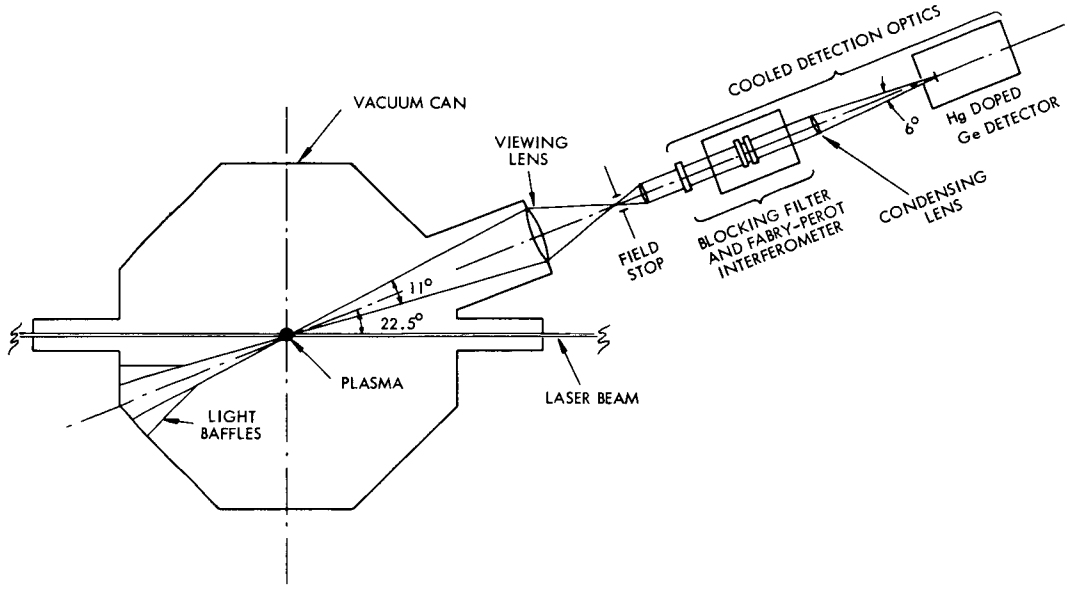

Fig. XI-33. Detection optics.

several watts. With reference to Fig. XI-33, the observational result of scattered radiation at 22.5° (with solid angle $\Delta\Omega = \pi \times 10^{-2}$ and bandpass $\Delta\lambda$ = 10 Å) for the hollow-cathode arc plasma ($n_e \sim 10^{14}/cm^3$, $Te \approx 4$ ev) in the worst case, is expected to be 4×10^{-16} Po watts, where Po is incident power. The calculated noise power from the arc, resulting chiefly from Bremsstrahlung is $10^{-15}(\Delta f)^{1/2}$ watts, where Δf is the bandwidth of receiver. Evidently, with several hundred watts incident power the plasma noise can be neglected.

In fact, the experimental noise to be contended with results from fluctuations in thermal black-body radiation at 300°K, the corresponding wavelength maximum occurring at 9.6 μ. Once again, referring to the geometry of the detection optics, we can calculate the noise power at 10.6 μ for the plasma vacuum wall and collection lenses at room temperature, and the remaining optics at dry-ice temperature (cooling results in a significant reduction of noise). The detector (an Hg doped Ge solid-state device) $\approx 10^{-3}$ cm^2 in area, subtending a field of view of 6°, as a result, sees an equivalent noise power from all surfaces of $\sim 10^{-13}(\Delta f)^{1/2}$ watts. Only noise in a 10 Å bandpass from the vacuum wall and collector lenses emerges to the detector, and noise from emission by surfaces following the interferometer is nominally integrated over 10 μ. As a consequence, Po = 250 watts would yield signal-to-noise of unity for a 1-cps receiver bandwidth.

The laser arrangement is shown in Fig. XI-34. A hemispherical mirror mode will be employed with two 10 ft, 1-inch diameter, tubes of optically active media. The plasma

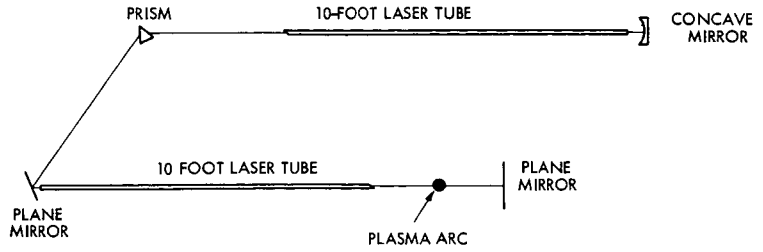

Fig. XI-34. Laser cavity arrangement.

will be placed inside the optical cavity and, with 20 ft of optical gain, the laser power available for scattering should be substantial. A prism is to be used for wavelength isolation; a half-dozen modes separated by 200 Å at 10.6 μ are normally present and are of no consequence to this experiment. The hemispherical mode not only provides efficient use of the laser volume for power generation but also, since the light focuses to a diffraction limited spot on the plane mirror, makes it possible to determine the desired beamwidth at the scattering point merely by positioning the plasma arc back from the plane mirror.

The laser beam will be chopped, and the scattered signal plus noise synchronously detected by using a PARL lock-in amplifier with low-noise preamplifiers. The output will be plotted on an X-Y recorder, with spectral scan achieved by varying the optical path in the Fabry-Perot interferometer (pressurizing with nitrogen). The spectral scan is to be 300 Å in 10 Å steps, to yield good resolution of the enhanced scattering effect that is sought.

A. A. Offenberger

References

1. C. K. N. Patel, Phys. Rev. Letters 13, 617 (1964).

XII. PLASMA MAGNETOHYDRODYNAMICS AND ENERGY CONVERSION*

Prof. G. A. Brown
Prof. R. S. Cooper
Prof. W. H. Heiser
Prof. M. A. Hoffman
Prof. W. D. Jackson
Prof. J. L. Kerrebrock
Prof. J. E. McCune
Prof. G. C. Oates
Prof. E. S. Pierson
Prof. A. H. Shapiro
Prof. R. E. Stickney

Dr. J. B. Heywood
R. Dethlefsen
K. R. Edwards
W. Engelmaier
J. W. Gadzuk
T. K. Gustafson
A. S. Kalelkar
R. F. Keating
G. B. Kliman
A. G. F. Kniazzeh
R. M. Logan
B. T. Lubin

M. A. Lutz
C. A. McNary
P. Ponthus
R. P. Porter
D. S. Shupe
C. V. Smith, Jr.
A. Solbes
R. J. Thome
J. C. Wissmiller
S. Yamamoto
G. W. Zeiders

A. STEAM-WATER CONDENSING EJECTOR TEST FACILITY

The use of a condensing ejector in a liquid-metal MHD power system has been previously reviewed by Brown.[1] Even though experimental performance data[2,3] for a steam-water condensing ejector has demonstrated the feasibility of obtaining exit stagnation pressures greater than either of the inlet stagnation pressures, data are lacking in the range of high area contraction ratios, high inlet vapor velocities and low flow-rate ratios. Brown has reviewed the need for these conditions in order to obtain high efficiency performance (based on an availability definition) from a condensing ejector. Thus, as previously reported,[1] a steam-water test facility was constructed to operate with the flow, geometry, and thermodynamic conditions required to yield operating efficiencies for a condensing ejector in the 60-70 per cent range.

The facility is represented schematically in Fig. XII-1.

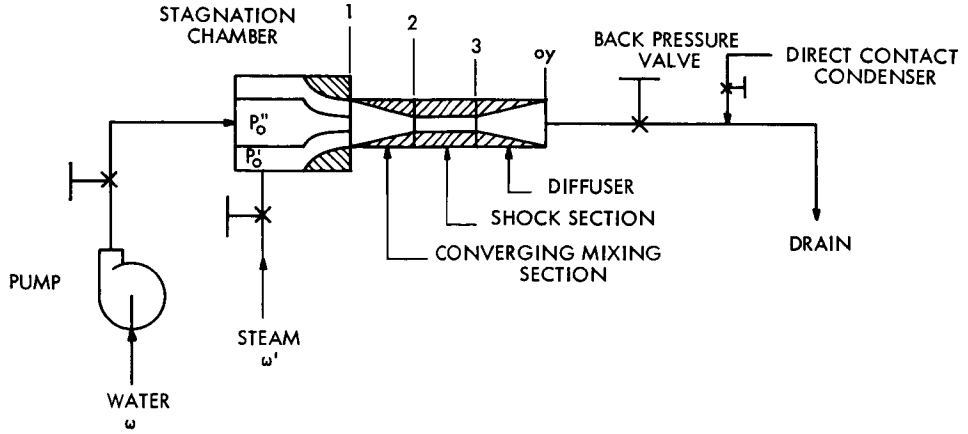

Fig. XII-1. Schematic diagram of the condensing ejector test facility.

*This work was supported principally by the U.S. Air Force (Research and Technology Division) under Contract AF33(615)-1083 with the Air Force Aero Propulsion Laboratory, Wright-Patterson Air Force Base, Ohio.

The facility has been designed with a large amount of flexibility so that both inlet and test sections can be replaced with a minimum of difficulty. Stagnation-pressure operation will be 50-180 psia, with a design flow-rate ratio of 2.73 and an area contraction ratio (A_1/A_2) of 11.0. Exit pressures (P_{0y}) of 400-800 psia should be theoretically obtainable.

In order to check out the facility, the previous tests[2] were repeated. The results of the new series of tests are shown in Fig. XII-2, in which the data of the other tests are included. These data cover a range liquid-to-steam flow ratio from 12 to 6.8. Figure XII-3 shows a comparison between the theoretical calculations for (P_{0y}/P_0'') and the experimental values obtained from the present facility. Agreement is within 10 per cent.

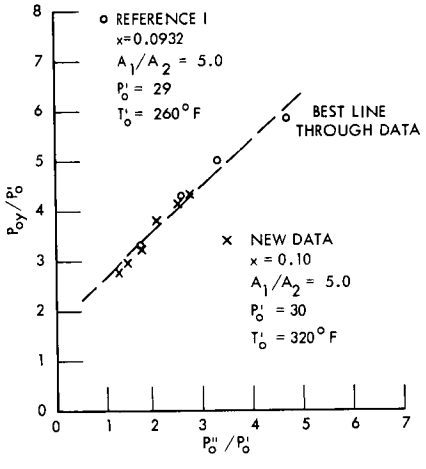

Fig. XII-2.

Experimental data: Exit stagnation pressure ratio vs inlet stagnation pressure ratio.

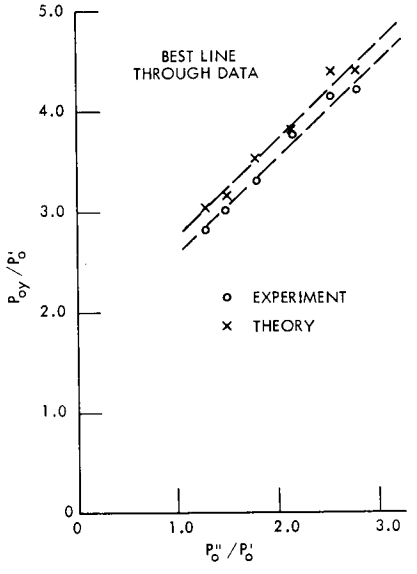

Fig. XII-3.

Theory and experiment: Exit stagnation pressure ratio vs inlet stagnation pressure ratio.

Our immediate concern in the test program is to improve the comparison between theoretical and experimental flow rates, as well as to carry out an enthalpy balance on the facility. Subsequent tests will then be undertaken with a test section having higher contraction ratio geometry and lower flow-rate ratios.

B. T. Lubin, G. A. Brown

References

1. G. A. Brown, "Magnetohydrodynamic Power Generation with Liquid Metals," Quarterly Progress Report No. 76, Research Laboratory of Electronics, M. I. T., January 15, 1965, pp. 149-153.

2. G. A. Brown, "An Analysis of NUOS Condensuctor Test Data with a New Theory for the Variable Area Condensuctor," Report 44, Joseph Kaye and Company, Inc., Cambridge, Mass., 1961.

3. J. Miguel and G. A. Brown, "An Analytical and Experimental Investigation of a Condensing Ejector with a Condensable Vapor," AIAA Paper 64-469, July 1964.

B. MAGNETOHYDRODYNAMIC CHANNEL FLOW VELOCITY PROFILES AND ENTRY LENGTH

Preliminary experiments were conducted with magnetohydrodynamic (MHD) channel flows to determine MHD entry lengths from pitot tube measurements of velocity profiles. The entry length – the length of flow in a magnetic field region required for full profile development – is important in the design of MHD power-generating equipment and in the interpretation of MHD friction factor measurements.

The pitot tube (length 0.9 inch, tip diameter 0.028 inch) shown in Fig. XII-4 was traversed across the 0.5-cm height of a 0.5 × 5 cm stainless-steel rectangular channel

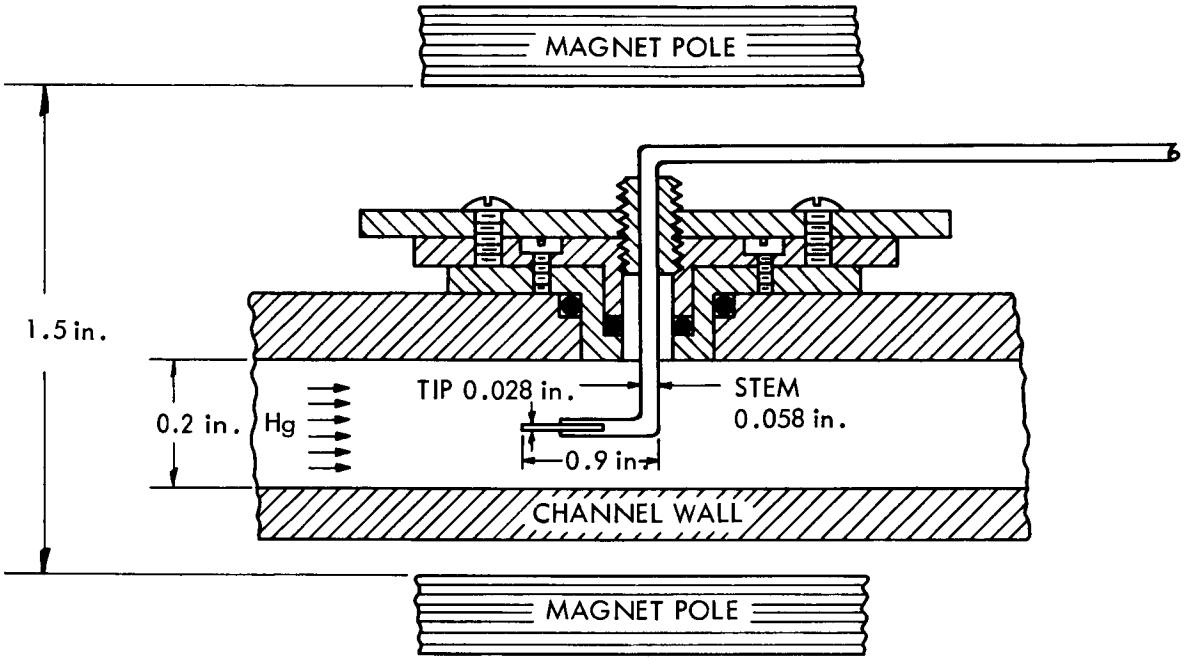

Fig. XII-4. Cross-section view of the pitot tube apparatus.

at a point 50 hydraulic diameters downstream of the channel entrance and 35 hydraulic diameters upstream of the exit. A magnet of length equivalent to 20 hydraulic diameters of the channel was located at several positions relative to the pitot tube as shown in Fig. XII-5. Velocities were computed from pressure measurements by using Bernoulli's equation.[1]

Figure XII-5 is a record of MHD profile development. At an approximately constant Reynolds number the velocity profile (drawn on an expanded scale) flattens as the field is brought from downstream of the pitot tube to a location where the field interacts with the fluid before the fluid reaches the pitot tube. In this flow an approximately fully

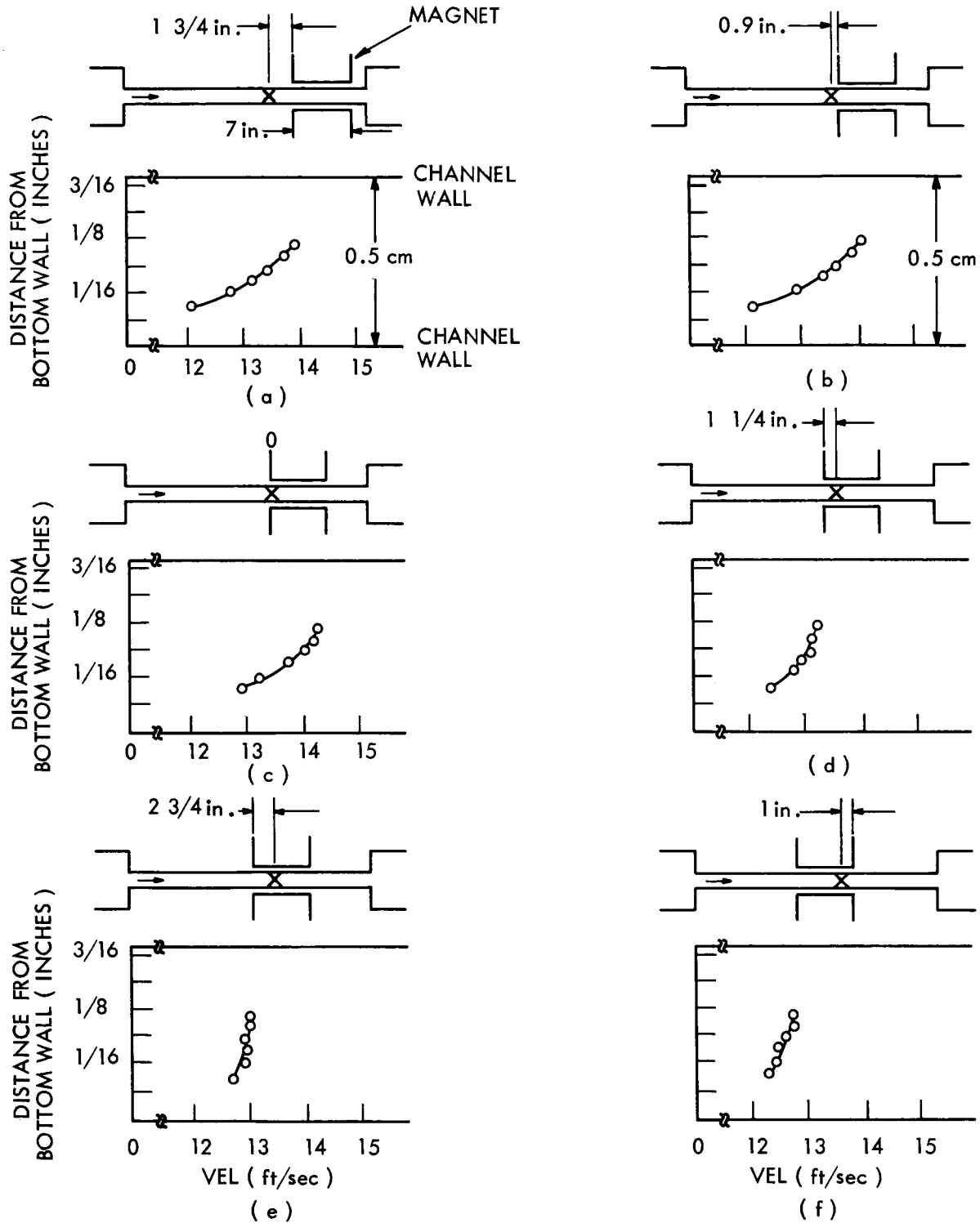

Fig. XII-5. Development of magnetohydrodynamic velocity profile ($M \approx 66$, $Re \approx 2.9 \times 10^5$).

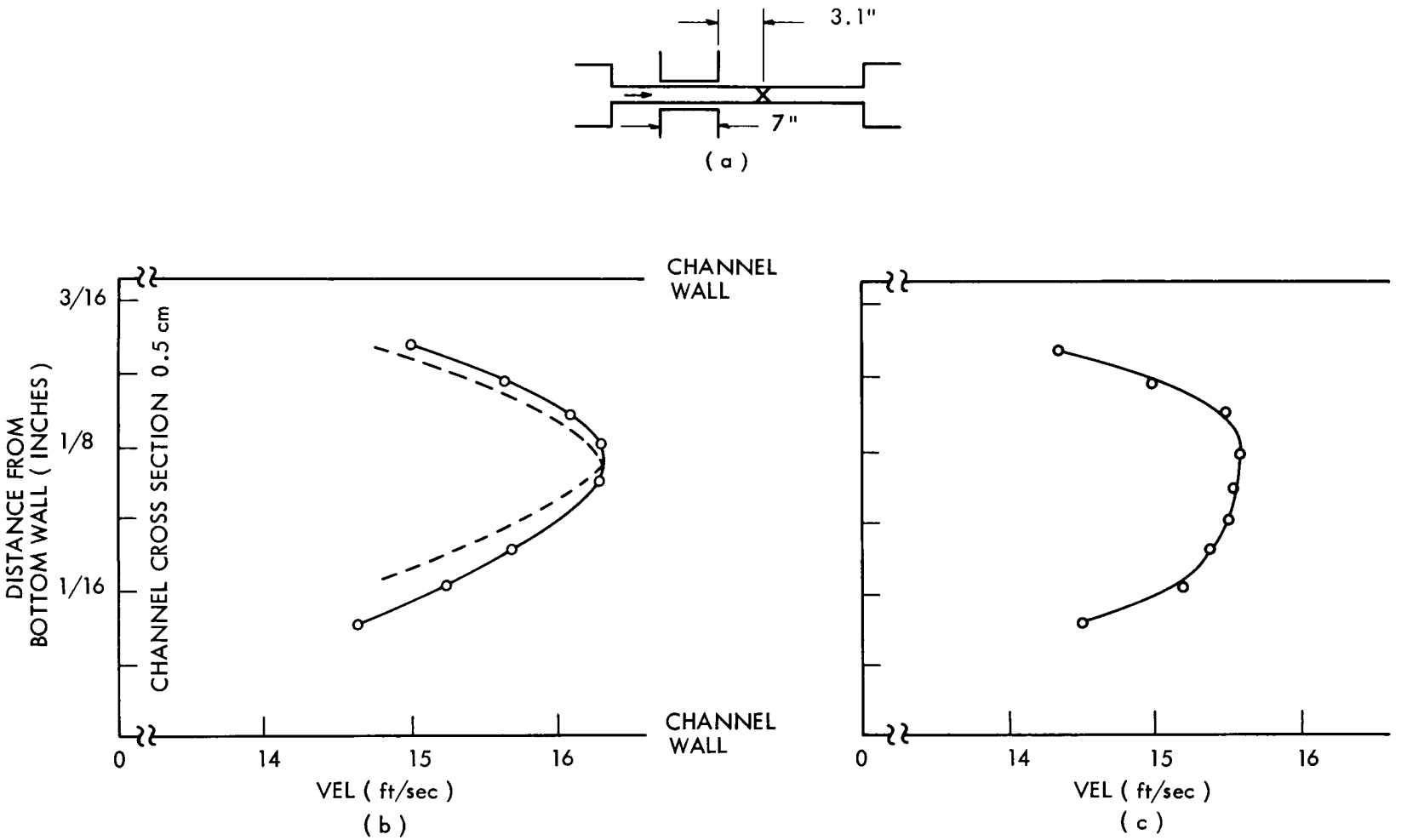

Fig. XII-6. Velocity profiles 3.1 inches downstream of field region. (a) Hg average flow velocity (15.6 ft/sec) from venturi measurements (M = 0 under magnet). (b) Hg average flow velocity (15.6 ft/sec) from venturi measurements (M = 70 under magnet).
o = Measured values.
- - - = $\frac{1}{7}$ th power law profile with $V_{max} = V_{max\ measured}$

developed turbulent stream of mercury at Reynolds number, $Re \approx 2.9 \times 10^5$, enters a magnetic field region having a Hartmann number, $M \approx 66$, with an MHD entry length of approximately 10 hydraulic diameters. The profile in Fig. XII-5a, with the field downstream of the pitot tube, is similar to the profile measured with no field.

The friction Reynolds number, R^*, based on friction velocity and channel half-height is approximately 4300 for the flow shown in Fig. XII-5. The ratio, M^2/R^*, is approximately 1. Harris[2] computed velocity profiles for turbulent MHD flows. Comparison of our measured profiles with the predicted profiles given by Harris shows qualitative agreement at $M^2/R^* = 1$.

A measured profile at zero field and a computed $\frac{1}{7}^{th}$ power law profile are shown in Fig. XII-6a. This profile has been slightly translated to account for probe misalignment. At a similar Reynolds number Fig. XII-6b shows an MHD profile 3.1 inches downstream of the magnetic field region. Some partial ordinary hydrodynamic recovery is observed in the MHD case. In these two flows, with the pitot tube mechanism not obstructed by the magnet, most of the channel could be traversed.

The small channel dimension that was studied, and the necessity of measuring static pressure at the channel wall limited the accuracy of individual profile data. The measurements, however, are adequate for showing the relative rate of profile development. Further work is planned and the preliminary observations reported here provide a clear indication that the MHD flow develops rapidly in a channel of uniform cross section when significant MHD forces are present.

S. Sachs, W. D. Jackson, G. A. Brown

References

1. D. A. East, "The Pitot Tube in a Magnetohydrodynamic Flow," Ph. D. Thesis, Department of Mechanical Engineering, Massachusetts Institute of Technology, September 1964.

2. L. P. Harris, Hydromagnetic Channel Flows (The Technology Press, Cambridge, Mass., and John Wiley and Sons, Inc., New York, 1960).

3. S. Sachs, "Magnetohydrodynamic Entry Lengths as Determined by Pitot Tube Velocity Profile Measurements," S. B. Thesis, Department of Mechanical Engineering, Massachusetts Institute of Technology, June 1965.

C. THERMIONIC EMISSION FROM A TUNGSTEN MONOCRYSTAL IN OXYGEN

1. Introduction

The purpose of this study is to determine the effect of the carbon impurities in tungsten filaments on the thermionic properties, and to investigate experimentally the electron emission from a single-crystal tungsten filament as a function of crystallographic direction, filament temperature, and oxygen pressure. Tungsten can be cleansed quite thoroughly because of its refractory properties which allow high flashing temperatures. This does not, however, eliminate the carbon impurities in tungsten. The technique for removing the carbon impurities from tungsten, found by Becker and his co-workers,[1] has been used in this study to find the effects, if any, of carbon on the thermionic emission from tungsten. In a recent study[2] it has been found that the adsorption of cesium on tungsten results in a complete reversal in the form of the emission map. One purpose of the present study is to determine whether or not similar changes take place with adsorbed oxygen.

2. Description of the Apparatus

A schematic diagram of the tube and the circuit used in taking the measurements is shown in Fig. XII-7. The filament is tungsten wire, 7.2×10^{-3} cm in diameter, grown

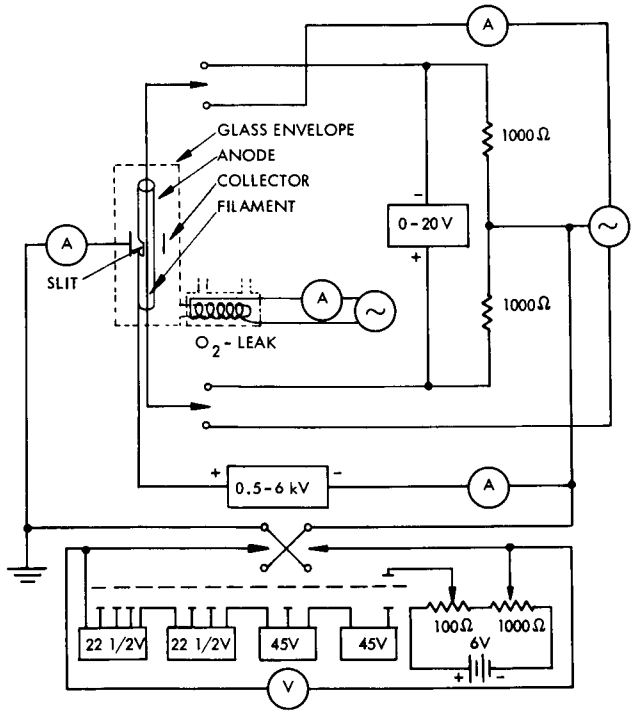

Fig. XII-7. Schematic diagram of the tube and the circuit used for the measurements.

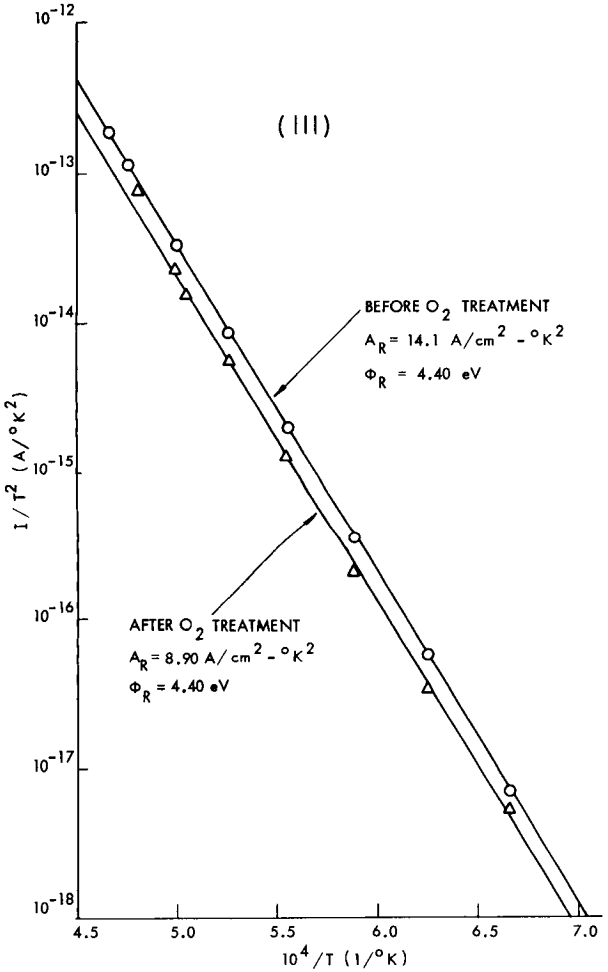

Fig. XII-8. Richardson plots for the (111) crystallographic direction in vacuum before and after O_2-treatment.

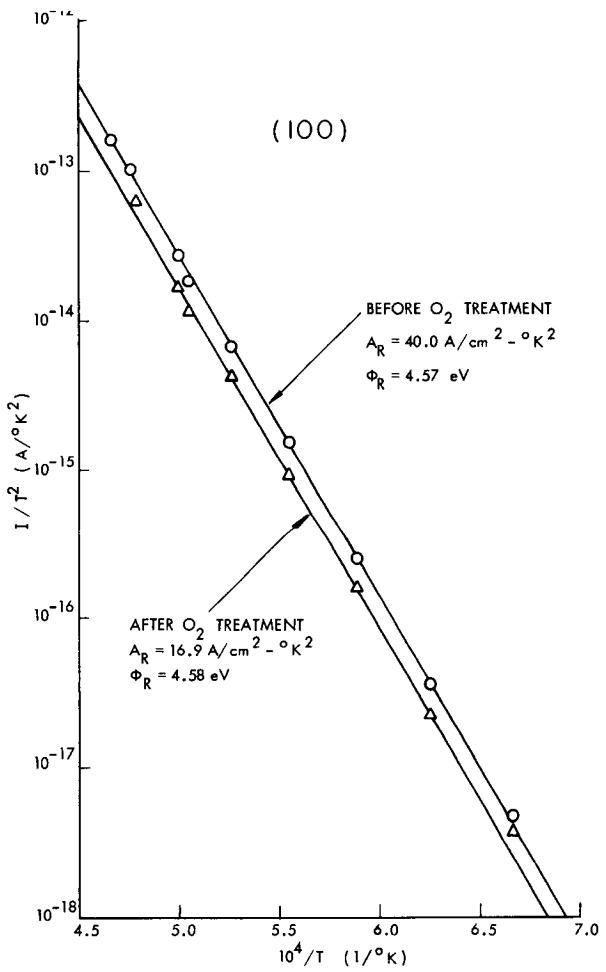

Fig. XII-9. Richardson plots for the (100) crystallographic direction in vacuum before and after O_2-treatment.

into a single crystal and mounted in the center of the tube. It is surrounded by a concentric tantalum anode, 2 cm in diameter, with a slit, 0.75 mm wide and 1 cm long. This slit which subtends an angle of 4.30° on the filament, enables the electrons emitted from an area of 2.7×10^{-4} cm^2 on the crystal to reach a collector. The collector, a nickel cylinder, 3 cm in diameter, is covered with platinum black on the inside in order to reduce electron reflection. Two iron slugs mounted on the anode permit rotation of the slit from outside the tube by using magnets. To take the emission maps, the anode and the collector were biased 1 kv and 4 v positive with respect to the filament, respectively.

3. Results

The work functions obtained in vacuum for the (111) and (100) directions compare well with data obtained by Nichols,[3] Smith,[4] and Coggins.[2] The vacuum measurements, including collector and anode bias data, Schottky and Richardson plots, and an emission map of the tungsten crystal, indicated a satisfactory condition of test tube and filament.

Following Becker's[1] technique to remove the carbon impurities from the filament, the tungsten filament was held at 2200°K in oxygen at 1×10^{-6} torr for 63 hours. Figures XII-8 and XII-9 show Richardson plots with the collector current reduced to zero

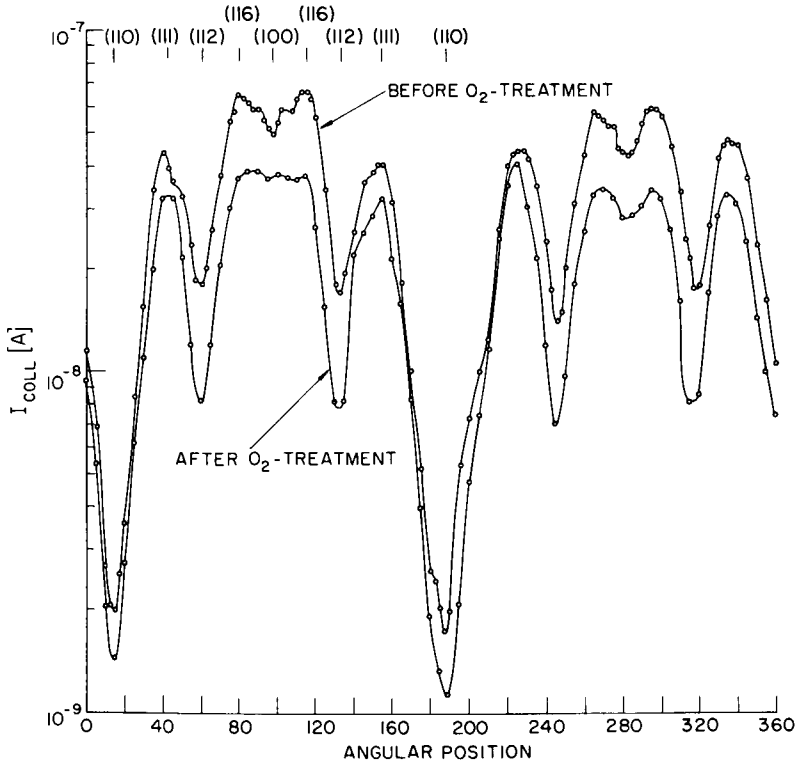

Fig. XII-10. Emission maps for 1900°K before and after O_2-treatment in vacuum.

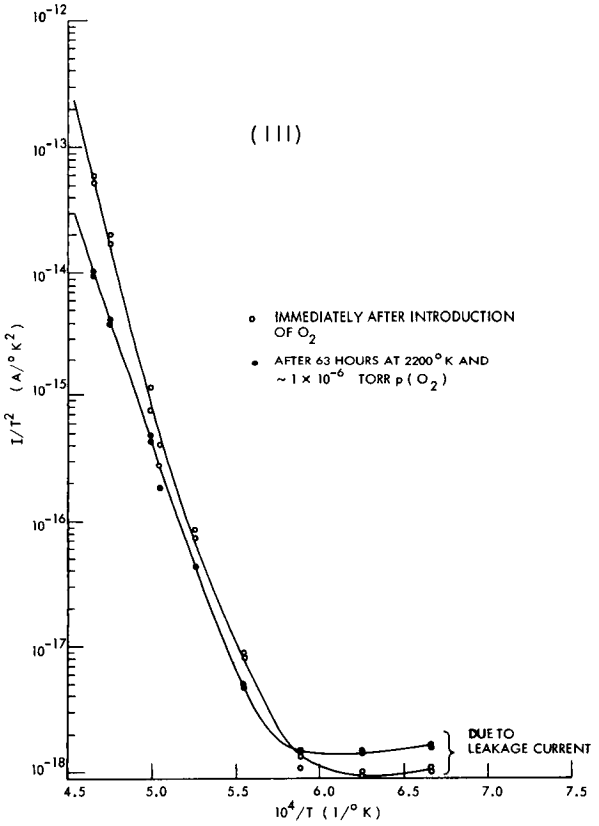

Fig. XII-11. Richardson plots for the (111) crystallographic direction in 1×10^{-6} torr oxygen before and after O_2-treatment.

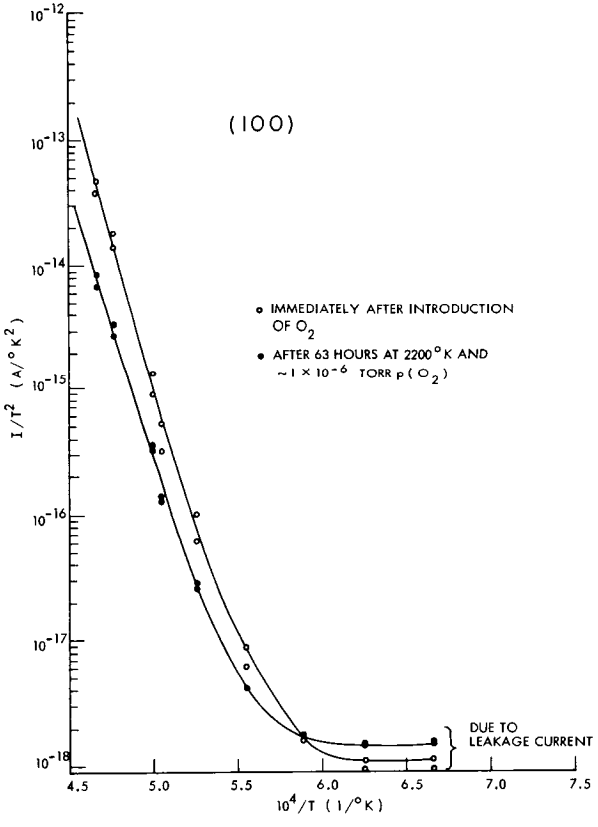

Fig. XII-12. Richardson plots for the (100) crystallographic direction in 1×10^{-6} torr oxygen before and after O_2-treatment.

field for the (111) and (100) directions taken in vacuum before and after the treatment with oxygen. For both crystallographic directions the Richardson work functions, ϕ_R, remained the same, but the Richardson constants, A_R, decreased. This decrease in emission appears also in the vacuum emission maps for a 1900°K filament temperature taken before and after the O_2-treatment (Fig. XII-10). A comparison of the two emission maps also shows marked differences in the vicinity of the (100) crystallographic directions. The difference between the (116) and the (100) directions has greatly diminished, even though the emission in the (100) direction is still less than in the (116) crystallographic direction. These differences could be due to lattice rearrangements, as suggested by Ehrlich.[5]

Richardson plots for the (111) and (100) crystallographic directions taken in oxygen at $\sim 1 \times 10^{-6}$ torr before and after the 63-hour oxygen treatment of the filament are shown in Figs. XII-11 and XII-12. Here too, the decrease in emission is apparent; however, the Richardson plots are now curves instead of straight lines with the tangents indicating an increasing work function for increasing temperature. This seems to be a transition Richardson plot, as suggested by Johnson and Vick,[6] in the region between half and full coverage. A meaningful Richardson plot from which the work function can be determined cannot be obtained by this method, since the surface coverage varies with filament temperature.

Richardson plots taken in $p(O_2) = 1 \times 10^{-8}$ torr appear to be the same as the plots taken in vacuum. The close similarity of the emission maps shown in Figs. XII-13 and XII-14 indicates that an oxygen pressure of 1×10^{28} torr has no significant effect upon the emission from a tungsten filament at temperatures above 1500°K.

Emission maps taken at various oxygen pressures and filament temperatures are shown in Figs. XII-13 through XII-16. In comparison, these show that, in addition to the expected decrease of the electron emission, the contrast between the emission in the (111) direction and that in the (100)-(116) range decreases with increasing oxygen pressure and decreasing filament temperature, that is, with increasing oxygen coverage of the tungsten filament. A similar decrease in contrast is observed for the (112) and (110) directions; in fact, the emission in the (112) direction becomes less than the emission in the (110) direction at $T_{Fil} = 1900$°K in $p(O_2) = 1 \times 10^{-7}$ torr. Similarly, the relative magnitudes of the electron emission in the (100) and (116) directions reverse at the higher oxygen pressures. A possible explanation for these phenomena could be found in a preferential affinity of the oxygen for different crystallographic faces.

Figure XII-17 shows the effective work functions ϕ_E as functions of filament temperature for the various oxygen pressures and crystallographic directions. In principle, it should be possible to present these data on a plot of ϕ_E against coverage θ. We have not been able to do this because it is not possible to determine the coverage in this experiment and appropriate reliable data do not exist for single crystals.

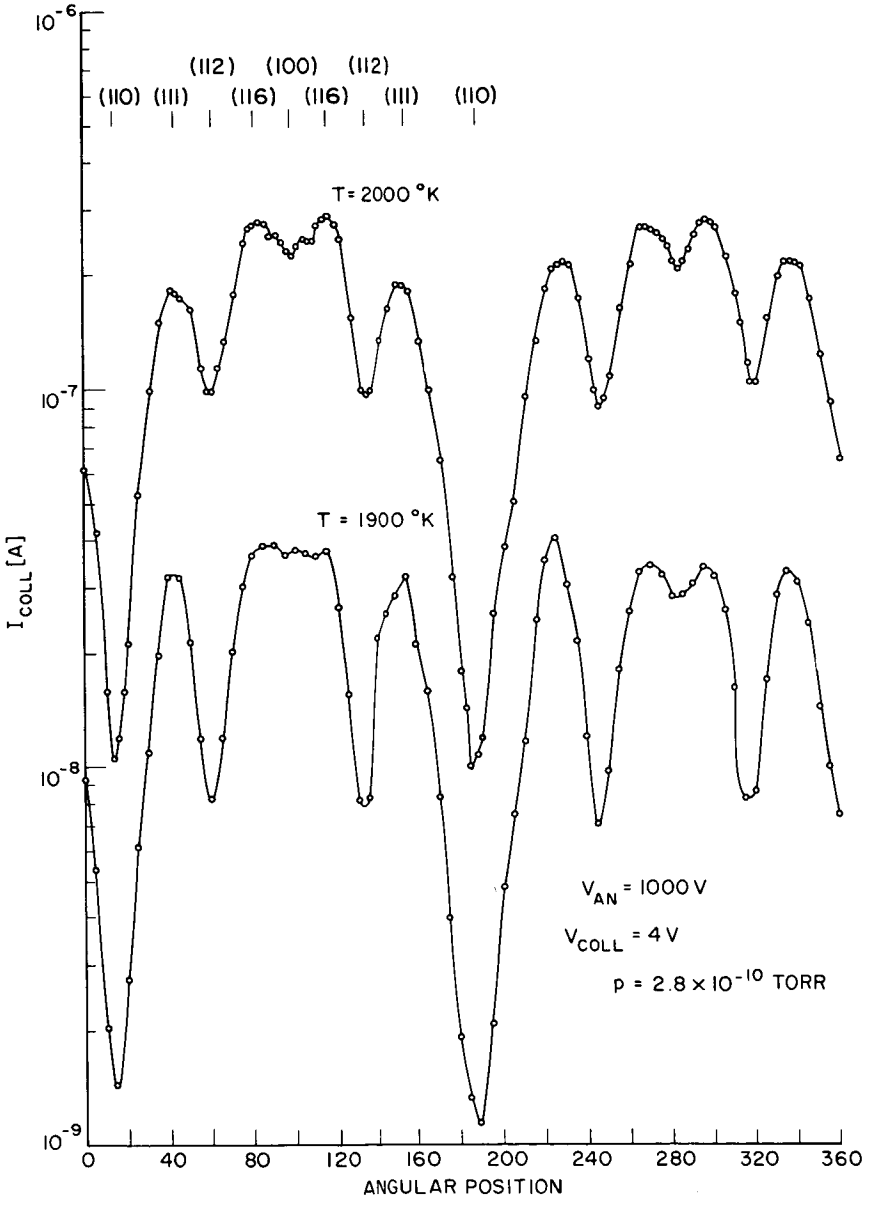

Fig. XII-13. Emission maps in vacuum.

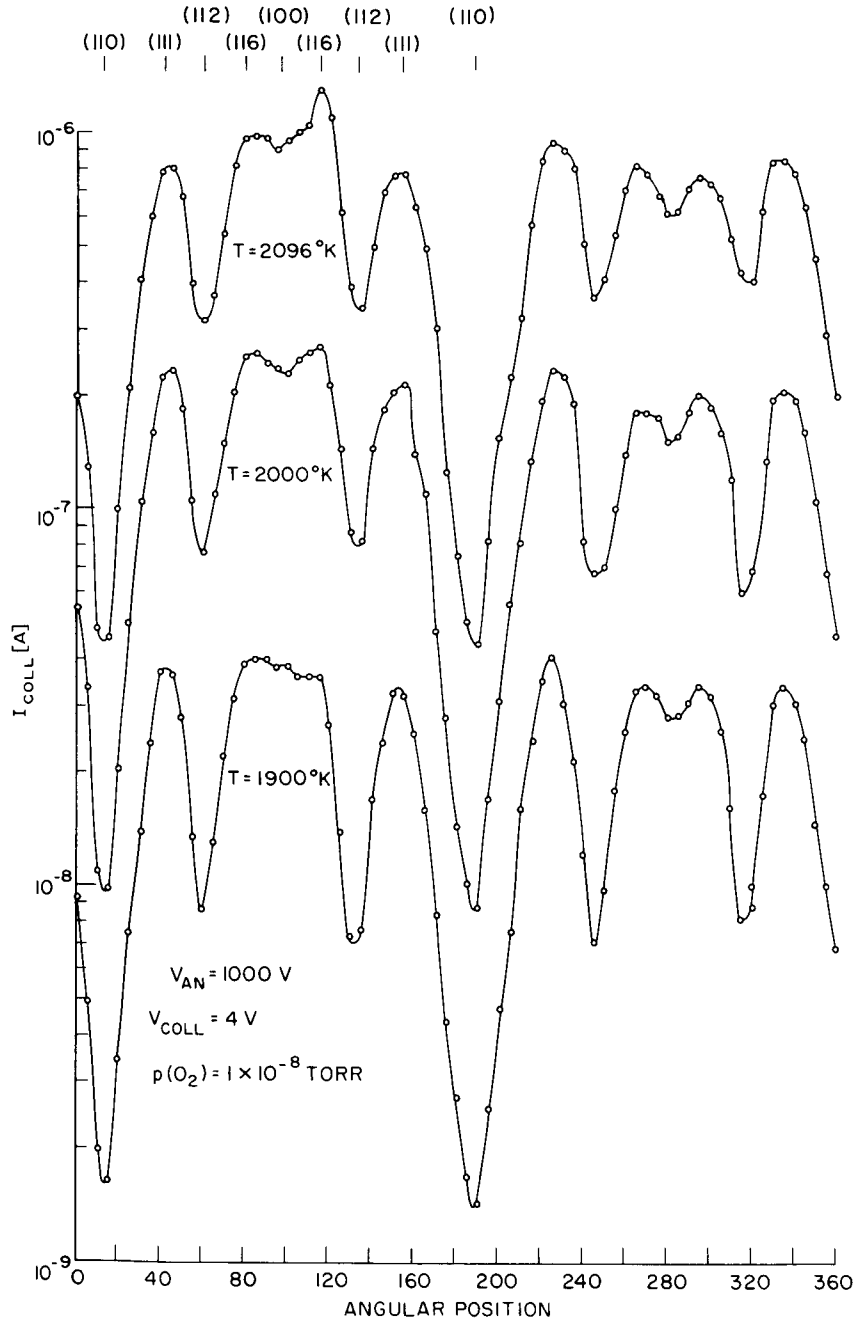

Fig. XII-14. Emission maps in oxygen at 1×10^{-8} torr.

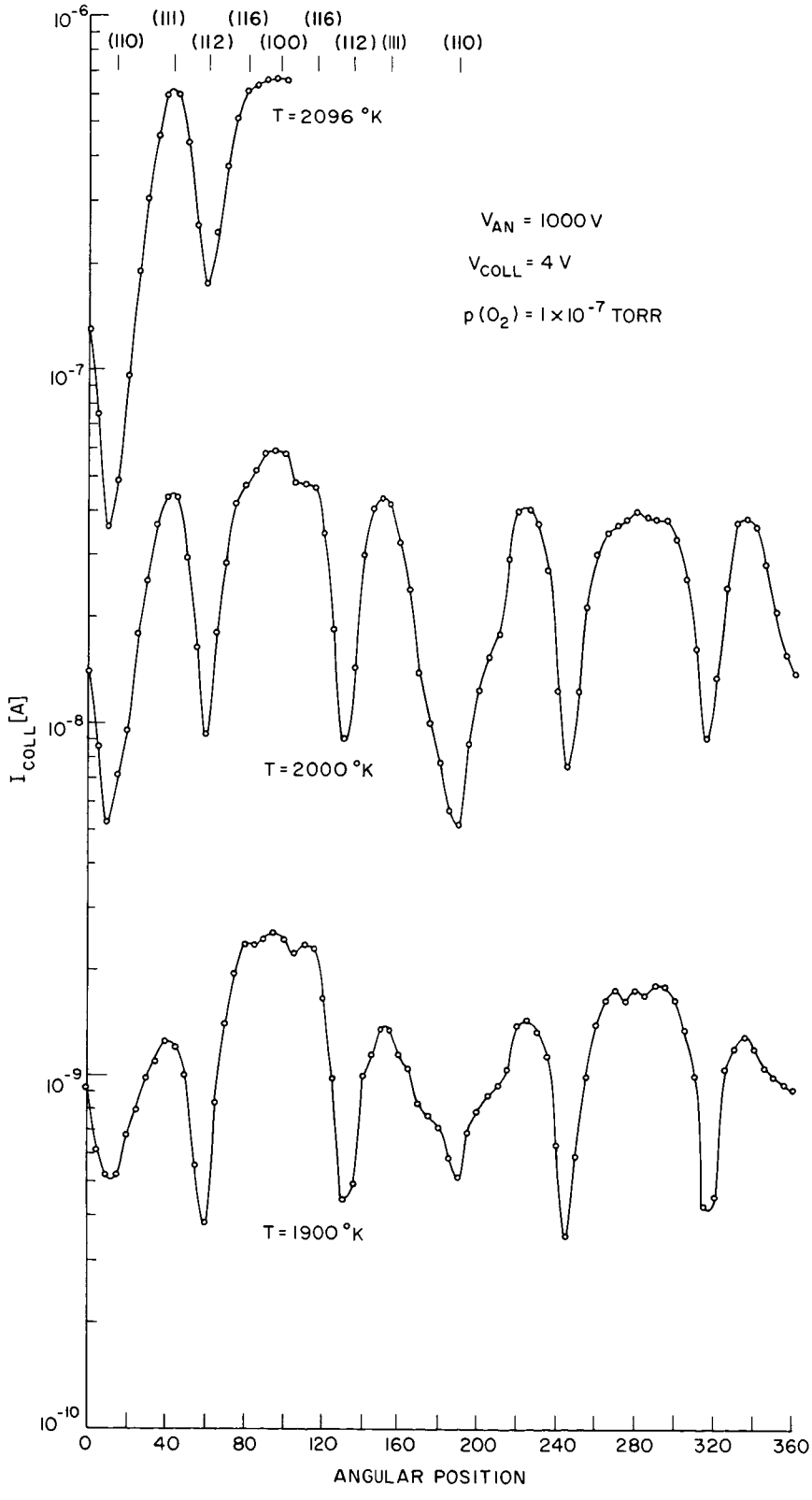

Fig. XII-15. Emission maps in oxygen at 1×10^{-7} torr.

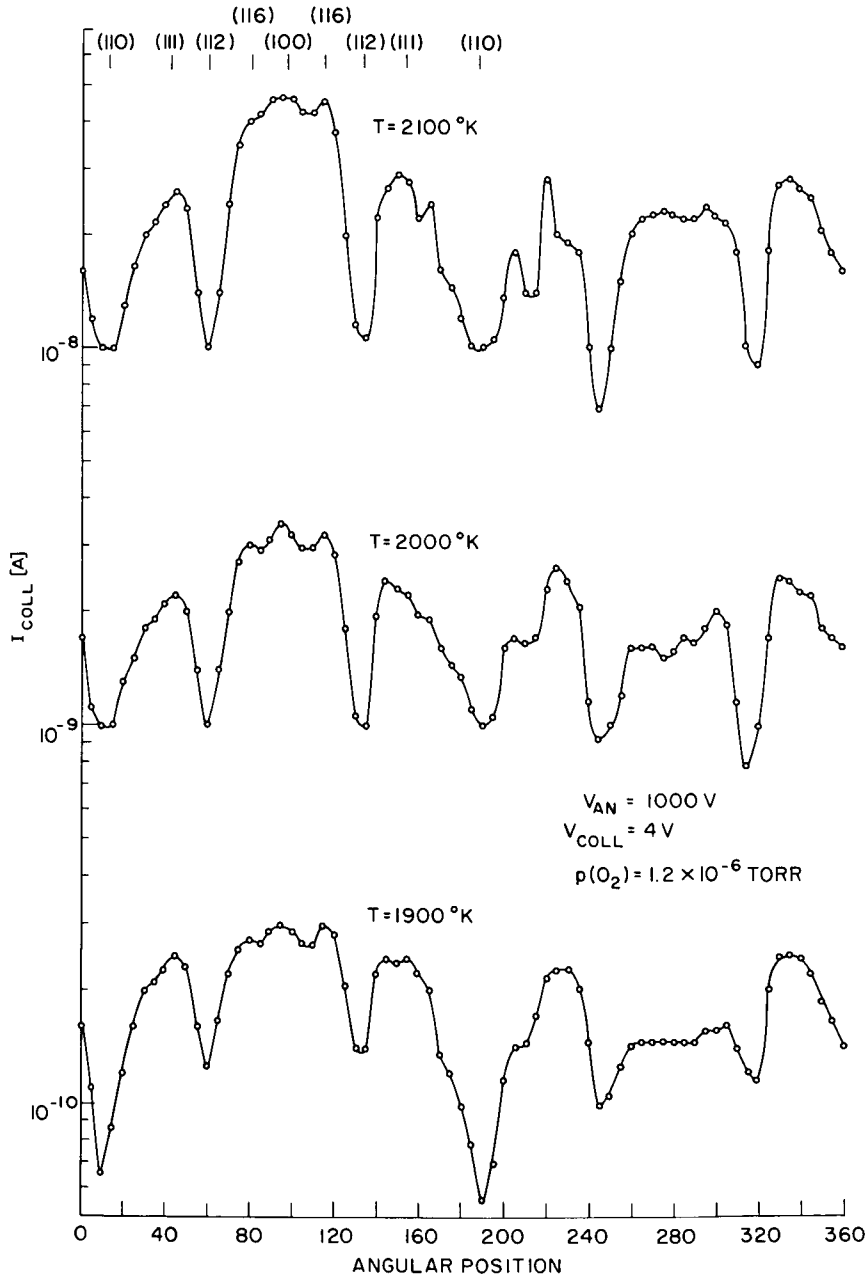

Fig. XII-16. Emission maps in oxygen at 1.2×10^{-6} torr.

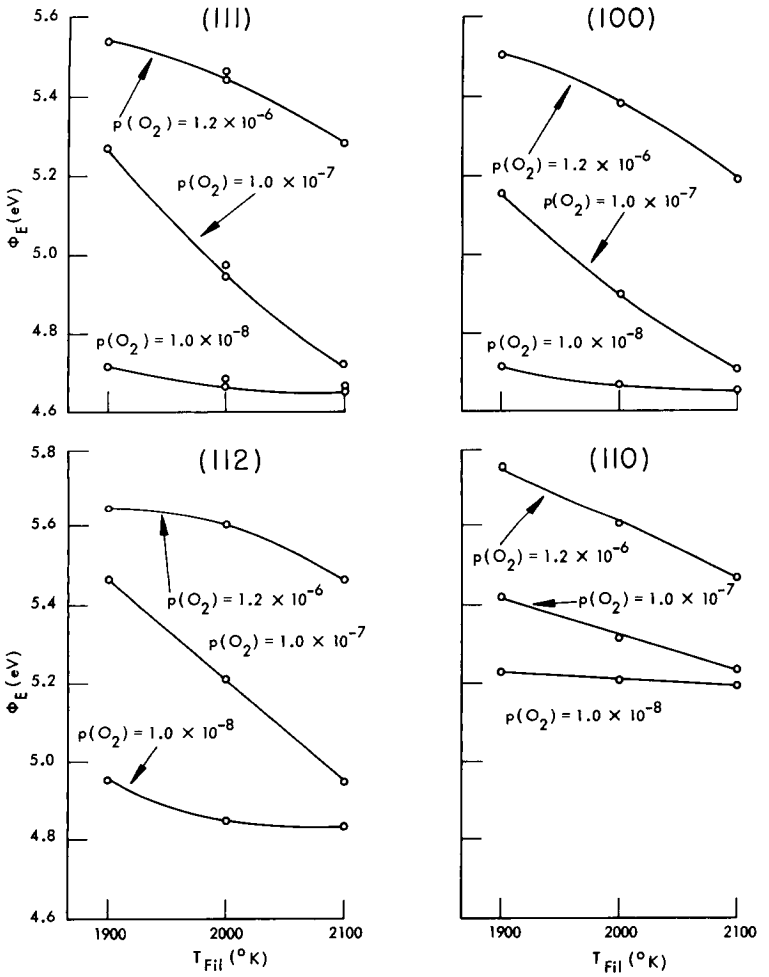

Fig. XII-17. Effective work function of different crystallographic directions as a function of filament temperature and oxygen pressure.

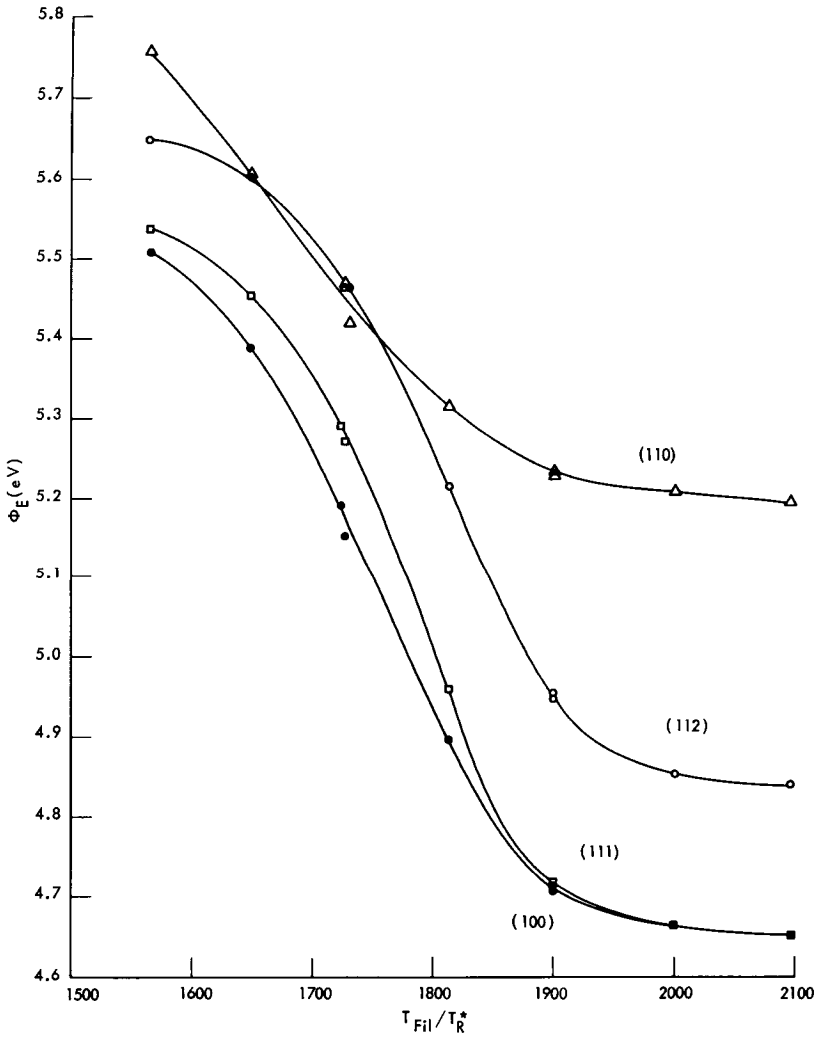

Fig. XII-18. Effective work function vs the ratio of filament temperature to effective reservoir temperature for various crystallographic directions.

An attempt to find an empirical parameter related to the coverage was quite successful, as shown in Fig. XII-18. The effective reservoir temperature T_R^* used in this parameter, T_{Fil/T_R^*}, is defined as

$$T_R^* = 1 + 0.0447 \ln \frac{p}{1 \times 10^{-8}}, \quad (1)$$

where p, the oxygen pressure, is in torr. Although no definite significance can be ascribed to the exact value of T_R^*, the curves in Fig. 3.3.12 are quite similar to the ϕ_E versus T/T_R plots for cesium on tungsten (for example, see Rasor and Warner[7]).

By comparing Figs. XII-13 through XII-16 it was previously found that the relative positions of the (110) and (112) directions reverse at $T_{Fil} = 1900°K$ and $p(O_2) = 1 \times 10^{-7}$ torr, which corresponds to $T_{Fil/T_R^*} = 1726$; this is also clearly shown in the overlapping of the curves for these crystallographic directions between $T_{Fil/T_R^*} = 1656$ and 1750. The variation of the (111) and (100) directions relative to each other is also obvious.

A strong decay in the electron emission, especially in an oxygen atmosphere, made flashing the filament at short intervals necessary. The breakage of the filament terminated any further investigation.

4. Summary

We found that the carbon impurities do not influence the work function of tungsten. The Richardson constant decreases slightly after the oxygen treatment. Adsorption of oxygen produces the expected decrease in emission, but the changes are not as strongly dependent on crystallographic direction as for cesium on tungsten.[2]

W. Engelmaier, R. E. Stickney

References

1. J. A. Becker, E. J. Becker, and R. G. Brandes, J. Appl. Phys. 32, 411 (1961).
2. J. L. Coggins, Ph.D. Thesis, Department of Mechanical Engineering, Massachusetts Institute of Technology, 1965.
3. M. H. Nichols, Phys. Rev. 57, 297 (1940).
4. G. F. Smith, Phys. Rev. 94, 295 (1954).
5. G. Ehrlich, Ann. N.Y. Acad. Science 101, 722 (1963).
6. M. C. Johnson and F. A. Vick, Proc. Roy. Soc. (London) A158, 55 (1937).
7. N. S. Rasor and C. Warner, J. Appl. Phys. 35, 2589 (1964).

D. CHARACTERISTICS OF A PURE ALKALI-METAL VAPOR PLASMA

The alkali vapor has been studied as a multicomponent system in which aggregates of atoms and electrons are characterized by a mass factor g and a charge factor Z, the mass of the aggregate being equal to g times the mass m_a of an atom and its charge to Z times the absolute value of the electron charge. As we deal with states out of thermodynamic equilibrium, a kinetic approach is used for which distribution functions f_g^Z are defined, their space and time evolution being governed by equations of the Liouville type. Collisional effects are exhibited in the usual way, with correlations between velocity and position for particles neglected. This limits us to densities for charged particles low enough so that the 90° Coulomb impact parameter is much smaller than the mean distance between particles. For aggregates consisting of a large enough number of atoms (approximately 10), the liquid-drop model[1,2] is used. Furthermore, all collisions except drop-drop collisions are taken into account. Finally, we limit ourselves to large Knudsen numbers based on the size of the particles, but small Knudsen numbers based on the characteristic length of the phenomenon under study. The study of the collisions with drops is done in the length scale characterizing the "range" of such interactions, and taking a Maxwellian as a first approximation to the electron, ion and atom distribution functions. Taking successive moments of the Boltzmann equations, the evolution of these moments is found (on a length scale much larger than the one characterizing the collisional operators). From such an analysis a generalization of the condensation and of the nonequilibrium ionization theories resulted.

1. Condensation

It has been found that below degrees of ionization of approximately 2 per cent the classical nucleation theory[1,2] applies. At pressures of ~1/100 of an atmosphere, a critical supersaturation ratio of ~5 is found.

For higher degrees of ionization, the drops will tend to be negatively charged, thereby increasing the number of ions condensing per unit surface and the time by a factor of s_i, which can be as high as 50 for small drops of nucleation size. An effective supersaturation ratio then has to be introduced which will be expressed by

$$(S_a)_{eff} = S_a\left[1 + \frac{(s_i-1)N_i}{N_a + N_i}\right],$$

where S_a is the classical supersaturation ratio, N_i and N_a the ion and atom number densities. For N_i/N_a = 2 per cent, it is seen that $(S_a)_{eff}/S_a$ is approximately 2.

Given a supersaturation ratio, the critical size for nucleation is also decreased, because of the electrostatic pressure term. This effect is less important, however, than the preceding effect. The drop growth is, as usual, limited by heat transfer from the

drops. In particular, for very high electron densities, the growth rate is further reduced because of the energy released by ion-electron recombination on the drop.

2. Ionization

For a given degree of moisture, two important plasma regimes can be identified, as shown in Fig. XII-19.

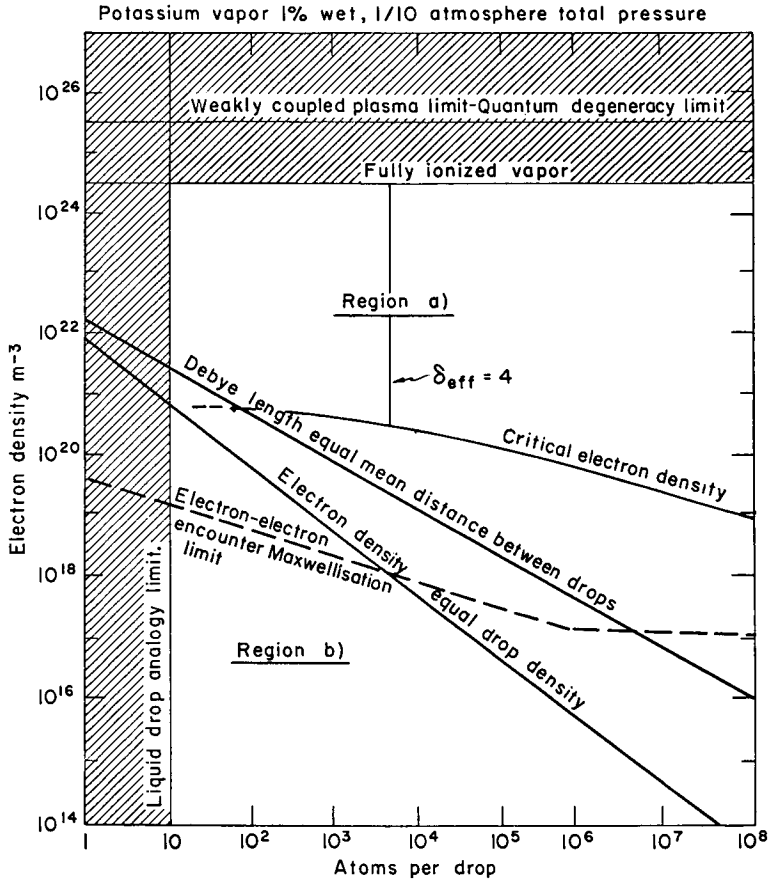

Fig. XII-19. Plasma regime classification for wet potassium vapor.

High electron densities: When the mean distance between drops is much larger than the Debye shielding length, most of the plasma consists of a region in which the electron and ion densities are equal. Drops are shielded from each other by sheaths.

Low electron densities: The Debye length is much larger than the mean distance between drops, so that an electron interacts simultaneously with a large number of them. In Fig. XII-19 the limits for the liquid-drop model are presented, as well as those for the Maxwellization of the electron distribution function through electron-electron encounters.

For high electron densities the rate at which drops charge is much faster than their evolution in size. Hence, at every instant an equilibrium distribution with charge can be assumed for the drops, together with an ionization equilibrium.

The study of the steady-state distribution of drops with charge shows that they will be predominantly negative in charge, the steady-state regime being reached when the number of electrons and ions condensing per unit time is equal. This leads to a decrease in the electron condensation rate by a factor which for potassium at 1/100 atmosphere is ~30, and the ion condensation rate increases by a factor $s_i \approx 10$. The right-hand side of the continuity equation for electrons is then set equal to zero so that

$$R_{ioniz} N_e \left[(N_e)^2_{Saha} - N_e^2 \right] + N_D 4\pi \overline{R^2} s_i \sqrt{\frac{kT_a}{2\pi m_a}} \left(N_i^* - N_e \right) = 0.$$

Here, we have supposed atom ionization by electron impact and three-body recombination in the presence of an electron, $(N_e)_{Saha}$ being the local electron density as evaluated through the Saha equation at the local electron temperature, and R_{ioniz} an ionization rate constant evaluated by Byron and his co-workers[3] for potassium, which is a function of the electron temperature. N_D is the drop number density, $4\pi R^2$ their mean physical surface, T_a the atom temperature, and N_i^* has the dimension of a number density and characterizes ion evaporation from drops.

For a dry vapor, $N_D = 0$, so the $N_e = (N_e)_{Saha}$, as expected from Kerrebrock's two-temperature model theory.[4] For a wet vapor, it is convenient to set

$$\eta_e = \frac{N_e}{(N_e)_{Saha}} \qquad \eta_i = \frac{N_i^*}{(N_e)_{Saha}}$$

$$K = \frac{(4\pi \overline{R^2}) s_i N_D \sqrt{\frac{kT_a}{2\pi m_a}}}{R_{ioniz} (N_e)^2_{Saha}} = \left(\frac{\mu}{\overline{R}} s_i \right) f(T_e),$$

where the gas temperature is supposed to remain constant, and μ is the degree of moisture defined as

$$\mu = \frac{N_D \overline{g}}{N_a}.$$

The term η_i^* in general is very small for the vapor pressures (and hence temperature) that we shall consider (approximately 10^{-6}), so that the continuity equation which is now written

$$1 - \eta_e^2 = K\left(1 - \frac{\eta_i^*}{\eta_e}\right)$$

has the following solutions

$$K < 1 \qquad \eta_e^2 \cong 1 - K$$

$$K > 1 \qquad \eta_e \cong \eta_i^*\left(\frac{K}{K-1}\right) \ll 1.$$

The transition from one solution to the other as K goes through the value of one is very sharp as exhibited in Fig. XII-20, which represents an evolution at constant electron temperature and constant mean radius, the degree of moisture being variable. This

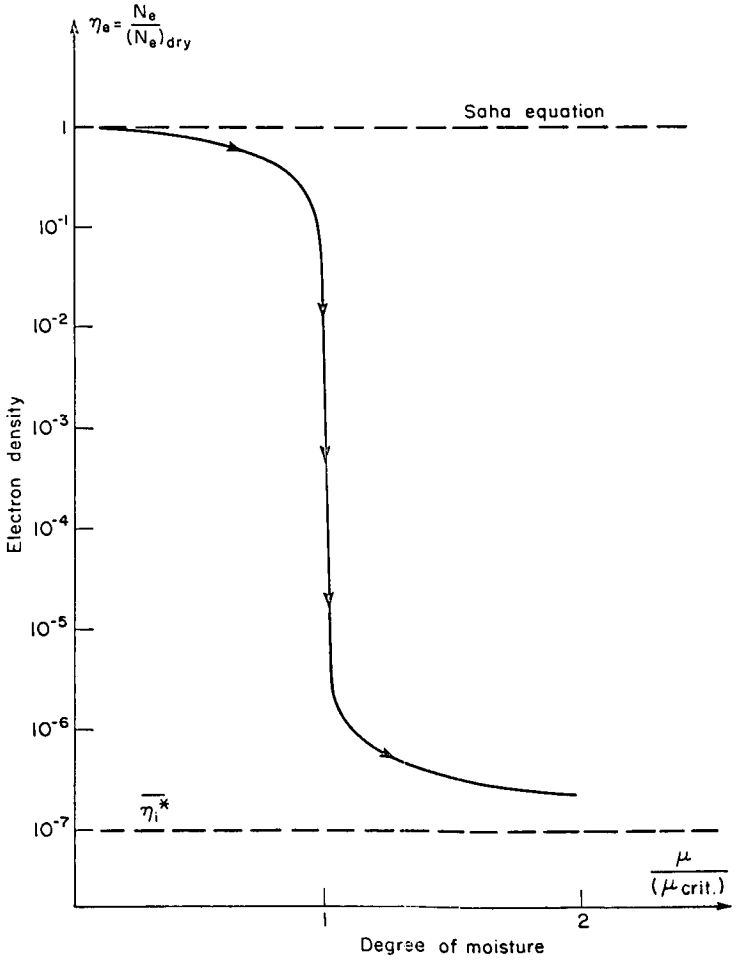

Fig. XII-20. Typical electron density variation with degree of moisture at constant electron temperature and mean drop size.

behavior can be stated in the following way. Given an electron temperature and a mean drop size, there exists a critical degree of moisture above which nonequilibrium ionization cannot be sustained. (We may also alternatively for a given degree of moisture, drop radius, and pressure define a critical electron density; this is represented in Fig. XII-19.) The condition under which an electron temperature can be maintained above the gas temperature can be found through the energy equation which is written, where J is the current density and σ the electrical conductivity,

$$\frac{J^2}{\sigma} = \delta \frac{m_e}{m_a} N_e (N_a Q_{ea} + N_i Q_{ei}) \sqrt{\frac{8kT_e}{\pi m_e}} \frac{3}{2} k(T_e - T_a) + N_D 4\pi \overline{R^2} s_i \sqrt{\frac{kT_a}{2\pi m_a}} N_e (eV_i) + Q_R.$$

Here, the joule heating is seen to be balanced by the energy loss terms. The elastic energy loss with atoms and ions is represented by the first term on the right-hand side. The second term represents the inelastic energy loss due to electron-ion recombination on drops (V_i is ionization potential), and the last term represents the energy loss by

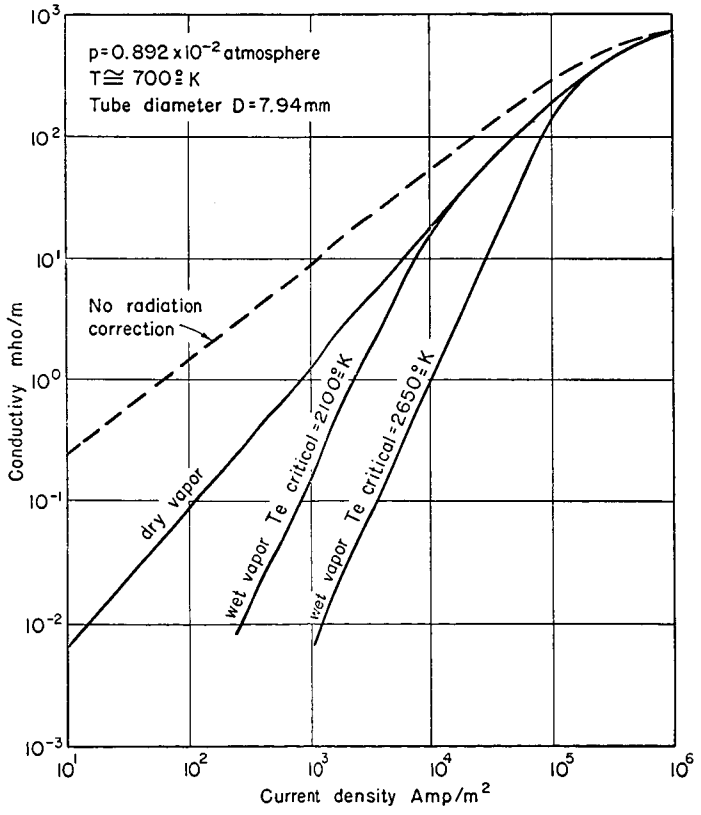

Fig. XII-21. Electrical conductivity of dry and wet potassium vapor vs current density ($\delta_{eff} \sim 2$).

radiation. For a monatomic alkali metal vapor δ is equal to 2.

As the first and second terms on the right-hand side are proportional to the electron density, N_e, an effective energy loss parameter δ_{eff} can be defined so as to put the inelastic drop losses in a form comparable to the elastic losses. The value $\delta_{eff} = 4$ corresponds to equality of the two terms and is represented in Fig. XII-19. This was selected as a reasonable maximum allowable value for an MHD generator.

With this model, it has been shown that for the degrees of moisture considered here (a few per cent), the total cross section for momentum exchange between electrons and drops is much smaller than the cross section with atoms and ions. Hence, changes in conductivity will be due primarily to changes in electron density, and the Hall parameter is practically unaffected by condensation.

The expected behavior of σ versus current density J is presented in Fig. XII-21. The branches corresponding to the departure from the dry state have a slope equal to 2 on the log (σ) vs log (J) plot. This is due to the fact that as K approaches 1, the electron temperature on this branch remains almost constant but the electron density decreases. This causes both elastic and inelastic losses to decrease so that the energy equation for these branches is approximately

$$\frac{J^2}{\sigma} = Q_R = \text{constant}.$$

This remains valid as long as the first two excited states for atoms, which give most of the contribution to the radiation term, are in equilibrium at the electron temperature.

3. Experimental Results

Experiments were conducted for a dry potassium vapor. The experimental apparatus has been described in a previous report,[4] in which Hall parameter measurements were seen to be in good agreement with the theoretical predictions based on a cross section of 250 Å for potassium. More refined electrical conductivity measurements were made for the dry vapor. Some characteristic results are presented in Fig. XII-22. The agreement with theory is seen to be quite good except at high current densities for which, owing to the low pressure (1/100 atm), the joule heating of the gas is quite important. At very low current densities, the measured electrical conductivity is abnormally high. This has been reported elsewhere[5] in connection with electrical conductivity measurements of argon-seeded plasmas.

For a wet vapor, due to the fact that the kinetics of condensation at this pressure is very slow, condensation was started before the test section entrance. Supersaturation ratios as high as 7 have been observed, in the absence of ionization, which suggest that nucleation in this case is correctly predicted by the classical nucleation theory.[1,2]

Measurements of electrical conductivity in a wet vapor are difficult because of the

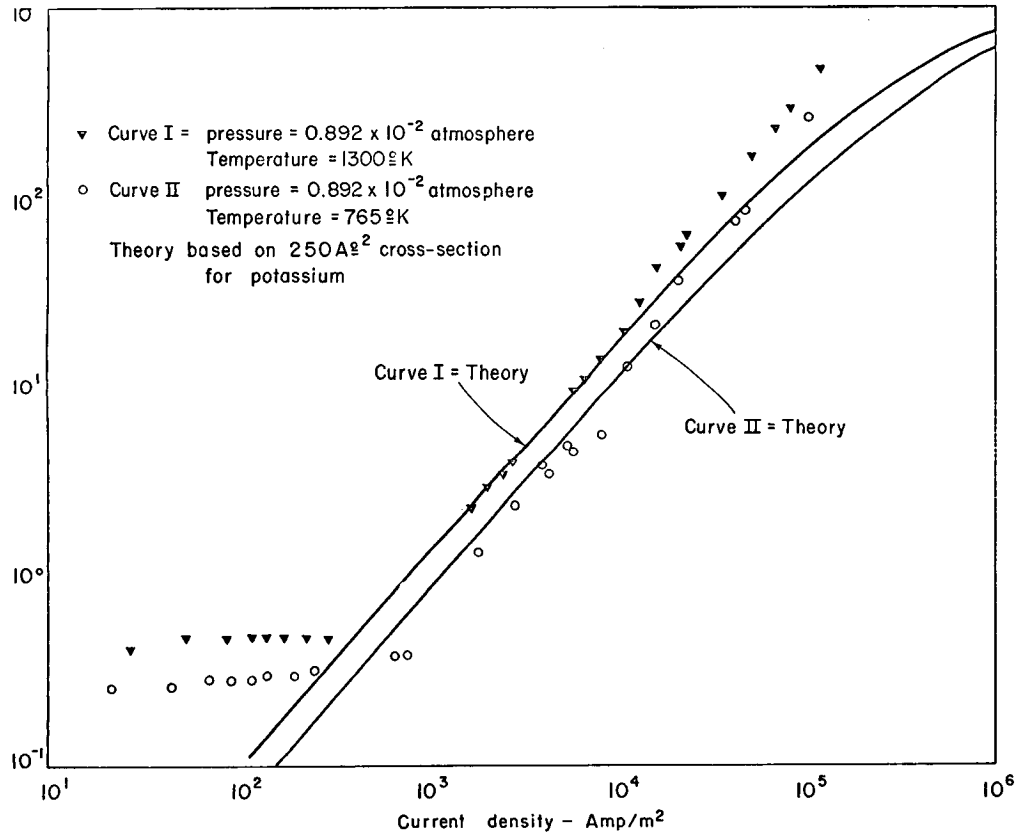

Fig. XII-22. Dry potassium vapor electrical conductivity.

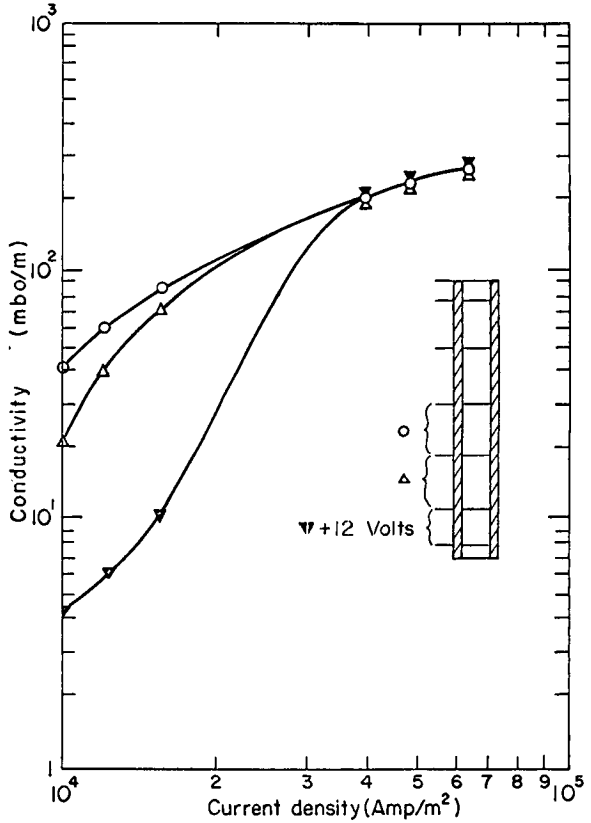

Fig. XII-23. Wet potassium vapor conductivity at different test section locations.

joule heating of the gas which at high current densities tends to evaporate the drops. At current densities of ~1 amp/cm^2, the voltages at the inlet of the test region increased because of the effect of condensation. Only a semiquantitative comparison with theory can be made by plotting the average electrical conductivities in the interprobe space. This has been done and is presented in Fig. XII-23, in which a good qualitative agreement with theory is seen to exist (compare with Fig. XII-21).

J. L. Kerrebrock, M. A. Hoffman, A. Solbes

References

1. J. Frenkel, Kinetic Theory of Liquids (Clarendon Press, Oxford, 1946).
2. P. Hill "Homogeneous Nucleation of Supersaturated Water Vapor in Nozzles," Report No. 78, Gas Turbine Laboratory, Massachusetts Institute of Technology, Cambridge, Massachusetts, January 1965.
3. S. Byron, et al., "Electron-Ion Reaction Rate Theory," Proc. Fourth Symposium on Engineering Aspects of Magnetohydrodynamics, University of California, Berkeley, April 1963.
4. J. L. Kerrebrock, M. A. Hoffman, and A. Solbes, "Behavior of Dry Potassium Vapor in Electric and Magnetic Fields," Quarterly Progress Report No. 77, Research Laboratory of Electronics, M.I.T., April 15, 1965, pp. 232-237.
5. J. L. Kerrebrock, "Nonequilibrium Ionization due to Electron Heating, I and II," AIAA J. 2, 1072-1087 (June 1964).

E. BRAYTON CYCLE MAGNETOHYDRODYNAMIC POWER GENERATION

The research reported here was undertaken to obtain a thorough understanding of closed Brayton cycle MHD power generation and to provide data for comparison with other competitive power generation techniques. The current state of the art in magnetics, reactor design, and high-temperature materials technology has fixed upper limits on the operation of the cycle and its components. Results of the analysis indicate the feasibility of the cycle for terrestrial applications. The MHD Brayton cycle is not competitive with Rankine cycle systems now in operation, because of large refrigeration requirements necessary for operation of superconducting coils that provide the generator's magnetic field.

1. Brayton Cycle Magnetohydrodynamic Power Generation

A detailed analysis has been undertaken to determine the feasibility of closed Brayton cycle magnetohydrodynamic power generation.[1] The two primary constraints on such a system – the maximum available stagnation temperature from the heat source, and the minimum generator exit temperature below which efficient power generation is impossible – have been determined in the light of current technological capabilities.

Operating with a maximum stagnation temperature in the range of 1500°K from a gas-cooled nuclear heat source requires nonequilibrium conductivity considerations for the working fluid. The coupled working fluid requirements of compatibility with a nuclear environment and satisfactory electrical conductivity (in excess of 100 mhos/meter) result in the selection of neon seeded with cesium as the working fluid. Heat-transfer considerations would favor a helium-cesium mixture; however, the electrical conductivity of this mixture is unsatisfactory at operating pressures of approximately 15 atm which yield acceptable heat transfer areas in the heat source and sink.

Cycle operation with the neon-cesium mixture is feasible with the indicated maximum stagnation temperature and current density levels of $1.0 \cdot 10^5$ to $3.0 \cdot 10^5$ amps/m^2 in the MHD generator. The magnetic field intensities necessary to sustain these current density levels range from 7.5 to 20 webers/m^2, and thus require superconducting coils. The minimum cycle heat-rejection temperature is in the range 300-400°K, with the result that space application of this system would be unsatisfactory. The heat-rejection temperature is too low for efficient utilization of space radiators. Terrestrial operation of the system is feasible with cycle efficiencies in the range 39-49%. The analysis yielding this range of efficiency has considered viscous dissipation in the high velocity flow through the MHD generator, nonisentropic operation of the cycle diffuser and compressor, and utilization of the rejected heat as the heat source for a secondary cycle. Power from this secondary cycle must be utilized to drive the Brayton cycle compressor, since the compressor power is a significant fraction of the electric power output, and cannot

be efficiently supplied from the primary Brayton cycle. Additional restrictions on this analysis include operation of the secondary cycle at an efficiency of 40%, and neglect of power requirements for refrigeration of the superconducting coils.

Although the analysis indicates feasibility of the MHD Brayton cycle, the system is not competitive with Rankine cycle systems using water as the working fluid and operating conventional generators. The unattractiveness of the MHD system stems from the low electrical conductivity of the working fluid at thermodynamic states compatible with available heat sources. As a result, high levels of the applied magnetic field are required, sustainable only with superconducting coils. The refrigeration requirements for such coils degrades the otherwise acceptable cycle efficiency to an uncompetitive level.

C. A. McNary

References

1. C. A. McNary, M. E. Thesis, Department of Mechanical Engineering, M.I.T., 1965.

COMMUNICATION SCIENCES
AND
ENGINEERING

XIII. STATISTICAL COMMUNICATION THEORY*

Prof. Y. W. Lee
Prof. A. G. Bose
Prof. M. Schetzen
Prof. H. L. Van Trees
Prof. V. R. Algazi
Prof. J. D. Bruce
Prof. A. V. Oppenheim
R. Alter
M. Austin
A. B. Baggeroer
R. F. Bauer
L. D. Collins
T. A. Froeschle
J. W. Giffin
L. M. Goodman
K. Grace, Jr.
T. Huang
D. E. Nelsen
T. H. Nyman
M. O. Pace
R. B. Parente
L. R. Poulo
J. E. Schindall
D. L. Snyder
J. J. Wawzonek
D. H. Wolaver

A. WORK COMPLETED

[Titles followed by a dagger (†) are theses that were supervised by members of this group, although the work was not sponsored by the Research Laboratory of Electronics. Summaries are included because they might be of interest to workers in this field.]

1. BIOELECTRIC CONTROL OF PROSTHESES

This study has been completed by R. Alter. In August 1965, he submitted the results to the Department of Electrical Engineering, M.I.T., as a thesis in partial fulfillment of the requirements for the degree of Doctor of Science. This study will appear as Technical Report 446 of the Research Laboratory of Electronics.

A. G. Bose

2. FUNCTIONAL ANALYSIS OF SYSTEMS CHARACTERIZED BY NONLINEAR DIFFERENTIAL EQUATIONS

This study has been completed by R. B. Parente. In August 1965, he submitted the results to the Department of Electrical Engineering, M.I.T., as a thesis in partial fulfillment of the requirements for the degree of Doctor of Philosophy. This study will appear as Technical Report 444 of the Research Laboratory of Electronics.

Y. W. Lee

3. OPTIMUM LAGUERRE EXPANSION OF SYMMETRIC N^{th}-ORDER FUNCTIONS

This study has been completed by J. W. Giffin. In August 1965, he submitted the results to the Department of Electrical Engineering, M.I.T., as a thesis in partial fulfillment of the requirements for the degree of Master of Science.

M. Schetzen

*This work was supported in part by the Joint Services Electronics Program (Contract DA36-039-AMC-03200(E)), the National Science Foundation (Grant GP-2495), and the National Aeronautics and Space Administration (Grants NsG-334 and NsG-496).

4. SOME PROBLEMS IN THE STUDY OF NONLINEAR SYSTEMS WITH FEEDBACK LOOPS†

This study has been completed by Cynthia L. K. Whitney. In August 1965, she submitted the results to the Department of Electrical Engineering, M.I.T., as a thesis in partial fulfillment of the requirements for the degree of Master of Science.

M. Schetzen

5. MEASUREMENT OF VOLTERRA KERNELS OF A NONLINEAR SYSTEM OF FINITE ORDER

This study has been completed by T. Huang. In August 1965, he submitted the results to the Department of Electrical Engineering, M.I.T., as a thesis in partial fulfillment of the requirements for the degree of Master of Science.

M. Schetzen

6. SEVERAL ADAPTIVE BINARY DETECTION PROBLEMS†

This study has been completed by D. W. Boyd. In August 1965, he submitted the results to the Department of Electrical Engineering, M.I.T., as a thesis in partial fulfillment of the requirements for the degree of Master of Science.

H. L. Van Trees

7. DIGITAL SIMULATION OF ANALOG MODULATION TECHNIQUES OVER THE RAYLEIGH CHANNEL†

This study has been completed by T. J. Cruise. In June 1965, he submitted the results to the Department of Electrical Engineering, M.I.T., as a thesis in partial fulfillment of the requirements for the degree of Master of Science.

H. L. Van Trees

8. SPACE-TIME SIGNAL PROCESSING

This study has been completed by K. Grace, Jr. In August 1965, he submitted the results to the Department of Electrical Engineering, M.I.T., as a thesis in partial fulfillment of the requirements for the degree of Master of Science.

H. L. Van Trees

9. ANALOG COMMUNICATION THROUGH SEPARABLE MULTIPATH CHANNELS CHARACTERIZED BY TIME-VARYING PATH DELAYS†

This study has been completed by R. R. Kurth. In August 1965, he submitted the results to the Department of Electrical Engineering, M.I.T., as a thesis in partial fulfillment of the requirements for the degree of Master of Science.

H. L. Van Trees

10. PREDISTORTION IN NO-MEMORY FILTERING AND IN QUANTIZATION

This study has been completed by M. O. Pace. In June 1965, he submitted the results to the Department of Electrical Engineering, M.I.T., as a thesis in partial fulfillment of the requirements for the degree of Master of Science and the degree of Electrical Engineer.

V. R. Algazi

11. A STATISTICAL STUDY OF VLF ATMOSPHERIC NOISE†

This study has been completed by R. A. Grant, Jr. In August 1965, he submitted the results to the Department of Electrical Engineering, M.I.T., as a thesis in partial fulfillment of the requirements for the degree of Master of Science.

V. R. Algazi

B. DETERMINATION OF OPTIMUM NONLINEAR SYSTEMS FOR GAUSSIAN INPUTS BY CROSSCORRELATION

1. Optimum Systems with White Gaussian Inputs

In the Wiener theory of nonlinear systems, the input, $x(t)$, of a system A, as shown in Fig. XIII-1, is a white Gaussian process. The output, $y_a(t)$, of the system is represented by the orthogonal expansion

$$y_a(t) = \sum_{n=0}^{\infty} G_n[h_n, x(t)] \tag{1}$$

in which $\{h_n\}$ is the set of Wiener kernels of the nonlinear system A, and $\{G_n\}$ is a complete set of orthogonal functionals. The orthogonal property of the functionals is expressed by the fact that the time average $\overline{G_m[h_n, x(t)]\, G_n[h_n, x(t)]} = 0$ for $m \neq n$. The power density spectrum of the Gaussian input, $x(t)$, is $\Phi_{xx}(\omega) = \frac{K}{2\pi}$ watts per radian per second so that the autocorrelator function of the input is $\phi_{xx}(\tau) = K\mu(\tau)$ where $\mu(\tau)$ is the unit impulse function.

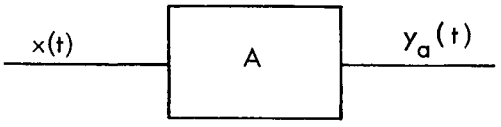

Fig. XIII-1. Nonlinear system with white Gaussian input.

If the desired output of the nonlinear system A is $z(t)$, the error, $\epsilon_a(t)$, is

$$\epsilon_a(t) = z(t) - y_a(t) \tag{2}$$

We shall show in this report that the Wiener kernels of the optimum nonlinear system A for which the mean-square error, $\overline{\epsilon_a^2(t)}$, is a minimum are given by

$$h_n(\sigma_1, \ldots, \sigma_n) = \begin{cases} \dfrac{1}{n!K^n} \overline{z(t)\, x(t-\sigma_1) \ldots x(t-\sigma_n)} & \sigma_i \geq 0 \qquad i = 1, 2, \ldots, n \\ & \qquad\qquad n = 0, 1, 2, \ldots \\ 0 \qquad \text{otherwise} \end{cases} \tag{3}$$

except when two or more σ's are equal.

To show this result, let us write the n^{th}-degree functional with $x(t-\sigma_1) \ldots x(t-\sigma_n)$ as the leading term in an orthogonal set $\{H_n[k_n, x(t)]\}$ as

$$\left.\begin{aligned} & H_o[k_o, x(t)] = 1 \\ & H_n[k_n, x(t)] = \int \cdots \int k_n(\tau_1, \ldots, \tau_n)\, x(t-\tau_1) \ldots x(t-\tau_n)\, d\tau_1 \ldots d\tau_n + F \\ & \qquad\qquad\qquad\qquad\qquad\qquad\qquad\qquad\qquad\qquad n = 1, 2, 3, \ldots \end{aligned}\right\} \tag{4}$$

in which F is a sum of homogeneous functionals of degrees lower than n and

$$k_n(\tau_1, \ldots, \tau_n) = u(\tau_1 - \sigma_1) \ldots u(\tau_n - \sigma_n); \tag{5}$$

in which u(t) is the unit impulse function. It has been shown[1] that

$$\overline{y_a(t)\, H_n[k_n, x(t)]} = n!K^n h_n(\sigma_1, \ldots, \sigma_n) \qquad n = 0, 1, 2, \ldots \tag{6}$$

in which there are no restrictions on the σ's.

Now construct the system A with the Wiener kernels given by

$$h_n(\sigma_1, \ldots, \sigma_n) = \begin{cases} \dfrac{1}{n!K^n} \overline{z(t)\, H_n[k_n, x(t)]}; & \sigma_i \geq 0 \qquad n = 0, 1, 2, \ldots \\ 0 \qquad \text{any } \sigma_i < 0 \end{cases} \tag{7}$$

This system is the optimum nonlinear system. To show this, we first observe from (6) and (7) that by our construction A,

$$\overline{y_a(t)\, H_n[k_n, x(t)]} = \overline{z(t)\, H_n[k_n, x(t)]} \qquad \sigma_i \geq 0 \qquad n = 0, 1, 2, \ldots \tag{8}$$

so that from (2)

$$\overline{\epsilon_a(t)\, H_n[k_n, x(t)]} = 0 \qquad \text{for } \sigma_i \geq 0 \qquad n = 0, 1, 2, \ldots . \tag{9}$$

Equation 9 implies that

$$\overline{\epsilon_a(t)\, x(t-\sigma_1) \ldots x(t-\sigma_n)} = 0 \qquad \text{for } \sigma_i \geq 0 \qquad n = 0, 1, 2, \ldots \tag{10}$$

This is easily seen by induction from Eqs. 4 and 9, since

$$\overline{\epsilon_a(t)\, H_o[k_o, x(t)]} = \overline{\epsilon_a(t)} = 0 \tag{11}$$

$$\overline{\epsilon_a(t)\, H_1[k_1, x(t)]} = \overline{\epsilon_a(t)\, x(t-\sigma_1)} = 0; \quad \sigma_1 \geq 0 \tag{12}$$

For n = 2 in Eq. 9

$$\epsilon_a(t)\, H_2[k_2, x(t)] = \overline{\epsilon_a(t)\, x(t-\sigma_1)\, x(t-\sigma_2)} + \overline{\epsilon_a(t) F}$$

$$= 0 \qquad \text{for } \sigma_1, \sigma_2 \geq 0 \tag{13}$$

Since F in Eq. 13 is the sum of homogeneous functionals of degrees less than 2, we have from (11) and (12) that in Eq. 13, $\overline{\epsilon_a(t)\, F} = 0$ and thus

$$\overline{\epsilon_a(t)\, x(t-\sigma_1)\, x(t-\sigma_2)} = 0 \qquad \text{for } \sigma_1, \sigma_2 \geq 0. \tag{14}$$

By continuing in this manner, the validity of Eq. 10 for any value of n can be established. We note that Eq. 10 implies that the average of the product of $\epsilon_a(t)$ with any realizable functional of x(t) is zero, since

$$\overline{\epsilon_a(t) \int_0^\infty \cdots \int_0^\infty g_n(\tau_1, \ldots, \tau_n)\, x(t-\tau_1) \cdots x(t-\tau_n)\, d\tau_1 \cdots d\tau_n}$$

$$= \int_0^\infty \cdots \int_0^\infty g_n(\tau_1, \ldots, \tau_n)\, \overline{\epsilon_a(t)\, x(t-\tau_1) \cdots x(t-\tau_n)}\, d\tau_1 \cdots d\tau_n = 0. \tag{15}$$

By use of this result, we can now show that no other nonlinear system of the Wiener class can have a mean-square error smaller than $\overline{\epsilon_a^2(t)}$ so that the System A is the optimum system. To show this, we consider another system B with the output $y_b(t)$ for the input x(t). Let $\{g_n\}$ be the set of Wiener kernels of System B so that

$$y_b(t) = \sum_{n=0}^{\infty} G_n[g_n, x(t)]. \tag{16}$$

The error, $\epsilon_b(t)$, obtained when using System B is

$$\epsilon_b(t) = z(t) - y_b(t)$$

$$= z(t) - y_a(t) + y_a(t) - y_b(t)$$

$$= \epsilon_a(t) + y_a(t) - y_b(t). \tag{17}$$

The mean-square error thus can be written

$$\overline{\epsilon_b^2(t)} = \overline{\epsilon_a^2(t)} + \overline{[y_a(t)-y_b(t)]^2} + \overline{2\epsilon_a(t)\,[y_a(t)-y_b(t)]}. \tag{18}$$

Now

$$y_a(t) - y_b(t) = \sum_{n=0}^{\infty} G_n[h_n-g_n, x(t)]. \tag{19}$$

Thus by use of Eq. 15, the last term of Eq. 18 is zero and

$$\overline{\epsilon_b^2(t)} = \overline{\epsilon_a^2(t)} + \overline{[y_a(t)-y_b(t)]^2}. \tag{20}$$

From Eq. 20, $\overline{\epsilon_b^2(t)}$ is a minimum if $y_b(t) = y_a(t)$ which implies that System B is identical with System A. Thus no other system can have a mean-square error smaller than $\overline{\epsilon_a^2(t)}$ and System A with the Wiener kernels given by Eq. 7 is the optimum system. If no two σ's are equal, it can be shown that F in Eq. 4 is zero so that Eq. 3 follows from Eq. 7 and our result is proved.

To develop a procedure of measurement that is valid for all values of the σ's, we need not construct the functional F in Eq. 4. The restriction in (3) on the equality of the σ's arises from the presence of G-functionals of order lower than n which produce an impulse when two or more σ's are equal.[1] For example, the restriction in the determination of h_2 is due to G_o which produces an impulse when $\sigma_1 = \sigma_2$. From (3), $G_o[h_o, x(t)] = \overline{z(t)}$. Hence if we subtract G_o from the desired output, we have

$$h_2(\sigma_1,\sigma_2) = \frac{1}{2!K^2}\,\overline{\{z(t)-G_o[k_o, x(t)]\}\,x(t-\sigma_1)\,x(t-\sigma_2)}$$

$$\sigma_1,\sigma_2 \geq 0 \quad \text{including } \sigma_1 = \sigma_2. \tag{21}$$

In general, when we determine the n^{th}-order kernel, all of the lower order kernels have been determined so that all of the G-functionals of order less than n could be formed. For the determination of h_n, instead of (3) we would have the unrestricted expression

$$h_n(\sigma_1,\ldots,\sigma_n) = \frac{1}{n!K^n}\,\overline{\left\{z(t) - \sum_{m=0}^{n-1} G_m[h_m, x(t)]\right\} x(t-\sigma_1)\ldots x(t-\sigma_n)}$$

$$\sigma_i \geq 0 \qquad i = 1,2,\ldots,n \tag{22}$$

in which there is no restriction on the equality of the σ's

2. Optimum Systems with Non-White Gaussian Inputs

The theory that has been presented can be generalized to the case for a non-white Gaussian process. Consider that the optimum nonlinear system N shown in Fig. XIII-2 is to be determined for a desired output z(t) and an input, v(t), which is a non-white Gaussian process for which the power density spectrum is factorable.[2] It can be written

$$\Phi_{vv}(\omega) = \Phi^{+}_{vv}(\omega)\ \Phi^{-}_{vv}(\omega) \tag{23}$$

in which $\Phi^{+}_{vv}(\omega)$ is the complex conjugate of $\Phi^{-}_{vv}(\omega)$; also all of the poles and zeros of $\Phi^{+}_{vv}(\omega)$ are in the left-half of the complex s-plane in which $s = \sigma + j\omega$. Thus $\Phi^{+}_{vv}(\omega)$ and $\frac{1}{\Phi^{+}_{vv}(\omega)}$ are each realizable as the transfer function of a linear system. We then can

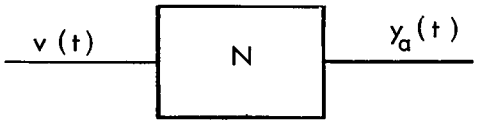

Fig. XIII-2. Nonlinear system with non-white Gaussian input.

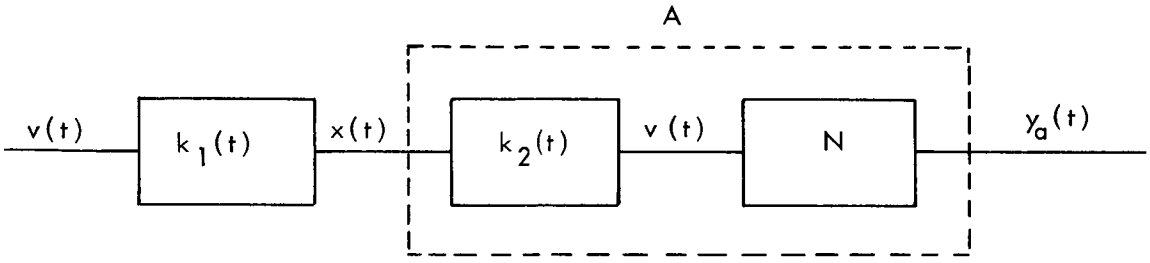

Fig. XIII-3. Equivalent form of the nonlinear system N.

consider the system of Fig. XIII-2 in the equivalent form shown in Fig. XIII-3 in which the transfer functions of the two linear systems $k_1(t)$ and $k_2(t)$ are

$$K_1(\omega) = \frac{1}{\Phi^{+}_{vv}(\omega)} \tag{24}$$

and

$$K_2(\omega) = \Phi^{+}_{vv}(\omega) \tag{25}$$

Also as shown, the system A is the system formed by the tandem connection of the linear system $k_2(t)$ and the system N. We observe that x(t), the input to the system A, is a white Gaussian process whose power density spectrum is 1 watt per radian per second;

the output of the system A is $y_a(t)$. The Wiener kernels of the optimum nonlinear system A for which the mean-square error, $\overline{\epsilon_a^2(t)} = \overline{[z(t)-y_a(t)]^2}$ is a minimum, according to Eq. 3, are

$$h_n(\sigma_1,\ldots,\sigma_n) = \frac{(2\pi)^n}{n}\,\overline{z(t)\,x(t-\sigma_1)\ldots x(t-\sigma_n)} \qquad \text{for } \sigma_i \geq 0 \qquad i = 1,2,\ldots,n \quad n = 0,1,2,\ldots \tag{26}$$

except when two or more σ's are equal. The resulting system N is the optimum nonlinear system. To show this, we first observe that

$$\overline{\epsilon_a(t)\,v(t-\sigma_1)\ldots v(t-\sigma_n)} = 0 \qquad \text{for } \sigma_i \geq 0 \qquad i = 1,2,\ldots,n \quad n = 0,1,2,\ldots \tag{27}$$

This result is obtained by substituting the relation

$$v(t) = \int_0^\infty k_2(\sigma)\,x(t-\sigma)\,d\sigma \tag{28}$$

in Eq. 27 and making use of Eq. 10. By the use of Eq. 27 and an argument identical with that given for a white Gaussian process, it is easy to show that no other system can have a mean-square error smaller than $\overline{\epsilon_a^2(t)}$ so that the system N is the optimum system.

The desired crosscorrelation function of Eq. 26 can be expressed in terms of only v(t) by substituting the relation

$$x(t) = \int_0^\infty k_1(\sigma)\,v(t-\sigma)\,d\sigma \tag{29}$$

in Eq. 26. The result is

$$\overline{z(t)\,x(t-\sigma_1)\ldots x(t-\sigma_n)} = \int_0^\infty k_1(\tau_1)\,d\tau_1 \ldots \int_0^\infty k_1(\tau_n)\,d\tau_n\,\overline{z(t)\,v(t-\sigma_1-\tau_1)\ldots v(t-\sigma_n-\tau_n)}. \tag{30}$$

other forms and interpretations for this crosscorrelation function have been given elsewhere.[3]

M. Schetzen

References

1. Y. W. Lee and M. Schetzen, "Measurement of the Kernels of a Nonlinear System by Crosscorrelation," Quarterly Progress Report No. 60, Research Laboratory of Electronics, M.I.T., January 15, 1961, pp. 126-129.
2. Y. W. Lee, Statistical Theory of Communication (John Wiley and Sons, Inc., New York, 1960), Chap. 14, Sec. 8.

3. M. Schetzen, "Measurement of the Kernels of a Nonlinear System by Crosscorrelation with Gaussian Non-White Inputs," Quarterly Progress Report No. 63, Research Laboratory of Electronics, M.I.T., October 15, 1961, pp. 113-117; also see Errata, Quarterly Progress Report No. 64, Research Laboratory of Electronics, M.I.T., January 15, 1962, p. 163.

C. USEFUL APPROXIMATIONS TO OPTIMUM QUANTIZATION

The quantization of random signals has been considered by Max[1] and, more recently, by Bruce.[2] Max considers the selection of an optimum step size in a uniform quantizer and also the determination of the optimum nonuniform quantizer and carries out computations for a Gaussian input and a mean-square distortion measure. Bruce gives a computer algorithm for the determination of the optimum nonuniform quantizer for an arbitrary distortion measure. These exact approaches to quantization give little insight and confront someone who has a new quantization problem with a considerable amount of digital computation. Schteyn[3] and Roe[4] have proposed approximations to the optimum nonuniform quantizer which are of practical interest. In this report we present useful approximations to the optimum quantizer and to the resulting distortion in uniform and nonuniform quantization for arbitrary distortion measures.

1. Uniform Quantization

The equation for the quantization step that minimizes the distortion has been given by Max[1] and can be solved on a computer by an iterative procedure. Here we obtain a simple solution by using the following facts.

1. The first-order effect will be due to the truncation of the tail of the distribution.
2. Except for the tails, the probability density of the signal can be simply approximated between successive quantization steps.

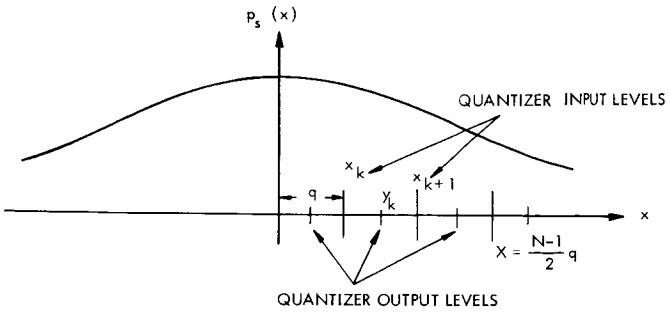

Fig. XIII-4. Uniform quantizer.

Consider Fig. XIII-4 which illustrates the problem. It is clear that a difficulty in selecting the step size will occur whenever the signal probability density has a long tail. Let D_k be the conditional distortion whenever the input signal, x, is between the input

quantizer levels of x_k and x_{k+1}, and let the probability of this event be p_k. Let W(e) be an even error-weighting function and $W_1(e)$, its antiderivative. Then D_k is given approximately by

$$D_k = \frac{2W_1\left[\frac{q}{2}\right]}{q} \tag{1}$$

in which q is the size of the uniform step. This result is easily obtained by assuming that the $p_s(x)$ is well approximated by a straight line between x_k and x_{k+1}. Since D_k is independent of k, we have

$$D = \sum_k p_k D_k + p_T D_T \tag{2}$$

in which D_T is the distortion in the tails. Let p_T be the probability of the tails. We have then

$$\sum_k p_k = 1 - p_T$$

from which we obtain

$$D = \frac{2W_1\left[\frac{q}{2}\right]}{q}\left[1 - \int_{-\infty}^{\frac{N-1}{2}q} p_s(x)\,dx - \int_{\frac{N-1}{2}q}^{\infty} p_s(x)\,dx\right]$$

$$+ \int_{-\infty}^{-\frac{N-1}{2}q} W\left[x + \frac{N-1}{2}q\right] p_s(x)\,dx + \int_{\frac{N-1}{2}q}^{\infty} W\left[x - \frac{N-1}{2}q\right] p_s(x)\,dx \tag{3}$$

when $p_s(x)$ is even we have the simpler expression

$$D = 2W_1\left[\frac{q}{2}\right]\left[1 - 2\int_{\frac{N-1}{2}q}^{\infty} p_s(x)\,dx\right] + 2\int_{\frac{N-1}{2}q}^{\infty} W\left[x - \frac{N-1}{2}q\right] p_s(x)\,dx. \tag{4}$$

Equation 4 is an approximate expression for the distortion as a function of the step size and has to be minimized by proper choice of q. We could formally set the derivative equal to zero, but it is generally quite simple to obtain D as a function q and get an idea of the sensitivity of the distortion to the step size. In Fig. XIII-5 we give as an illustration the distortion versus the quantization range $x = \frac{N-1}{2}q$ for a Gaussian probability density, a mean-square distortion measure, and 8 quantization steps. We observe that the curve has a well-marked minimum and that the proper choice of step size is definitely worthwhile. Equation 4 gives

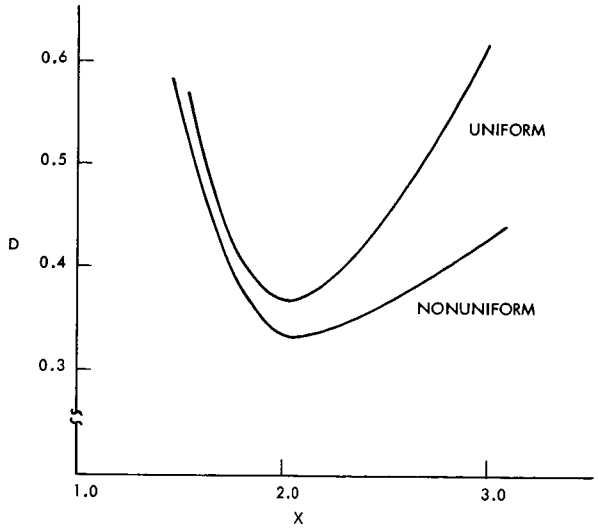

Fig. XIII-5. Distortion vs quantization range.

minimum distortions in good agreement (within 0.2 db) with the exact values given by Max for a Gaussian probability density.

2. Nonuniform Quantization

We consider the nonuniform quantizer to be the cascade of two nonlinear devices and of a uniform quantizer as shown in Fig. XIII-6. For a given uniform quantizer and a given signal probability density $p_s(x)$ the two nonlinear devices f( ) and g( ) are chosen

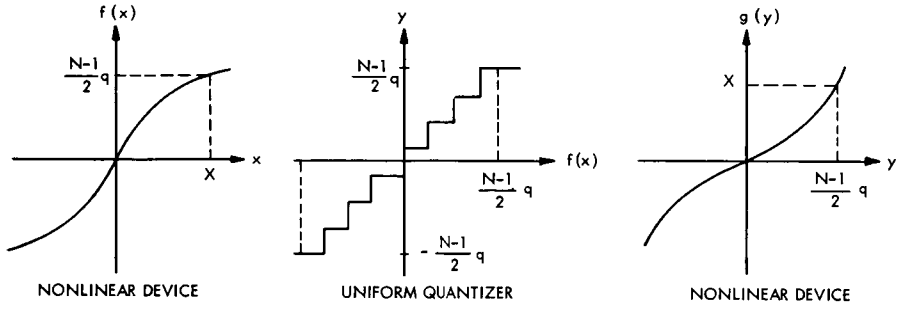

Fig. XIII-6. Nonuniform quantizer.

so as to minimize the distortion $D = E\{W[s-g(y)]\}$. The distortion D is made up of two parts: (i) distortion D_n obtained within the range of the uniform quantizer, and (ii) distortion in the tails D_T for which the nonlinear devices f( ) and g( ) are completely ineffective.

The distortion D_n can be conveniently discussed in terms of an analog model in which

the uniform quantizer is replaced by additive noise. We obtain an expression for the minimum D_n as a function of X such that $f(X) = \frac{N-1}{2} q$. The optimum selection of X is then done as for uniform quantization by trading off between D_n and D_T.

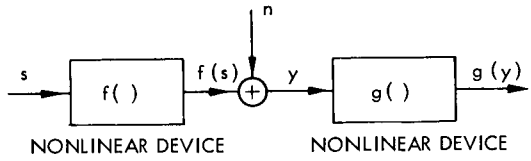

Fig. XIII-7. Analog model.

Consider the analog system shown in Fig. XIII-7. The additive, statistically independent noise, n, models the effect of the uniform quantizer. Note that Widrow[5] has shown that the quantization noise was independent of the signal for a large number of quantization levels. Here again the nonlinear devices f( ) and g( ) are chosen so as to minimize the distortion.

$$D_n = E\{W[s-g(y)]\}.$$

To keep the problem relevant to quantization we shall assume that the noise is small, and it can then be shown that f( ) and g( ) are inverses.

We can now solve easily the analog filtering problem. We write

$$D_n = \iint W\{g[f(x)+\beta]-x\}\, p_s(x)\, p_n(\beta)\, dx d\beta. \tag{5}$$

For small noise we have

$$g[f(x)+\beta] \approx g[f(x)] + \beta g'[f(x)].$$

But since f( ) and g( ) are inverses

$$g[f(x)] = x \qquad g'[f(x)] = \frac{1}{f'(x)}$$

and we have

$$D_n = \iint W\left[\frac{\beta}{f'(x)}\right] p_s(x)\, p_n(\beta)\, dx d\beta. \tag{6}$$

To proceed with an arbitrary error-weighting function W(e) we have to model the noise as uniform from $-q/2$ to $q/2$; again, this is a reasonable model quantization noise.[5] Then we carry out the integral with respect to β and use the calculus of variations to minimize D_n by proper choice of f( ). More specific results can be obtained whenever

$$W\left[\frac{\beta}{f'(x)}\right] = W[\beta]\, W\left[\frac{1}{f'(x)}\right] \tag{7}$$

which is the class of error-weighting functions $W(e) = |e|^c$. We have then

$$D_n = \int |\beta|^c \, p_n(\beta) \, d\beta \int \frac{p_s(x)}{[f'(x)]^c} \, dx. \tag{8}$$

It can be shown by the calculus of variations that D_n is minimized by taking

$$f(x) = K_1 \int [p_s(x)]^{\frac{1}{c+1}} \, dx + K_2 \tag{9}$$

which corresponds to Roe's expression for the approximate quantizer. The constants K_1 and K_2 have to be chosen to give the best fit for the quantization problem. Roe examines the behavior of the exact quantizer for a large number of levels and large inputs (mean-square error) and determines accordingly the approximate quantizer. Pace[6] selected the constant so as to match the exact two-level quantizer. We proceed here as for uniform quantization and obtain an approximate expression for the resulting distortion. Note that under the approximation that the probability density at the input of the uniform quantizer is piecewise linear, we have again

$$\int |\beta|^c \, p_n(\beta) \, d\beta = \frac{2W_1\left[\frac{q}{2}\right]}{q} = \frac{q^c}{2^c(c+1)}.$$

Now we select K_1 and K_2 in Eq. 9 to give the total range of the uniform quantizer. From Fig. XIII-5 we have

$$f(x_2) - f(x_1) = (N-1)q$$

from which we get

$$f'(x) = \frac{(N-1)\, q[p_s(x)]^{\frac{1}{c+1}}}{\int_{x_1}^{x_2} [p_s(x)]^{\frac{1}{c+1}} \, dx} \tag{10}$$

and by substituting Eq. 10 in Eq. 8 we obtain

$$D_n = \frac{1}{2^c(c+1)(N-1)^c} \left[\int_{x_1}^{x_2} [p_s(x)]^{\frac{1}{c+1}} \, dx \right]^{c+1}. \tag{11}$$

If we take into account the probability of occurrence of D_n and D_T, we have

$$D = D_n\left[1 - \int_{-\infty}^{x_1} p_s(x)\,dx - \int_{x_2}^{\infty} p_s(x)\,dx\right] + \int_{-\infty}^{x_1} |x-x_1|^c\, p_s(x)\,dx$$

$$- \int_{x_2}^{\infty} |x-x_2|^c\, p_s(x)\,dx \tag{12}$$

For an even signal probability density we have $x_2 = -x_1 = X$, and

$$D = \frac{2}{(c+1)(N-1)^c}\left[\int_0^X [p_s(x)]^{\frac{1}{c+1}}\,dx\right]^{c+1}\left[1 - 2\int_X^{\infty} p_s(x)\,dx\right]$$

$$+ 2\int_X^{\infty} |x-X|^c\, p_s(x)\,dx \tag{13}$$

which has to be minimized by proper choice of X. Once X is determined, we have

$$f(x) = \frac{(N-1)q\int_0^x [p_s(a)]^{\frac{1}{c+1}}\,da}{2\int_0^X [p_s(a)]^{\frac{1}{c+1}}\,da}. \tag{14}$$

Note that the step size of the uniform quantizer will not affect the resulting nonuniform quantizer.

As an example we consider a Gaussian signal, mean-square error and 8 quantization steps. The distortion versus X is shown in Fig. XIII-5, and its minimum is in good agreement with the value given by Max.

3. Uniform Versus Nonuniform Quantization

By comparing the distortion for uniform and nonuniform quantization in Fig. XIII-5, it appears that there is little to be gained by nonuniform quantization and the added complexity in equipment. To discuss this point more generally we consider again Eqs. 4 and 13. If we rewrite Eq. 4 for $W(e) = |e|^c$ and take $X = \frac{N-1}{2}q$ we have for uniform quantization

$$D_u = \frac{X^c}{(N-1)(c+1)}\left[1 - 2\int_X^{\infty} p_s(x)\,dx\right] + 2\int_X^{\infty} |x-X|^c\, p_s(x)\,dx. \tag{15}$$

By comparing Eqs. 15 and 13, we see that the two expressions are quite similar except for the two factors

$$F_u \triangleq X^c$$

$$F_{nu} \triangleq 2\left[\int_0^X [p_s(x)]^{\frac{1}{c+1}}\, dx\right]^{c+1}.$$

The factors F_u and F_{nu} affect the distortion within the quantization range. It can be shown that F_{nu} is maximized by a signal probability density $p_s(x)$ that is uniform between -X and X. We then have $F_{nu} = X^c$ as expected. An indication of the effect of nonuniform quantization can be obtained by forming the ratio $F(X) = F_{nu}/F_u$ of the quantization errors within the quantization range. For a Gaussian $p_s(x)$ and large X we obtain

$$F(X) = \frac{[2\pi\sigma^2(c+1)]^{\frac{c+1}{2}}}{X^c}.$$

Since F(X) goes to zero as X goes to infinity, we obtain a large improvement in distortion by nonuniform quantization as N goes to infinity. Note, however, that $D_{nu}/D_u = 0.7$ for N = 36 and c = 2; therefore, the asymptotic behavior is not too meaningful here.

V. R. Algazi

References

1. J. Max, "Quantizing for Minimum Distortion," IRE Trans., Vol. IT-6, No. 1, pp. 7-12, March 1960.
2. J. D. Bruce, "Optimum Quantization," Technical Report 429, Research Laboratory of Electronics, M.I.T., Cambridge, Massachusetts, March 1, 1965.
3. V. M. Schteyn, "On Group Transmission with Frequency Division of Channels by the Pulse Code Modulation Method," Telecommunications (Russian) 1959, pp. 178-180.
4. G. M. Roe, "Quantizing for Minimum Distortion," IEEE Trans., Vol. IT-10 (Letter), October 1964.
5. B. Widrow, "A Study of Rough Amplitude Quantization by Means of Nyquist Sampling Theory," Sc.D. Thesis, Department of Electrical Engineering, Massachusetts Institute of Technology, 1956.
6. M. O. Pace, "Predistortion in No-Memory Filtering and in Quantization," E.E. Thesis Massachusetts Institute of Technology, June 1965.

D. TIME JITTER IN TUNNEL DIODE THRESHOLD-CROSSING DETECTORS

In Quarterly Progress Report No. 78 a model was presented which describes the time jitter arising in a tunnel diode threshold-crossing detector.[1] Analysis of the model by dimensional methods indicated close agreement with experimental observations. Since then a more complete and exact analysis of this model has been performed with the help of the IBM 7094 computer. It has been predicted that the jitter should have a Gaussian distribution. The mean and standard deviation of this distribution is related to the

shot noise that is present near the peak of the tunnel diode i-v relation, to the slope of the input signal, and to other circuit parameters. This predicted behavior agrees closely with experimental measurements made thus far.

In this report we shall outline the method used in analyzing the model, discuss the derived results, and present comparisons of these results with experimental observations.

1. Model for Predicting Switching Jitter

The model[1] used for predicting the switching behavior is shown in Fig. XIII-8. The circuitry to the right of the input current source is a commonly accepted model for the

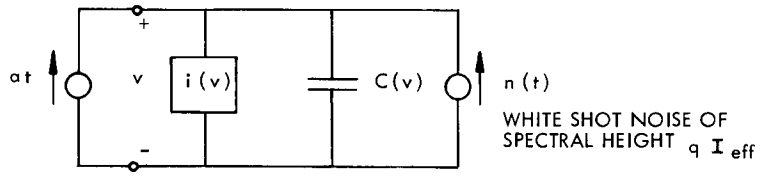

Fig. XIII-8. Equivalent-circuit model for tunnel-diode threshold detector.

tunnel diode.[2,3] Lead inductance and resistance are neglected. We consider i(v), the familiar static tunnel diode i-v curve, to be an instantaneous relation between i and v. The total capacitance across the junction, C(v), is considered to be constant and equal to C in the vicinity of the current peak. I_{eff} is the effective shot noise current, and in the region near the peak is approximately equal to the actual tunnel diode current.

Using Kirchhoff's current law, we may write for the network of Fig. XIII-8

$$C \frac{dv}{dt} + i(v) = \alpha t + n(t). \tag{1}$$

If we translate our coordinate system so that its origin is at the peak of i(v) and fit a parabola to the curve at that point, we obtain a new i-v relation

$$i(v) = -kv^2, \tag{2}$$

where k is a measure of the curvature at the tunnel diode peak, and v and t are understood to be new variables. Substituting this new relation in (1), we obtain

$$C \frac{dv}{dt} - kv^2 = \alpha t, \tag{3}$$

where n(t) is white noise of spectral height, N_o. It is from this "switching" equation that the statistics of the jitter are derived.

2. Analysis of the Switching Equation (3)

By suitably grouping the parameters a, k, and C, we obtain the new dimensionless variables

$$v' = \left(\frac{k^2}{Ca}\right)^{1/3} v$$

$$t' = \left(\frac{ka}{C^2}\right)^{1/3} t \tag{4}$$

$$N_o' = \frac{k}{C^2 a} N_o.$$

By substituting these variables in Eq. 3, we obtain the dimensionless equation

$$\frac{dv'}{dt'} - v'^2 = t' + n'(t'), \tag{5}$$

where $n'(t')$ is white noise of spectral height N_o'.

A property of this equation is that if the right side is negative, then $v'(t')$ will tend to some stable finite value. If the right side becomes positive, then $v'(t')$ will grow until it reaches infinity at some finite time. We shall consider this to be the time at which the tunnel diode switches and denote it by the variable T_s'.

For a given set of initial conditions and $n'(t') = 0$ the system will always "switch" at the same time, T_s. When noise is added, however, T_s becomes a random variable, taking on values distributed around some mean. We shall call this distribution of T_s',

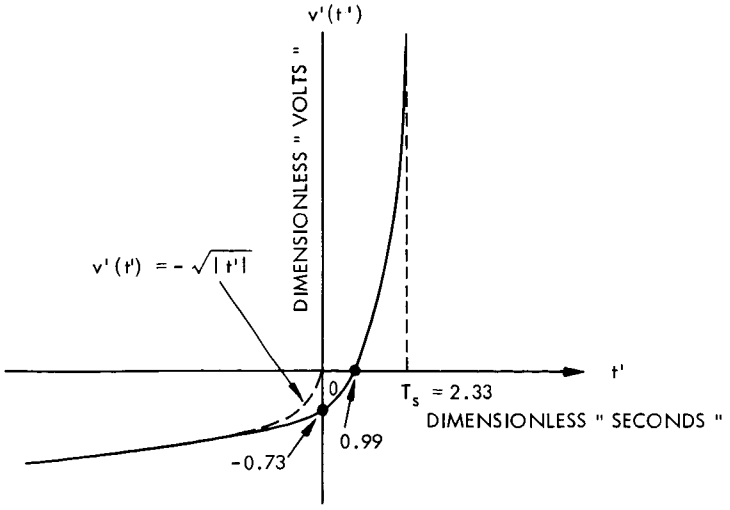

Fig. XIII-9. Solution of the dimensionless switching equation with $n'(t') = 0$.

$P_{T'_s}(\tau'; N'_o)$, where τ' is a range variable for T'_s. The distribution will depend on the noise spectral height N'_o and also on the initial conditions.

We shall henceforth take the initial conditions to be those for which the system would be in "equilibrium" at a large negative time t_o:

$$v'_o = -\sqrt{|t'_o|} \,. \tag{6}$$

These initial conditions ensure that the operating point essentially follows the curve i'(v') until the region of switching is reached. The solution for these conditions and no noise is shown in Fig. XIII-9.

With noise present the standard deviation and mean of T'_s will be functions of N'_o. We shall denote these functions by $\sigma'_T(N'_o)$ and $\overline{T'_s}(N'_o)$. The computation of these functions will be described.

3. Computer Solution of the Switching Equation

The computation was performed using the Fortran language on the IBM 7094 computer. The dimensionless switching Eq. 5 was solved by using standard one-step difference methods. Noise was introduced by adding a random number at each iteration of the difference equation. The random number sequence was obtained by using the "RANNOF" routine. This routine generates a pseudo-random sequence of numbers that are uniformly distributed from 0 to 1 and which, for our purposes, can be considered to be mutually independent. The sequence was then adjusted to have zero mean and to have a variance corresponding to a given spectral height N'_o.

The computation was started far enough back in time, subject to the initial conditions of (6), to ensure that the process would appear to have been going indefinitely. When v'(t') became large enough to ensure that the noise would have negligible effect on the future course of the signal, the computation was stopped and the final values of v' and t' were substituted in an asymptotic form of the solution that is valid for large v'. From this asymptotic form the switching time T_s could be obtained.

N'_o was set to some specified value and this solution procedure was carried out 1000 times, resulting in that many values of the random variable T'_s. By means of standard computing techniques, the mean, standard deviation, and distribution of T'_s were calculated. These statistics were obtained for N'_o varying over a range that was slightly wider than that covered in the actual measurements.

4. Results of the Computation

Graphs of $\sigma'_T(N'_o)$ and $\overline{T'_s}(N'_o)$ are presented in Figs. XIII-10 and XIII-11. The fact that $\sigma'_T(N'_o)$ varies linearly with $\sqrt{N'_o}$ indicates that the result obtained previously[1] by assuming this linearity is valid at least over the range of the present computation. It

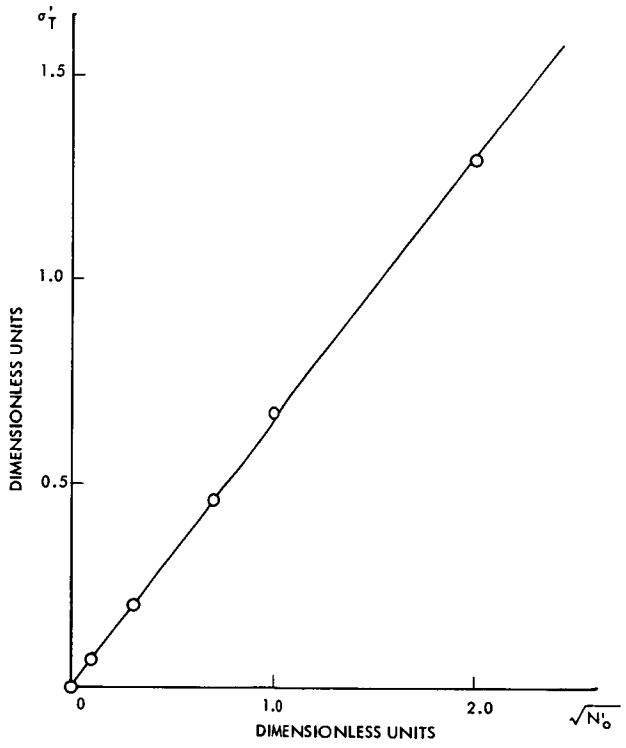

Fig. XIII-10. Jitter standard deviation σ'_T vs $\sqrt{N'_o}$ (in dimensionless units).

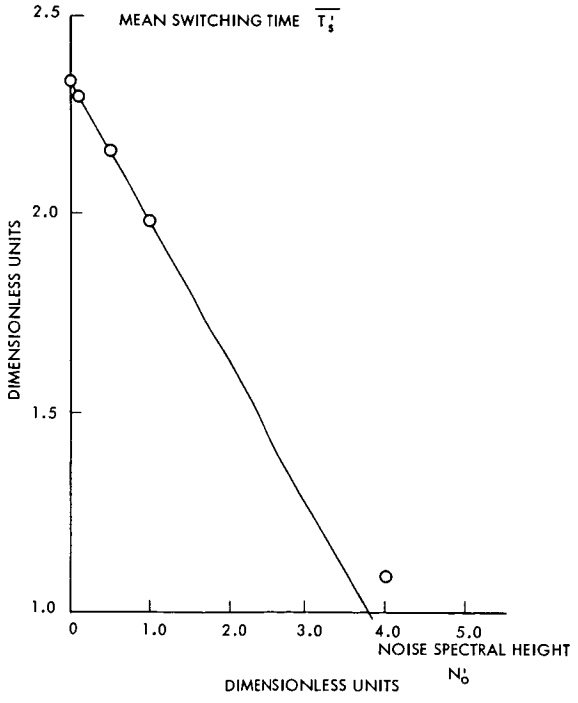

Fig. XIII-11. Mean switching time $\overline{T'_s}$ vs N'_o (in dimensionless units).

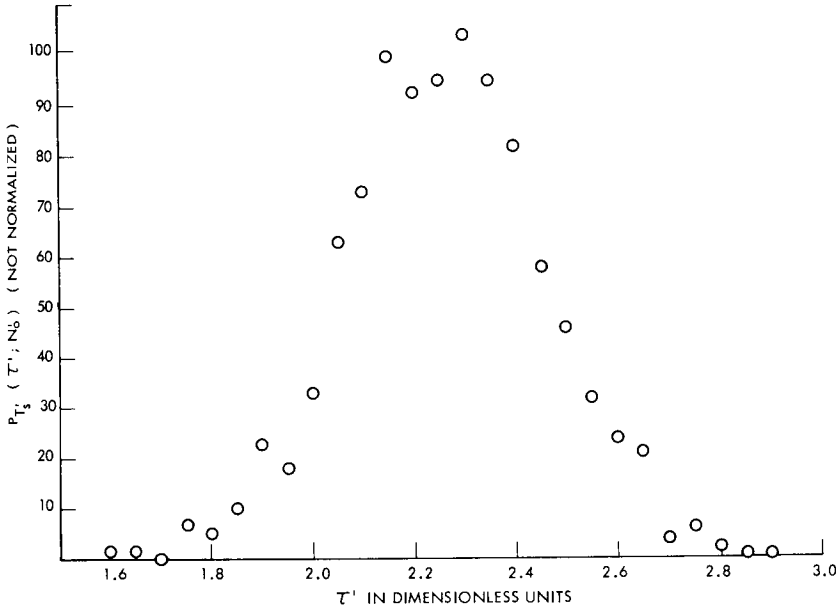

Fig. XIII-12. Un-normalized form of $P_{T_s'}$ vs $(\tau'; N_o')$ for $N_o' = 0.1$.

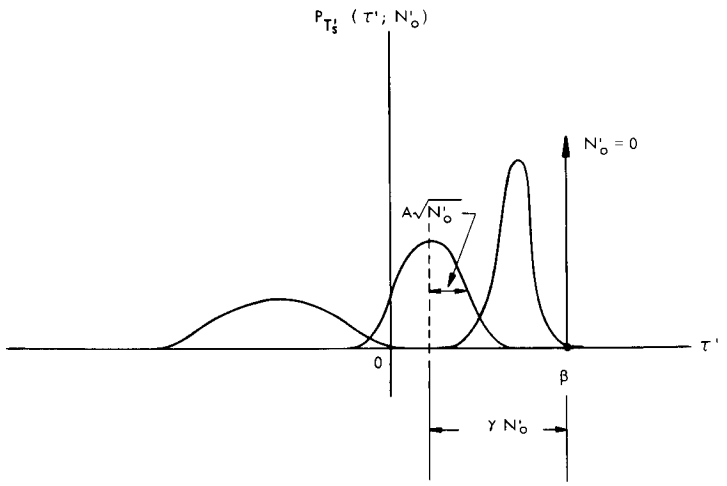

Fig. XIII-13. Gaussian-shaped distribution function moves toward the left and grows wider as noise N_o is increased.

is interesting that, on the average, switching occurs earlier as noise is increased. The advance in the mean switching time is directly proportional to N_o'.

It appears that $T_s'(N_o')$ is beginning to deviate from its linear behavior at large values of N_o'. Since the required computation time increases with $\sqrt{N_o'}$, we have hesitated to push the range further until we are certain that an analytic solution could not be obtained by some other method. Knowledge of how this linear behavior breaks down (if it does) would be useful for a complete description of the statistical behavior of the jitter.

Within the accuracy of the statistics, the distributions obtained were Gaussian. A typical distribution is shown in Fig. XIII-12.

The functions $\sigma_T'(N_o')$ and $\overline{T_s'}(N_o')$ can be approximated analytically from Figs. XIII-10 and XIII-11 by

$$\sigma_T'(N_o') = A\sqrt{N_o'}$$

and (7)

$$\overline{T_s'}(N_o') = \beta - \gamma N_o',$$

where A, β, and γ are constants.

Using these forms, we can express the jitter distribution analytically as

$$P_{T_s'}(\tau'; N_o') = \frac{1}{\sqrt{2\pi N_o'}\,A} \exp - \frac{1}{2}\left[\frac{(\tau'-\beta+\gamma N_o')^2}{A^2 N_o'}\right]. \tag{8}$$

The behavior of $P_{T_s'}(\tau'; N_o')$ with increasing noise is shown in Fig. XIII-13. It is interesting to note that $P_{T_s'}(\tau'; N_o')$ satisfies the equation for diffusion in a moving medium. Thus far we have not been able to relate this diffusion equation to the switching process in any fundamental manner.

5. Transformation of $\sigma_T'(N_o')$ and $\overline{T_s'}(N_o')$ back into the Dimensional Domain

Using the relations of Eq. 4, we can transform $\sigma_T'(N_o')$ and $\overline{T_s'}(N_o')$ back into the dimensional domain and thus relate the jitter statistics to the circuit parameters a, C, k, and N_o. Performing this operation, we obtain

$$\sigma_T = \frac{A N_o^{1/2} k^{1/6}}{a^{5/6} C^{1/3}} \tag{9}$$

and

$$\overline{T_s} = \beta\left(\frac{C^2}{ka}\right)^{1/3} - \gamma\left(\frac{k^{2/3} N_o}{C^{4/3} a^{4/3}}\right). \tag{10}$$

The distribution of the jitter can be obtained as a function of the circuit parameters by substituting σ_T and $\overline{T_s}$ in the Gaussian distribution

$$p(\tau) = \frac{1}{\sqrt{2\pi}\,\sigma_T} \exp\left[-\frac{1}{2}\frac{(\tau-\overline{T_s})^2}{\sigma_T^2}\right]. \tag{11}$$

6. Comparison of Results with Experimental Observations

Using the value of A determined from Fig. XIII-11 and values of N_o, C, and k corresponding to those existing in a circuit studied experimentally, we plot the relation between σ_T and a expressed by Eq. 9. Experimentally measured points superimposed on this curve are shown in Fig. XIII-14.

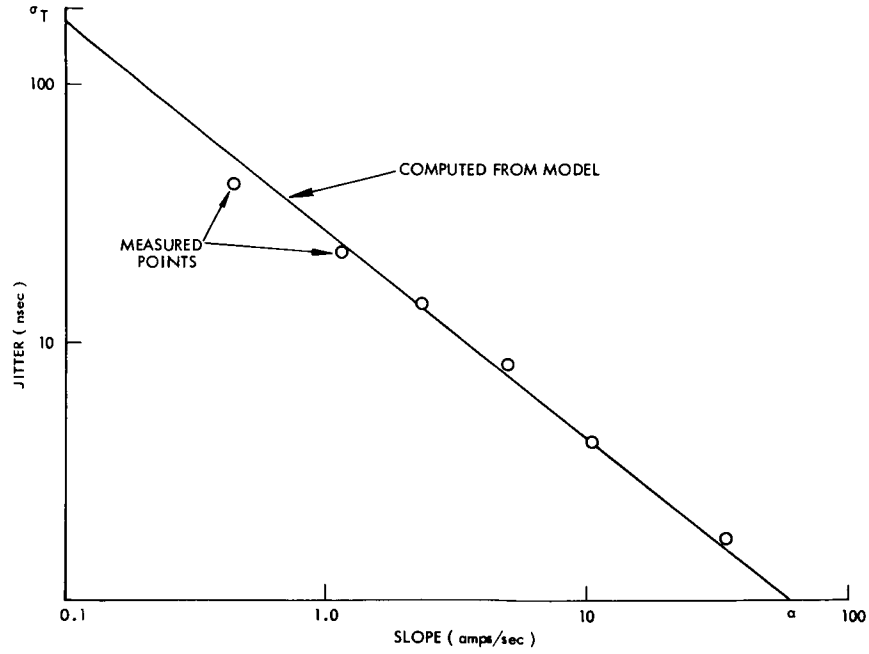

Fig. XIII-14. Jitter standard deviation σ_T vs slope a: a comparison between behavior predicted by model and experimentally observed behavior.

The experimentally measured distributions were Gaussian.[1] This observation is in agreement with the results obtained from the model.

We have not yet checked the validity of (10) experimentally. Since a differential method was used for measuring the switching jitter, all information concerning the mean T_s was cancelled out.

This work was done partly at the Computation Center of the Massachusetts Institute

of Technology, Cambridge, Massachusetts.

D. E. Nelsen

References

1. D. E. Nelsen, "Time Jitter in Tunnel Diode Threshold-Crossing Detectors," Quarterly Progress Report No. 78, Research Laboratory of Electronics, M. I. T., July 15, 1965, pp. 178-188.

2. R. A. Pucel, "The Equivalent Noise Current of Esaki Diodes," Proc. IRE 49, 49 (1961).

3. B. E. Turner and R. E. Burgess, "Direct Tunnel-Current Noise in Tunnel Diodes for Small Biases," Can. J. Phys. 42, 1046 (June 1964).

E. NONLINEAR MINIMUM-MEAN SQUARE FILTERING WITH APPLICATION TO ANALOG COMMUNICATION

The purpose of this report is to briefly describe an approach to nonlinear, minimum-mean-square filtering and estimation and to mention some applications of the approach which have been made to analog communications through randomly time-varying channels. The approach differs significantly from the linear, minimum-mean-square approach of Wiener[1] and of Kalman and Bucy[2] because the estimate is not restricted to being a linear transformation of the observed process. On the other hand, the approach bears a resemblance to the technique of Kalman and Bucy, rather than to the more classic technique of Wiener, because of the use of the state variable representation of random processes. This representation is used because it is the most convenient way to represent continuous Markov processes, upon which the approach is theoretically based, and also because it allows the consideration of multilevel estimation problems without any added theoretical or manipulative difficulties.

The results presented here are an extension of those of Snyder[3] for the scalar case. The procedure closely parallels that used for the simpler case.

1. Notation

Underscored, lower-case letters denote column vectors and capital letters denote matrices. Supperscript "τ" and "-1" denote transpose and inverse. The exact and approximate minimum-mean-square estimates of $\underline{x}(t)$ are denoted by $\hat{\underline{x}}_{mv}(t)$ and $\underline{x}^{*}_{mv}(t)$, respectively.

$D[\underline{f}(t:\underline{x})]$ denotes the Jacobian associated with any vector $\underline{f}[t:\underline{x}(t)]$ whose components are memoryless transformations of $\underline{x}(t)$. The i-row, j-column element of $D[\underline{f}(t:\underline{x})]$ is $\frac{\partial}{\partial x_i} f_j(t:\underline{x})$.

2. Estimation Model and Equation for $\underline{x}^*_{mv}(t)$

Define the two vector processes, $\underline{x}(t)$ and $\underline{y}(t)$, by

$$d\underline{x}(t) = F\,\underline{x}(t)\,dt + d\underline{\chi}(t) \tag{1}$$

$$d\underline{y}(t) = \underline{g}[t:\underline{x}(t)]\,dt + d\underline{\eta}(t) \tag{2}$$

where the components of $\underline{\chi}(t)$ and $\underline{\eta}(t)$ are Wiener processes and

$$E[\underline{\chi}(t)\,\underline{\chi}^T(t)] = X \min(t,u) \tag{3}$$

$$E[\underline{\eta}(t)\,\underline{\eta}^T(t)] = N \min(t,u). \tag{4}$$

Here, $\underline{\chi}(t)$ and $\underline{\eta}(t)$ are assumed to be independent, $\underline{g}[t:\underline{x}(t)]$ represents a memoryless transformation of $\underline{x}(t)$. As defined by (1) and (2), $\underline{x}(t)$ and $\underline{y}(t)$ jointly form a continuous vector Markov process.

It is assumed that the observed process, $\underline{r}(t) = \frac{d}{dt}\underline{y}(t)$, is available from an initial time, t_0, until the present time, t. The observed waveform is denoted by $\underline{r}_{0,t}$.

Given $\underline{r}_{0,t}$ we seek to determine $\hat{\underline{x}}_{mv}(t)$. An equation for $\hat{\underline{x}}_{mv}(t)$ can be obtained in a straightforward way from the equation for the conditional probability density functional, $p(\underline{x};t|\underline{r}_{0,t})$, correctly derived by Kushner.[4] Using the fact that $\hat{\underline{x}}_{mv}(t)$ is the conditional mean, the result is

$$d\hat{\underline{x}}_{mv}(t) = F\,\hat{\underline{x}}_{mv}(t) + E[\{\underline{x}-\hat{\underline{x}}_{mv}(t)\}\underline{g}^T(t:\underline{x})]\,N^{-1}[d\underline{y}(t)-E\,\underline{g}(t:\underline{x})\,dt], \tag{5}$$

where the expectations are with respect to $p(\underline{x};t|\underline{r}_{0,t})$. An alternative expression for $\hat{\underline{x}}_{mv}(t)$ can be obtained by substituting the multidimensional Taylor expansion for $\underline{g}(t:\underline{x})$, which is assumed to exist, in (5). The resulting expression cannot be solved nor readily implemented. By assuming, however, that the error, $\underline{x} - \hat{\underline{x}}_{mv}(t)$, is small, an approximate estimate, $\underline{x}^*_{mv}(t)$, can be obtained. Keeping terms leading to the second moment of the error, we obtain

$$\frac{d}{dt}\underline{x}^*_{mv}(t) = F\,\underline{x}^*_{mv}(t) + VD\left[\underline{g}\left(t:\underline{x}^*_{mv}\right)\right]N^{-1}\{\underline{r}(t)-\underline{g}[t:\underline{x}^*_{mv}(t)]\}, \tag{6}$$

where $V = V(t)$ is an error-covariance matrix satisfying

$$\frac{d}{dt}V(t) = FV + VF^T + X + VD\left[D\left[\underline{g}\left(t:\underline{x}^*_{mv}\right)\right]N^{-1}\left\{\underline{r}(t)-\underline{g}\left(t:\underline{x}^*_{mv}\right)\right\}\right]V. \tag{7}$$

Under steady-state conditions (7) reduces to

$$0 = FV + VF^T + X - \overline{VD\left[\underline{g}\left(t:\underline{x}^*_{mv}\right)\right]N^{-1}D^T\left[\underline{g}\left(t:\underline{x}^*_{mv}\right)\right]V} \tag{8}$$

in which the bar indicates time or ensemble averaging which are assumed to be equivalent.

3. Communication Model

The communication model is shown in Fig. XIII-15. $\underline{a}(t)$ and $\underline{b}(t)$ are defined by

$$d\underline{a}(t) = F_a\, \underline{a}(t)\, dt + d\underline{\alpha}(t) \tag{9}$$

$$d\underline{b}(t) = F_b\, \underline{b}(t)\, dt + d\underline{\beta}(t), \tag{10}$$

where the components of $\underline{\alpha}(t)$ and $\underline{\beta}(t)$ are Wiener processes with the associated covariance matrices A min (t, u) and B min (t, u). $\underline{a}(t)$ and $\underline{b}(t)$ can represent one or more Gaussian processes occurring as messages and channel disturbances.

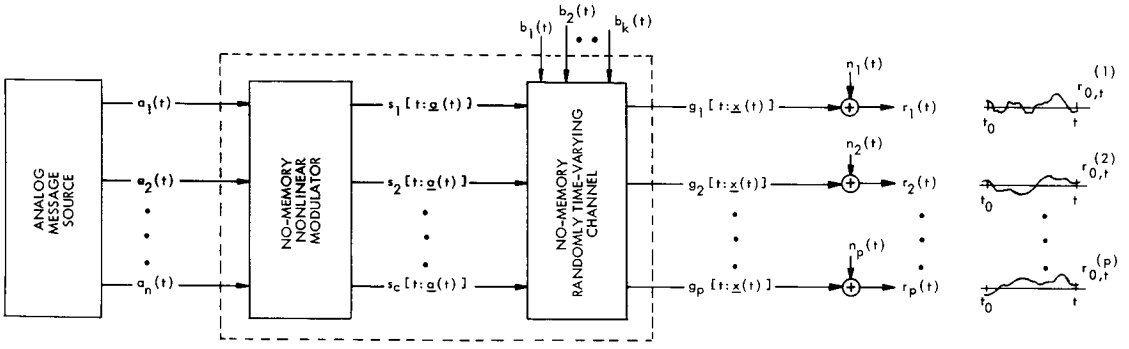

Fig. XIII-15. Communication model.

$\underline{a}(t)$ is transformed by a memoryless, nonlinear modulator into c signals represented by $\underline{s}[t:\underline{a}(t)]$. By a suitable interpretation of $\underline{a}(t)$, modulation schemes with memory, such as FM, fall within the scope of the model.

$\underline{s}[t:\underline{a}(t)]$ is transformed into p signals by the "randomly time-varying" portion of the channel. The resulting signals are represented by $\underline{g}[t:\underline{x}(t)]$ and are observed in additive white Gaussian noise.

The relationship between the estimation model and the communication model is evident when it is noted that $\underline{x}(t)$ represents the vector obtained by adjoining $\underline{a}(t)$ and $\underline{b}(t)$. $\underline{x}^*_{mv}(t)$ is then a vector whose elements are the approximate minimum-mean-square estimates of the message vector and channel-disturbance vector.

4. Examples

When $\underline{g}[t:\underline{x}(t)]$ is a linear transformation of x(t), the exact and approximate estimates are equal, and (6) and (7) reduce to the equations of Kalman and Bucy.[2] Communication

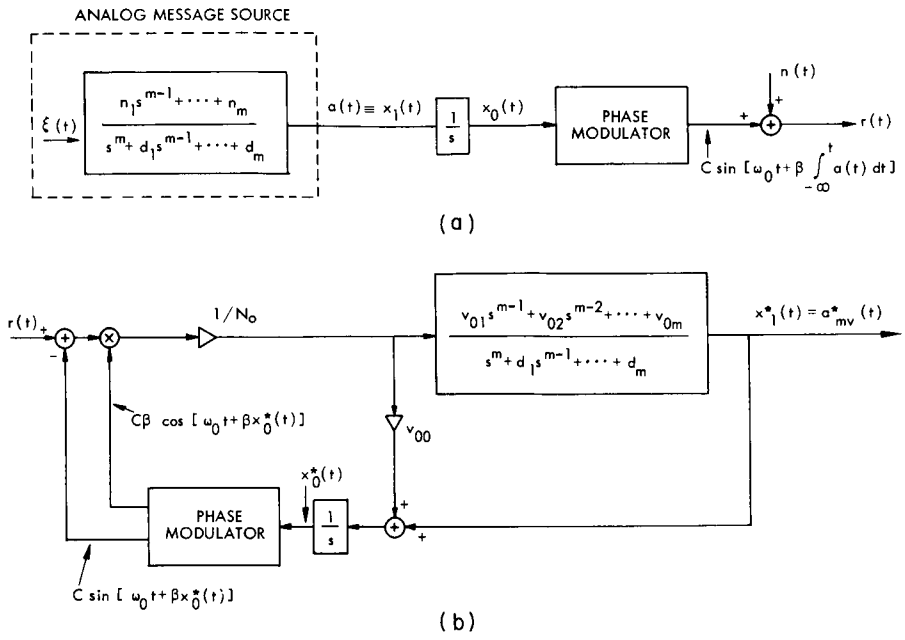

Fig. XIII-16. (a) FM communication model.
(b) Approximate minimum-mean-square FM demodulator.

models with linear modulation schemes, such as suppressed-carrier AM and single-sideband AM, fall within this case and can be easily treated.

For the case when $\underline{g}[t:\underline{x}(t)]$ is a nonlinear transformation of $\underline{x}(t)$, several examples have been studied and reported by Snyder.[5] For brevity, we give only the result for frequency modulation and cite other examples of interest which have been discussed elsewhere.[5] These are listed here.

1. Single message, general modulation, additive channel.
2. Single message, phase modulation, additive channel.
3. Single message, frequency modulation, additive channel.
   (The communication model and resulting demodulator for this case are shown in Fig. III-16. The v_{ij} occurring in the demodulator are the components of V in the steady-state and $\xi(t)$ is a white Gaussian process.)
4. Single message, general modulation, c diversity or multipath channels.
5. Single message, phase modulation, c diversity or multipath channels.
   (For this case, the demodulator structure is in the form of a maximal ratio combiner followed by a phase-locked loop.)
6. Single message, phase-modulation, simple multiplicative channel.
   (In this instance, the demodulator is in the form of a joint message and channel estimator.)
7. Single message, phase modulation, Rayleigh channel.

8. Single message, phase modulation, random phase channel (oscillator instability).
9. m messages, PM_m/PM, additive channel.

5. Conclusion

An approach has been outlined for nonlinear, minimum-mean-square filtering. The resulting fibers (or demodulators) bear a close relation to the demodulators obtained by the maximum a posteriori estimation procedure described, for example, by Van Trees.[6] The minimum-mean-square demodulators are identical to the realizable portion of the cascade realization of the maximum a posteriori demodulators. The communication model discussed in this report was used by Van Trees[7] who studied it with the alternative approach.

D. L. Snyder

References

1. N. Wiener, "The Extrapolation, Interpolation, and Smoothing of Stationary Time Series," John Wiley and Sons, Inc., New York, 1949.
2. R. E. Kalman and R. Bucy, "New Results in Linear Filtering and Prediction Theory," ASME J. Basic Eng. 83, 95-108 (March 1961).
3. D. L. Snyder, "An Application of an Equation for the Conditional Probability Density Functional of Markov Processes to Nonlinear Minimum Variance Filtering and Estimation," Quarterly Progress Report No. 78, Research Laboratory of Electronics, M.I.T., July 15, 1965, pp. 192-201.
4. H. J. Kushner, "On the Differential Equations Satisfied by Conditional Probability Densities of Markov Processes, with Applications," J. SIAM Control, Ser. A, Vol. 2, No. 1, pp. 106-119, 1964.
5. D. L. Snyder, "An approach to nonlinear minimum-variance filtering with application to analog communication via randomly-time-varying channels," Internal Memorandum No. IM-DS-5, M.I.T., August 1965.
6. H. L. Van Trees, "Analog Modulation and Continuous Estimation Theory," Class notes for Course 6.576, Massachusetts Institute of Technology, Cambridge, Mass., 1965 (printed).
7. H. L. Van Trees, "Analog Communication over Randomly-Time-Varying Channels," 1964 WESCON Convention Record, Part 4, August 1964.

XIV. PROCESSING AND TRANSMISSION OF INFORMATION*

Prof. P. Elias	D. Chase	C. W. Niessen
Prof. R. G. Gallager	J. R. Colton	J. H. Nyman
Prof. F. C. Hennie III	P. M. Ebert	G. C. O'Leary
Prof. I. M. Jacobs	D. D. Falconer	R. Pilc
Prof. R. E. Kahn	L. M. Goodman	J. T. Pinkston III
Prof. R. S. Kennedy	C. J. Johnson	E. W. Portner, Jr.
Prof. C. E. Shannon	J. Max	J. S. Richters
Prof. H. L. Van Trees	R. F. McCann	D. L. Snyder
Prof. J. M. Wozencraft	G. Q. McDowell	R. N. Spann
D. S. Arnstein	J. H. Meyn	W. R. Sutherland
R. A. Carpenter	J. C. Molden	M. G. Taylor

A. OPTICAL COMMUNICATION SYSTEMS

An interferometric demodulator for use with frequency-position modulation has been investigated by R. E. Olsen in a thesis entitled "Interferometric Demodulation of FM at Optical Frequencies." His work suggests that interferometric techniques can be used to implement practical and nearly optimal processors for such alphabets. The alphabet size is limited by the Finesse if the best performance is to be realized.

Methods of generating desirable communication signals have been studied by C. J. Johnson in a Master's thesis entitled "Electro-optic Properties and Communication Applications of $BaTiO_3$." He investigated those properties of large single crystal samples of $BaTiO_3$ which are relevant to optical modulators. These crystals were grown by Dr. A. Linz and V. Belruss of the Massachusetts Institute of Technology.

In a third investigation, J. R. Colton has established a mathematical model for transmission channels employing optical waveguides that distort the signals because of surface imperfections. He envisaged the imperfections as random in character and applied a Central Limit Theorem argument to Helmholtz's Equation; he concluded that the resultant channel output may be approximated by a Gaussian random process. His work will culminate in a thesis to be entitled "Analysis of an Optical Fiber as a Discrete Communications Channel," which will be submitted to the Department of Electrical Engineering, M.I.T., in partial fulfillment of the requirements for the degree of Master of Science.

R. S. Kennedy

*This work was supported in part by the Joint Services Electronics Program (Contract DA36-039-AMC-03200(E)), the National Science Foundation (Grant GP-2495), and the National Aeronautics and Space Administration (Grants NsG-334 and NsG-496).

XV. COGNITIVE INFORMATION PROCESSING*

Prof. S. J. Mason
Prof. M. Eden
Prof. T. S. Huang
Prof. O. J. Tretiak
Prof. D. E. Troxel
Dr. P. A. Kolers
A. L. Citron
J. K. Clemens
R. W. Donaldson
J. K. Dupress
C. L. Fontaine
K. R. Ingham
E. E. Landsman
M. B. Lazarus
F. F. Lee
R. M. Mason
Kathryn F. Rosenthal
T. L. Saxton
F. W. Scoville
A. Spiridan

A. COGNITIVE PROCESSES

1. VARIATIONS OF PERCEIVED DISTANCE WITH APPARENT MOTION

Apparent visual movement occurs when two visual targets are flashed briefly in sequence. If the space separating the two flashes and the time relations between them are set properly, one sees a single target appear briefly in the region of the first flash and then move smoothly and continuously across the intervening space to the region of the second one, where it disappears. Apparent visual movement under optimal conditions is indistinguishable from "real", or veridical, movement, and this similarity in appearance of the two perceptions has been taken as evidence that the two have an identical physiological basis. This argument of identity has recently been shown to be wrong, however, and several criteria distinguishing the two perceptions have been discovered.[1]

Our finding of a basic difference in the coding of the two perceptions with respect to their rates, formation times, and masking effects prompted us to examine other properties attributed to the illusion, particularly the variations in distance that are often reported.

If one observes two lights flashing at a rate that produces apparent movement, the distance seemingly travelled by the illusory object varies; however, the published accounts are ambiguous about the nature of this variation. Some writers report that the apparent distance is less than the physical distance; others report that it is greater. Irrespective of whether the apparent distance is less or greater than the physical distance, the fact that there is a difference, and one which has been related more or less systematically to the stimulus conditions producing the basic phenomenon, creates a condition requiring further investigation. The question under study has to do with the formation of the visual space in which we ambulate, and the conditions affecting its psychological representation.

We have studied the variations in apparent distance of the apparently moving object in three ways. In one experiment two fiducial marks, dim points of light (M_1 and M_2), were set some distance apart, just below two lines of light (A and B) whose flashing gives the appearance of motion (see Fig. XV-1). The distance separating the two fiducial

*This work was supported through the Joint Services Electronics Program by the U.S. Army Research Office, Durham, under Contract DA36-039-AMC-03200(E); and in part by the National Science Foundation (Grant GP-2495), the National Institutes of Health (Grant MH-04737-05), and the National Aeronautics and Space Administration (Grant NsG-496).

marks was varied and made either greater or less than the physical distance separating the flashing lines. The subject's task was to say, after each flash of the lines, whether the distance traveled by the object in apparent motion appeared greater or less than the distance separating the fiducial marks. The flashes were varied in duration, but were typically 40 msec each; the interval between the offset of the first and the onset of the second (the interstimulus interval (ISI)) was varied 10-250 msec; and the interval between the offset of the second and the recurrence of the first, the intercycle interval, was 3250 msec. The experiment was performed with 3 subjects who made between 20 and 30 observations each at each temporal separation of the interstimulus interval.

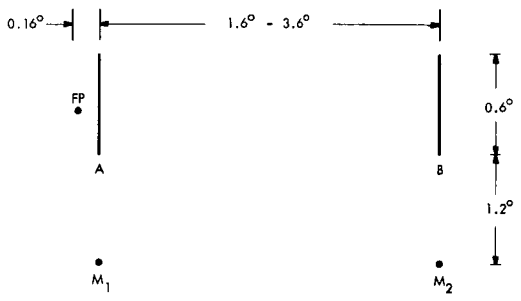

Fig. XV-1.
Physical arrangement of flashing lights (A, B), marker lights (M_1, M_2), and point of fixation (FP).

When the flashing lights were 12.5 cm apart at a viewing distance of 282 cm (~2.4°) separations of the marker lights greater than 14 cm and less than 12 cm were almost always perceived correctly; that is to say, the subjects reported that the distance traveled by the apparently moving object was either less or greater than the distance set by the fiducial marks, which is in conformity with physical reality. When the fiducial marks were 13 cm apart, the subjects tended to report the apparent distance as greater, the probability of these reports increasing slightly with increases in ISI. Thus there was an apparent overshoot of perceived distance, a physical separation of 12.5 cm being perceived as greater than 13 cm, but not as great as 14 cm. This, at most, is an overshoot of 4-8%, far less than the 25-40% reported by others.[2] Furthermore, we find the overshoot is not a U-shaped function of that temporal interval (see Fig. XV-2.)

In an effort to reproduce the phenomena reported by others, another effort was made to measure the overshoot in apparent distance. In this case the two lights were flashed repeatedly with the dark intervals equal, so that the subject saw a line of light in a continuous oscillation whose period was varied between trials. During each trial, which lasted 3-5 sec, the fiducial lights were moved physically until they appeared to match the distance traveled by the oscillating object. In this case again, there was no systematic deviation from physical reality as a function of the temporal interval separating the two lights: the subjects' judgments describing a match between the marker lights and the apparently moving line were in good agreement with the physical conditions.

Despite these two negative results we persisted with a third experiment, for it will be recalled that the apparent distance does appear to vary with stimulus conditions. The results of this third experiment provide a clue to the basis of the phenomenon.

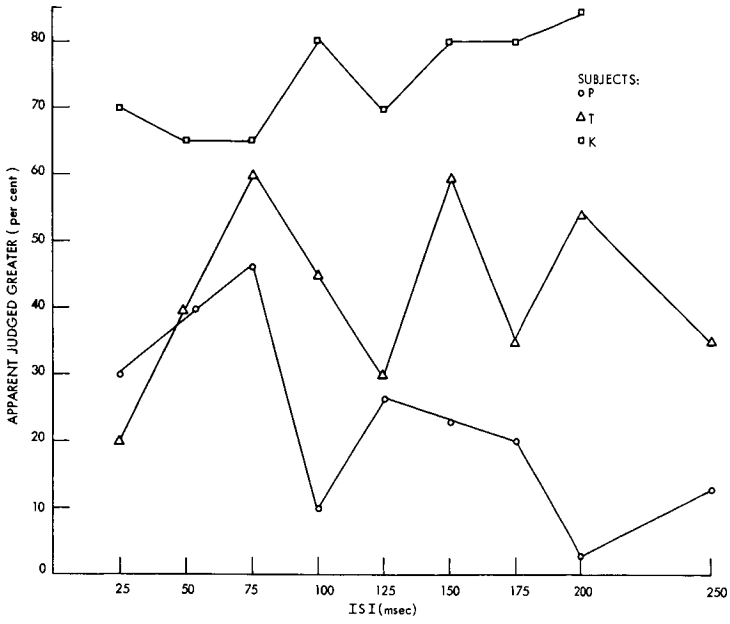

Fig. XV-2.

The percentage of judgments showing apparent distance perceived as greater than physical distance, as a function of the interval between the flashes.

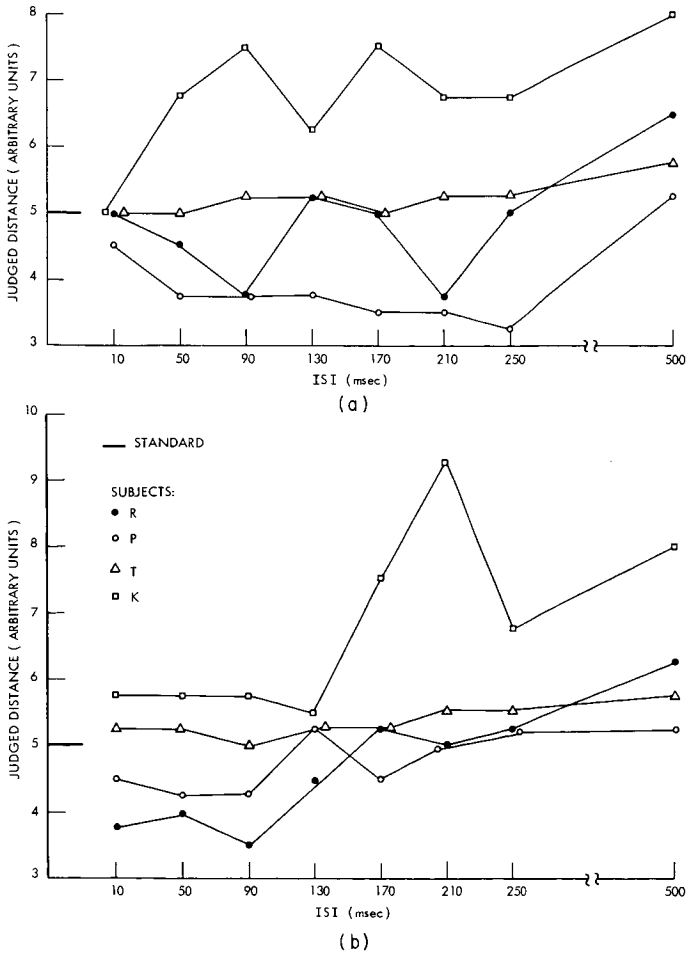

Fig. XV-3.

Judged distance travelled by illusory line. (a) Two lines flashed at 90 msec each; (b) Two lines flashed at 310 msec each. The ordinate value 5 indicates the identity of illusory and physical distance. Values less than 5 indicate that the apparent distance is perceived to be less than the physical distance.

First, subjects estimated numerically the magnitude of the spatial separation of the two fiducial lights alone, using a subjective scale of distance. Four subjects tested individually generated essentially linear relations between judged distance and physical distance. The subjects were then shown the line in apparent motion, with the fiducial lights no longer present, and again used a subjective scale to estimate the distance traveled by the illusory object. The duration of each flash was 90 msec in one set of trials and 310 msec in another. The judgments were made with an intercycle interval (ICI) of 3250 msec, one judgment per presentation; and with an ICI of 2000 msec, a judgment made on the basis of three flashes. The results in both cases were similar but highly variable. Moreover, the subjects found it difficult to make a single estimation based on three flashes because, as they reported it, the apparent distance varied from flash to flash. Figure XV-3 shows the results for the last estimation; it can be seen that two subjects characteristically produce an undershoot for the shorter ISI values, two characteristically produce an overshoot, and all subjects produce an overshoot at the longest ISI values. Notice also that the variations in apparent distance are not correlated with the ISI values that produce good apparent motion. If they were so correlated, the curves would begin at 5 (the value for the two lamps that are on continuously), depart smoothly from that value to some peak, and then return to 5.

In these experiments, the subject always looked with one eye only through a 4-mm artificial pupil at a small dot of red light (the fixation point) placed just to the left of the first of the flashing lines. It is known, however, that a fixated eye is not entirely immobile; small involuntary motions characterize even the best fixated eye.[3] These involuntary motions, we now believe, are the basis of the variations in apparent distance of an object in illusory motion. The effects do not seem to be due to any particular excitation pattern established by the temporal relations between the flashes per se, nor to the occurrence of the illusion of motion, as others have claimed. They appear to be due to involuntary motions of the eye that occur between the offset of the first flash and the onset of the second. We have not, of course, proved this assertion; our apparatus does not lend itself to such exactitude. Significant proof would come from studies of apparent motion with the lines of light established as stabilized retinal images, either optically or by means of a suitably programmed computer that moved a stimulus display to compensate for movements of the eye. Our data, however, are consistent with this belief.

That it is involuntary eye movements that seem to play the predominant role is suggested also by the fact that voluntary movements of the eye undertaken during a stimulus sequence do not affect the apparent distance between the lights when the ISI is short. Thus, if ISI and ICI are both approximately 25 msec with the on-times of the lamps approximately 40 msec, sweeping the eyes across the display does not change the apparent distance between the lights. Involuntary eye movements on the other hand, can directly affect the spatial representation of an object, as demonstrated by Matin.[4] The

variations in perceived distance in apparent movement seem to be due to just such movements and not to any figural or temporal interaction. What is more intriguing now is the manner in which such eye movements contribute to the representation of visual space. The implication of these results is that the coding of space occurs in terms of some form of monitored retinal local sign.

P. A. Kolers, G. E. Touchstone

References

1. P. A. Kolers, "The Illusion of Movement," Sci. American, Vol. 211, No. 4, pp. 98-108, 1964.

2. W. Scholz, "Experimentelle Untersuchungen über die phänomenale Grösse von Raumstrecken, die durch Sukzessiv-Darbietung zweier Reize begrenzt werden," Psychol. Forsch. 5, 219-272 (1925); W. Neuhaus, "Experimentelle Untersuchung der Scheinbewegung," Arch gesam. Psychol. 75, 315-458 (1930).

3. T. N. Cornsweet, "Determination of the Stimuli for Involuntary Drifts and Saccadic Eye Movements," J. Opt. Soc. Am. 46, 987-993 (1956); R. M. Steinman, "Effect of Target Size, Luminance, and Color on Monocular Fixation," J. Opt. Soc. Am. 55, 1158-1165 (1965).

4. L. Matin and G. E. MacKinnon, "Autokinetic Movement; Selective Manipulation of Directional Components by Image Stabilization," Science 143, 147-148 (1964).

B. PICTURE PROCESSING

1. EFFICIENT FACSIMILE TRANSMISSION BY SUPERPOSITION OF PSEUDORANDOMLY SCANNED PICTURES

Introduction

Pseudorandom scanning has been used by Deutsch[1] to reduce television frame rate and hence bandwidth. In pseudorandom scanning, the scanning beam does not travel sequentially as in ordinary television, but hops from point to point in a seemingly random fashion. In order to recover the picture, the scanner at the receiving end has to be completely synchronous with the transmitter scanner. If the receiver scanner is out of step, or if it is controlled by a different pseudorandom sequence than that of the transmitter scanner, the reconstructed picture will appear as random noise. In this report, we describe an efficient facsimile transmission system utilizing the property of pseudorandom scanning which has just been mentioned.

The System

Our efficient facsimile transmission system is shown in Fig. XV-4. It is to be used for transmitting two-livel (black and white) digital pictures in which the white areas constitute only a small fraction of the total frame. The M pseudorandom scanners are

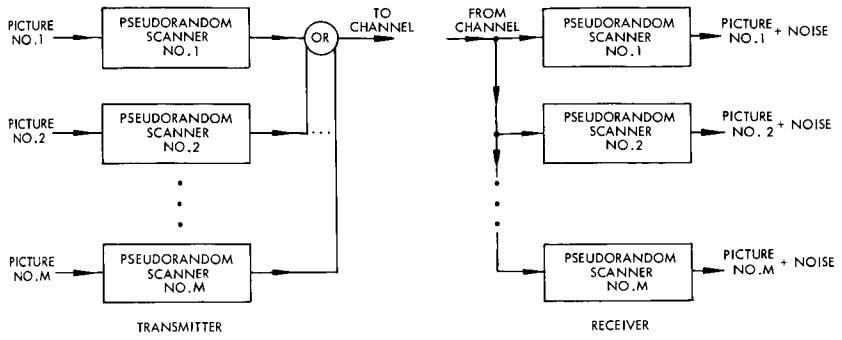

Fig. XV-4. An efficient facsimile transmission system.

controlled by different pseudorandom sequences. At the transmitting end, the output binary sequences (black = 0, white = 1) of the scanners are "ored" and the resulting binary sequence is sent to the channel. At the receiving end, the received binary sequence is fed to M scanners that are identical to those at the transmitter. The output of each receiver scanner will be the picture put into the corresponding transmitter scanner plus random noise caused by the other pictures and the channel. The noise will consist of white points scattered more or less randomly over the picture. Under the assumption that the channel is noiseless, the probability of error (black points received as white) is

$$P \leq (M-1)\, p, \tag{1}$$

where M is the total number of pictures transmitted at the same time, and p is the fraction of white in each picture. For example, if a probability of error of 0.3 can be tolerated and if the amount of white if 1/20 of the total picture, then 5 pictures can be transmitted at the same time.

Experimental Results

The system described here was simulated on the IBM 7094 computer. Some of the results are shown in Figs. XV-5 and XV-6. The original pictures used were white characters on black, the amount of white being approximately 1/10 of the total picture. Figure XV-5 shows the received pictures for M = 2 and Fig. XV-6 for M = 4. Since the noise is randomly scattered over the picture, it can probably be reduced substantially by some noise-reduction scheme.

Discussion

The system described here is quite suitable for use as a party-line system. As the number of users increases, the noise in the received pictures will increase; however, in our system, as contrasted with ordinary party-line systems, any user can transmit

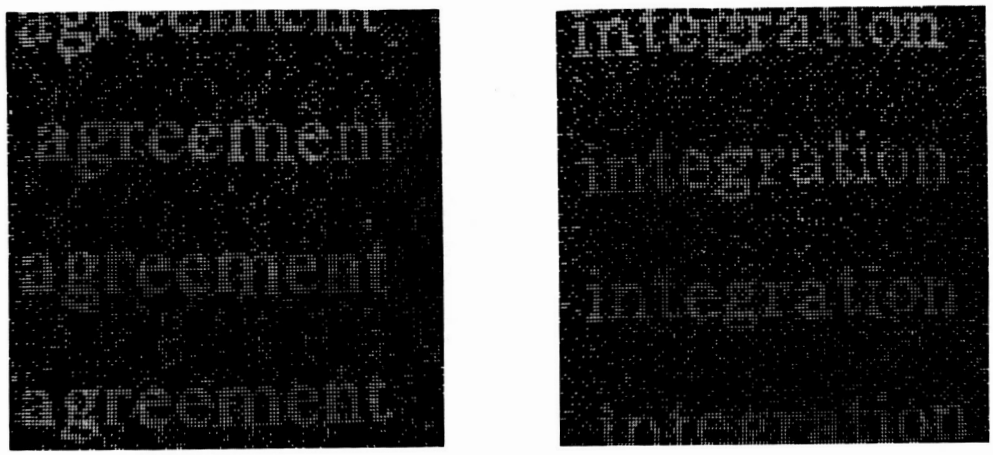

(a) (b)

Fig. XV-5. Pictures from computer simulation of the system of Fig. XV-4 (M = 2).

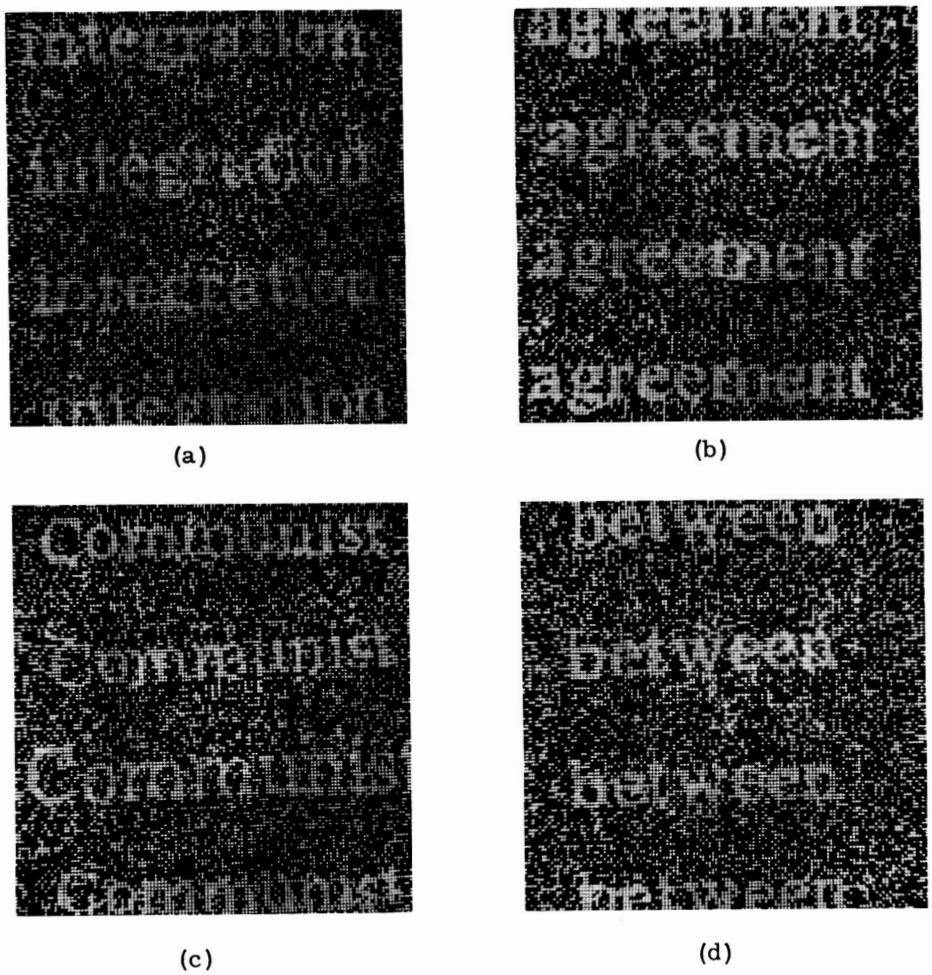

(a) (b)

(c) (d)

Fig. XV-6. Pictures from computer simulation of the system of Fig. XV-4 (M = 4).

pictures at any time: the line never refuses service to the use, it only degrades gracefully.

The computer programming for this experiment was skillfully done by John Currano.

T. S. Huang, O. J. Tretiak

References

1. S. Deutsch, "Narrow-Band TV Uses Pseudorandom Scan," Electronics, Vol. 35, pp. 49-51, April 27, 1962.

2. OPTIMUM BINARY CODE

Introduction

In Quarterly Progress Report No. 78 (pages 231-233) we considered the problem of transmitting digital data over a binary symmetric channel (BSC) using fixed-lingth binary codes. In particular, we were interested in finding the optimum code that minimizes the mean-square error or average noise power. We reported that if the input data are uniformly distributed over the integers 0 to $2^n - 1$, then the natural code minimizes the single-bit average noise power, e_1^2, which was defined as the part of the average noise power resulting from single-bit errors in the received code words. If the error probability p of the BSC is small, then the total average noise power is essentially the same as the single-bit average noise power, and therefore the natural code minimizes the total noise power. We believed that the natural code, in face, minimizes the total average noise for any value of $p \leq \frac{1}{2}$; however, we have no proof thus far. We remark that the results of the last report depend only on the first-order statistics of the channel, and hence are valid for all binary channels, if p is interpreted as the average bit-error rate.

It was shown in the previous report that both natural and Gray codes are good as far as the average noise power is concerned. The purpose of the present report is to compare these two codes in more detail. First, we make a conjecture about the total average noise power of the Gray code. Then, we discuss the effect of the input data on noise power. Finally, natural and Gray codes are compared in connection with picture transmission.

Average Noise Power of the Gray Code

We first write formally our previous conjecture.

Conjecture 1. If the input data are uniformly distributed over the integers 0 to $2^n - 1$, and if the average bit-error rate is $p \leq \frac{1}{2}$, then the natural code minimizes the (total) average noise power.

A particular case of this conjecture maybe expressed as follows.

Conjecture 2. Under the same assumptions as in Conjecture 1, the natural code yields a smaller (total) average noise power than the gray code.

An expression for the total average noise power of a natural code was given in the previous report. One approach to proving Conjecture 2 would be to find an expression for the total average noise power of the gray code; then we could compare the expressions for the average noise powers of the two codes. In carrying out this approach, we formulated the following conjecture.

Conjecture 3. Under the same assumptions as in Conjecture 1, we have

$$(G_n - N_n) = (1-2p)\, G_{n-1}, \tag{1}$$

where G_i is the total average noise power of an i-bit gray code, and N_i is the total average noise power of an i-bit natural code.

Equation 1 has been verified up to n = 6, but we have not been able to prove it in general. It is clear that Conjecture 2 follows readily from Eq. 1.

Noise as a Function of Signal Amplitude

In order to calculate average noise powers for input data with various probability distributions, it is helpful to have curves of noise power (or rms amplitude) as a function of the signal amplitude. The average noise power is equal to the area under the curve which is the product of the input probability distribution curve and the curve of noise power versus signal amplitude.

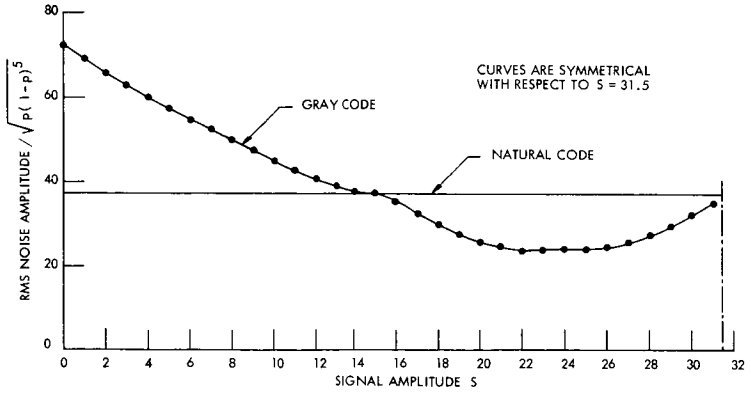

Fig. XV-7. Curves of rms noise amplitude vs signal amplitude, for natural and gray codes.

For natural and gray codes, the curves of single-bit rms noise amplitude versus signal amplitude are shown in Fig. XV-7 for n = 6. It is seen that if the input probability distribution has a peak near the center and is small at the extremes, then the gray code might yield less single-error average noise power than the natural code.

For a natural code, it is clear that the curves of noise power versus signal amplitude are flat for all n. For the Gray code, we observed empirically that the curves for different values of n are very close to each other if they are properly normalized by powers of 2 in both the horizontal and the vertical directions. An interesting problem would be to find the asymptotic ($n \to \infty$) form of the normalized curve and estimate the deviation of the normalized curves for finite values of n from this asymptotic curve.

Picture Transmission

In our discussion we took the mean-square error as our fidelity criterion. If the input data are samples of a digitalized picture, then the question in which we are interested is, Which received picture has better quality? This "best-quality" criterion depends, of course, on high-order statistics of the channel.

Picture transmission through the BSC has been simulated on the IBM 7094 computer, with both natural and Gray codes used. The received pictures are shown in Fig. XV-8. The picture consisted of 256×256 samples, and the bright was quantized to 64 levels (6 bits). The probability of error of the BSC was $p = 0.003$. The distribution of the brightness levels in the input picture is shown in Fig. XV-9. The peak-signal-to-rms-noise ratio is 29.9 db for the natural-code received picture, and 27.5 db for the Gray-code received picture. The noise in the Gray-code picture appears more visually objectionable than that in the natural-code picture. The poorer performance of the Gray code is evidently due to the fact that the input brightness distribution had peaks at the two extremes. It is quite possible that the subjective quality of a picture received through a BSC could be measured objectively by a weighted mean-square error, the weighting function being chosen to acount for the noise visibility over the Gray scale.

Y. Yamaguchi, T. S. Huang

C. SENSORY AIDS

1. MOBILITY AID SIMULATOR

This report describes the development of the mobility aid simulation facility which was described in Quarterly Progress Report No. 73 (pages 233-235).

More accurate position-monitoring equipment has been constructed. The original system used receivers located in the corners of a room. The signal processing involved taking the difference of squares of voltages. The path between the "dummy"

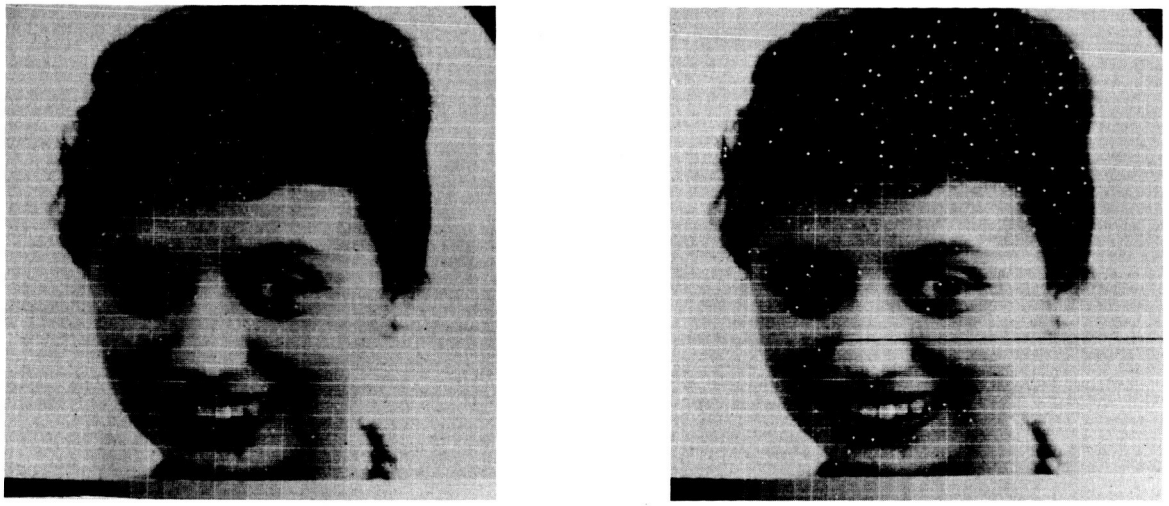

(a) (b)

Fig. XV-8. Pictures received through a binary symmetrical channel (p = 0.003). (a) Natural code. (b) Gray code.

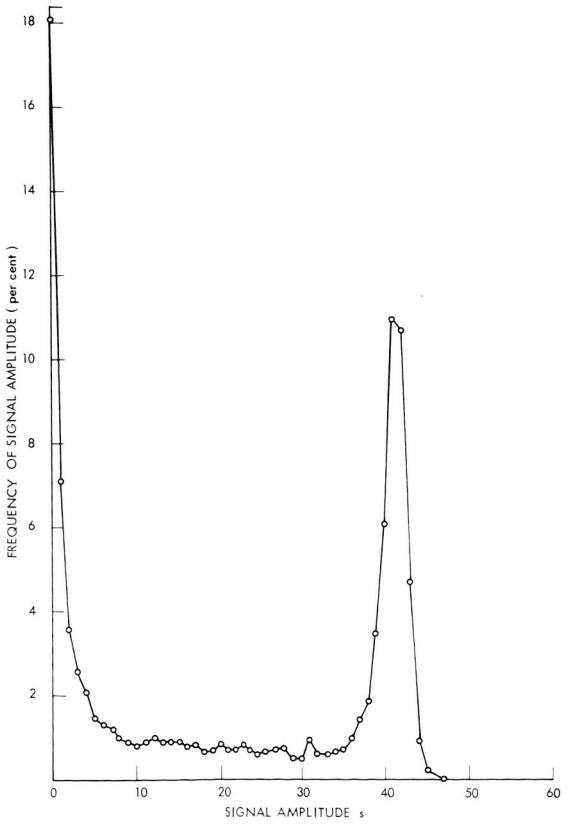

Fig. 9. Frequency distribution of signal amplitudes (brightness levels) of the picture used in Fig. XV-8.

mobility aid and a receiver could easily be interfered with by the subject who was holding the aid, and the difference of squares operation was implemented by an analog scheme that was subject to drift.

The new system uses a set of three mutually perpendicular polystyrene rods. Each rod provides one dimension of a Cartesian coordinate system. Two microphones are attached to each rod, one at each end. The microphones are Barium Titanate units and

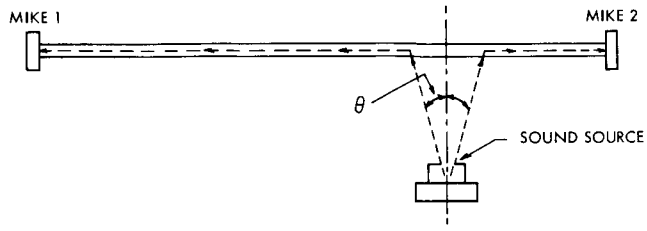

Fig. XV-10. Sound-path geometry.

are fastened to the rods with beeswax. The "x" rod, 20 ft long, is composed of four 5-ft rods held together by epoxy. The first signals to be received at the ends of the rod after each transmitted pulse take the paths shown in Fig. XV-10. The angle θ between the perpendicular and the sound path in the air is just the critical angle for the passage of sound from air to polystyrene and is given by

$$\theta = \sin^{-1}\left(\frac{v_A}{v_R}\right),$$

where v_A is the velocity of sound in air, and v_R is the velocity of sound in the rod. Since v_R is approximately 5 times that of air, $\theta = 11°$. Since the rod is mounted overhead and θ is a small angle, it is much more difficult to interfere with the sound path. Polystyrene was chosen as the rod material because it has the lowest transmission loss of any plastic tested and v_R is not high enough to produce timing problems. It can be seen from Fig. XV-10 that the difference between the arrival times of the first pulse received at one end of the rod and the first pulse received at the other end is directly proportional to distance along the rod, is independent of the radial distance from the rod, and depends only on the velocity of sound in the rod. The velocity of sound in air does not matter, as long as it is the same for both air paths, nor does the time of emission of the sound matter as it did in the old system. A zero crossing of the signal arriving at one end is used to turn on a counter, and the counter is turned off by the corresponding zero crossing of the signal arriving at the other end. A sign bit is derived by detecting which

end received a pulse first (see Fig. XV-11). The linearity of the system is now being

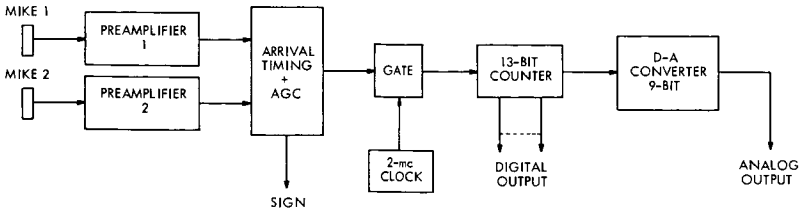

Fig. XV-11. System diagram.

determined. The peak-to-jitter is less than 0.1 inch over at least 15 ft of the "x" rod, and the radial distance from the rod can be as much as 10 ft without degrading performance.

E. Landsman

2. OPTICAL CHARACTER RECOGNITION FOR READING MACHINE APPLICATIONS

Introduction

Optical character recognition (OCR) was applied to a very special problem, that of a reading machine for the blind. Since the proposed machine was, in fact, a personal one, interplay between the machine and the reader could be used to advantage. Figure XV-12 shows a possible reading machine system.

In normal operation the output of the data-reducing equipment will be connected by the switch to the recognition equipment. Whether or not the recognition equipment recognizes a letter depends on the distortion of the printed letter. If it is recognized it will be presented. If we assume, for example, that the output is spoken letters, the letter will be spoken to the operator. If it is not recognized an appropriate signal will be given to the operator. It is now up to the operator to decide whether he wants the distorted letter to be presented by a recoding device such as a two dimensional pattern, or wants the machine to go on.

As an example let us assume that the "e" in the word "the" is distorted beyond machine recognition. The machine could say t-h-beep. The operator would either understand the word or not. If he did not he would throw the switch and the pattern of the distorted "e" would be presented as a tactile two-dimensional pattern (or some other recoded output), independently of how many correct letters had been read after this bad "e". The

operator could now feel the letter and tell the machine to go on.

The requirements of OCR in this application were found to be quite different than the requirements in electronic data processing. The most significant changes are the reduction of speed and error-rate requirements and the increase in the requirements of low cost and the ability to recognize type fonts of various styles. No existing OCR techniques were found to be suitable for this purpose and a new technique was developed.

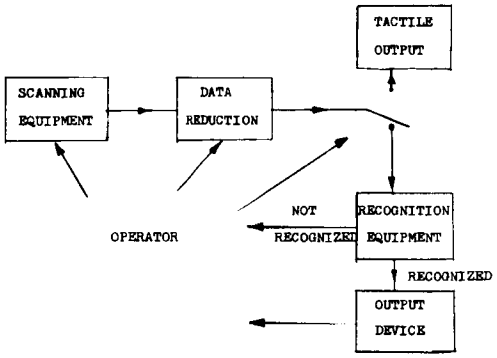

Fig. XV-12.
A personal reading machine system.

Contour Tracing Technique

The technique used here is based upon tracing the outside black-white boundary of the printed character. It was found that in the Roman alphabet the outside contour contained enough information to describe the characters. The outside contour of the character is traced by means of a digitally controlled flying-spot scanner. A column scan is generated which proceeds from left to right until a character is contacted. The scanner then traces the contour of this letter by means of simply generated local operations until the trace is complete. The basis of description of this trace is the local maxima and minima of the horizontal and vertical waveforms of the trace as it proceeds around the character and the positions at which these extrema occur. The details of the trace generation are given in the author's thesis.[1]

A method for smoothing had to be developed which would eliminate extraneous extreme caused by printing noise, and yet preserve the extrema arising from significant features of the character. The smoothing method used is a nonlinear technique employing hysteresis. This smoothing is analogous to "gear-backlash." Figure XV-13a shows the electrical model of a "gear-backlash" system. Figure XV-13b shows an input curve and an output curve that is the smoothed curve. Notice that the smoothed curve still has sharp turns and inflection points along it. If a maxima or minima is only detected when the slope of the smoothed curve changes sign, then the extrema pairs that are separated by less than 2E units are eliminated, where 2E is the smoothing threshold.

We found that this smoothing threshold could be one-fourth the letter extent and still retain enough information to recognize the characters of the Roman alphabet. With this large noise threshold most of the variability of the characters caused by style variations

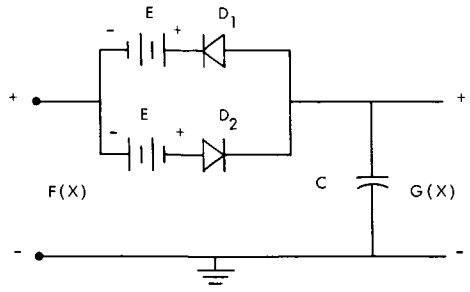

(a)

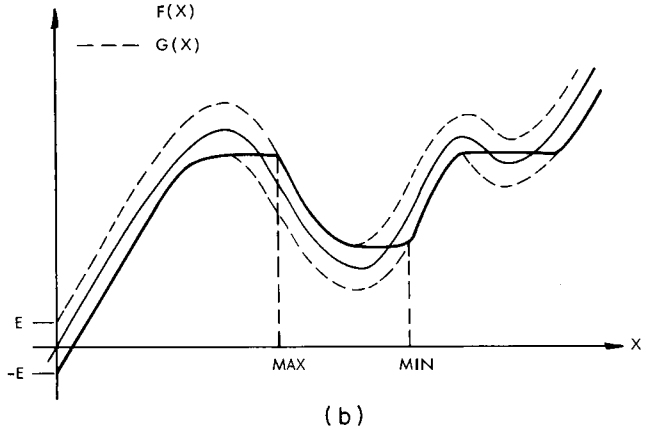

(b)

Fig. XV-13. Hysteresis smoothing.

and printing noise is eliminated in the scanner itself.

Generation of Binary Descriptions of Characters

There are three separate binary words used in the recognition of the letters, the height-to-width ratio of the letter, the sequence of the maxima and minima, and the coordinates of the maxima and minima.

The generation of these binary words will be explained by an example. Figure XV-14 shows a letter to be scanned and recognized. The search is started by a column scan, bottom to top, which moves from left to right until the letter is contacted. This will occur at the point labelled "start" in Fig. XV-14. The captive scan is then initiated and the outside contour of the letter is traced. During this trace only two pieces of information are recorded, the letter extent in the vertical, or y direction and the letter extent in the horizontal, or x, direction. From this information, the height-to-width ratio is calculated. This information is also used to set the actual values of the smoothing thresholds. The waveforms occurring in the horizontal and vertical directions during

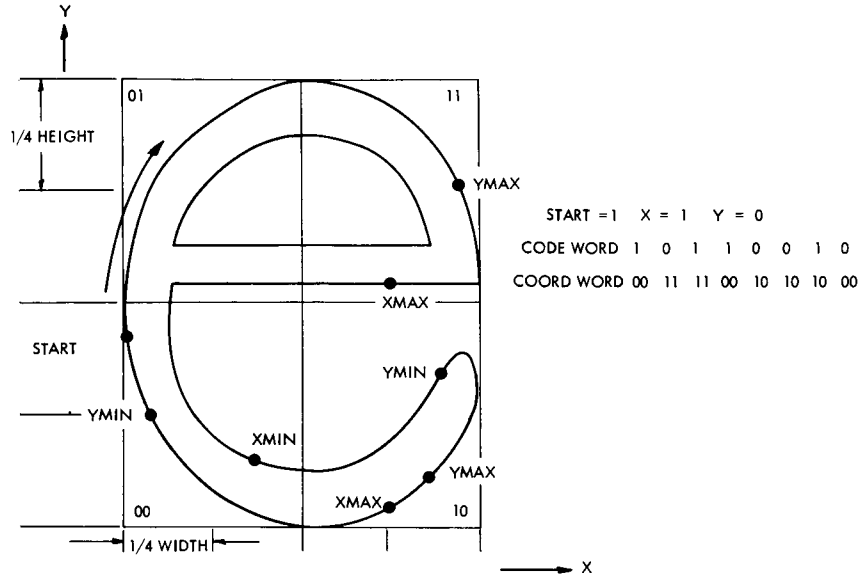

Fig. XV-14. Binary description of unknown character.

the contour trace are considered independently. In this example the threshold for the vertical (y) waveform is set to one-fourth the vertical extent and the threshold for the horizontal (x) direction is set to one-fourth the horizontal extent. These thresholds are in general different as can be seen in Fig. XV-14.

The trace routine is then initiated for the second time. During this trace the maxima and minima in the x and y directions are detected. Notice that it is not necessary to draw the smoothed curve described above to determine the position at which an extremum is detected. The extremum will always be detected when the trace moves one threshold unit from the extremum in the coordinate direction in which the extremum occurred. A description of the detection of the extrema for the letter in Fig. XV-14 will now be given.

When the second trace is initiated both x and y increase until the top of the letter in Fig. XV-14 is reached. At this point, y starts to decrease and x continues to increase. When y decreases the amount of the threshold, a y maximum is detected and is so labelled on the letter. As the trace continues y continues to decrease and x reaches a maximum and then decreases. When x decreases one-fourth the letter width a maximum is detected and is so labelled. As the trace continues again x reaches a minimum and increases. Notice that this minimum is detected at one-fourth the distance from the minimum, and not one-fourth the distance from the edge of the letter. The trace continues detecting a y minimum, a y maximum, an x maximum, and a y minimum before completing the trace.

The sequence of maxima and minima can be coded into a binary word, which will be called the code word. Each extremum of the trace can be determined unambiguously

with one bit of information if it is assumed that the starting position is at a y minimum, as well as at an x minimum. The first extremum encountered on the trace must then be either a y maximum or an x maximum. This is a binary choice and can be designated with 1 bit of information. Each extremum can be designated by 1 bit, since it is always known what the past extremum was in each coordinate direction. That is, although it may appear that there is a four-way choice of the next extremum along a trace, there is in fact only a two-way choice, because of the history of extrema along the trace.

The code word is generated by recording a 1 for the start position, a 1 for an x extremum and a 0 for a y extremum. This is done in sequence with new extrema added on the right of the word. The code word for the letter in Fig. XV-14 would be 10110010. The start position is labelled as a 1 so that the number of extrema is recorded, otherwise leading zeros would make the code word appear short.

In order to give information about where the extrema were detected, another binary word, called the coord word (coordinate word) is generated. The letter is divided in half in both the vertical and horizontal direction with the information obtained in the first trace. The four areas are labelled as shown in Fig. XV-14. Whenever an extremum is detected it is appropriately recorded in the code word. Also, the label of the area in which the extremum is detected is recorded in the coord word. The coord word is formed in the same manner as the code word. That is, the two bits describing the coordinates of each extremum are added sequentially to the right side of the coord word. The coord word for the letter in Fig. XV-14 is 0011110010101000.

To summarize, the binary description of a character is very simply generated. It is based on a contour trace of the letter which is performed twice. The first trace determines the height-to-width ratio and the thresholds used in the smoothing operation. During the second trace the smoothing and the code-word and coord-word generation are performed simultaneously. When the second trace is complete all pertinent information has been taken and the scan moves on to the next letter.

For purposes of efficient data handling, the maximum length of the 3 binary words is fixed. A maximum length of 12 bits for the code words was found experimentally to be sufficient. The maximum length of the coord word was fixed as 18 bits instead of 24. We found that if the letter was so complicated that it had more than 9 extrema the code word itself carried enough information to determine the letter uniquely. The height-to-width ratio is divided into 4 classes and therefore requires a two-bit word.

The total information about the unknown letter is thereby contained in 32 bits of information. Most of the multifont machines in use today use a factor of 10 more information to describe the character in binary form immediately after scanning. Since, by means of this technique, a large part of the variability of the unknown is eliminated by the scanning technique, a great deal of data reduction has taken place in the scanner itself.

SpACE

ClOSl*ng the Gop
(See Cover)
He stood on top of his spaceship*s white titanium hull* He touched it with his bulky thermal gloves* He burned around like Duck Rogers propelling himself with his hand*held jet* He floated lazily on his back* He loked and laughed* He gazed down at the earth id3 miles below* spotted the Houston* Galveston Day area where he lives and tried to take a picture of it* Like a gas station Dttendant* he ehecked the space* craft*s thrusters* wiped its wlndshield* Ordered to get back into the capsule* he protested like a scolded kid* **I*m doing great*** he said* **It*s fun* I*m not eoming in*** When* after 2d minutes of space gymnasties* U*S* Astponaut Edward Higgins White II* 34* finally did agree to squeeze himself baek into his Gemini q ship* he still had not had enough of spaee walking* Said he to Command Pilot James Alton McDivitt* **It*s the saddest day of my life***
White*s exhilarating spaee stroll pro* vided the moments of highest drama during Gemini 4* scheduled 62* orbit* 98*hour* i*7dd*ddd mile flight* White spent twice the time outside the space* eraft that Soviet Cosmonaut Aleksei Leonov did last March 18* and he had much more maneuverablllty* all Leonov did was somersault around at the end of a tethep* getting dizzy* while White moved around pretty much at will*
Seeond Genepotl*on* Still* Gemini*s planners would have serubbed White*s EVA (for Extra*Vehicular Actlvityl expedltion in a second if they had thought it might detract from the flight*s basic missions*

Fig. XV-15. Example of reading "Time Magazine."

Recognition of the Unknown Character

The classification of the unknown character is made in three steps. The code word of the unknown is compared with the list of previously found code words. When a match is found, the coord word of the unknown is compared with all coord words that previously

occurred with that code word. Finally, the height-to-width ratio is compared and the appropriate character is given as output. The search can be terminated at any step if the unknown is uniquely classified at that step. If no match is found, an appropriate signal is given.

Experimental Data

In order to make a realistic test of the variable font capability of this character-recognition technique, a set of 10 popular scripts was compiled. These type fonts were all of the Roman style but are quite different in design. Transparencies of these type fonts were taken from actual printed material so printing noise was included.

These 10 fonts were used also to experiment with various threshold settings. For each setting of the thresholds the letters were scanned and the results compiled. On the basis of these data the letters were then classified in terms of their code words, coord words, and height-to-width ratio. The number of code words encountered was recorded, as well as the number of coord words needed to distinguish letters that had the same code word. This is a measure of the amount of storage required to recognize the letters. The number of confusions represents the number of letters which could not be distinguished. If 10 B's fell into the classification used for D's, this was called 10 confusions.

In order to make the results meaningful, it was assumed that ascenders and descenders of the letters were detected. This would certainly be done in any reading machine using this technique. The method for obtaining these is straightforward (see Earnest[2]). It can be done even when there are only several letters in a line of type. Although almost all letters are distinguished by their contours alone, the i, j, and l of the mixed type fonts are more readily distinguished with ascender and descender detection. Rarely are other letter pairs distinguished too.

Details of the various runs are given in the author's thesis.[1] Possibly the best run has a large smoothing threshold with a high recognition rate. This was obtained with the smoothing threshold for the vertical waveform set to 1/4 the letter height and the smoothing threshold for the horizontal waveform set to 1/4 the letter width. The vertical division of the character was set at 9/32 rather than 1/2. The reason for this was that in some cases, notably in the letter "P", the bulge of the letter, although shorter than the letter height, was larger than 1/2 the letter and was not detected as being short. In this case 61 code words and 67 coord words were needed.

In the run of the 10 fonts there were no confusions between upper-case and lower-case letters. There were 30 confusions among the 260 upper-case letters and 1 confusion among the 260 lower-case letters.

If the letters are assumed to be equally likely, the error rate for the lower-case letters, which make up the majority of letters in common usage, is 0.4 per cent. In this run the following confusions were made: B for D, Q for O, R for A, Y for V, c for e, H for N and C for G. It is interesting to note that the machine confuses letters that are readily confused by the eye. Possibly the two most surprising confusions were H for N because noise made the crossbar appear slanted, and C for G. The crossbar on the G is always more than 1/4 the horizontal extent of the letter; however, the line leading to the crossbar is in general very thick and hides the fact from the contour trace. All of these letters can be distinguished by further operations based on the technique described here. They are discussed in the author's thesis.[1]

In order to test the validity of this character-recognition technique for reading-machine applications a full page of "Time Magazine" was read. To be as impartial as possible the first page of text was taken from the issue of June 11, 1965. Over 3300 characters were encountered. There were no touching letters and only one broken letter. The page was scanned once and the data from all the characters were compiled. From these data the appropriate division for the 4 clases of height-to-width ratio was set and the characters were classified according to these code words, coord words, and height-to-width ratio. Only 68 code words and 86 coord words were needed. The number of points around the contour of a letter was counted. If it was more than 16 but less than 64 points, it was called a general punctuation mark and no further data were recorded. The page was then read from the data collected. This is equivalent to reading with a completely trained machine.

Unfortunately, the property of detecting ascenders and descenders was not incorporated in this reading program. Therefore the reading error rate is higher than it need be. The error rate, including letters and punctuation from titles and text, is approximately 3 per cent. If ascenders and descenders were detected, the reading error rate would drop to 1 per cent. This error rate is quite sufficient for reading-machine applications, because of the redundancy of the English Language. English text can be reconstructed from passages for which the error rate approaches 10 per cent.

The major confusions in reading this printed page were the letters l for i and j, p for r, and e for c. Numbers were also confused with letters, the major confusion being d for 0. The titles were printed in sans-serif type so some additional confusions exist there, mainly a for 0. Other confusions are listed in the author's thesis.

Figure XV-15 shows the results from the passage in "Time Magazine," including the confusions. The page is relatively easy to read if the possible confusions are kept in mind.

Conclusions

It is the contour tracing with the incorporation of the large-threshold hysteresis smoothing which permitted on approach to the OCR for the reading-machine applications

problem. The variability of the data after scanning causes expensive data reduction when other techniques are used. Almost all of the variability of the character is eliminated in the scanning process itself, while the information describing the character is maintained. This is evidenced by the fact that the unknown characters can be described by 32 bits of information immediately after scanning and by the small amount of storage needed for the classification of characters. The simple operations used to generate the trace, the hysteresis smoothing technique used to reduce variability, and the small storage requirements suggest the real possibility of an inexpensive reading machine. We estimate that a reading machine operating as described here, including all optical scanning equipment, could now be built for a few thousand dollars, which makes a personal reading machine feasible.

J. K. Clemens

References

1. J. K. Clemens, "Optical Character Recognition for Reading Machine Applications," Ph.D. Thesis, Department of Electrical Engineering, M.I.T., August 1965.

2. L. D. Earnest, "Machine Recognition of Cursive Writing," Information Processing 1962, Proc. IFIP Congress, 1962, edited by C. M. Popplewell (North-Holland Publishing Company, Amsterdam, 1962), pp. 462-466.

3. PERCEPTUAL MODEL

When humans are required to identify a stimulus selected from a given set, the probability of a correct identification usually depends on several stimulus parameters. There is a class of stimuli, however, for the probability of a correct identification depending on only three parameters: the stimulus probability distribution, the stimulus rate, and the error costs.[1] The purpose of this report is to present a model that allows the channel matrixabetween stimulus and response to be expressed in terms of these three stimulus paramaters.

The model is valid under the following conditions. (In this report a stimulus is characterized by its coordinate values along a set of stimulus dimension, analogous to the way in which a vector is characterized by its coordinates along a set of spatial axes.)

1. Each stimulus can assume one of at most two values along any one stimulus dimension.
2. The distance between coordinates along each dimension is well above threshold.
3. Only one of a finite number of stimuli occurs at any time.
4. The probability of occurrence of each stimulus is known by the observer.
5. The cost associated with each type of error is known by the observer.

Postulates of the Model

The model is based on the following postulates.

(i) The channel between the sensory stimuli and that portion of the nervous system where stimulus identification occurs can be modelled by a large number of identical parallel binary channels (not necessarily symmetric), followed by a decision-making network.

(ii) Each binary channel can transmit information about the coordinates of certain stimulus dimensions. Each channel can transmit information about only one stimulus dimension during any short space of time.

(iii) In general, the probability that a binary channel will correctly transmit the coordinate value of any one stimulus dimension depends on the coordinates along the other dimensions.

(iv) Each individual channel is unreliable, and operates with a probability of error which is slightly less than 1/2.

(v) Decisions as to the identity of the original messages are made in such a way that the observers' risk is minimized.

The following discussion should help to illustrate these postulates.

Assume that a human is faced with the task of distinguishing 4 pure tones that vary along the dimensions of frequency and duration. The frequency is low or high; the duration long or short. In accordance with the second assumption, N_1 of the channels can be used for discrimination of frequency and N_2 for discrimination of duration, while N_{12} of the channels can be used for the discrimination of frequency or duration (see Fig. XV-16).

The fraction of the N_{12} channels used for the discrimination of frequency will depend on the message probabilities. If, for example, the two messages that are represented by tones of high frequency occur with probability zero, then all N_{12} channels will be used

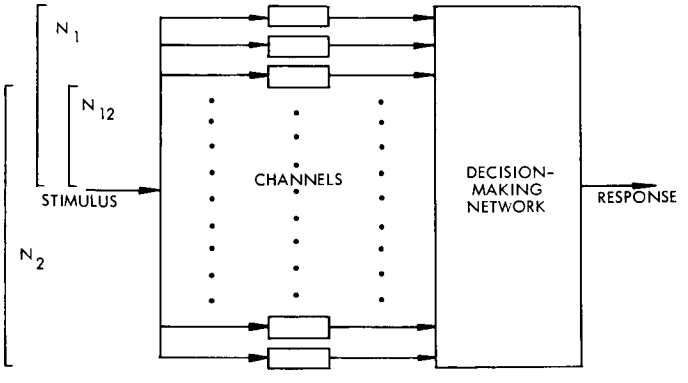

Fig. XV-16. Illustrating the model.

for discrimination of duration, in accordance with the fifth assumption.

In general, the probability of correctly identifying a high-frequency tone will depend on its duration, in accordance with the third assumption. Similarly, the probability of correctly identifying a short-duration tone will depend on its frequency.

Some Special Cases

Consider the problem of discriminating between two stimuli that vary along only one dimension. Stimulus s_0 is represented by the digit zero, stimulus s_1 by the digit one. Each digit is transmitted through N identical channels as a zero or a one. These transmitted digits constitute an output sequence, on which a decision as to the identity of the original stimulus is based.

Define

v, any one of the 2^N possible output sequences;

c_{ij}, cost of receiving the i^{th} stimulus when the j^{th} stimulus was sent;

$p(s_i)$, probability of occurrence of the i^{th} stimulus;

$p(v|s_i)$, probability of occurrence of the v^{th} output sequence, given that stimulus s_i was sent;

w_i, the set of all channel output giving rise to a decision that the i^{th} stimulus occurred; and

p, the probability of error per channel. (Without loss of generality, the channels be considered symmetric.)

The expected cost, or risk c, can be minimized by choosing w_0 to contain all sequences v for which

$$\frac{p(v|s_1)}{p(v|s_0)} \leq L_{01}$$

$$L_{01} = \frac{(C_{10}-C_{00})\ p(s_0)}{(C_{01}-C_{11})\ p(s_1)}.$$

If v_r denotes any output sequence containing r ones (and therefore N-r zeros), then the set w_0 contains all sequences for which

$$\left(\frac{1-p}{p}\right)^r \left(\frac{p}{1-p}\right)^{N-r} \leq L_{01}.$$

Substitution of $\sigma = 1/2 - p$ in this inequality yields

$$\left(\frac{\frac{1}{2}+\sigma}{\frac{1}{2}+\sigma}\right)^r \left(\frac{\frac{1}{2}-\sigma}{\frac{1}{2}+\sigma}\right)^{N-r} \leq L_{01}.$$

If this inequality is solved for r, and if second and higher order terms in σ are neglected, the set w_o is found to contain all output sequences v for which $r \leq Nc$.

$$N_c = \begin{cases} N & N_c' > N \\ \frac{N}{2} + \frac{\log L_{01}}{8\sigma} = N_c' & 0 \leq N_c' \leq N \\ 0 & N_c' < 0 \end{cases} \tag{1}$$

From Eq. 1, the channel matrix for the over-all system can be evaluated. If $P(w_i|s_j)$ is the probability that the output sequence v falls in the set w_i when the stimulus s_j occurs, then

$$P(w_o|s_o) = \sum_{r=0}^{N_c} \frac{N!}{r!\,(N-r)} p^r (1-p)^{N-r} \tag{2}$$

$$P(w_o|s_1) = \sum_{r=0}^{N_c} \frac{N!}{r!\,(N-r)!} (1-p)^r p^{N-r}. \tag{3}$$

Approximation of these sums by integrals (2) yields the channel matrix for the over-all system.

$$\begin{bmatrix} P(w_o|s_o) & P(w_1|s_o) \\ P(w_o|s_1) & P(w_1|s_1) \end{bmatrix} = \begin{bmatrix} \operatorname{erf}\left(2\sqrt{N}\sigma + \frac{\log L_{01}}{4\sqrt{N}\sigma}\right) & \operatorname{erf}\left(-2\sqrt{N}\sigma - \frac{\log L_{01}}{4\sqrt{N}\sigma}\right) \\ \operatorname{erf}\left(-2\sqrt{N}\sigma + \frac{\log L_{01}}{4\sqrt{N}\sigma}\right) & \operatorname{erf}\left(2\sqrt{N}\sigma - \frac{\log L_{01}}{4\sqrt{N}\sigma}\right) \end{bmatrix}$$

$$\operatorname{erf}(x) = \frac{1}{\sqrt{2\pi}} \int_{-\infty}^{x} e^{-y^2/2}\, dy.$$

Next, consider the problem of discriminating among 4 stimuli that vary along two dimensions. In this case, n_1 channels are used for discrimination along dimension 1, and n_2 channels are used for discrimination along dimension 2. Thus,

$$n_1 = N_1 - a_{12}^1 N_{12}$$

$$n_2 = N_2 - a_{12}^2 N_{12}$$

$$a_{12}^1 + a_{12}^2 = 1.$$

The constants α_{12}^{1} and α_{12}^{2} are chosen for minimum average risk.

If one assumes a unity cost matrix, minimizing the average risk is equivalent to maximizing the probability of a correct response, P(c).

$$P(c) = \sum_{i=0}^{3} p(w_i|s_i)\, p(s_i).$$

This sum is maximized by choosing w_i to include all output sequences v for which

$$\frac{p(v|s_j)}{p(v|s_j)} \leqslant \frac{p(s_i)}{p(s_j)} \qquad (j=0,1,2,3;\ j\neq i).$$

Thus, the set w_o corresponding to stimulus s_o contains all sequences v for which

$$\frac{p(v|s_j)}{p(v|s_o)} \leqslant \frac{p(s_o)}{p(s_j)} \qquad (j=1,2,3).$$

If one assumes that the probability of correctly identifying the coordinate value along one dimension is independent of the coordinates along the other dimension, then substitution of the appropriate liklihood ratios in this inequality gives the following equations. (r_1 is the number of one's transmitted by the n_1 channels; r_2 is the number of one's transmitted by the n_2 channels. It is assumed that n_1, and n_2 lie between 0 and $n_1+n_2 = N_1+N_2-N_{12}$.)

$$r_1 \leqslant \frac{n_1}{2} + \frac{\log \dfrac{p(s_o)}{p(s_1)}}{8\sigma}$$

$$r_2 \leqslant \frac{n_2}{2} + \frac{\log \dfrac{p(s_o)}{p(s_2)}}{8\sigma}$$

$$r_1 + r_2 \leqslant \frac{n_1 + n_2}{2} + \frac{\log \dfrac{p(s_o)}{p(s_3)}}{8\sigma}.$$

The members of w_1, w_2, and w_3 are determined in a similar way.

Once the numbers of w_o, w_1, and w_3 have been determined, the over-all channel matrix can be evaluated. For example, if all four messages are equiprobable, then

$$P(w_o|s_o) = \sum_{r_1=0}^{n_1/2} \frac{n_1!}{r_1!\,(n_1-r_1)!}\, p^{r_1}(1-p)^{n_1-r_1} \sum_{r_2=0}^{n_2/2} \frac{n_2!}{r_2(n_2-r_2)!}\, p^{r_2}(1-p)^{n_2-r_2}$$

$$= \operatorname{erf}(2\sqrt{n_1}\sigma)\operatorname{erf}(2\sqrt{n_2}\sigma).$$

If one lets

$$p_1 = \operatorname{erf}(2\sqrt{n_1}\sigma)$$

$$p_2 = \operatorname{erf}(2\sqrt{n_2}\sigma),$$

then the channel matrix for the over-all system is

$$\begin{bmatrix} P(w_o|s_o) & P(w_1|s_o) & P(w_2|s_o) & P(w_3|s_o) \\ P(w_o|s_1) & P(w_1|s_1) & P(w_2|s_1) & P(w_3|s_1) \\ P(w_o|s_2) & P(w_1|s_2) & P(w_2|s_2) & P(w_3|s_2) \\ P(w_o|s_3) & P(w_1|s_3) & P(w_2|s_3) & P(w_3|s_3) \end{bmatrix} = \begin{bmatrix} p_2p_1 & p_2(1-p_1) & (1-p_2)p_1 & (1-p_2)(1-p_1) \\ p_2(1-p_1) & p_2p_1 & (1-p_2)(1-p_1) & (1-p_2)p_1 \\ (1-p_2)p_1 & (1-p_2)(1-p_1) & p_2p_1 & p_2(1-p_1) \\ (1-p_2)(1-p_1) & (1-p_2)p_1 & p_2(1-p_1) & p_2p_1 \end{bmatrix} \tag{4}$$

Once the parameters $\sqrt{N_1}\,\sigma$, $\sqrt{N_2}\,\sigma$, and $\sqrt{N_{12}}\,\sigma$ have been evaluated, the quantities p_1 and p_2 can be determined by choosing α_{12}^1 and α_{12}^2 to minimize the probability of error.

The parameters can be determined by evaluating the channel matrix that results when an observer is required to discriminate between judiciously chosen pairs of stimuli. By measuring the channel matrix that results when an observer discriminates between two equiprobable stimuli that vary along dimension 1, $\sqrt{N_1}\,\sigma$ can be determined from

$$P(w_o|s_o) = \operatorname{erf}(2\sqrt{N_1}\,\sigma).$$

By measuring the matrix resulting when an observer discriminates between two equiprobable stimuli that vary along dimension two, $\sqrt{N_2}\,\sigma$ can be evaluated from

$$P(w_o|s_o) = \operatorname{erf}(2\sqrt{N_2}\,\sigma).$$

Finally, determination of the matrix resulting when an observer discriminates between two equiprobable stimuli that vary along both dimensions allows $\sqrt{N_{12}}\,\sigma$ to be determined from the two previous equations and from

$$P(w_o|s_o) = \text{erf}\left[2(\sqrt{N_1}\,\sigma + \sqrt{N_2}\,\sigma - \sqrt{N_{12}}\,\sigma)\right].$$

General Case – Discrimination among 2^m m-dimensional Stimuli

A set of stimuli which can assume one of two coordinate values along m stimulus dimensions can contain 2^m different stimuli. In order to evaluate the confusion matrix for the over-all system, considerable algebraic manipulation is sometimes required. In principle, the computation is always possible It can be shown that when the N's and σ's appear in various terms in the over-all matrix, they always occur as products of the form $\sqrt{N}\,\sigma$. It can also be shown that all such products can be determined from the channel matrices that result when an observer is required to discriminate between judiciously chosen pairs of stimuli.[3]

a. Qualitative Comparisons of the Model with Experimental Data

The model is in qualitative agreement with several experimental facts. For example, when 2^m messages are mapped into sensory stimuli that vary along m dimensions, the model predicts that the probability of error will increase with m, since the number of channels available for discrimination decreases as m increases. When two messages are mapped into stimuli that vary along dimension 1, N_1 channels are available for discrimination. When the messages are mapped in stimuli that vary along dimension 2, N_2 channels are available. When 4 messages are mapped into stimuli that vary along dimensions 1 and 2, $N_1 - a_{12}^1 N_{12}$ channels are available for discrimination along dimension 1, and $N_2 - a_{12}^2 N_{12}$ channels for dimension 2. If N_{12} is nonzero, then the probability of a correct identification along each dimension decreases. Such an effect was observed by Pollace,[4] and is consistent with earlier results.[1]

The model also predicts that a redundant use of stimulus dimensions will reduce the probability of a transmission error. When two messages are mapped into stimuli that vary along two dimensions, $N_1 + N_2 - N_{12}$ channels become available for discrimination. Since N_1 and N_2 are always larger than N_{12}, the number of channels increases, and P(e) decreases. Some earlier experiments,[1] as well as experiments performed by Ericsen,[5] support this prediction.

The fact that many of the channels can be used for discrimination along one of several dimensions suggests that people are able to focus attention on a few stimulus features, while paying little attention to others. We as humans seem to possess this flexibility.

b. Qualitative Comparisons of the Model with Experiments

When humans are required to discriminate between 2 m-dimensional stimuli, it can be shown that

$$P(w_o|s_o) = \text{erf}\left[\frac{8(\sqrt{N}\sigma)^2 + \log L_{01}}{4\sqrt{N}\sigma}\right] \tag{5}$$

$$P(w_o|s_1) = \text{erf}\left[\frac{-8(\sqrt{N}\sigma)^2 + \log L_{01}}{4\sqrt{N}\sigma}\right], \tag{6}$$

where N is the total number of channels available for discrimination.

$$\left(N = \sum_{i=1}^{m} N_i - \sum_{\substack{i=1 \\ i\neq j}}^{m}\sum_{j=1}^{m} N_{ij} + \sum_{\substack{i=1 \\ i\neq j\neq k}}^{m}\sum_{j=1}^{m}\sum_{k=1}^{m} N_{ijk} \cdots (-1)^{m+1} N_{ij\ldots k}\right)$$

These equations support the hypothesis that when one of two stimuli can occur, sensory data can be described as varying continuously along a single axis, partitioned to minimize the observer's expected risk. In fact, (5) and (6) are almost identical to those used by Swets, Tanner, and Birdsall,[6] Egan,[7] and others to derive their receiver operating characteristics. The only difference is that the variances in (5) and (6) are equal. Although some workers do not impose this restriction, the experimentally determined variance ratio is often close to unity. Even when the data are best fitted with unequal variances, reasonable agreement between theory and experiment is obtained by assuming equal variances.

When an observer was required to discriminate between 4 equiprobable pure tones which varied in frequency and duration, the channel matrix shown in Fig. XV-17 resulted. It was found that the probability of correctly identifying the coordinate along one dimension was independent of the coordinate value along the other dimension. Thus, the theoretical matrix is given by (4). If dimension 1 is the frequency dimension, it was found that $\sqrt{N_1}\,\sigma = .46$; $\sqrt{N_2}\,\sigma = .19$; and $\sqrt{N_{12}}\,\sigma = .08$.

	1	2	3	4
1	.69	.11	.17	.03
2	.11	.69	.03	.17
3	.17	.03	.69	.11
4	.03	.17	.11	.69

Theoretical

.58	.10	.27	.05
.17	.55	.04	.24
.20	.05	.64	.11
.07	.22	.09	.62

Experimental

Tone 1: 1000 cps, 50-msec duration
Tone 2: 3000 cps, 50-msec duration
Tone 3: 1000 cps, 150-msec duration
Tone 4: 3000 cps, 150-msec duration
Stimulus Rate: 1.6 stimuli/sec

Fig. XV-17. Auditory channel matrices.

When an observer was required to decide whether or not each of two adjacent fingers was stimulated tactually by a poke probe, the probability of correctly identifying a poke on one finger was larger when the other finger was poked than when it was not poked (in accordance with Weber's law). An equal number of channels were available to each finger. If the subscript of σ is used to designate a poke (1) or no poke (0) on the other finger, then, at a stimulus rate of 2.6 stimuli/sec, $\sqrt{N_1}\,\sigma_0 = .41$; $\sqrt{N_1}\,\sigma_1 = .33$; $\sqrt{N_{12}}\,\sigma_0 = .15$; and $\sqrt{N_{12}}\,\sigma_1 = .13$. It was found that the number of channels common to pairs of fingers decreased as the distance between fingers increased, as did the ratio of σ_0/σ_1. The same was true when the fingers were stimulated kinesthetically, rather than tactually.

When an observer was required to simultaneously identify pure tones differing in frequency, and decide whether or not a finger was poked, approximately one-quarter of the total number of channels was common to the auditory and tactile dimensions.

Variation of the Parameters with Stimulus Rate

When the distance between the stimulus coordinates is well above threshold, the $\sqrt{N}\,\sigma$'s are independent of all stimulus parameters except rate.[1] When subjects were required to discriminate between several pairs of stimuli, it was found that the $\sqrt{N}\,\sigma$'s were linear functions of stimulus period.

$$\sqrt{N}\,\sigma = c(T-0.25).$$

The constant c depends on the stimulus pair. The time T is in seconds.

Thus, parameters measured at T_1 can be scaled to T_2 as follows:

$$\sqrt{N}\,\sigma\,(T_2) = \sqrt{N}\,\sigma\,(T_1)\,\frac{(T_2-.25)}{(T_2-.25)}.$$

Dimensional Goodness and Dimensional Independence

The model suggests a quantitative comparison of the goodness of a set of sensory dimensions, and a measure of the degree of dependence of two or more dimensions. The numbers $N_1\sigma^2$, $N_2\sigma^2$, $N_3\sigma^2$, etc., all evaluated for the same coordinate values and stimulus rate, can be used as a numerical measure of dimensional goodness. Evaluation of the ratio N_1/N_2 allows one to say whether dimension 1 is twice as good, three times as good, or half as good as dimension 2.

The ratio $\frac{N_{12}}{N_1 + N_2 - N_{12}}$ provides a measure of the degree of interdependence of two dimensions. A unity ratio indicates strong dependence, as all channels can be used for discrimination along other dimensions. A zero ratio indicates dimensional

independence. Similarly, the ratio

$$\frac{N_{123}}{N_1 + N_2 + N_3 - N_{12} - N_{13} - N_{23} + N_{123}}$$

is the measure of the degree of interdependence of three dimensions.

When the coordinates along a set of stimulus dimensions are statistically independent, and when all the N_{ij}'s, N_{ijk}'s, etc. are zero, the information transmitted is equal to the sum of the information transmitted by each dimension. The probability of a correct identification is the product of the probabilities of a correct identification of each coordinate value. These statements follow directly from the discussion in Fano.[8] When the dimensions are not mutually independent, the information transmitted and probability of error is less than if they were independent.

Although the numerical goodness of each dimension varies with coordinate values and stimulus rate, ratios of these goodness values do not. Thus, the relative goodness and interdependence of a set of dimensions are virtually independent of all stimulus parameters.

It is interesting that no independent dimensions were found experimentally. One might expect that dimensions belonging to different senses would be independent, especially when signals from the receptors of different senses to to different regions of the cortex. Apparently such is not the case.

R. W. Donaldson

References

1. R. W. Donaldson, "Information Rates for Multidimensional, Multimodality Sensory Stimuli," Quarterly Progress Report No. 78, Research Laboratory of Electronics, M.I.T., July 15, 1965, pp. 241-248.
2. E. Parzen, Modern Probability Theory and its Applications (John Wiley and Sons, Inc., New York, 1963), pp. 239-245.
3. T. W. Donaldson, "Multimodality Sensory Communication," Ph.D. Thesis, Department of Electrical Engineering, M.I.T., June 1965.
4. I. Pollack and L. Fitts, "Information of Multidimensional Auditory Displays," J. Acoust. Soc. Am. 26, 1954, pp. 155-158.
5. C. W. Ericsen, "Multidimensional Stimulus Differences and the Accuracy of Discrimination," U.S.A.F. WADC Technical Report (1954), pp. 54-165.
6. J. A. Swets, W. P. Tanner, and T. G. Birdsall, "Decision Processes in Perception," Psychol. Rev 68, 301-340 (1961).
7. J. P. Egan, A. I. Schulman, and G. Z. Greenberg, "Operating Characteristics Determined by Binary Decisions and by Ratings," J. Acoust. Soc. Am. 31, 768-773 (1959).
8. R. M. Fano, Transmission of Information (the M.I.T. Press, New York, 1961), p. 31.

4. EXPERIMENTS IN READING NONVISUAL TEXT

It has been shown experimentally[1] that the speed and accuracy with which humans are able to identify sensory stimuli depends on the dimensions along which the stimuli vary. These experiments showed that, in general, identification is easiest when stimuli vary along many dimensions and assume one of two coordinate values along each dimension. In this case, a few simple measurements allow the channel matrix to be evaluated once the stimulus probabilities, stimulus rates, and error costs are known (see Sec. XV-C. 3).

These results were applied to the problem of transmitting English text by means of the nonvisual senses. Each letter was coded into a unique sensory stimulus. In the initial tests, a restricted alphabet of eight letters was used. Finally, the entire alphabet was used.

Description of the Experimental System

In order to enable stimuli to be presented sequentially to a human, the system shown in Fig. XV-18 was designed and constructed.

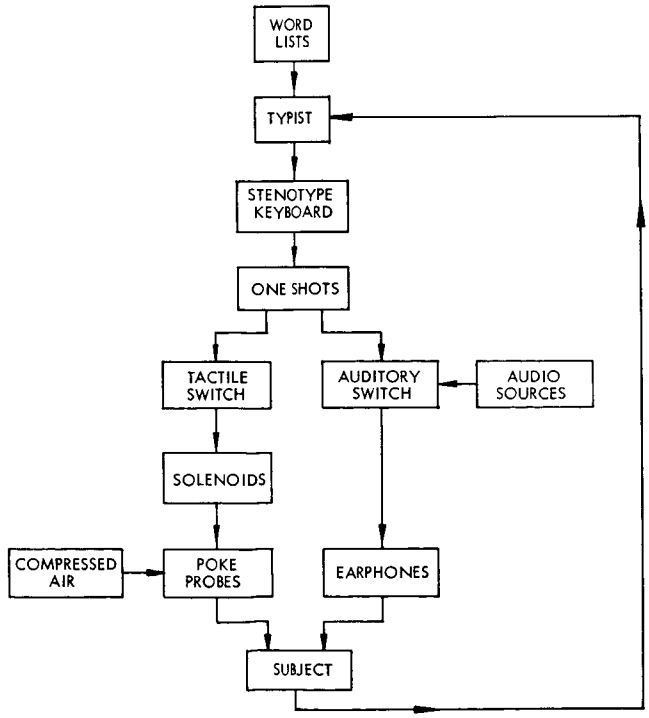

Fig. XV-18. Experimental system.

By depressing certain keys on a stenotype keyboard, a typist was able to convert English letters into a unique set of voltage pulses. These pulses triggered appropriate one shots. The triggering of a one shot resulted in a change in its state. This change in state caused an auditory, tactile, or kinesthetic switch to open for the duration of the state change.

Each auditory stimulus was delivered by separately wired PDR-8 earphones. The tactile stimulators were in air-operated poke probes, designed by Troxel.[2]

The time between successive stimuli was controlled by the typist. Other stimulus parameters, such as stimulus intensity and duration, were controlled by dial settings on the one shots, on the audio-energy sources, and on the compressed-air source.

Eight-Letter Multidimensional Auditory Alphabet

The eight most common letters of the alphabet were coded into sensory stimuli which varied along the following dimensions.

1. frequency of a pure tone (700 cps or 3000 cps)
2. duration of a tone (30 msec or 150 msec)
3. intensity of a tone (zero or well above threshold)
4. ear stimulated by tone
5. frequency range of a noise burst (0-400 cps or 10 kc-∞; 12 db per decade fall-off rate).
6. duration of a noise burst (30 msec or 150 msec)
7. intensity of a noise burst (zero or well above threshold)
8. ear stimulated by noise burst.

Thus, there are 256 points in an eight-dimensional stimulus space. Those points with coordinate values of zero along the third and seventh dimensions could not be used. Also, a pilot experiment showed that identification of a tone or noise is easier when either one occurs in the absence of the other. To facilitate learning, all vowels were pure tones, and all consonants were noise bursts. With these restrictions, the code that minimizes the probability of error is the following one. (The stimulated ear is designated by a capital letter.)

a: 700 cps, 30 msec, L	n: 0-400 cps, 30 msec, L
e: 3 kc, 30 msec, L	r: 10 kc-∞, 30 msec, L
i: 700 cps, 150 msec, R	s: 0-400 cps, 150 msec, R
o: 3 kc, 150 msec, R	t: 10 kc-∞, 150 msec, R

Four subjects were given practice in identifying letters and words containing only these letters. The subjects worked in pairs, each subject transmitting a word to his partner. After the typist had transmitted the word, the reader identified it orally. If his response was correct, the typist sent the next work. the response was

incorrect, the typist transmitted the word again until the correct response was made. The roles of typist and reader were reversed several times each day.

For half-hour periods were spent sending and receiving words (or letters) selected at random from a given list. The lists appear below.

List 1: a, e, i, o, n, r, s, t.

List 2: an, as, at, in, is, it, on, or, no, so, to.

List 3: are, its, one, not, ran, sit, sat, set, see, too.

List 4: into, near, none, rain, rose, seat, seen, soon, star, tree

List 5: enter, noise, start, stone, store, entire, insist, reason, series, street

List 6: a, I, and all the words in Lists 2, 3, 4, and 5.

A contest was held every 5 days. On the contest days, the subjects' pay depended on their performance relative to the performance of the other team. The error-free transmission rate in words per minute on the contest days appears in Table 1. The rates opposite each subject were computed on those trials for which the subject was the reader. Team 1 did not participate in the last contest.

Table XV-1. Reading rates.

Team	Subject	List Number					
		1	2	3	4	5	6
1	B. P.	39	22	23	29	23	
1	D. M.	38	27	23	30	18	
2	W. O.	54	49	37	35	39	33
2	J. B.	59	41	40	43	39	29

During the contests, most of the messages were transmitted correctly the first time. Approximately one message in ten had to be sent more than once; one in 30 had to be sent more than twice; and 30% of the errors were typing errors. The tendency toward error, especially by the reader, increased with the length of the words. This increase was most pronounced for the words from List 5. Approximately 20% of these words had to be sent more than onee. In any given list, the words that were confused most often were those that differed from other words in only one letter. In List 3, "sit" was often confused with "sat" or "set", but rarely with "are" or "one".

All four typists tended to type in such a way that the time between successive letters in a word was the same for all letters. When a new list was being learned, the time between successive letters was approximately 1 second. This time was gradually decreased as the readers became more and more familiar with the words.

All 4 subjects felt that the reading rate would increase if oral responses and sending errors were eliminated. In order to test this hypothesis, computer prepared punched

paper tape and a tape reader replaced the word lists, the typist, and the stenotype machine. The time between successive letters was controlled by the subject. The time between successive words was four times the time between successive letters. After 2 days of practice (1/2 hour per day), W.O. was able to read 42 wpm, while J. B. was able to read 35 wpm. At these rates, 90% of the words were correctly identified.

Both subjects were given an additional day of practice in making silent responses. The speed control on the tape reader was set in such a way that each subject felt that he was identifying 90% of the words correctly. After one day of practice, W.O.'s rate was 71 wpm, while J. B.'s was 59 wpm. Both subjects felt that a proportional reduction in the duration of all tones, a relative increase in the time between words, and more practice would permit even higher rates.

Eight-Letter Multimodality Alphabet

The eight most common letters were coded into auditory or tactile stimuli. The vowels were pure tones which varied along the same dimensions as in the previous section. A tactile stimulus represented each consonant. The finger stimulated was the one used to produce the stimulation by typing. With these constraints, the optimal coding shheme is the following one. The fingers are numbered consecutively from left to right, thumbs excluded.

a, e, i, o: Same as above

n, r, s, t: A poke on fingers 3, 4, 5, and 6, respectively

The experimental procedure was identical to that described above. The general remarks concerning errors also apply here. The transmission rate in words per minute on the contest days appear in Table XV-2. As before, the senders typed in such a way that the time between successive letters was constant.

Table XV-2. Reading rates.

Team	Subject	List Number					
		1	2	3	4	5	6
1	A.G.	57	40	41	33	23	27
1	G.T.	53	43	38	35	20	29
2	D.C.	54	48	53			
2	F.K.	45	39	52			

Both subjects were given two days of practice in receiving the words in List List 6, presented by the tape reader. At the end of the practice period, A.G. was able to read 38 wpm, while G.T. read 44 wpm. At these rates, 90% of the

words were correctly identified.

After an additional day of practice during which oral responses were replaced by silent responses, A. G. felt that he was correctly identifying 90% of the words at a rate of 61 wpm. G. T.'s rate was 55 wpm. Both subjects stated that an increase in the time between words relative to the time between letters, as well as more practice, would result in an increase in reading rate.

Eight-Letter Tactile Alphabet

The 8 available tactile dimensions gave the intensity with which a finger could be poked. The finger poked was the one used to produce the stimulation when typing. The coding scheme is the following.

Letter	Finger Stimulated	Letter	Finger Stimulated
a	1	n	3
e	2	r	4
i	7	s	5
o	8	t	6

The experimental procedure was identical to that above, with one exception. Only one team was used. The earnings on the contest days were computed by averaging the transmission times of all other subjects who were tested on the same word lists. The transmission rates on the contest days appear in Table XV-3. The general remarks concerning errors made above apply here, except that approximately 25% fewer errors were made by the reader.

Table XV-3. Reading rates.

Subject	List Number					
	1	2	3	4	5	6
P. S.	61	48	42	38	32	37
T. B.	60	56	43	42	31	36

After two days of practice with the tape reader, P. S. was able to read orally 49 wpm. T. B. read 46 wpm. At these rates, 90% of the words were correctly identified.

After an additional day of practice with silent responses, P. B. read at a speed of 68 wpm, and T. B. read at a rate of 63 wpm. Both subjects thought that they

were correctly identifying 90% of the words.

Twenty-six Letter Alphabet

The dimensions along which stimuli representing the 26 letters of the alphabet could vary were the 8 auditory dimensions and the 8 tactile dimensions described above. The vowels were either pure tones or pokes on the left or right little finger. (The subjects were told to regard y as a vowel.) No more than two fingers were poked at any one time.

The coding scheme appears in Table XV-4. (The stimulated ear is designated by a capital letter. The fingers are numbered consecutively from left to right.)

Again, subjects worked in pairs; one subject always acted as the typist, the other as the reader. The teams practiced half an hour each day, three days a week. During the first two days, only letters were sent. Thereafter, the few minutes of each day were spent sending letters. The remainder of the time was spent sending

Table XV-4. Twenty-six letter multimodality code.

a: 700 cps, 30 msec, L	n: 0-400 cps, 30 msec, L
b: 1,8	o: 700 cps, 150 msec, R
c: 6	p: 2,7
d: 4	q: 5,8
e: 3 kc, 30 msec, L	r: 10 kc-∞, 30 msec, L
f: 4,5	s: 0-400 cps, 150 msec, R
g: 3,6	t: 10 kc-∞, 150 msec, R
h: 3	u: 1
i: 3 kc, 150 msec, R	v: 2,3
j: 1,5	w: 2
k: 6,7	x: 1,4
l: 5	y: 8
m: 7	z: 4,8

English text. The passages were chosen from Aesop's "Fables," "The Little Prince," "The Reader's Digest," and a daily newspaper. The learning curves appear in Figs. XV-19, XV-20, and XV-21. Common syllables, and short common words were quickly learned by the receivers. These were sent faster than the longer less familiar words. Words whose length exceeded 6 letters sometimes had to be sent two or three times. The reason given by all subjects was that they tended to forget the first letters of the word while receiving the last letters. This difficulty was

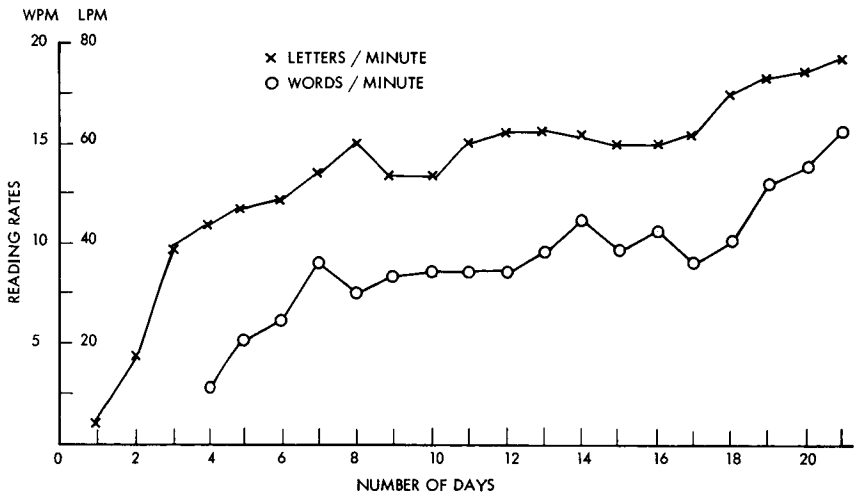

Fig. XV-19.
Reading rates – Team 1.

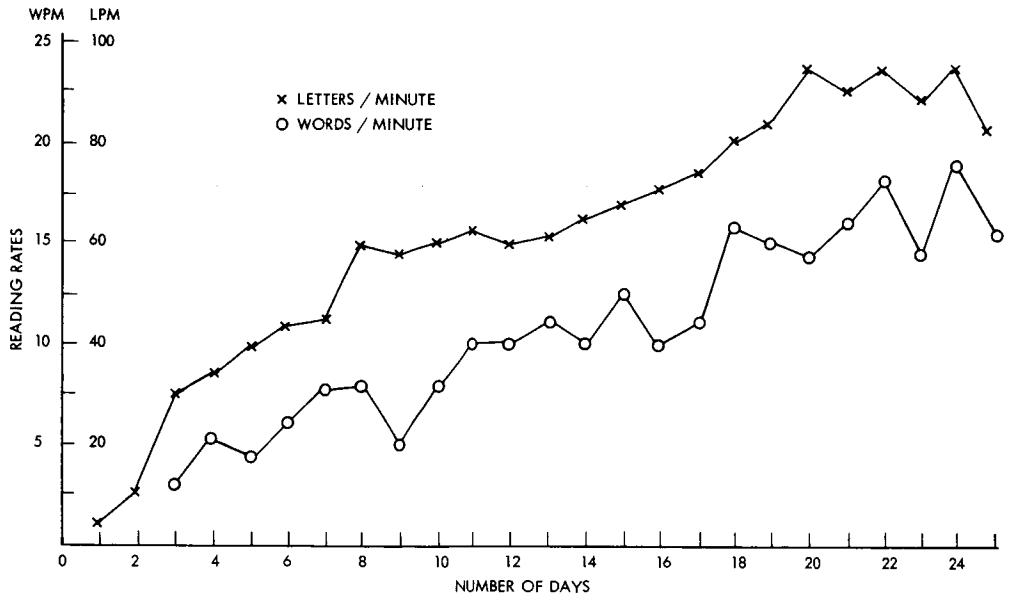

Fig. XV-20. Reading rates – Team 2.

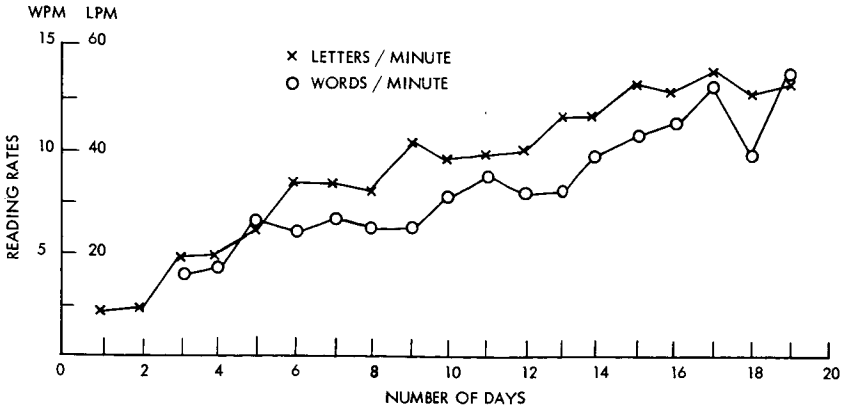

Fig. XV-21.
Reading rates – Team 3.

partly overcome by having the sender pause between successive syllables of long words.

Discussion

All subjects who learned the twenty-six letter multimodality alphabet stated that words and syllables consisting of both auditory and tactile stimuli felt as natural as words and syllables consisting of single modality stimuli. This result is in accordance with earlier experiments[1] which indicated that stimuli that simultaneously excite more than one sense modality can be identified as easily as single-modality stimuli.

In order to read text at reasonably high rates, it is necessary that the letters be easily distinguished one from another, and that the reader by given practice in identifying letters, words, and groups of words. The relative ease with which subjects learned to identify words made up from letters coded into easily distinguishable stimuli suggests that these two conditions (letter distinguishability and practice) may also be sufficient for high reading rates.

R. W. Donaldson

References

1. R. W. Donaldson, "Information Rates for Multidimensional, Multimodality Sensory Stimuli," Quarterly Progress Report No. 78, Research Laboratory of Electronics, M.I.T., July 15, 1965, 241-248.
2. D. E. Troxel, "Tactile Communication," Ph.D. Thesis, Department of Electrical Engineering, Massachusetts Institute of Technology, August 1962.

XVI. COMMUNICATIONS BIOPHYSICS*

Prof. M. Eden
Prof. W. T. Peake†
Prof. R. R. Pfeiffer†
Prof. W. A. Rosenblith
Prof. W. M. Siebert
Prof. T. F. Weiss†
Dr. J. S. Barlow‡
Dr. A. W. B. Cunningham**
Dr. H. Fischler††
Dr. R. D. Hall
Dr. N. Y-s. Kiang†
Dr. R. R. Rojas Corona
Dr. R. Shofer‡‡
Dr. W. Simon***
Dr. G. F. Songster‡‡
Dr. E. B. Vidale
J. A. Anderson
JoAnn Arnn
T. H. Baker
R. M. Brown†
S. K. Burns
F. H. Byers
R. J. Clayton
A. H. Crist†
N. I. Durlach
J. A. Freeman
P. R. Gray
J. J. Guinan, Jr.†
F. N. Jordan
L. J. Krakauer
D. P. Langbein†
P. H. Levine
R. G. Mark
E. G. Merrill
S. A. Miller
D. C. Milne
C. E. Molnar
E. C. Moxon
M. Nahvi
P. H. O'Lague
Ann M. O'Rourke
D. J. M. Poussart
L. R. Rabiner
J. J. Reynolds, Jr.
M. B. Sachs
M. M. Scholl
J. J. Singer
Judith E. Swensen
I. H. Thomae
D. G. Tweed
G. von Bismarck
M. L. Wiederhold

A. TISSUE DYNAMICS OF BRAIN TISSUE IN VITRO

Our group is in the process of quantifying potentials that occur in small pieces (1 mm^3) of living brain tissue in a suitable in vitro environment and identifying the responsible cells. This phenomenon has been noted in brain tissue from mammals (including adult human[1]), birds,[2] amphibians,[3] fish,[4] and insects[5]; however, we usually use chick embryo brain tissue in our studies. The region of the brain to be used is exposed and cooled in a stream of cold (10-20°C) nutrient fluid.[2] Approximately 1 cubic millimeter of tissue is excised rapidly either manually or with the automatic apparatus developed by us to provide uniform explants (Fig. XVI-10). The piece of tissue is floated in cold nutrient fluid to remove blood and membranes. It is transferred onto a thin plate of sintered glass partly immersed in a reservoir of warm (35°C) nutrient fluid in a glass culture vessel whose shape depends on the investigation to be undertaken. The explant

*This work was supported in part by the Joint Services Electronics Program (Contract DA36-039-AMC-03200(E)), the National Science Foundation (Grant GP-2495), the National Institutes of Health (Grants MH-04737-05 and 5 RO1 NB-05462-02), and the National Aeronautics and Space Administration (Grant NsG-496).

†Also at Eaton-Peabody Laboratory, Massachusetts Eye and Ear Infirmary, Boston, Massachusetts.

‡Research affiliate in Communication Sciences from the Neurophysiological Laboratory of the Neurology Service of the Massachusetts General Hospital, Boston, Massachusetts.

**Special Research Fellow, National Institutes of Health.

††From the Department of Electronics, Weizmann Institute of Science, Rehovot, Israel.

‡‡Special Fellow, National Institutes of Health.

***Research Associate, Department of Electrical Engineering, M.I.T.; also Research Associate, Department of Physiology, Harvard Medical School.

is placed a few millimeters above the surface of the reservoir, nutrient fluid being brought to it by the capillary action of the sintered glass. The high surface tension in the sintered plate ensures that a sufficiently small, relatively static, volume of fluid is in contact with the living tissue. The explant can then modify (and maintain) the small volume of fluid in contact with it into a proper environment for itself. (Simple pH studies illustrate this – the fluid in the sintered glass for 1-2 mm around the explant remains at pH 7.2, while that in the rest of the sintered glass and the reservoir may vary as widely as 8.4.) Sintered glass of suitable dimensions (2 mm thick half-circle, 1 cm diameter) and of 'coarse' or 'very coarse' porosity brings sufficient fresh fluid to the living tissue by diffusion to keep it in a functional state for some days.

A 40-gauge platinum electrode insulated to its tip with teflon lies between the explant and the sintered glass and a 36-gauge bare platinum reference electrode dips into the free fluid in the reservoir. By using these electrodes, negative signals can be detected in the explants. The form of the signal sequences is individually characteristic for telencephalon and cerebellum (possibly for other areas of the brain also). The form and amplitude of the individual signals is also characteristic for the area of brain involved.

1. The Signals

A technical report on this subject is to be written by P. L. Marcus, so only the salient details will be given here.

The signals usually have a sinusoidal rise with a period of ~15 msec (for telencephalon) and invariably an exponential decay with a time constant of ~20 msec. This varies little for the signals of any one explant and for the signals from different explants of the same area of the brain, but it changes by a factor of four between cerebellar and telencephalic signals. The form of the cerebellar signal is a simple negative pulse, but the telencephalic signal has an inherent secondary positive pulse and is sometimes even more complex. The amplitude of cerebellar and telencephalic signals also differs – the cerebellar ones range between 2 and 20 μvolts, while those from telencephalon may be as high as 500 μvolts.

2. Grouping of Signals

Cerebellum: Cerebellar potentials are originally in groups of 20-30 signals,[6] but after approximately 12 hours the signals become considerably simplified and the number per sequence drops to 10-15 (Fig. XVI-1c). For any one explant, there is little variation in the number of signals per sequence (Fig. XVI-2a). The amplitude and duration, and the interval following each, of the different signals within a sequence are very similar (Fig. XVI-3). The amplitude, duration and interval following each individual signal seem to be in a constant direct relationship, i.e., the larger the amplitude the longer the signal and the interval that follows it. This may suggest a restricted metabolic

capability necessitating a recovery time whose duration is related to the size of the previous signal. The duration of entire sequences of signals and the interval between sequences is very uniform, the only variation being an increase in the duration of a sequence with an increase in the number of component signals. The composition and form of cerebellar sequences is stable over periods of time up to several days. Figure XVI-4a shows only minor cyclic variations in the duration of the first signal in each of 1000 consecutive sequences containing more than 7 signals. The other parameters of the first and subsequent signals in cerebellar sequences are equally stable.

Telencephalon: The telencephalic sequence is more complex than the cerebellar one (Fig. XVI-1a and 1b). It starts with a short series of large-amplitude, long-duration,

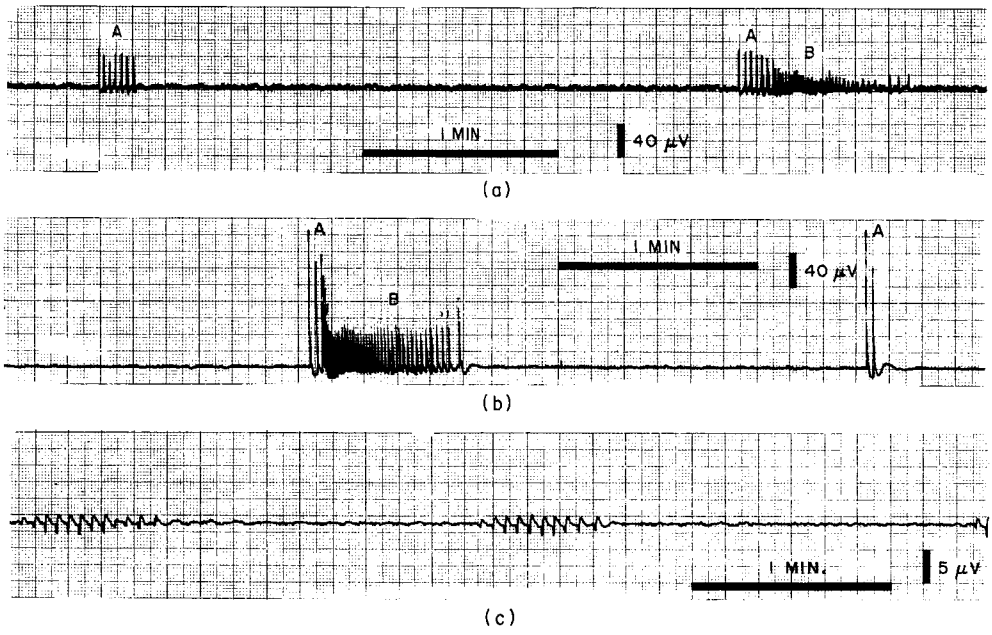

Fig. XVI-1. (a) and (b). Oscilloriter recording of activity from two separate explants of 14-day chick embryo telencephalon after 2 days in vitro. Complete sequences of signals containing both A and B types of activity are shown and also an example of type A activity alone.

(c). Oscilloriter recording of spontaneous activity from an explant of 10-day chick embryo cerebellum after 4 days in vitro.

widely spaced signals (Group A activity) followed or overlapped by a longer series of signals of smaller amplitude, duration, and intersignal interval (Group B activity). This second series of signals undergoes one or more cyclic changes in these three parameters, usually ending in a phase of relatively large, long, widely spaced signals (but not as long, large or widely spaced as in Group A activity). Group A and B activity have well-marked differences. Group A activity often occurs alone (Fig. XVI-1). Group B

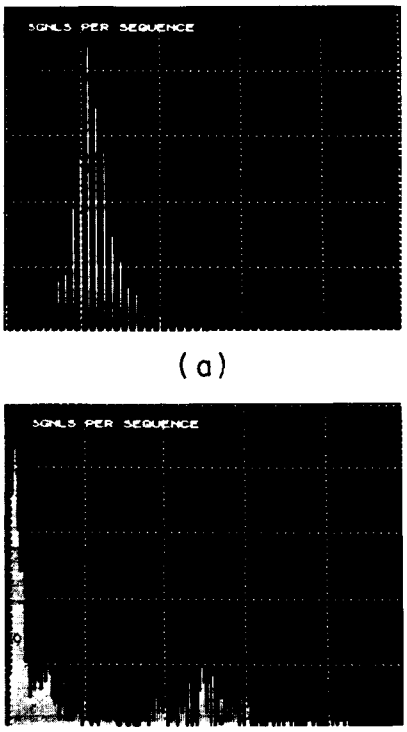

Fig. XVI-2.

Distribution of number of signals per sequence for (a) cerebellar and (b) telencephalic explants in vitro. Ordinate, number of sequences; abscissa, number of signals per sequence. In the cerebellum the peak is at 12 signals per sequence and in the telencephalon the peak is at 1 (spurious signals) and around 83.

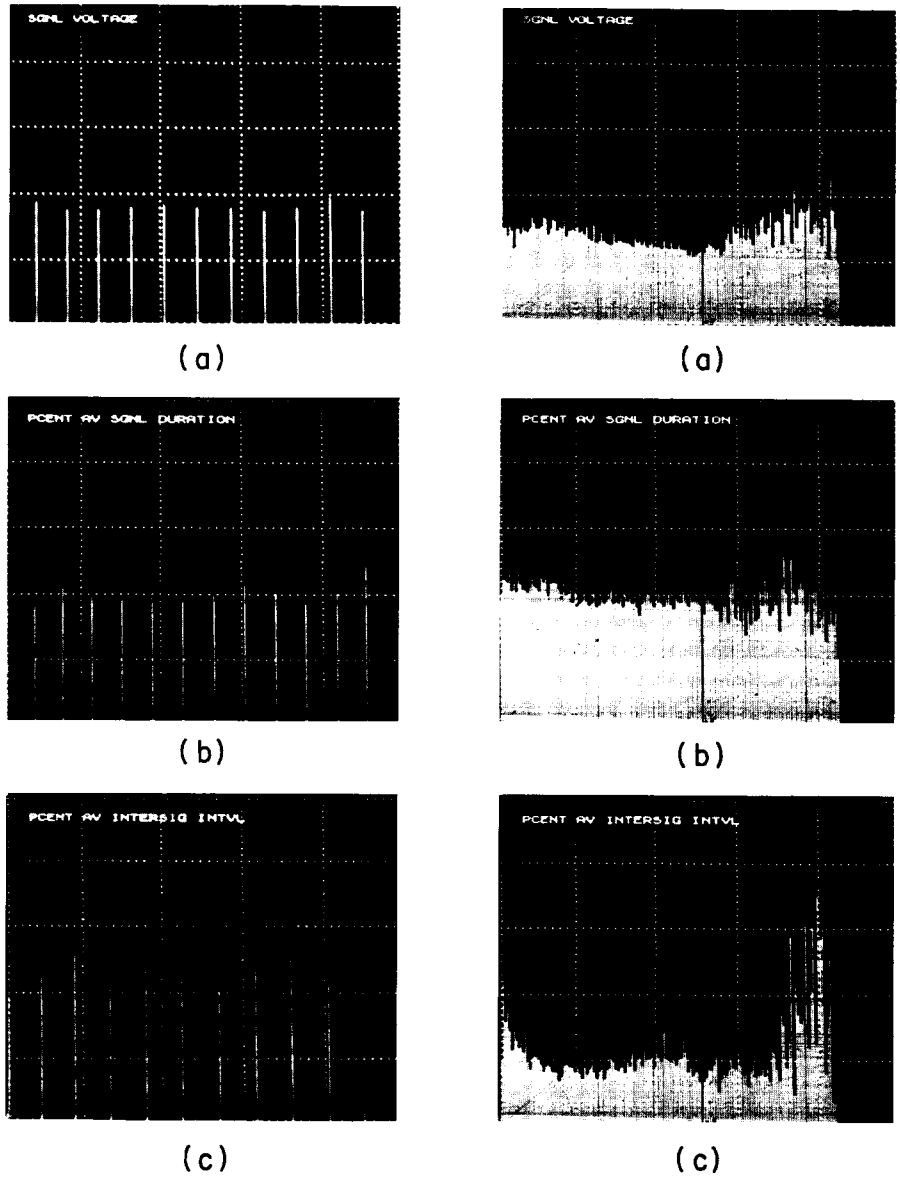

Fig. XVI-3. Comparison of the form of cerebellar and telencephalic signal sequences. Data from 200 sequences each with 12 signals were used for the cerebellum, and from 120 sequences containing between 64 and 152 signals were used for telencephalon. The original data for each signal in (b) and (c) were expressed as a percentage of the average value for the requisite parameter for the sequence in which the signal occurred. All values for the first signal were averaged, and the average is represented by the first continuous vertical line. Values for the second signal were averaged and represented by the second continuous vertical line, and so on. The final product is the average form of sequences for the tissue involved. Data for cerebellum are on the left, and the equivalent data for telencephalon on the right. For all cerebellar figures and for the per cent average duration in telencephalon, each division of the vertical axis represents 50%. In the other two figures each such division represents 100%. (a) Signal amplitude (× 80 for cerebellum and × 40 for telencephalon). (b) Duration of the signal. (c) Inter signal interval.

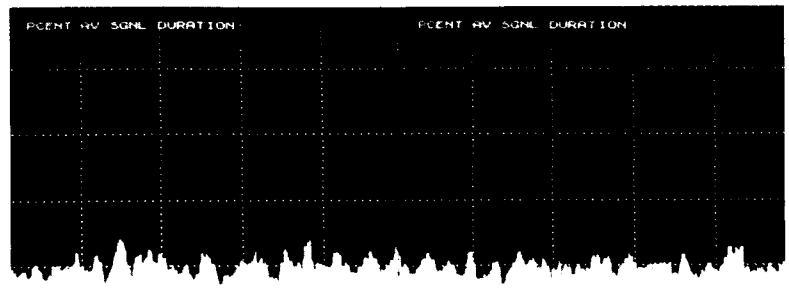

(a)

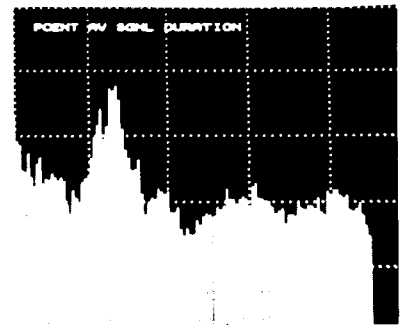

(b)

Fig. XVI-4. (a) Duration of the first signal of each of 1000 consecutive cerebellar sequences with 8-17 signals per sequence. This value is expressed as a percentage of the average for the sequence in which it occurs and the data have been smoothed by a 10-place moving average (each division of the vertical axis represents 100%).
(b) Duration of first signal of each of 120 consecutive telencephalic sequences containing 66-152 signals (the value is expressed as in (a)). This represents only 12% of the data in (a), and the vertical scale is twice as great. Considering the difference in scales, the degree of variation in the data is similar in cerebellum and telencephalon.

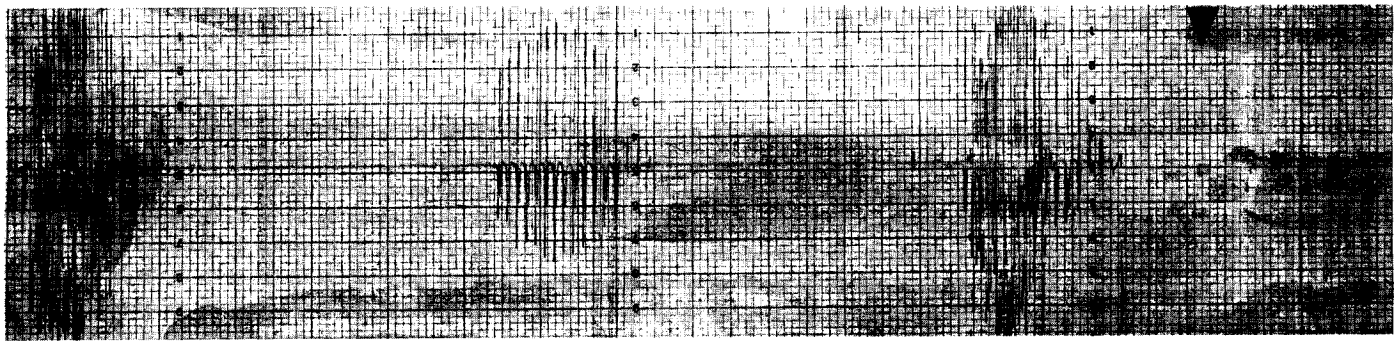

(a)

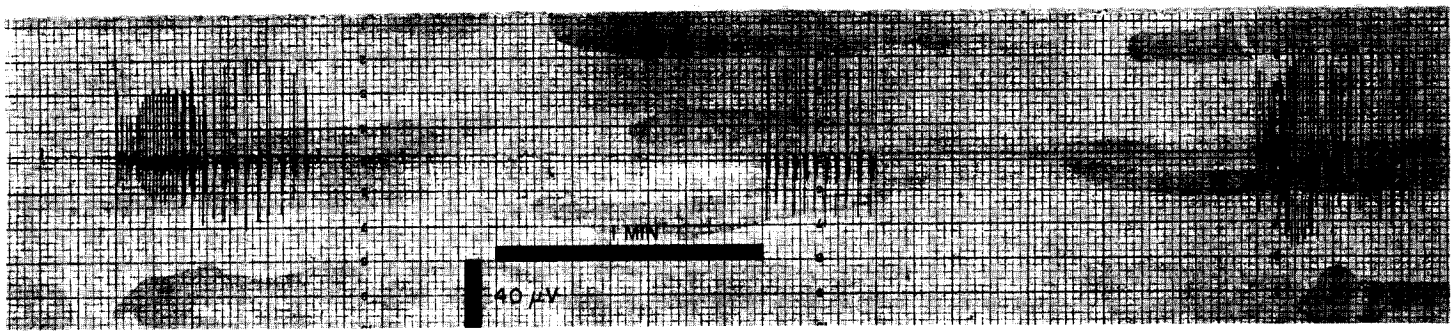

(b)

15 mcg/cc SODIUM
PHENOBARBITAL
PAPER SPEED 3"/MIN

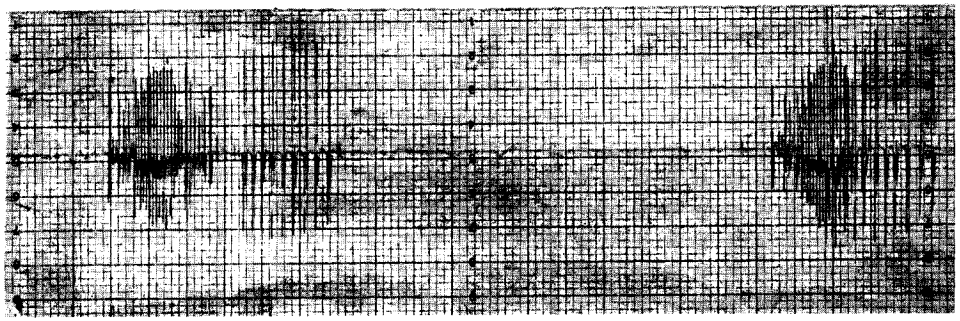

(c)

Fig. XVI-5. Effect of 15 mcg/cc Sodium Phenobarbital on the spontaneous activity from an explant of 15-day chick embryo telencephalon.

very seldom does (always being preceded by and perhaps even initiated by Group A activity). Group A activity changes much less with aging in culture and persists for some time after the Group B type of activity has disappeared. They respond differently to the administration of drugs, e.g., barbiturates. In Fig. XVI-5 the first three sequences represent the normal behavior of the explant. The first and the third sequences are composed of both Group A and Group B activity superimposed, whereas the second sequence is composed only of Group A activity. Between the third and fourth sequences Sodium Phenobarbital in a concentration of 15 mcg/cc of nutrient fluid is administered to the explant. The occurrence of the fourth sequence is delayed and the intervals between subsequent sequences are significantly increased. It can be seen that the two types of activity are affected to different degrees both in amplitude and in the interval between them.

Since Group A and Group B types of activity overlap in time, it is unlikely that they come from one cell. Either more than one type of originating cell is present or the product of a single originating cell is modified by at least one secondary functional cell. In either case more than one type of functional cell must be present and must contribute to the formation of the telencephalic sequence.

The average form of the sequences in terms of duration of signal, magnitude of signal, and interval between signals in an explant of telencephalon (Fig. XVI-3) shows much the same features as that of the individual sequences (Fig. XVI-1). It shows the same direct relationship between changes in amplitude, duration, and intersignal interval noted in cerebellum. There are progressive slow reduction in the duration of the signal and a sharp terminal increase in the intersignal interval. In metabolic terms, this may indicate temporary exhaustion of some metabolic material needed for signal production. Equally, it may be just the natural termination of a series of mutual exchanges of subthreshold stimuli with summation within a natural network of functional cells in the explant.

Occasionally, telencephalic explants show only Group A type of activity, in which case the average form and behavior of the sequence is very like that of cerebellar tissue.

The long-term activity from a single cluster of active cells in telencephalon in vitro is relatively stable over a period of up to a day (Fig. XVI-4b). Over longer periods of time, however, Group A activity is as stable as cerebellar activity (and thus it is possible that it arises from a similar type of cell), while Group B activity is less stable and alters considerably over periods of days.

3. Number of Signals per Sequence

The number of signals per sequence (Fig. XVI-1) in cerebellar explants is small (7-14) and does not vary much, whereas in telencephalon the number of signals per sequence is greater (up to 200, but usually between 40 and 120) as is the scatter. The number of signals per telencephalic sequence varies for several reasons. (a) Group A

activity often occurs on its own and contains a smaller number of signals than the full sequence. (b) Activity may be recorded from more than one active cluster of cells in any one explant and each such cluster may give rise to a different number and arrangement of signal (while retaining the general telencephalic pattern). (c) Extra single or double signals are much more frequent in telencephalic explants than in cerebellar explants.

Thus, as far as the form of the individual signal and of the natural sequences of signals is concerned, the spontaneous activity from cerebellum and telencephalon differs significantly, each having its own characteristic sequence behavior.

4. Multiple Electrode Studies

If an explant is placed on the cut end of an array of gross (40-gauge) platinum electrodes (insulated from each other and bound at ~100-μ separation into a microcable with Teflon), it is possible to monitor a wide area of the explant for the occurrence of spontaneous potentials. Such studies have shown that there may be several discrete active clusters of cells within a single explant, each with its own variant on the characteristic form of sequence for the tissue. They have also shown that the electrical disturbance associated with signal production does not spread uniformly through the tissue, but is directional, often being detectable by one electrode but not by its immediate neighbor.

5. Identification of the Cells of Origin of the Signals

In a previous publication[2] we have considered the similarity in the CNS response of the whole animal and of the spontaneous potentials from brain tissue in vitro to the administration of strychnine and barbiturates and the reversible effects of anesthetic gases, changes in oxygen, carbon dioxide and nitrogen concentrations and the temperature of the explant. We concluded that the activity must arise in living functional brain cells in the explant. It is necessary to identify these cells, to ascertain the part played by individual units in the activity of the whole explant and the inter-relationships between the activity of the several individual units. A combination of microelectrode and histological techniques is the obvious choice for this investigation.

Special culture chambers and a microscope stage incubator (to maintain the temperature and humidity in the environment of the explant) have been designed and built for this purpose (Fig. XVI-7). We decided to use Methylene Blue's well-known property of vitally staining the granules in neurons to identify them during functional activity. A concentrated solution of Methylene Blue in balanced salt solution is diluted one in a hundred parts in nutrient fluid and used in place of the regular nutrient fluid. The granules in the neurons at the surface of the tissue then become clearly visible while those in the depth of the tissue are also distinguishable. In any explant, only the cells within 0.2 mm of the surface oxygen and the same distance from a source of nutrient can survive – all

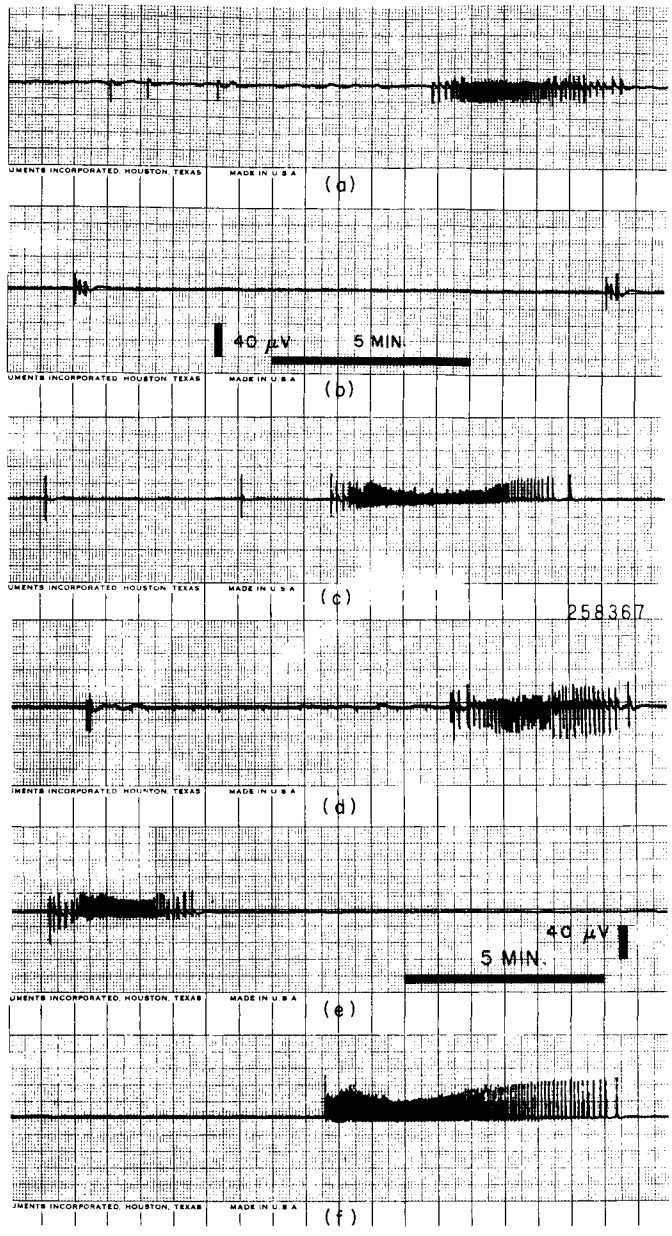

Fig. XVI-6. Activity of three separate explants of telencephalon from 14-day chick embryo 3 days in vitro before addition of Methylene Blue in (a), (b), and (c) and 7 1/2 hours after the addition of Methylene Blue (d), (e), and (f). Increase in magnitude of signals between (a) and (d) and (c) and (f) is obvious, as is the appearance of signals in (e) where none had been present for the previous 24 hours before which this explant had shown small sequences of signals.

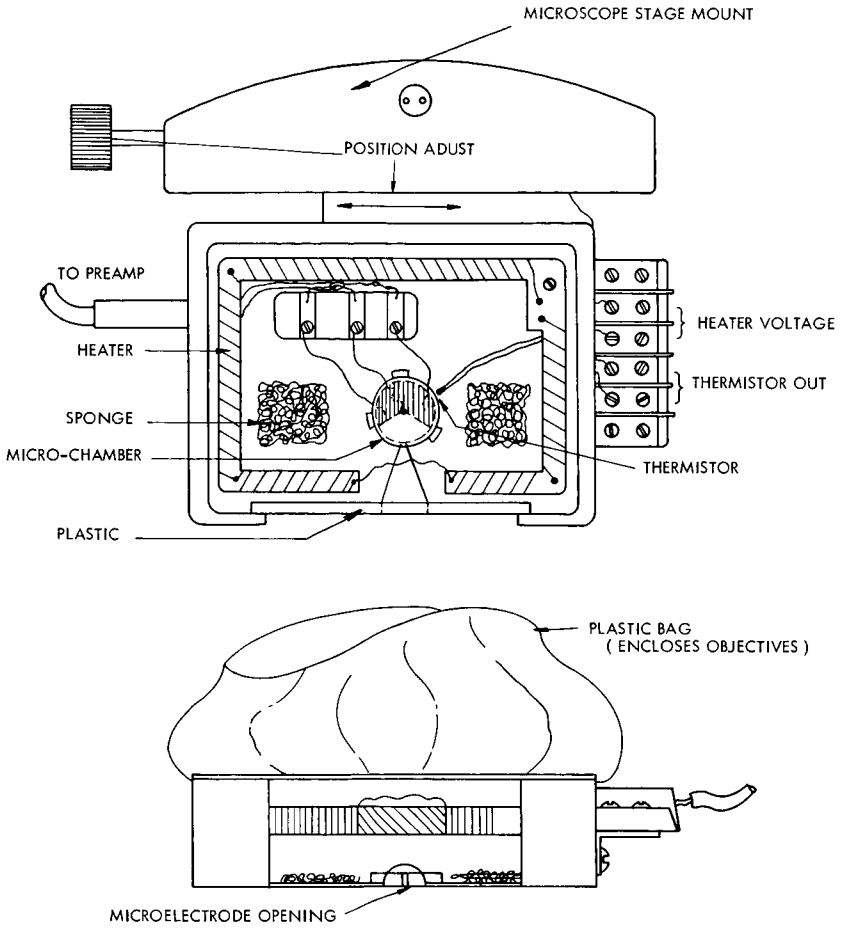

Fig. XVI-7. Microscope Stage Incubator: This has the purpose of ensuring proper temperature and humidity control for the microelectrode culture chamber described in this report. It must also be small enough to fit on the microscope stage without interfering with the freedom of movement of the stage or of the microscope objectives. The heating coil and temperature sensing and controlling devices are DC devices to minimize the background electrical noise and allow adequate recording of potential changes within explants. The humidity is supplied by a slow flow of air saturated with water vapor by being passed through air-washing bottles and then through a water trap so that water condensing in the conducting rubber tubing does not drip into the chamber. This flow of air also helps to ensure even distribution of heat within the incubator arrangement by overcoming the effects of radiation from the heating coils. Further humidification is achieved by evaporation from moist sponges in the chamber. The walls of the incubator are made from readily distorted plastic material to give a maximum of freedom of movement of the stage and rotation of the lenses. This plastic bag extends from the microscope objective collar to the lip of the microincubator.

such cells can be detected with the Methylene Blue technique. If necessary (and we have not had to use it yet), the fluorescence of Methylene Blue in ultraviolet light can be used to help identify the cells deep in the tissue. To avoid the damage to the tissue by the activating wavelengths of light, a technique such as the 'flying spot' microscope will have to be used. Methylene Blue was tested for toxic effects on the functional behavior of the explants, and (Fig. XVI-6a and XVI-6d, also Fig. XVI-6c and XVI-6f) the addition of this dye was found to cause a sustained increase in the magnitude of signals and the duration and complexity of sequences after a period of approximately 6 hours. Also, it caused the revival of spontaneous activity in explants where it has lapsed (Fig. XVI-6b and XVI-6e). The mode of this action of Methylene Blue is not known.

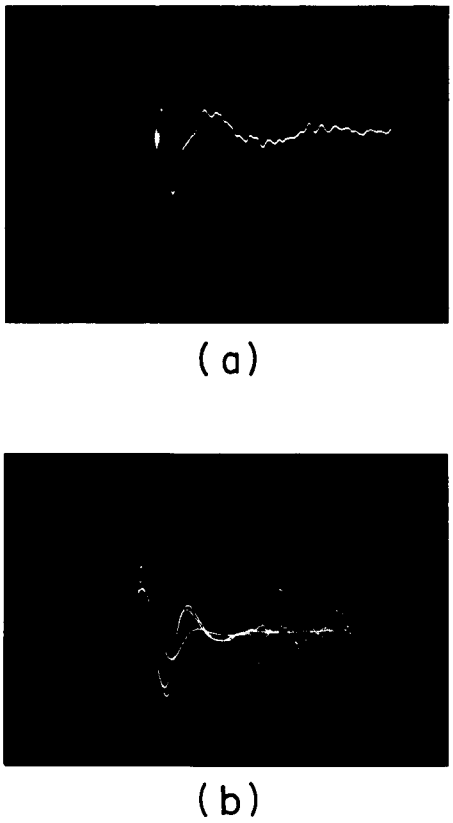

Fig. XVI-8. Five milliseconds of activity showing extracellular spikes of approximately 2 mvolts. The lower illustration shows several superimposed extracellular spikes.

6. Microelectrode Studies

By using the Methylene Blue technique, a microculture chamber, and the microscope stage incubator (see Fig. XVI-7) neurons have been visualized in explants of 14-day chick embryo telencephalon and penetrated with glass micropipettes (tip diameter, 0.2 μ). With a Medistor A35 negative resistance electrometer amplifier, membrane potentials (DC shifts) of 50 mv were observed on penetrating these cells. Spikelike spontaneous potentials of 20 mv, lasting 1-3 msec were obtained subsequently; work is in progress to ascertain if these were intracellular in origin. Some of these spikes were synchronous with those from the gross electrodes (occurring in the typical sequences). Others seemed to bear no time relation to the activity recorded with the gross electrodes. These potentials were similar to those obtained by Stanley Crain – after stimulation.

Extracellular potentials of 2-3 mv (Fig. XVI-8) were obtained during microelectrode penetrations (when the microelectrode tip was close to neurons). Many of these were in sequences similar in form,

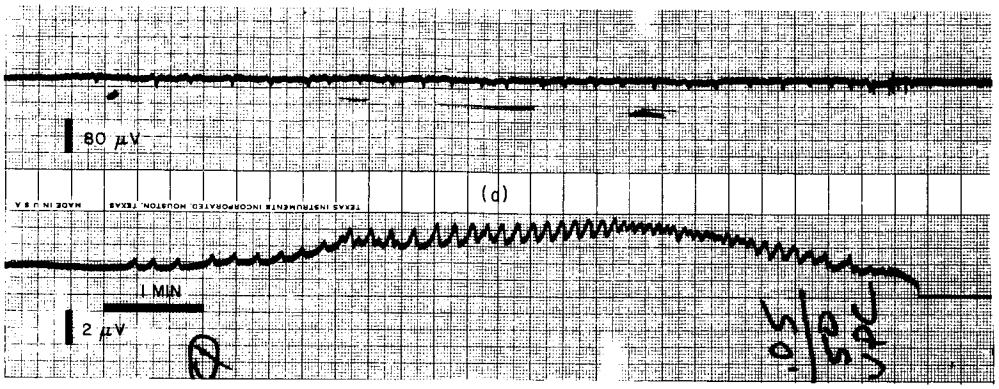

(b)

Fig. XVI-9. Simultaneous recordings from a gross 40-gauge platinum electrode with a Grass P511 R amplifier in (a) and extracellular microelectrode (0.2-μ tip diameter and ~50 MΩ resistance); a Medistor A-35 negative resistance electrometer amplifier and a differential DC Oscilloriter were used in (b).

duration, number of constituent signals, and intersequence intervals to those recorded with gross electrodes from the same explant (Fig. XVI-9). Each sequence recorded with microelectrodes was associated with a DC shift. "Group A" and "Group B" types of activity were recognizable, and when "Group A" type of activity occurred alone, it was associated with a small DC shift. This DC shift seems to be an integral part of the sequence and is more marked during the "Group B" type of activity than during the "Group A" activity. Thus there are functional neurons in the explant and, although much more work remains to be done, it seems likely from the similarities between the patterns of potentials obtained with gross electrodes and with microelectrodes placed close to visually identifiable neurons, that these neurons participate in the phenomenon that we are investigating (see Fig. XVI-10).

7. Computer Processing of Data

During experiments, the activity from explants is recorded on analog tape with Grass P511 R amplifiers (or for DC recordings, the Medistor amplifier described above). These analog tapes are processed by using programs written for the PDP 4 computer and accessory equipment that is available in our laboratory. Figures XVI-2, XVI-3, and XVI-4 are the product of this computer processing of data.

In summary, the signals and the signal groups occurring spontaneously in explants of chick embryo telencephalon and cerebellum in vitro have been described. Each has its own characteristic features and we conclude that in telencephalon at least two types of functional brain cells must be involved. Evidence has been given for the presence of living neurons in the explants and for their participation in the formation of the

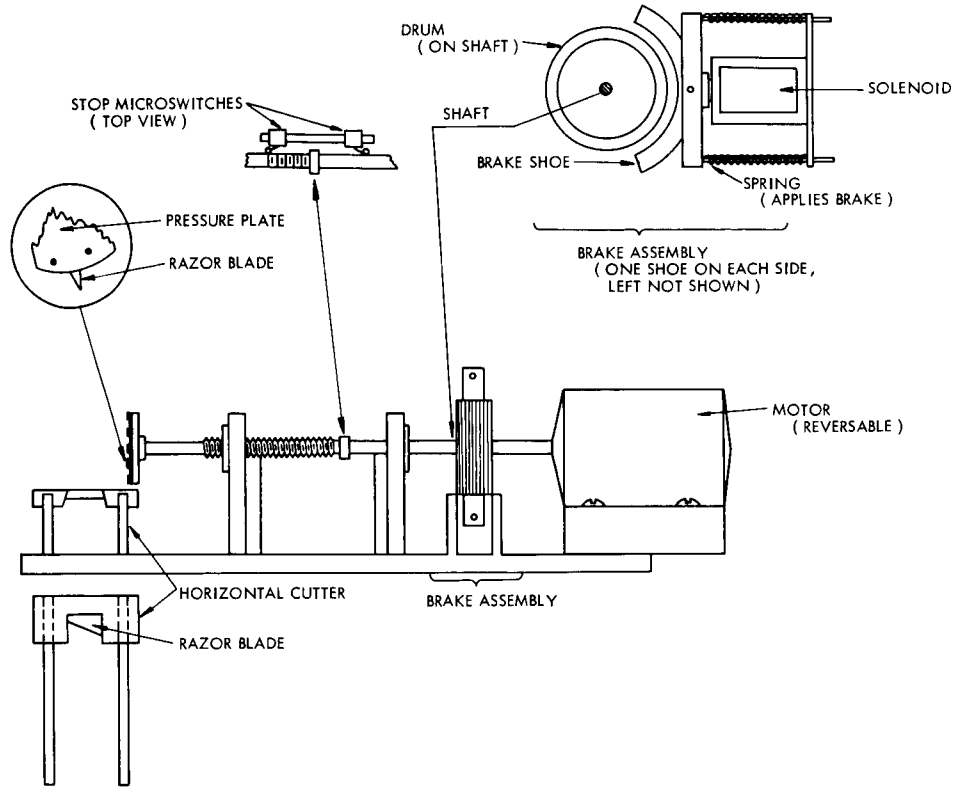

Fig. XVI-10. Automatic Explant Cutter: This provides uniformly thick slices of brain tissue rapidly and with a minimum of distortion. It is now used with chick embryo brain tissue. The chick with its brain exposed and cooled in a stream of cold nutrient fluid is placed between the guide channels for the horizontal blade of the cutter and under the rotatory blade. It is positioned precisely with the aid of a simple optical system that aligns the upper surface of the area of brain to be cut with the upper portion of the razor blade inserted in the rotatory wheel. Thus the depth of cut is controlled and the wheel itself cannot injure the brain. A reversible electric motor drives a threaded shaft by means of a sliding keyway, thereby allowing the threaded shaft to advance while the motor remains stationary. The cutting blade is a piece of razor blade held in a wheel at the end of the threaded shaft. This blade advances through the brain as it rotates and cuts nearly vertical slices. The thickness of the cut can be varied by using different threaded shafts or by placing two or three blades in the cutting wheel. The blade cannot over-run its course because it is stopped by a safety microswitch that is tripped automatically as the end of the thread approaches the front bushing. The blade can be stopped either by pressing a push-button manually or depressing a floor switch. The blade is stopped rapidly even at high speeds by the solenoid activation of the clamping of 2 spring-loaded brake shoes onto a 3-inch aluminum drum mounted on the drive shaft directly ahead of the motor. In this way, the blade can be halted within one revolution. Once the vertical cuts have been made, the horizontal blade is slid rapidly across the section of the brain that has already been cut vertically, and the slices of brain are carried forward with the horizontal blade and can be washed from its upper surface into a Petri dish.

spontaneous potentials. Techniques have been described which offer an almost two-dimensional display of functional brain cells in an active living network, where each cell can be directly visualized.

A. W. B. Cunningham, R. R. Rojas Corona, J. A. Freeman, P. H. Levine

References

1. A. W. B. Cunningham, "Spontaneous Potentials from Explants of Human Adult Cerebellum in Culture," Nature 190, 918 (1961).
2. A. W. B. Cunningham, "Qualitative Behavior of Spontaneous Potentials from Explants of 15-Day Chick Embryo Telencephalon in Vitro," J. Gen. Physiol. 45, 1074 (1962).
3. R. W. Gerard and J. Z. Young in Proc. Roy. Soc. (London) 122B, 343 (1937).
4. E. D. Adrian and F. J. J. Burtendijk, J. Physiol. 71, 121 (1931).
5. E. D. Arian, J. Physiol. 72, 132 (1931).
6. A. W. B. Cunningham and B. J. Rylander, "Behavior of Spontaneous Potentials from Chick Cerebellar Explant During 120 Hours in Culture," J. Neurophysiol. 24, 141 (1961).

XVII. COMPUTATION RESEARCH*

Martha M. Pennell
Gail M. Fratar
R. L. Rappaport
Veronica E. McLoud
Kathleen A. Szabo

A. GENERALIZED POLYNOMIAL ROOT-FINDING PROGRAM FOR A TIME-SHARED COMPUTER

The availability of the Project MAC time-sharing system[1] has enabled us to write a computer program, called Quixot Dulcin (see below), which in turn automatically writes, compiles and executes a MAD[2] program to find roots of polynomials whose coefficients may be expressed symbolically as functions of variables called parameters. There may be any number of parameters and the user has the option of declaring one of these to be varying. At execution time the program loops around the value of this parameter thus enabling the user to compute the functional dependence of the roots.

To use this program all one needs to know is how to write his coefficients as MAD arithmetic expressions[3] and how to operate his remote console. Quixot Dulcin leads the user through a series of questions and from his responses creates the necessary MAD code. Only in a time-sharing environment is such an approach feasible. In their studies of dispersion relations, members of the Plasma Electronics Group have made such extensive use of Quixot Dulcin that we no longer have any requests to program such a problem.

The user is first queried for the degree of his polynomial (it must be ≤ 19) and the name he wishes his program to have so that he may refer to it in the future. He then is asked to state the symbols (6 or less alphanumeric characters) he wishes to use for his parameters. Next he is asked for the MAD algebraic expression for the real and imaginary part of each coefficient. These expressions are functions of the symbols he has just typed in and may contain the following: sine, cosine, square root, arctangent, arcosine, absolute value. With this information Quixot Dulcin writes a program in the MAD language and tries to translate it into the equivalent binary code. If, however, the user has typed in an incorrect MAD expression (i.e., an incomplete set of parentheses or a missing operation), Quixot Dulcin enters a correction mode whereby the user may make the necessary changes and a second try to compile the binary code is attempted. The correction mode is entered and re-entered automatically until the binary code is created. Quixot Dulcin then loads this program and transfers control to it. Immediately the user is asked for the numerical values for each of the parameters whose symbols he had just previously typed in. The program then computes the coefficients and roots, and types them both on the user's console. The user is then asked for the next value of the parameter he had declared to be varying. One push on the break button enables him to

*This work was supported in part by the National Science Foundation (Grant GK-524).

```
LOADGO QUIXOT DULCIN
W 2331.7
EXECUTION.
COMPLEX ROOTS OF A COMPLEX POLYNOMIAL, GIVEN ALGEBRAIC COEFFICIENTS
WHAT WOULD YOU LIKE TO NAME YOUR PROGRAM.  (SIX LETTERS OR LESS, PLEASE.)
   ***   ***   ***   ***
*** BE CAREFUL*** FOR IF THERE ARE ANY EXISTING FILES WITH THIS FIRST NAME,
THEY WILL BE DESTROYED
   ***   ***   ***   ***
TEST
TYPE THE DEGREE OF YOUR POLYNOMIAL AS A TWO-DIGIT INTEGER,E.G. 12 OR 05
03
DO NOT USE AS PARAMETER NAMES 'I' AND      'DEG'
TYPE THE NAME OF THE VARYING PARAMETER.
ALPHA
TYPE THE NAMES OF ALL OTHER PARAMETERS, ONE PER LINE, THEN SKIP A LINE.
BETA
GAMMA

COEFFICIENTS--SKIP A LINE AFTER TYPING EACH COEFFICIENT.
DO NOT TYPE PAST POSITION MARKED BY                    *
TYPE REAL ALGEBRAIC COEFFICIENT OF THE  0 POWER.       *
ALPHA+BETA+GAMMA

TYPE IMAG ALGEBRAIC COEFFICIENT OF THE  0 POWER.       *
2.+SQRT.(ALPHA*ALPHA)

TYPE REAL ALGEBRAIC COEFFICIENT OF THE  1 POWER.       *
3.

TYPE IMAG ALGEBRAIC COEFFICIENT OF THE  1 POWER.       *
0.

TYPE REAL ALGEBRAIC COEFFICIENT OF THE  2 POWER.       *
-GAMMA+5.

TYPE IMAG ALGEBRAIC COEFFICIENT OF THE  2 POWER.       *
0.

TYPE REAL ALGEBRAIC COEFFICIENT OF THE  3 POWER.       *
0.

TYPE IMAG ALGEBRAIC COEFFICIENT OF THE  3 POWER.       *
-BETA

DO YOU WANT TO MAKE CORRECTIONS
NO
 FILE   TEST   MAD CREATED
LENGTH 00407.  TV SIZE 00012.  ENTRY 00151
   ***   ***   ***   ***
```

```
IN ØRDEP TØ RERUN YØUR PRØGRAM IN THE FUTURE, YØU MUST TYPE THE FØLLØWING SEQUENCE.
LØADGØ   TEST BUTTØN MADINT RØØTS
   ***   ***   ***   ***
EXECUTIØN.
PRESS 'BREAK' BUTTØN TØ CHANGE PARAMETERS.
TYPE  BETA
.1
TYPE  GAMMA
-.2
TYPE  ALPHA
3.


CØEFFICIENTS

 PØWER   REAL          IMAG

    0   .29000E 01    .50000E 01
    1   .30000E 01    .00000E 00
    2   .52000E 01    .00000E 00
    3   .00000E 00  -1.00000E-01

  3 RØØTS
      REAL            IMAG
     .558653E 00    -.519951E 02
    -.819058E 00     .881453E 00
     .260404E 00    -.886375E 00

TYPE  ALPHA
2.


CØEFFICIENTS

 PØWER   REAL          IMAG

    0   .19000E 01    .40000E 01
    1   .30000E 01    .00000E 00
    2   .52000E 01    .00000E 00
    3   .00000E 00  -1.00000E-01

  3 RØØTS
      REAL            IMAG
     .562232E 00    -.519989E 02
    -.793484E 00     .745879E 00
     .231252E 00    -.746986E 00

TYPE  ALPHA
> QUIT,
R  26.816+19.800
```

change the values of all the parameters; two pushes ends the program.

The subroutine which actually computes the roots is Share Distribution No. 692 modified for use on the time-sharing system. It uses Muller's Method.[4] The main control program written in MAD works as follows. MAD statements are created from the MAD expressions that the user has typed in. These statements are inserted between already existing MAD statements which query the user for his numerical values and MAD statements to compute and print out the answers.

Currently work is being done to improve both the accuracy and the speed of the subroutine to compute the roots. In addition a second program is being checked out which will enable the user to type in a complex algebraic expression for his coefficients, i.e., he will not have to perform the algebra to separate his coefficients into their real and imaginary parts.

Martha M. Pennell

References

1. C. Marceau, a former member of the Research Laboratory of Electronics, wrote the original program.
2. B. Arden, B. Galler, and R. Graham, "The Michigan Algorithm Decoder," University of Michigan, April 1965.
3. Ibid, p. 12.
4. D. E. Muller, "A Method for Solving Algebraic Equations Using an Automatic Computer," Mathematical Tables and Other Aids to Computation (National Research Council, Washington, D.C., October 1956), pp. 208-215.

Author Index

Algazi, V. R., 179,185
Andrews, J. M., Jr., 6,7
Azevedo, J. C. A., 94
Barrett, A. H., 30
Bers, A., 99,104,107,113
Bose, A. G., 177
Breeding, R. J., 47
Brown, G. A., 149,152
Clarke, J. F., 134,139
Clemens, J. K., 219
Cunningham, A. W. B., 247
DeWolf, J. B., 45
Doane, J. L., 64
Donaldson, R. W., 227,237
Engelmaier, W., 156
Fiocco, G., 43,45
Fukumoto, A., 14
Geick, R., 37
Halverson, W. D., 43
Haus, H. A., 51
Hoffman, M. A., 167
Hooper, E. B., Jr., 77
Huang, T. S., 211,214
Jackson, W. D., 152
Kennedy, R. S., 205
Kerrebrock, J. L., 167
Kolers, P. A., 207
Kyhl, R. L., 5
Landsman, E., 216
Lee, Y. W., 177
Lenoir, W. B., 17
Lidsky, L. M., 131
Lieberman, M. A., 118,126
Loewenthal, M., 34
Logan, R. M., 67
Lubin, B. T., 149
Lubin, M. D., 133
McNary, C. A., 175
Moir, R. W., 131
Musha, T. 99,104
Nelsen, D. E., 191
Nolan, J. J., 83
Offenberger, A. A., 145
Pauwels, H. J., 58
Pennell, Martha M., 263
Robertson, E. A., 107
Rogers, A. E. E., 30
Rosenthal, Kathryn F., 229
Sachs, W. D., 152
Samis, M. A., 143
Schetzen, M., 177,178,179
Solbes, A., 167
Snyder, D. L., 199
Speck, C. E., 113
Stickney, R. E., 67,156
Strandberg, M. W. P., 5
Touchstone, G. E., 207
Tretiak, O. J., 211
Vander Vorst, A. S., 19
Van Trees, H. L., 178
Waletzko, J. A., 95
Willke, H. L., Jr., 73
Yamaguchi, Y., 214

JOINT SERVICES DISTRIBUTION LIST

Department of Defense

Defense Documentation Center
Attn: TISIA
Cameron Station, Bldg. 5
Alexandria, Virginia 22314

Director, National Security Agency
Attn: C3/TDL
Fort George G. Meade, Maryland 20755

Mr. Charles Yost, Director
For Materials Sciences
Advanced Research Projects Agency, DOD
Washington, D.C. 20301

Director
Advanced Research Projects Agency
Department of Defense
Washington, D.C. 20301

Dr. James A. Ward
Office of Deputy Director (Research and Information Rm. 3D1037) DOD
The Pentagon
Washington, D.C. 20301

Dr. Edward M. Reilley
Asst. Director (Research)
Ofc of Defense Res. & Eng., DOD
Washington, D.C. 20301

Department of the Army

Librarian PTA130
United States Military Academy
West Point, New York 10996

Director
U.S. Army Electronics Laboratories
Fort Monmouth, New Jersey 07703
Attn: AMSEL-RD-ADT

	NP	SE
DR	NR	SR
FU#1	PE	SS
GF	PF	X
NE	PR	XC
NO	SA	XE
		XS

Commanding General
U.S. Army Electronics Command
Attn: AMSEL-SC
Fort Monmouth, New Jersey 07703

C.O., Harry Diamond Laboratories
Attn: Mr. Berthold Altman
Connecticut Ave. & Van Ness St. N.W.
Washington, D.C. 20438

The Walter Reed Institute of Research
Walter Reed Army Medical Center
Washington, D.C. 20012

Director
U.S. Army Electronics Laboratories
Attn: Mr. Robert O. Parker, Executive Secretary, JSTAC (AMSEL-RD-X)
Fort Monmouth, New Jersey 07703

Director
U.S. Army Electronics Laboratories
Attn: Dr. S. Benedict Levin, Director Institute of Exploratory Research
Fort Monmouth, New Jersey 07703

Commanding Officer
U.S. Army Research Office (Durham)
Attn: CRD-AA-IP (Richard O. Ulsh)
P.O. Box CM, Duke Station
Durham, North Carolina 27706

Commanding Officer
U.S. Army Medical Research Laboratory
Fort Knox, Kentucky

Commanding Officer
U.S. Army Personnel Research Office
Washington, D.C.

Dr. H. Robl, Deputy Director
U.S. Army Research Office (Durham)
P.O. Box CM, Duke Station
Durham, North Carolina 27706

Commandant
U.S. Command and General Staff College
Attn: Secretary
Fort Leavenworth, Kansas 66207

Director
U.S. Army Eng. Geodesy, Intell. and Mapping
Research & Development Agcy.
Fort Belvoir, Virginia 22060

Commanding Officer
Human Engineering Laboratories
Aberdeen Proving Ground, Maryland 21005

Commanding Officer
U.S. Limited War Laboratory
Attn: Technical Director
Aberdeen Proving Ground, Maryland 21005

Commanding Officer
U.S. Army Security Agency
Arlington Hall, Arlington, Virginia 22212

C.O., Harry Diamond Laboratories
Attn: Dr. R. T. Young, Elec. Tubes Div.
Connecticut Ave. & Van Ness St., N.W.
Washington, D.C. 20438

U.S. Army Munitions Command
Attn: Technical Information Branch
Picatinney Arsenal
Dover, New Jersey 07801

Commanding General
Frankford Arsenal
Attn: SMUFA-1310 (Dr. Sidney Ross)
Philadelphia, Pennsylvania 19137

Commanding General
U.S. Army Missile Command
Attn: Technical Library
Redstone Arsenal, Alabama 35809

Commandant
U.S. Army Air Defense School
Attn: Missile Sciences Division, C&S Dept.
P.O. Box 9390
Fort Bliss, Texas 79916

Commanding Officer
U.S. Army Ballistics Research Lab.
Attn: V.W. Richards
Aberdeen Proving Ground
Aberdeen, Maryland 21005

Commanding Officer
U.S. Army Materials Research Agency
Watertown Arsenal
Watertown, Massachusetts 02172

Commanding General
U.S. Army Strategic Communications Command
Washington, D.C. 20315

Commanding General
U.S. Army Materiel Command
Attn: AMCRD-RS-PE-E
Washington, D.C. 20315

Commanding Officer
Foreign Service & Technology Center
Arlington Hall
Arlington, Virginia

Research Plans Office
U.S. Army Research Office
3045 Columbia Pike
Arlington, Virginia 22204

Chief of Research and Development
Headquarters, Department of the Army
Attn: Physical Sciences Division P&E
Washington, D.C. 20310

Director
Human Resources Research Office
The George Washington University
300 N. Washington Street
Alexandria, Virginia 22314

Commanding Officer
U.S. Army Electronics R&D Activity
White Sands Missile Range
New Mexico 88002

Commanding Officer
U.S. Army Engineers R&D Laboratory
Attn: STINFO Branch
Fort Belvoir, Virginia 22060

Commanding Officer
U.S. Army Electronics R&D Activity
Fort Huachuca, Arizona 85163

Mr. Alvin D. Bedrosian
Room 26-131
Massachusetts Institute of Technology
Cambridge, Massachusetts 02139

Department of the Air Force

Battelle Memorial Inst.
Technical Library
505 King Avenue
Columbus, Ohio 43201

Goddard Space Flight Center
NASA
Greenbelt, Maryland 20771

Research and Tech. Div. (AFAPL)
Attn: APIE-2, Mr. Robert F. Cooper
Wright-Patterson AFB, Ohio 45433

Technical Library
White Sands Missile Range
New Mexico 88002

AFSC (Tech Library)
Andrews AFB
Washington, D.C. 20031

AUL-3T-9663
Maxwell AFB
Alabama 36112

JOINT SERVICES DISTRIBUTION LIST (continued)

DDR&E (Tech Library)
Rm. 3C 128
The Pentagon
Washington, D.C. 20301

Systems Engineering Group
Deputy for Systems Eng'g., SEPRR
Directorate of Tech. Pubs. & Specs.
Wright-Patterson AFB, Ohio 45433

APGC (PGBAP-1)
Eglin AFB
Florida 32542

RTD (Tech Library)
Bolling AFB
District of Columbia 20332

BSD (Tech Library)
Norton AFB
California 92409

ASD (Tech Library)
Wright-Patterson AFB
Ohio 45433

Industrial College of the Armed Forces
Attn: Library
Washington, D. C.

Southwest Research Institute
Library
8500 Culebra Road
San Antonio, Texas

Stanford Research Institute
Library
820 Mission St.
South Pasadena, Calif. 91030

Library
National Science Foundation
Washington 25, D.C.

Linda Hall Library
5109 Cherry St.
Kansas City, Mo.

Dr. H. Harrison
NASA (Code RRE)
Fourth and Independence Sts.
Washington, D.C. 20546

Mr. James Tippett
National Security Agency
Fort Meade, Maryland

Brig. Gen. J. T. Stewart
Director of Science & Technology
Deputy Chief of Staff (R&D)
USAF
Washington 25, D.C.

Dr. R. L. Sproull, Director
Advanced Research Projects Agency
Washington 25, D.C.

Lt. Col. Edwin M. Myers
Headquarters USAF (AFRDR)
Washington 25, D.C.

Dr. John M. Ide
Div. Director for Eng'g.
National Science Foundation
Washington 25, D.C.

Dr. Zohrab Kaprielian
University of Southern California
University Park
Los Angeles 7, California

Dr. Lowell M. Hollingsworth
AFCRL
L. G. Hanscom Field
Bedford, Massachusetts

Professor Nicholas George
California Institute of Technology
EE Department
Pasadena, California

Hon. Alexander H. Flax
Asst. Secretary of the Air Force
Office of the Secretary of the Air Force
(R&D)
Washington 25, D.C.

Prof. Arwin Dougal
University of Texas
EE Department
Austin, Texas

Mr. Roland Chase
National Aeronautics & Space Admin.
1512 H Street, N.W.
Washington 25, D.C.

AFAL (AVTE)
Wright-Patterson AFB
Ohio 45433

Systems Engineering Group (RTD)
Attn: SEPIR
Wright-Patterson AFB
Ohio 45433

JOINT SERVICES DISTRIBUTION LIST (continued)

AFAPL (APIE-2, Lt. Barthelmey)
Wright-Patterson AFB, Ohio. 45433

Rome Air Dev. Center (RAWL, H. Webb)
Griffiss Air Force Base, New York 13442

S. H. Sternick
Aerospace Com - Attn: ESNC
Waltham Federal Center
424 Trapelo Road
Waltham, Massachusetts 02154

AFCRL (CRFE-Dr. Nicholas Yannoni)
L. G. Hanscom Field
Bedford, Massachusetts

Mr. Rocco H. Urbano, Chief
AFCRL, Appl Math. Branch
Data Sciences Laboratory
Laurence G. Hanscom Field
Bedford, Massachusetts

AFCRL
Office of Aerospace Res., USAF
Bedford, Mass.
Attn: CRDA

Dr. Louis C. Block
AFCRL (CROO)
Laurence G. Hanscom Field
Bedford, Massachusetts 01731

Commander, AFCRL
Attn: C. P. Smith (CRBS)
L. G. Hanscom Field
Bedford, Massachusetts

AFETR (Tech Library MU-135)
Patrick AFB, Florida 32925

Mr. C. N. Hasert
Scientific Advisory Board
Hq. USAF
Washington 25, D. C.

Dr. Harvey E. Savely, SRL
Air Force Office of Sci. Res.
Office Aerospace Research, USAF
Washington 25, D. C.

Department of the Air Force
Headquarters, United States Air Force
Washington 25, D. C.
Attn: AFTAC/TD-1

John Crerar Library
35 West 33rd St.
Chicago, Ill.

LOOAR (Library)
AF Unit Post Office
Los Angeles, Calif. 90045

Office of Research Analyses
Library
Holloman AFB, New Mexico 88330

Office of Research Analyses
Attn: Col. K. W. Gallup
Holloman AFB, New Mexico 88330

ARL (ARD/Col. R. E. Fontana)
Wright-Patterson AFB
Ohio 45433

Brig. Gen. B. G. Holzman, USAF (Ret.)
National Aeronautics and Space Admin.
Code RS
Washington, D. C. 20546

AFRST (SC/EN)
Lt. Col. L. Stone
Room 4C 341
The Pentagon
Washington, D. C. 20301

Commander
Rome Air Development Center
AFSC
Office of the Scientific Director
Griffiss AFB, Rome, New York

Commander
Research & Technology Division (AFSC)
Office of the Scientific Director
Bolling AFB 25, D. C.

Commander
Air Force Systems Command
Office of the Chief Scientist
Andrews AFB, Maryland

Commander
Air Force Cambridge Research Lab.
Office of the Scientific Director
L. G. Hanscom Field
Bedford, Massachusetts

Commander
Aerospace Research Laboratories (OAR)
Office of the Scientific Director
Wright-Patterson AFB, Ohio

Commander, Aerospace Systems Division
AFSC
Office of the Scientific Director
Wright-Patterson AFB, Ohio

JOINT SERVICES DISTRIBUTION LIST (Continued)

Commander
Space Systems Division (AFSC)
Office of the Scientific Director
Inglewood, California

Dr. G. E. Knausenberger
c/o Hq Co. Munich Post
APO 09407, New York, N.Y.

AVCO Research Lab, Library
2385 Revere Beach Parkway
Everett, Mass. 02149

California Institute of Technology
Aeronautics Library
1201 East California St.
Pasadena 4, Calif. 91102

Carnegie Institute of Technology
Science & Engineering Hunt Library
Schenley Park
Pittsburgh, Pa. 15213

Rand Corporation
1700 Main St.
Santa Monica, Calif. 90401

Aerospace Corp. (Tech Library)
P.O. Box 95085
Los Angeles, Calif. 90045

Lewis Research Center (NASA)
Technical Library
21000 Brookpark Road
Cleveland, Ohio

George C. Marshall Space Flight Center
(NASA)
Redstone Arsenal, Ala. 35808

High Speed Flight Center (NASA)
Technical Library
Edwards AFB, Calif. 93523

Ames Rsch. Center (NASA)
Technical Library
Moffett Field, Calif. 94035

CIA OCR/LY/IAS
IH 129 HQ
Washington, D.C. 20505

RADC (Tech Library)
Griffiss AFB, N.Y. 13442

AEDC (Tech Library)
Arnold AFS
Tennessee 37389

APGC (Tech Library)
Eglin AFB
Florida 32542

AFWL (WLIL, Technical Library)
Kirtland Air Force Base
New Mexico 87117

AFMDC (Tech Library)
Holloman AFB
New Mexico 88330

AFFTC (Tech Library)
Edwards AFB
California 93523

Space Systems Division
Los Angeles Air Force Station
Air Force Unit Post Office
Los Angeles, California 90045
Attn: SSSD

Churchill Research Range
Library
Fort Churchill
Manitoba, Canada

National Defense Library
Headquarters
Ottawa, Ontario, Canada

Director
National Aeronautical Establishment
Ottawa, Ontario, Canada

EDS (ESTI)
Laurence G. Hanscom Field
Bedford, Massachusetts 01731

Johns Hopkins University
Applied Physics Lab., Library
White Oak, Silver Spring, Maryland 20919

Los Alamos Scientific Lab
Attn: Technical Library
Los Alamos, New Mexico 87544

ARL (AROL)
Wright-Patterson AFB
Ohio 45433

Frank J. Seiler Rsch. Lab.
Library
USAF Academy, Colo. 80840

U.S. Atomic Energy Commission
Library
Gaithersburg, Maryland 20760

AFAL
AVR(L)
Wright-Patterson AFB
Ohio 45433

Air Force Cambridge Res. Lab.
L. G. Hanscom Field
Bedford, Massachusetts 01731
Attn: CRDM, Mr. Herskovitz

Commander
Air Force Office of Scientific Research
Washington 25, D.C.
Attn: SREE

Director
Air University Library
Maxwell A. F. Base, Alabama

NASA/AFSS/1 FOB6
Tech Library, Rm. 60084
Washington, D.C. 20546

USAFA (DLIB)
U. S. Air Force Academy
Colorado

ARPA
Tech Info Office
The Pentagon
Washington, D.C. 20301

AFCRL(CRXL)
L. G. Hanscom Field
Bedford, Mass. 01731

U. S. Regional Sci. Office (LAOAR)
U. S. Embassy
APO 676, New York, N. Y.

AEC
Div. of Tech Info. Ext.
P. O. Box 62
Oak Ridge, Tennessee

Dr. Hermann H. Kurzweg
Director of Research - OART
NASA
Washington, D.C. 20546

AFIT (MCLI)
Tech Library
Wright-Patterson AFB, Ohio 45433

Prof. W. H. Radford
Lincoln Laboratory, A-183
244 Wood Street
Lexington, Massachusetts

Department of the Navy

Chief of Naval Operations
Pentagon OP 07T
Washington, D.C.

Commanding Officer
Office of Naval Research Branch Office
Navy 100, Fleet P.O. Box 39
New York, New York

Library
U. S. Navy Electronics Lab.
San Diego, California 92152

Commander
U. S. Naval Air Development Center
Johnsville, Pennsylvania
Attn: NADC Library

Commanding Officer
Office of Naval Research Branch Office
495 Summer Street
Boston, Massachusetts 02110

Commanding Officer
U. S. Navy Underwater Sound Laboratory
Ft. Trumbull, New London, Connecticut

U. S. Navy Post Graduate School
Monterey, California
Attn: Electrical Engineering Department

Commander, Naval Ordnance Laboratory
White Oak, Maryland
Attn: Technical Library

Chief, Bureau of Ships, Attn: Code 680
Department of the Navy
Washington, D.C. 20360

Chief, Bureau of Weapons
Department of the Navy
Washington, D.C. 20360

Dr. Arnold Shostak, Code 427
Head, Electronics Branch
Physical Sciences Division
Office of Naval Research
Washington, D.C. 20360

Chief of Naval Research, Code 427
Department of the Navy
Washington, D.C. 20360

Director
Naval Research Laboratory
Washington, D.C. 20390